Numerical and Experimental Constraints on Trace Element Fractionation During Lunar Magma Ocean Solidification

A Thesis Presented for the
Master of Science
Degree
The University of Tennessee, Knoxville

Dian Ji
August 2023

Copyright © 2023 by Dian Ji
All rights reserved.

DEDICATION

I would like to dedicate this thesis to my beloved dog, Duoduo. I am sorry that I was not with you when you passed away, may you rest in peace.

ACKNOWLEDGEMENTS

I would like to first thank my advisor, Dr. Nicholas Dygert. He is an erudite advisor, as he always has an in-depth view of scientific issues. He is excellent at guiding my thinking, never imposing his ideas on me. He respects every question and idea I have and allows me to conduct my own research. At the same time, he means much more to me than an advisor, he is like a family member to me. When I came to the US alone in the summer of 2021, he selflessly gave me all the help I needed and made me feel that it was not difficult to start here. I can always get support from him when I feel helpless. Being his student is one of the most fortunate things in my life.

I would like to thank my parents and all my family members who have always supported me in all my decisions and given me everything they could offer. Without them, I wouldn't be the person I am today.

I would also like to thank my committee members, Dr. Molly McCanta, Dr. Shichun Huang, and Dr. Bradley Thomson, for all the time and effort they put into my thesis and for all the help they provided. I would like to thank Allan Patchen, for his help and guidance during my numerous electron microprobe analyses.

Finally, I would like to thank my lab mates and friends, Jena, Jesse, Megan, Udit, Noah, Jordan, and all the EPS graduate students, faculty, and staff for their continued help and support that making my graduate life so colorful.

ABSTRACT

Traditional lunar magma ocean (LMO) theory suggests the anorthositic lunar crust formed by floating of buoyant plagioclase, one of the major products of LMO solidification, on the surface of LMO. To test this model, after applying experimentally determined LMO solidification sequences, we compared calculated Rare Earth Element (REE) concentrations of lunar plagioclase to plagioclase in Apollo ferroan anorthosites and lunar anorthositic meteorites. Several initial LMO compositions, and lunar-relevant mineral-melt partition coefficient predictive models were tested (where the partition coefficient is the concentration ratio of a specific element between two phases). Compared with plagioclase in the natural samples, modeled plagioclase directly crystallized from the LMO exhibit incongruent REE patterns, making the relationship between the plagioclase and LMO uncertain. After testing the impact of a series of possible secondary processes on trace element fractionation, we found that subsolidus reequilibration after adding a small amount of KREEP (potassium, rare earth elements and phosphorus) component can explain the trace element concentrations of the lunar plagioclase. In these models, we constrained the oxygen fugacity and bulk trace element abundance of the LMO, and proposed a serial processing model to explain the physical evolution of the lunar crust (Chapter 1).

In the process of modeling LMO solidification, we found that there was no trace element partitioning model developed for apatite. Apatite has important petrological significance due to its capacity to substitute trace elements into its mineral structure in abundance. Accurate prediction of trace element concentrations of apatite can help determine the trace elemental fractionation during LMO evolution. We conducted high-temperature and high-pressure experiments with lunar-relevant starting compositions. Compiling our 12 new experiments together with published data, we developed predictive models for apatite-silicate melt trace element partitioning, and an Eu in apatite-plagioclase oxybarometer. Using the aforementioned models, we recovered anticipated oxygen fugacities for one of our piston-cylinder experiments, winonaite HaH 193, and samples from Sept Iles layered intrusion. Using the new models, we additionally investigated the petrogenesis of lunar KREEP basalts, and found that LMO cumulates with fluorapatite or hydroxylapatite in the source are consistent with their formation, suggesting relatively Cl depleted late-stage LMO cumulates (Chapter 2).

TABLE OF CONTENTS

INTRODUCTION 1
CHAPTER 1 TRACE ELEMENT EVIDENCE FOR SERIAL PROCESSING OF THE LUNAR FLOTATION CRUST AND A DEPLETED BULK MOON 3
Abstract 4
1.1. Introduction 4
1.2. Compositional characteristics of samples used for comparison to our models 5
1.3. Lunar magma ocean crystallization modeling 6
1.4. Eu anomalies in lunar plagioclase 8
1.4.1 Partial melting of the lunar cumulates 10
1.4.2 Subsolidus reequilibration 13
1.4.3 Subsolidus reequilibration with minor trapped LMO liquid or a chondritic component 14
1.4.4 Subsolidus reequilibration with addition of a minor KREEPy component 14
1.4.5 The effect of pyroxene species and LMO solidification 14
1.4.6 Feasibility of subsolidus reequilibration 15
1.5. Monte-Carlo simulations modeling the formation of lunar anorthosites 15
1.5.1 Simulations assuming fixed mineral modes 15
1.5.2 Simulations with reported mineral modes 20
1.5.3 Reconciling a LREE depleted bulk Moon with isotopic characteristics of lunar samples 20
1.6. Magmatic evolution after a cumulate mantle overturn event and its significance for geochronology 21
1.7. A depleted bulk Moon 24
1.8. Summary and Conclusions 24
1.9. Acknowledgments 25
REFERENCES 26
APPENDIX A 33
CHAPTER 2 TRACE ELEMENT PARTITIONING BETWEEN APATITE AND SILICATE MELTS 68
Abstract 69
2.1. Introduction 69
2.2. Methods 70
2.2.1. Starting materials 70
2.2.2 Capsules and preconditioning procedure 72
2.2.3 Run procedure and conditions 72
2.2.4. Analytical techniques 74
2.3. Experimental results 76
2.3.1. Experimental run products 76
2.3.2. Apatite major element compositions 76
2.3.3. Apatite trace element compositions 79
2.3.4. Oxygen fugacity of experiments 79
2.3.5. Apatite-silicate melt partition coefficients 83
2.4. Discussion 83

2.4.1. Insights into cation site occupancies from application of the lattice strain model 83
2.4.2. Calibrating dataset for predictive trace element partitioning models 87
2.4.3. Predictive trace element partitioning models 88
2.5. Application and Implication 96
2.5.1. Kinetic fractionation of divalent and trivalent Eu during subsolidus reequilibration and its effect on Eu in apatite-plagioclase oxybarometer 96
2.5.2. The volatile budget of lunar magma ocean cumulates 100
2.6. Conclusions 104
2.7. Acknowledgments 104
REFERENCES 105
APPENDIX B 112
CONCLUSION 141
VITA 143

LIST OF TABLES

Table 2.1 Major element compositions of the three starting materials utilized in this study. 71
Table 2.2. Experimental run conditions 73
Table 2.3. Unit formulas (cpfu) of apatite and the apatite-silicate melt trace element partition coefficients with 1 sigma uncertainties reported for each experiment. 77
Table 2.4 Calculated oxygen fugacities for experiments based on Pt-Fe alloy compositions. 80
Table 2.5. Lattice strain parameters calculated from experiments in this study calculated using nine-fold ionic radii. 86

LIST OF FIGURES

Figure 1.1. Major and trace elements in minerals from Apollo FANs and lunar anorthositic meteorites.. 7
Figure 1.2. Different initial bulk LMO trace element compositions and consequences for fractionation during and after LMO solidification..... 9
Figure 1.3. Plagioclase produced by LMO solidification compared to returned Apollo ferroan anorthosites and lunar anorthositic meteorites, and a series of secondary process that could be invoked to explain the elemental variations exhibited by the natural lunar samples, which are all unsuccessful.. 11
Figure 1.4. Figures illustrating that subsolidus reequilibration of plagioclase crystals produced by LMO solidification after addition of a KREEPy component successfully reproduces compositions of Apollo FANs and lunar anorthositic meteorites. 12
Figure 1.5. Diffusive equilibration timescales for plagioclase and pyroxene as a function of effective diffusion length..... 16
Figure 1.6. Histograms showing successful Monte-Carlo simulations testing conditions under which subsolidus reequilibration after minor KREEPy component addition reproduce the compositions of Apollo FANs and lunar anorthositic meteorites. 17
Figure 1.7. Successful Monte-Carlo simulation results assuming Ts between 1050 and 1250℃, fO_2 between IW-1 to IW-2, and addition of <2% KREEPy component..... 19
Figure 1.8. Schematic illustrations showing two scenarios for the magmatic evolution of the lunar crust after magma ocean solidification and a cumulate mantle overturn event..... 22
Figure 2.1. Representative backscatter electron and reflected light images of experimental run products.. 75
Figure 2.2. Apatite-silicate melt partition coefficients, and anomalies of partition coefficient of Eu (D_{Eu}/D_{Eu}^*) calculated based on LA-ICP-MS analysis. 82
Figure 2.3. Onuma diagram showing measured apatite-silicate melt partition coefficients as a function of ionic radius for divalent and trivalent elements derived from experiments. 84
Figure 2.4. Lattice strain terms plotted against selected apatite cation site occupancies for trivalent elements and divalent elements. 85
Figure 2.5. Comparison between measured partition coefficients and partition coefficients for trivalent elements and divalent elements by our predictive models and predictive models in Li et al. (2023).. 89
Figure 2.6. Comparison between measured and predicted partition coefficients of Eu ... 92
Figure 2.7. The partition coefficient of Eu as a function of predictive oxygen fugacity for Eu-in-apatite , Eu-in-plagioclase and Eu in apatite-plagioclase based on coexisting apatite and plagioclase from winonaite HaH 193..... 94
Figure 2.8. Diffusion profiles for Eu^{3+} and Eu^{2+} between apatite and plagioclase at 14 selected times during subsolidus reequilibration simulations..... 97
Figure 2.9. Figures illustrating the effect of grain size of plagioclase and apatite, initial temperature, subsolidus temperature and fO_2 of the system to our oxybarometer during subsolidus reequilibration..... 98

Figure 2.10. Modelling results of partial melting of LMO cumulates. 101

INTRODUCTION

The analysis, experiments, and numerical modeling of lunar samples and meteorites have been a hot topic for decades, and the Chang'e-5 samples returned a few years ago have pushed enthusiasm for lunar petrologic research to another level (e.g., Tian et al., 2021; Liu et al., 2021; Qian et al., 2021), and also inspired researchers to gain new insights by reinterpreting returned samples and lunar meteorites. According to the seminal studies on Apollo 11 samples, before differentiation of the Moon, during and after the accretion, there was global melting, which researchers describe as a lunar magma ocean (LMO). Previous studies proposed different bulk compositions to describe the initial geochemical compositions of the LMO (e.g., Longhi, 2006; Taylor, 1982; O'Neill, 1991). Different bulk lunar major element compositions, however, returned similar magma ocean solidification sequences according to the numerical modeling and experiments (e.g., Rapp and Draper, 2018; Lin et al., 2017; Charlier et al., 2018; Schmidt and Kraettli, 2022). The first crystallization product of the LMO is usually olivine. Low-Ca pyroxene, then high-Ca pyroxene, subsequently become liquidus phases. Plagioclase usually starts to crystallize after 60 percent solidification (PCS) of the LMO. Accessory minerals such as apatite, ilmenite and quartz begin to crystallize after 90 PCS. Due to its lower density compared with residual magma ocean liquid, plagioclase exhibited positive buoyancy and floated toward the top of the LMO, forming the lunar anorthositic crust (Namur et al., 2011). Previous studies suggested that a more complicated geologic history should be considered in order to explain the trace element concentrations of lunar plagioclase, e.g., partial melting (Haskin et al., 1981), and subsolidus reequilibration (Dygert et al., 2020). In Chapter 1 of this thesis, we use experimentally-determined fractional crystallization experiments and mineral-silicate melt partition coefficient models to track the trace elemental fractionation during solidification of the LMO, thus clarifying the petrogenesis of lunar anorthositic crust and helping us to understand the early physical evolution of the Moon. We utilized Monte-Carlo simulations to constrain the physical and chemical conditions under which the anorthosites evolved as well as the bulk LMO composition.

During the process of LMO crystallization modeling, we noticed that there was previously no trace element predictive model for apatite [$Ca_5(PO_4)_3(OH, F, Cl)$]. Apatite is an omnipresent accessory mineral in different kinds of rocks on Earth as well as other bodies in the Solar System (e.g., McCubbin and Jones, 2015). Although representing a small proportion of the rock and acting as a late-crystallizing mineral, it can harbor essential amounts of Rare Earth Elements (REE) and other trace elements in some magmatic systems because of the high partition coefficients of those elements in apatite (where the partition coefficient is the concentration ratio of a specific element between two phases) (Gromet and Silver, 1983). Apatites, as well as whitlockites [$Ca_3(PO_4)_2$], have also been discovered in returned Apollo samples (e.g., Shervais et al., 1984; Tartèse et al., 2014; Potts et al., 2018). Apatite also occurs in the late stages of LMO crystallization experiments (e.g., Rapp and Draper, 2018). Since it has much higher partition coefficients for REEs than other major minerals, apatite has an enormous potential to control trace element fractionation of the magma ocean residual liquid, and thereby affect trace element concentrations in major minerals during LMO crystallization as well as secondary processing (e.g., partial melting and subsolidus reequilibration). Therefore, developing a predictive elemental partitioning model for trace elements between apatite and silicate melts is critical. Trace element partitioning in apatite is complicated because of the uncertainty of the REE occupancy in the apatite structure. In apatite, forty percent of the Ca atoms occupy the larger lattice site (nine-fold coordination, Ca1 site), while the rest enter the seven-fold coordinated site (Ca2 site), surrounding the F (OH, Cl) (X-site). Recently, researchers found the REE occupancy may be dependent on the X-site anions (Pan and Fleet,

2002), further highlighting the complexity of substitutions into apatite. Previous studies reveal that temperature (Li and Hermann, 2017), as well as the structure of the melt (Prowatke and Klemme, 2006; Watson and Green, 1981), have large impacts on REE partition coefficients. However, because of a lack of data, relationships between the X-site occupancy (F, OH, Cl) and the REE partitioning parameters could not be quantified. In Chapter 2, we report results of 12 new high-temperature and high-pressure experiments that aimed to create apatites close to the three endmember compositions (fluorapatite, hydroxylapatite, and chlorapatite). Combining the new results with previously published apatite partitioning data, we developed temperature and composition-dependent predictive partitioning models that can be used to calculate trace element partition coefficients between apatite and silicate melt. A Eu in apatite-plagioclase oxybarometer was also developed to help future workers calculate the oxygen fugacity (fO_2) of apatite and plagioclase-bearing rocks. Application of our new predictive partitioning models constrains the petrogenesis of lunar KREEP basalt, and provides insights into the relative Cl, Fl, and OH abundances in the late LMO cumulates.

CHAPTER 1
TRACE ELEMENT EVIDENCE FOR SERIAL PROCESSING OF THE LUNAR FLOTATION CRUST AND A DEPLETED BULK MOON

A version of this chapter was originally published by Dian Ji and Nicholas Dygert:
Ji, D. and Dygert, N. (2023) Trace element evidence for serial processing of the lunar flotation crust and a depleted bulk Moon. *Earth and Planetary Science Letters* 602, 117958.

This work was submitted to Earth and Planetary Science Letters in September 22 and experienced two rounds of revision by Dr. Katherine Joy and Dr. Wim van Westrenen. As the first author, Dian conducted data compilation, data visualization, and writing. Dr. Nick Dygert provided the methodology, assisted writing, and provided excellent supervision.

Abstract

Plagioclase in lunar anorthositic crust has Rare Earth Element (REE) patterns and Eu abundances which cannot be directly produced by lunar magma ocean (LMO) solidification. This is surprising as the LMO is invoked to explain the mineralogy of the crust, and other lunar surface and interior properties. We explored geological processes subsequent to LMO solidification that could reconcile anorthositic compositions with the LMO, finding that subsolidus reequilibration after addition of a minor KREEPy component successfully reproduces REE variations in natural samples. Monte-Carlo simulations used to constrain conditions of subsolidus reequilibration suggest the Moon has a light-REE depleted bulk composition. We propose a post-LMO serial processing model to reconcile the petrological, geochronological, and isotopic characteristics of lunar anorthosites and contemporaneous magmatism. If the bulk Earth is chondritic and the Moon accreted from material ejected from a depleted terrestrial reservoir, Earth underwent an early differentiation event prior to the Moon-forming giant impact.

1.1. Introduction

In seminal studies of Apollo 11 samples, researchers found ubiquitous anorthositic lithologies and put forward the hypothesis of the lunar magma ocean (LMO; e.g., Binder, 1974). The model argues that the Moon underwent global melting, producing a magma ocean and that as the magma ocean solidified, relatively low-density anorthosites segregated at the surface because of their buoyancy. The formation of the lunar highland crust by LMO solidification would be accompanied by formation of complementary mafic cumulate layers in the lunar interior (Snyder et al., 1992a). Recently, researchers ran experiments that constrain the mineralogy and mineral compositions of LMO cumulates for different bulk LMO compositions (Figure A1; Charlier et al., 2018; Lin et al., 2017; Rapp and Draper, 2018; Schmidt and Kraetteli, 2022). Here, we use experimentally determined crystallization sequences to explore trace element fractionation during LMO solidification for different staring bulk compositions. Leveraging the experimental data and mineral-melt REE partitioning models, we calculate the predicted REE patterns of minerals in lunar anorthosites and compare the results to natural samples to evaluate their petrogenesis.

Our work is motivated by disagreement about the formation of lunar anorthosites (e.g., Gross and Joy, 2016). Some researchers argue the ferroan anorthosites are not a direct product of the LMO but formed from partial melting of the early mafic cumulates after LMO solidification, during gravitational restructuring of the Moon (e.g., Longhi, 2003). Arai et al. (2008) argued for an LMO origin, but suggested that asymmetric crystallization of LMO caused by a surface convectional force related to the shielding effect of the Earth, which affected the formation of anorthositic crust in a hemispheric way, leading to crystallization of the higher-Mg# anorthosite on the farside before crystallization of lower Mg# anorthosites on

the nearside. Other researchers argued that after LMO solidification, melts derived from decompression melting of ultramafic cumulates in the deep lunar interior would interact with crystallized anorthosites, which can explain the similarities in the geochemical, mineralogical and age characteristics of lunar anorthosites and the intrusive Mg-suite (Dygert et al., 2017; Pernet-Fisher et al., 2019). Haskin et al. (1981) proposed that partial melting of anorthosites with the addition of a small amount of trapped liquid can help to explain their REE patterns. Others highlight the role of trapped magma ocean liquid that may have been frozen in the anorthosites as they floated on the LMO (e.g., Raedeke and McCallum, 1980; Piskorz and Stevenson, 2014).

To assess the formation of the lunar anorthosites in an LMO and their subsequent modification in the context of the aforementioned models, we compared the geochemical characteristics of plagioclase calculated from different LMO solidification scenarios with Apollo samples and lunar anorthositic meteorites. Specifically, we focus on Eu anomalies (Eu/Eu*, where Eu is the chondrite normalized abundance and Eu* is the interpolated value from neighboring elements on a REE diagram) and the slope of REE patterns of plagioclase and test the consequences of partial melting, subsolidus reequilibration, and addition of chondritic, trapped LMO liquid, and KREEPy components on the compositions of the anorthosites. We evaluate the effects of these processes for LMOs with differing bulk major and trace element compositions. Finally, we evaluate the physical and chemical conditions under which the anorthosites formed and evolved using Monte-Carlo simulations that place constraints on the bulk LMO composition.

1.2. Compositional characteristics of samples used for comparison to our models

As the major rock type of the lunar crust, highland anorthosites are composed of calcic plagioclase (usually >90 vol %; Table A1 and Figure A2) with a small amount of pyroxene (orthopyroxene and/or pigeonite, which we refer to here and elsewhere as low-Ca pyroxene, and augite or clinopyroxene, which we refer to as high-Ca pyroxene). Some anorthosites also contain minor olivines (e.g., 62236 and 62237), and other accessory phases (e.g., ilmenite, chromite, troilite, (Zn,Fe)S, and FeNi metal, McGee, 1993; but not phosphates, Norman et al., 2003). We compiled plagioclase compositions from Apollo ferroan anorthosite (FAN) samples and lunar anorthositic meteorites (Cahill et al., 2004; Floss et al., 1998; Gross et al., 2014; McGee, 1993; Papike et al., 1997; Pernet-Fisher et al., 2019; Roberts et al., 2019; Russell et al., 2014, Treiman et al., 2010), and augmented the literature data with new analyses of lunar meteorite Dhofar 280 (an anorthositic fragmental breccia, see description in the Supplementary Materials, and analytical results in Table A2). Concentrations of REEs in plagioclase in the samples we investigate here, and their associated uncertainties, are summarized in Table A3. We include as much data as possible in our compilation, including anorthosites reported not to exhibit metamorphic texture (i.e., granulitic texture; McGee, 1993). An example is 60025, which been proposed to have undergone subsolidus reequilibration based on trace element distributions and age determinations (Torcivia and Neal, 2022). We note that some researchers divided FAN into petrological and geochemical subgroups (e.g., Floss et al., 1998; McGee, 1994), which were interpreted to reflect different petrogenetic histories. Here, we choose not to subdivide FANs because we conclude their ubiquitous REE patterns may be suggestive of a global post-formation process. However, we do not consider samples with plagioclase that display high shock states (e.g., 60015,125 in Pernet-Fisher et al., 2019) or those missing REE data required for modeling.

In general, the plagioclase in both Apollo FANs and lunar anorthositic meteorites show high An#s (94.8 – 98.0, where the An# = 100 × molar Ca/[Ca + Na + K], or An# = 100 × molar

Ca/[Ca + Na] where K is not reported), while the coexisting pyroxenes in lunar anorthositic meteorites are more magnesian (Figure 1.1A; e.g., Gross et al., 2014). Plagioclase show no linear relationship in major elements with coexisting pyroxenes, which is thought to be the result of trapped intercumulus liquid crystallization (e.g., Raedeke and McCallum, 1980) and/or evolution after secondary processing (McGee, 1993; Phinney, 1992). The REE patterns of plagioclase in both lunar anorthositic meteorites and Apollo FANs show variable slopes [$(La/Yb)_{CI}$ = 2 - 32], with positive but variable Eu anomalies (6 – 81; Figure 1.1B). A detailed description of the geochemical characteristics of plagioclase we compiled is reported in the Supplementary Materials.

1.3. Lunar magma ocean crystallization modeling

Researchers have studied the implications of LMO crystallization for decades (e.g., Longhi, 1978; Snyder et al., 1992a). However, in early investigations of LMO solidification, knowledge of the bulk LMO composition and phase equilibria constraints on magma ocean cumulates were limited. More recently, three laboratories experimentally determined crystallization sequences for LMOs with different bulk compositions (Figure A1; Charlier et al., 2018; Lin et al., 2017; Rapp and Draper, 2018). These models improve upon the widely cited Snyder et al. (1992a) study, by experimentally simulating complete polybaric solidification of the LMO for lunar bulk compositions consistent with modern crustal thickness estimates (e.g., Taylor and Wieczorek, 2014).

In the experiments, the residual magma ocean liquids reached plagioclase saturation at different percent solidification (PCS), and were cosaturated with different phases depending on the bulk compositions assumed. Lin et al. (2017) assumed a bulk LMO similar to Bulk Silicate Earth (McDonough and Sun, 1995), observing plagioclase saturation at 68 PCS, with olivine and high-Ca pyroxenes. Rapp and Draper (2018) utilized a Lunar Primitive Upper Mantle (Longhi, 2006) bulk LMO composition and observed plagioclase at 74 PCS with olivine, low-Ca pyroxenes and high-Ca pyroxenes. Charlier et al. (2018) tested three different bulk compositions: O'Neill (O'Neill, 1991), the Taylor Whole Moon (TWM; Taylor, 1982) and the Lunar Primitive Upper Mantle (LPUM) model (Longhi, 2006), which produced plagioclase at 78 PCS with high-Ca pyroxenes and low-Ca pyroxenes, 67 PCS with low-Ca pyroxenes, and 81 PCS with high-Ca pyroxenes and low-Ca pyroxenes, respectively. We note the more aluminous TWM model is untenable in the context of lunar gravimetric data, which suggests a relatively thin crust (40 km on average, Wieczorek et al., 2013). Nonetheless, we used all five crystallization sequences from the aforementioned studies to calculate elemental distributions in the magma ocean cumulates, including the lunar anorthosites. A most recent experimental lunar magma ocean solidification study by Schmidt and Kraettli (2022) recovered results comparable to the previous LMO crystallization experiments, and assumed a TWM bulk composition.

In previous work, researchers assumed a chondritic REE pattern as representing the initial bulk Moon (e.g., Rapp and Draper, 2018; Snyder et al., 1992a). However, given that abundant isotopic evidence suggests the initial bulk composition of the Moon may be closely related to the proto-Earth (e.g., Melosh, 2014, and references therein), we explored four distinct terrestrial trace element reservoirs as proxies for potential lunar bulk REE patterns (Table A4). These terrestrial reservoirs have different degrees of light-REE (LREE) enrichment or depletion and were diluted such that the average concentrations are consistent with CI chondrite. A LREE enriched Moon is represented by average continental crust from Earth (Rudnick and Gao, 2014, diluted by a factor of 20). A chondritic Moon is represented by the CI chondrite composition of Lodders (2021). A slightly LREE depleted Moon is represented

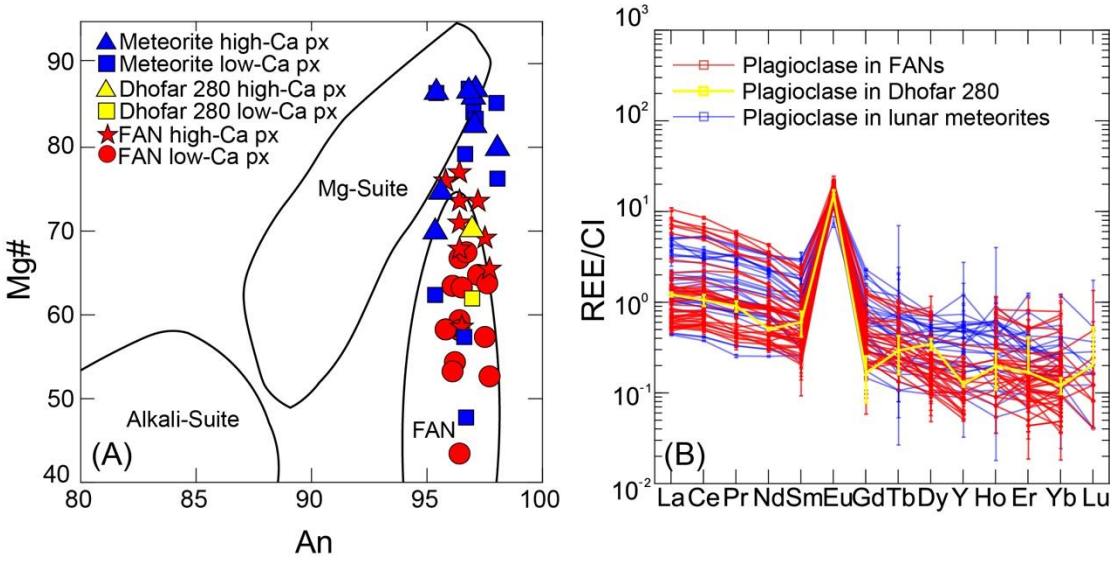


Figure 1.1. Major and trace elements in minerals from Apollo FANs and lunar anorthositic meteorites. (A) Mg# (100 × molar Mg/[Mg + Fe]) in pyroxenes (y-axis) versus An (100 × molar Ca/[Ca + Na + K] or 100 × molar Ca/[Ca + Na]) in coexisting plagioclase (x-axis). Fields of Alkali Suite, Mg-suite and FAN are from (Roberts et al., 2019). (B) Chondrite-normalized REE patterns for plagioclase in lunar FANs and meteorites (Table A3). Yellow line shows new data for Dhofar 280. Chondrite normalization is from Lodders (2021). Data sources are Cahill et al. (2004), Floss et al. (1998), Gross et al. (2014), McGee (1993), Papike et al. (1997), Pernet-Fisher et al. (2019), Roberts et al. (2019), Russell et al. (2014), Treiman et al. (2010), and this study (Table A2).

by the CI chondrite composition of Lodders (2021). A slightly LREE depleted Moon is represented by a log-normal mean global MORB pattern (Arevalo and McDonough, 2010, diluted by a factor of 20), and a moderately depleted Moon is represented by the depleted MORB mantle (or DMM) of Workman and Hart (2005), diluted by a factor of 2. These chondrite normalized REE patterns are plotted in Figure 1.2A. Exploration of variably depleted bulk Moon compositions is justified by isotopic similarities between the Moon and Earth, and the ^{142}Nd system, which suggests that ancient lunar and terrestrial reservoirs have superchondritic Sm/Nd (e.g., Borg et al., 1999; Boyet and Carlson, 2007), or formed from precursor materials with nucleosynthetically anomalous ^{142}Nd (Boyet et al., 2015). Using experimentally parameterized partition coefficient models for equilibrium between silicate melt and olivine (Sun and Liang, 2013a), low-Ca pyroxene (Sun and Liang, 2013b), high-Ca pyroxene (Dygert et al., 2014), plagioclase (Sun et al., 2017), and ilmenite (Dygert et al., 2013), we calculated trivalent REE abundances in minerals in each part of the LMO crystallization sequence for the different bulk Moon major and trace element compositions.

The middle REE Eu can be divalent or trivalent depending on oxygen fugacity (fO_2), strongly affecting its partitioning behavior. Previous research demonstrates that at fO_2 below the iron-wüstite (IW) buffer, as in a reduced Moon, much of the Eu in geologic systems is divalent, and its substitution is favored in plagioclase because Eu^{2+} has an ionic radius similar to Ca^{2+}. Dygert et al. (2020) developed a model which enables us to predict Eu partitioning as a function of fO_2, T and plagioclase composition. The new Eu-in-plagioclase model is employed along with the aforementioned models to calculate elemental fractionation of the full suite of REEs during LMO solidification. In simulations shown in the main text, we assume trivalent Eu partitioning in pyroxene, as preliminary fO_2-dependent Eu partitioning models for pyroxenes (Fabbrizio et al., 2021) produced results consistent with the trivalent Eu assumption for pyroxene (see Supplementary Figure A11 for more details). We do not consider tetravalent Ce here since Ce^{4+} cannot be stabilized under lunar fO_2s (Snyder et al., 1992b).

Elemental concentrations in melt from each crystallization sequence were calculated via the Rayleigh fractionation equation:

$$C_L^i = C_{Lo}^i \times F^{(D_{Bulk}^i - 1)} \quad (1.1),$$

where C_L^i is the concentration of element i in melt, C_{Lo}^i is the concentration of element i in the initial bulk LMO, F is the degree of melt, and D_{Bulk}^i is the bulk partition coefficient calculated by the weighted average partition coefficient between mineral and melt based on mineral modes. We note that in fractional crystallization, when crystallizing phases change, D_{Bulk}^i must account for contributions of phases during preceding parts of the solidification sequence to ensure mass conservation. The concentration of element *i* in each mineral is:

$$C_s^i = C_L^i \times D_s^i \quad (1.2),$$

where C_s^i is the concentration of element *i* the mineral, and D_s^i is the partition coefficient of element *i* between the mineral and melt.

1.4. Eu anomalies in lunar plagioclase

Using Eqs. 1.1 and 1.2, we calculate the REE concentrations in plagioclase crystallized from different bulk LMOs for the different solidification models, as a function of fO_2. We test three fO_2 conditions, two orders of magnitude below the iron-wüstite buffer (IW-2), along the fayalite-magnetite-quartz buffer (FMQ), and two log units more oxidizing than the FMQ buffer. The most reducing condition (IW-2) is most lunar relevant (e.g., Rutherford et al., 2017). To develop a threshold for evaluating successful numerical simulations, we estimated the uncertainty of Eu* and $(Ce/Sm)_{CI}$ calculated by a Taylor series expansion in the chondritic

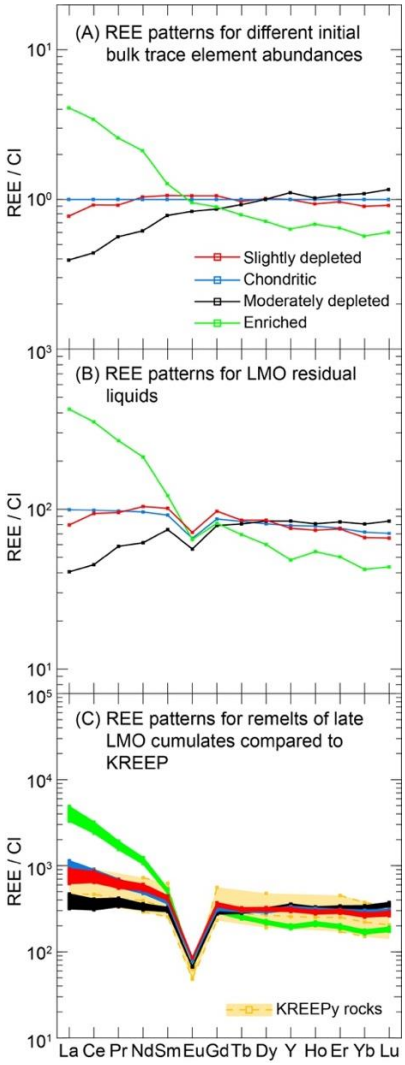


Figure 1.2. Different initial bulk LMO trace element compositions and consequences for fractionation during and after LMO solidification. (A) Chondrite-normalized REE patterns tested as possible bulk Moon trace element compositions (Table A4), (B) residual liquids after 99 percent solidification of the LMO, and (C) remelts of late LMO cumulates compared to KREEPy rocks (KREEP basalt 15386, KREEP breccia 15405 and high-K KREEP; Neal and Kramer, 2003; Nyquist et al., 1976; Warren, 1989). In Figure 1.2B, the $(Sm/Nd)_{CI}$ of LMO residual liquid with a slightly depleted, chondritic, moderately depleted and enriched initial bulk composition are 0.99, 0.97, 1.23 and 0.58, respectively. A $(Sm/Nd)_{CI} > 1$ (as in the moderately depleted case) may be inconsistent with Nd isotopic compositions of lunar materials. Figure 1.2C shows compositions of remelts of late LMO cumulates assuming a source with 57% high-Ca pyroxene + 40% plagioclase + 1% apatite + 2% ilmenite. Since the apatite/melt partition coefficients for the REEs are closely related to melt polymerization, we choose partition coefficients of experiment 59B in (Prowatke and Klemme, 2006), that has the most similar silicate concentration of the melt with the 99 PCS residual liquid in Charlier et al. (2018). Due to the lack of published partition coefficients for Eu between apatite and melt, we use the D_{Sr} as a proxy for Eu. Here we show 1-4% instantaneous fractional modal melts. Melts of late LMO cumulates with a slightly depleted and chondritic initial bulk composition reproduce KREEPy REE patterns. Chondrite normalization is from Lodders (2021).

normalization and the analyses of elemental concentrations in lunar plagioclase crystals using Eqs. 1.3 and 1.4 (e.g., Barford, 1985):

$$s_{Eu*} = \sqrt{\left(\frac{\partial Eu*}{\partial Eu}\right)^2 s_{Eu}^2 + \left(\frac{\partial Eu*}{\partial Eu_{CI}}\right) s_{Eu_{CI}}^2 + \left(\frac{\partial Eu*}{\partial Sm}\right)^2 s_{Sm}^2 + \left(\frac{\partial Eu*}{\partial Sm_{CI}}\right) s_{Sm_{CI}}^2 + \left(\frac{\partial Eu*}{\partial Gd}\right)^2 s_{Gd}^2 + \left(\frac{\partial Eu*}{\partial Gd_{CI}}\right) s_{Gd_{CI}}^2} \quad (1.3),$$

$$s_{(Ce/Sm)_{CI}} = \sqrt{\left(\frac{\partial (Ce/Sm)_{CI}}{\partial Ce}\right)^2 s_{Ce}^2 + \left(\frac{\partial (Ce/Sm)_{CI}}{\partial Ce_{CI}}\right) s_{Ce_{CI}}^2 + \left(\frac{\partial (Ce/Sm)_{CI}}{\partial Sm}\right)^2 s_{Sm}^2 + \left(\frac{\partial (Ce/Sm)_{CI}}{\partial Sm_{CI}}\right) s_{Sm_{CI}}^2} \quad (1.4),$$

where s_{Eu*} and $s_{(Ce/Sm)_{CI}}$ represent the errors (1σ) of Eu* and $(Ce/Sm)_{CI}$, S_{Eu} represents the error of Eu in plagioclase (Table A3), $S_{Eu_{CI}}$ represents the error of Eu in CI chondrites (Lodders, 2021), and so forth. $\frac{\partial Eu*}{\partial Eu}$ denotes the partial derivative of Eu* with respect to the Eu, $\frac{\partial (Ce/Sm)_{CI}}{\partial Ce}$ denotes the partial derivative of $(Ce/Sm)_{CI}$ with respect to the Ce, and so forth. For plagioclase in FANs and lunar anorthositic meteorites, the average percent error for $(Ce/Sm)_{CI}$ are 21.82% and 17.38%, while for Eu* are 17% and 14.3%, respectively (1σ). See Table A3 for sample-specific results of this error analysis.

In terms of Eu anomalies and in the slope of REE patterns, no matter which solidification sequence and trace element bulk composition combination we choose, the calculated plagioclase are inconsistent with many natural plagioclase from Apollo anorthosites and lunar anorthositic meteorites, even considering error propagation (Figure 1.3A; Figures A4 and A5). This is especially true for plagioclase produced in lunar-relevant low fO_2 scenarios, as the calculated plagioclase have larger Eu anomalies (163 to 355 in Figure 1.4A) than the overwhelming majority of the natural samples (6.06 ± 1.10 to 79.91 ± 6.10; Table A3).

1.4.1 Partial melting of the lunar cumulates

After failure of LMO solidification alone to match the Eu/Eu* and $(Ce/Sm)_{CI}$ of the lunar anorthosites, we considered partial melting of LMO flotation cumulates as a potential secondary process for affecting their trace element compositions (e.g., Longhi, 2003). We chose cumulates from LMO solidification models with modes of 95.1 % plagioclase and 4.9 % pyroxenes (Warren, 1990). We explored scenarios that assume all pyroxene is low-Ca pyroxene and others where all pyroxene is high-Ca pyroxene. We simplify the partial melting as non-modal fractional melting to calculate the concentrations of elements in the fractional liquid:

$$C_L^i = \frac{C_o^i}{D_{bulk}^i} \times \left(1 - \frac{P_{bulk}^i * F}{D_{bulk}^i}\right)^{\left(\frac{1}{D_{Bulk}^i - 1}\right)} \quad (1.5),$$

where C_L^i is the concentration of element i in the liquid, C_o^i is the initial concentration of element i in the anorthositic melting residue, F is the degree of melting, D_{Bulk}^i is the bulk partition coefficient of anorthosites calculated by the weighted average of partition coefficient between mineral and liquid based on mineral modes, and P_{Bulk}^i is the non-modal contribution of each phase in the melting reaction, where we assume 58% low-Ca pyroxene and 42% plagioclase. Using the relationship for equilibrium partitioning (Eq. 1.2), we obtain the concentration of element i in plagioclase in equilibrium with the melt.

In Figure 1.3B, we show the result of a representative simulation based on the solidification sequence of all experiments with slightly LREE depleted initial bulk LMO composition, because the trend of results from all solidification models and bulk trace element compositions

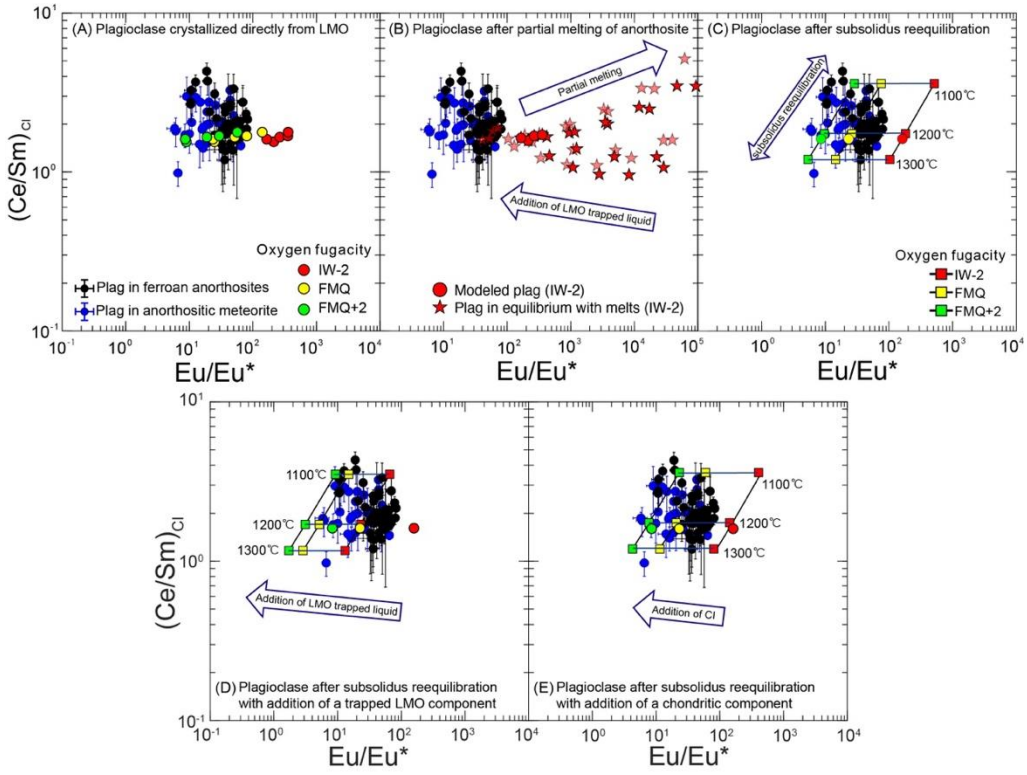


Figure 1.3. Plagioclase produced by LMO solidification compared to returned Apollo ferroan anorthosites and lunar anorthositic meteorites (A), and a series of secondary process that could be invoked to explain the elemental variations exhibited by the natural lunar samples, which are all unsuccessful (B)-(E). (A) Modeled plagioclase compositions after LMO solidification as a function of fO_2 (colored circles) compared to lunar plagioclase in Apollo FANs (black circles) and lunar anorthositic meteorites (blue circles; Table A3). Y axis shows chondrite-normalized Ce/Sm, x axis shows Eu/Eu*. (B) Plagioclase in equilibrium with melts from partial melting of the calculated anorthositic lunar crust (red stars; fO_2 = IW-2). Simulations assuming addition of 4% trapped LMO liquid are shown by the partially transparent stars. (C) Modeled plagioclase before (colored circles) and after subsolidus reequilibration (colored squares). (D) Modeled plagioclase after subsolidus reequilibration with the addition of 8% trapped LMO liquid, and (E) after addition of 8% (by mass) of a chondritic component. As lunar-relevant fO_2s likely approximate IW-2, none of these mechanisms successfully explain the elemental distributions of all samples even considering the propagation of errors. In all simulations shown, we assume the mineral mode of anorthosite is 95.1% plagioclase + 4.9% low-Ca pyroxene. The simulations show representative results based on the solidification sequence from Charlier et al. (2018), assuming an LMO with an LPUM bulk major element composition. The trace element composition of the bulk LMO assumed is slightly depleted (Arevalo and McDonough, 2010). Because plagioclase crystallizes in multiple experimental stages in each LMO solidification sequence, the plagioclase shown in (C), (D) and (E) are those crystallized from the relatively early stage (82 percent solidification). The error bars are calculated considering error propagation (Table A3).

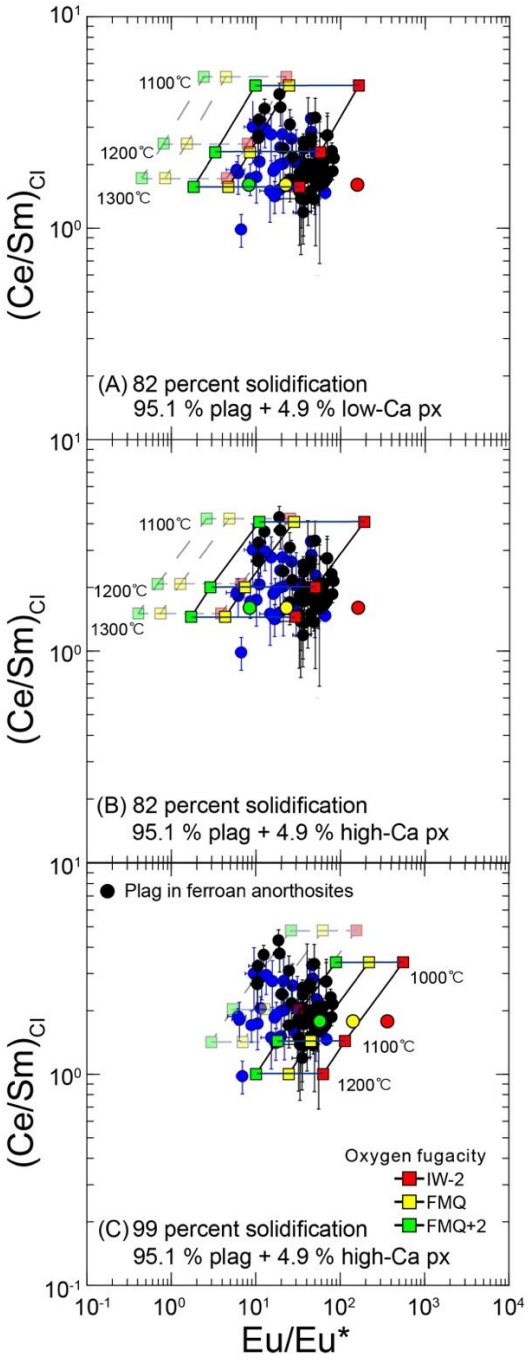


Figure 1.4. Figures illustrating that subsolidus reequilibration of plagioclase crystals produced by LMO solidification after addition of a KREEPy component successfully reproduces compositions of Apollo FANs and lunar anorthositic meteorites. Panels (A) and (B) compare models assuming subsolidus reequilibration with low- and high-Ca pyroxene when LMO solidification get 82 percent, while panel (C) shows subsolidus reequilibration with high-Ca pyroxene when LMO solidification is 99 percent. Simulations assuming addition of 0.25% KREEPy component are shown by opaque symbols and solid lines and simulations assuming addition of 2.5% KREEPy component are shown by the partially transparent symbols and dashed lines. Modeling conditions are otherwise as described in the caption to Figure 1.3.

are similar and all of the results failed to reproduce most plagioclase (Figures A6 and A7). After partial melting, we find that the slope of the REE patterns $(Ce/Sm)_{CI}$ of plagioclase in equilibrium with melts change, but the Eu anomalies become larger, opposite the direction needed to match the natural samples. It is apparent that partial melting exacerbates the Eu anomaly discrepancy, which is contrary to the trend of plagioclase in Apollo and anorthositic meteorite samples.

Haskin et al. (1981) proposed that adding a few percent of trapped liquid into the anorthosites can help explain the REE pattern variation after partial melting. Considering the amount of tapped LMO liquid fraction in the anorthosite cannot be greater than a few percent (Dygert et al., 2017; Krättli and Schmidt, 2021), we explored adding 4% of trapped LMO liquid and it indeed helped to reduce the Eu anomalies and increase the $(Ce/Sm)_{CI}$, but the effect is too limited to explain most of the plagioclase (Figure 1.4B, partially transparent stars).

1.4.2 Subsolidus reequilibration

As reported by McGee (1993), some lunar anorthosites (e.g., 67525, 67535, 67536 and 68515) show clearly granulitic texture that may be related to subsolidus reequilibration, which is also suggested by the concentrations and nonlinear relationship between FeO, MgO and An in plagioclase from lunar anorthosites (McGee, 1993; Phinney, 1992; Figure A3). Subsolidus reequilibration may redistribute elements among minerals in a closed system after crystallization, perturbing elemental distributions from those initially representing high-T magmatic processes (Sun and Liang, 2014). We evaluated T-dependent subsolidus reequilibration assuming a closed system composed of plagioclase and minor amounts of pyroxenes that are initially in equilibrium with coexisting residual LMO liquid (e.g., Pernet-Fisher et al., 2017). Assuming subsequent segregation from the magma ocean, we treat the cumulates as a new closed system with a fixed mineral composition (95.1 % plagioclase + 4.9 % low-Ca pyroxene; Warren, 1990). We calculate the concentration of elements in this closed system:

$$C_{Bulk}^{Subsolidus} = \phi_{plag} \times C_{plag}^{Magmatic} + \phi_{opx} \times C_{opx}^{Magmatic} \quad (1.6),$$

where $C_{Bulk}^{Subsolidus}$ is the bulk concentration, $C_{plag}^{Magmatic}$ and $C_{opx}^{Magmatic}$ are the concentrations of elements in crystallized plagioclase and low-Ca pyroxenes from LMO cumulates, and ϕ_{plag} and ϕ_{opx} are the mass proportions of the two minerals in the system, which we approximate here by volume proportions. In order to evaluate the redistribution of elements under subsolidus conditions, mineral-melt partition coefficients must be recalculated as mineral-mineral partition coefficients, e.g.,:

$$\frac{D_{opx-melt}(\mathrm{T},X)}{D_{plag-melt}(fO_2,\mathrm{T},X)} = D_{opx-plag}(fO_2,\mathrm{T},X) \quad (1.7),$$

where $D_{plag-melt}$ is the partition coefficient of elements between the plagioclase and melt, $D_{opx-melt}$ is the partition coefficient of elements between the low-Ca pyroxenes and melt, $D_{plag-opx}$ is the partition coefficient of elements between plagioclase and low-Ca pyroxenes. $D_{plag-opx}$ is temperature (T), composition (X) and fO_2 dependent. Then with assumed mineral modes and calculated REE concentrations in the system ($C_{Bulk}^{Subsolidus}$), we calculate REE concentrations in plagioclase under different T and fO_2 via a mass balance equation:

$$C_{plag}^{Subsolidus} = \frac{C_{Bulk}^{Subsolidus}}{\phi_{cpx} \times D_{opx-plag} + \phi_{plag}} \quad (1.8),$$

where $C_{plag}^{Subsolidus}$ is the concentration of elements in plagioclase after subsolidus reequilibration.

Here we show representative results based on the LPUM LMO solidification sequence from Charlier et al. (2018), assuming slightly depleted initial bulk trace element composition. We investigate plagioclase formed in the early stage of plagioclase precipitation from the LMO (82 PCS) as these cumulates would be located in the outmost layer of the Moon and are most likely to be sampled. We find that T-dependent closed-system subsolidus reequilibration expands the possible range of $(Ce/Sm)_{CI}$ as well as Eu anomalies in plagioclase (Figure 1.3C). Subsolidus reequilibration under different fO_2s affects the Eu anomalies, while T affects the Eu anomalies as well as the slope of REE patterns. The lower the T and fO_2, the more Eu tends to enter plagioclase after reequilibration. However, the variation of Eu anomalies is still limited and cannot fit many natural samples under fO_2 conditions relevant to a reduced Moon.

1.4.3 Subsolidus reequilibration with minor trapped LMO liquid or a chondritic component

The potential importance of interstitial trapped liquid in the petrogenesis of anorthosites has been noted in many studies (e.g., Jolliff and Haskin 1995; Piskorz and Stevenson, 2014; Raedeke and McCallum, 1980). To explore its effect on the elemental variations, here we added an ~8 % of trapped residual LMO liquid component to our closed system. We calculated the compositions of trapped liquid based on assumed LMO crystallization sequences for each initial bulk LMO assumed and PCS. We observe that even under different fO_2 conditions, if as much as 8% modal LMO liquid was added, the Eu anomaly magnitude and slope of REE patterns are reduced, but plagioclase with lower $(Ce/Sm)_{CI}$ and higher Eu anomalies are not reproduced (Figure 1.3D). As we mentioned earlier, in any case, research on the compaction of trapped liquids in plagioclase-melt mushes suggests contribution of so much trapped liquid to the closed system is implausible (e.g., Dygert et al., 2017; Krättli and Schmidt, 2021). A similar but weaker trend appears when we assume the addition of a chondritic meteoritic component to our closed system (Figure 1.3E).

1.4.4 Subsolidus reequilibration with addition of a minor KREEPy component

Finally, we explored subsolidus reequilibration after addition of a KREEPy component (Figure 1.4). The KREEPy component we choose in this study is KREEP basalt 15386 (Table A4; Neal and Kramer, 2003) that has a high REE concentration and an enrichment in LREEs compared with HREEs, with a strongly negative Eu anomaly (Figure 1.2C). Addition of minor KREEPy component reduces Eu anomalies and elevates Ce/Sm ratios, reproducing variations in the natural samples. The proportion of KREEPy component required depends on the bulk LMO composition assumed. The more KREEPy component is added, the more the Eu anomaly decreases and the greater the slope of REE patterns. In general, compared to Apollo anorthosites, plagioclase in lunar anorthositic meteorites have less pronounced Eu anomalies (e.g., Figure 1.4), requiring reequilibration at a higher temperature and/or addition of more KREEPy component.

1.4.5 The effect of pyroxene species and LMO solidification

Our compilation of reported Apollo anorthosite mineral modes (Table A1) reveals that in most cases, anorthosites contain both high-Ca pyroxenes and low-Ca pyroxenes, and high-Ca pyroxenes are even dominant in some samples (e.g., 15362, 15415 and 60055). Our previous calculations are based on the assumption that all pyroxenes are low-Ca pyroxenes, so it is necessary to evaluate how different kinds of pyroxenes would affect the Eu anomalies in

plagioclase after reequilibration. We calculate the partition coefficient for low-Ca and high-Ca pyroxene crystallized in the same PCS in Charlier et al. (2018), and find under different temperatures and fO_2, the effect of reequilibration on the slope of REE patterns and Eu anomalies when high-Ca pyroxenes are dominant in pyroxenes is very similar to the previous result (compare Figures 1.4A and 1.4B). Thus, subsolidus reequilibration after addition of a KREEPy component can explain most of the natural samples, regardless of the pyroxene type.

We note that with the solidification of the LMO (increasing PCS), the liquid in equilibrium with both plagioclase and pyroxene is progressively enriched, as are the minerals. Therefore, we need to add more KREEPy component and assume a lower temperature during subsolidus reequilibration in order to explain those plagioclase with higher $(Ce/Sm)_{CI}$ and lower Eu anomalies (compare Figures 1.4B and 1.4C).

1.4.6 Feasibility of subsolidus reequilibration

Diffusive redistribution of elements among minerals in geologic systems may be restricted by exchange kinetics. To test the feasibility of subsolidus reequilibration under lunar crustal conditions, we calculated characteristic diffusion timescales for REEs in plagioclase and pyroxene:

$$t = \frac{L^2}{D_o exp\left(\frac{-E}{RT}\right)} \quad (1.9),$$

where t is the time for diffusive interaction, E and D_o are the activation energy and pre-exponential factors for Arrhenius models of diffusivity, respectively, R is the gas constant, T is the temperature for elemental redistribution, and L is the effective diffusion length of minerals experiencing reequilibration. Assuming Arrhenius parameters reported in Table A5, we obtain timescales suggesting reequilibration occurs under lunar-relevant conditions (Figure 1.5). For plagioclase, the maximum observed half major axis is 3 mm in 60015,113 and 61016,218, and we assume an effective L one third of this maximum reported radius owing to the aspect ratio of plagioclase crystals. Maximum pyroxene radii are 0.5mm in 62255,3,42 in lunar anorthosite (McGee, 1993). At a T of 1000°C, the time needed to redistribute elements between plagioclase and pyroxenes is less than 200 Myr; diffusive reequilibration is approximately an order of magnitude faster for each 100°C increases in temperature. Given the young ages of many of the ferroan anorthosites (e.g., 4290 ± 85 Ma of sample 62236; Borg et al., 1999) compared to proposed lunar formation times (e.g., 4.425 ± 0.025 Ga; Maurice et al., 2020) and magma ocean solidification timescales (e.g., 150 to 200 Ma; Maurice et al., 2020), these reequilibration timescales are reasonable.

1.5. Monte-Carlo simulations modeling the formation of lunar anorthosites

1.5.1 Simulations assuming fixed mineral modes

In order to make a more specific evaluation of the conditions under which subsolidus reequilibration occurs, we ran 100,000 simulations per model using a Monte-Carlo approach assuming different temperatures, fO_2 and added KREEPy component proportion to determine which combinations of parameters produce acceptable fits to the lunar samples. In our simulations, we limit T to between 1000 and 1500°C, the fO_2 between IW-3 and IW+3, and the percentage of KREEPy component in anorthosites between 0 and 10%. We test a wide range of parameter combinations in the Monte-Carlo simulations to evaluate whether peaks in the T, fO_2, and the percentage of KREEPy component distribution results are physically reasonable. Though lunar researchers typically invoke low fO_2s (~IW-1, e.g., Rutherford et al., 2017),

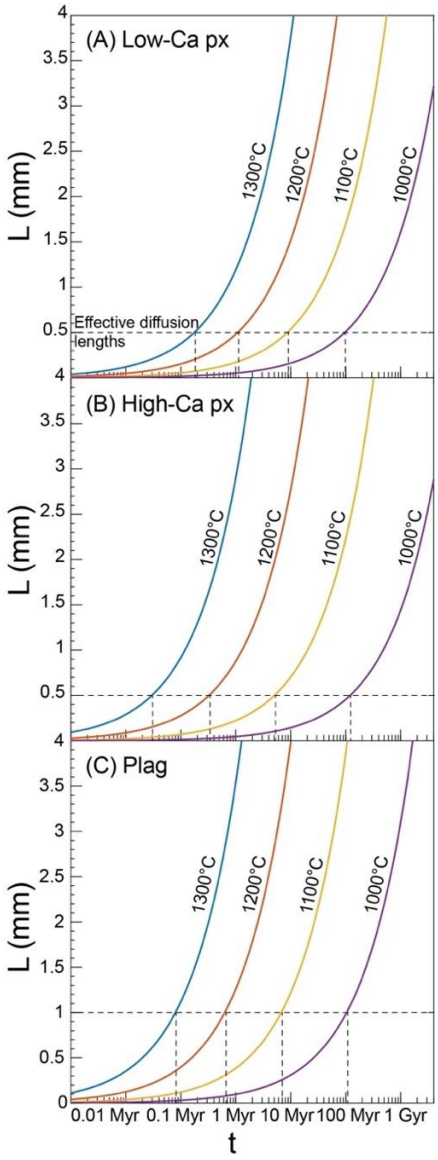


Figure 1.5. Diffusive equilibration timescales for plagioclase and pyroxene as a function of effective diffusion length; (A) low-Ca pyroxene, (B) high-Ca pyroxene and (C) plagioclase assuming volume diffusion for different temperatures. L represents the approximate effective diffusion length of a grain reequilibrated at the specified T and time (t) conditions. The horizontal dashed lines show maximum effective diffusion lengths reported for lunar samples. For plagioclase, the maximum observed half major axis is 3 mm in 60015,113 and 61016,218, but according to the typical aspect ratio of plagioclase, the effective L is estimated to be one third of this maximum reported radius. Maximum pyroxene radii are 0.5mm in 62255,3,42 in lunar anorthosite reported by McGee (1993). Volume diffusion in pyroxene is slower than plagioclase, which may be rate limiting in lunar anorthosites, depending on grain size. Diffusive reequilibration may be expected within timescales less than 200 Myr, even at 1000°C, and is approximately an order of magnitude faster for each 100°C increase in T. See Table A5 for a summary of Arrhenius parameters used in these calculations.

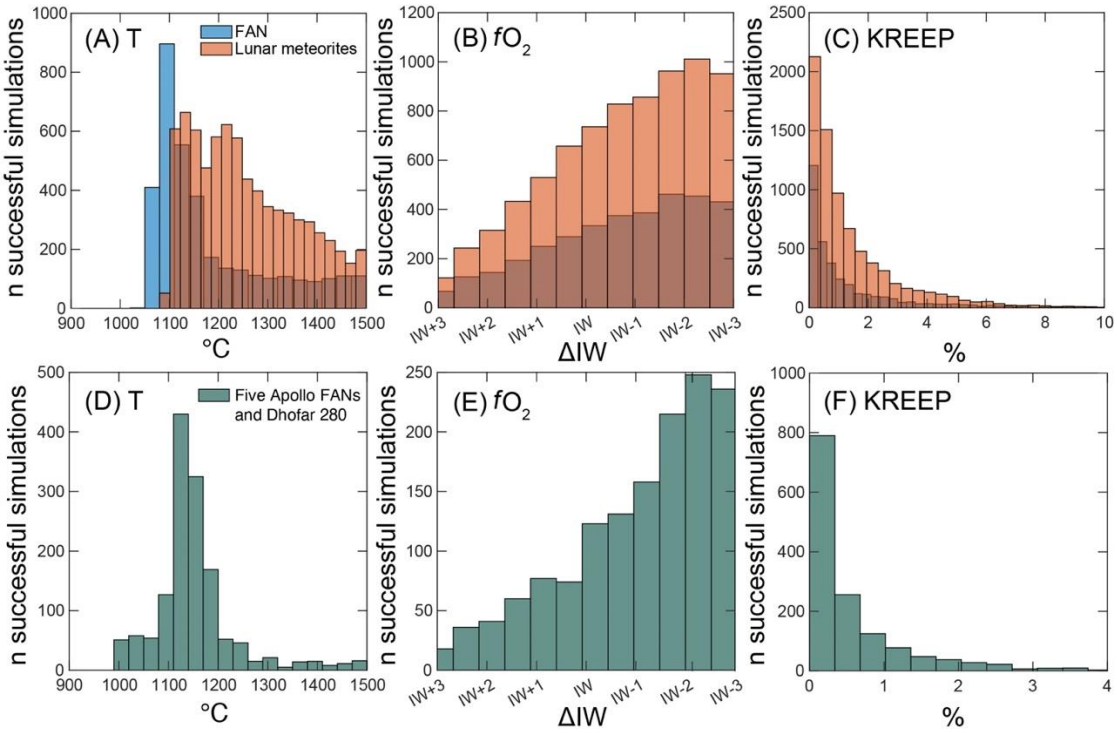


Figure 1.6. Histograms showing successful Monte-Carlo simulations testing conditions under which subsolidus reequilibration after minor KREEPy component addition reproduce the compositions of Apollo FANs and lunar anorthositic meteorites. The first row shows simulations assuming fixed mineral modes (95.2% plagioclase + 3.6% low-Ca pyroxene + 1.2% high-Ca pyroxene, (A)-(C), Table A2) and the second row shows simulations using measured mineral modes (data in Table A2, (D)-(F)). For simulations with fixed mineral modes (A)-(C), the models assume the pyroxenes crystallized from the LMO and partition coefficients are calculated using major elements in plagioclase and pyroxene from both FANs (data from McGee, 1993; Papike et al., 1997; Pernet-Fisher et al., 2019) and lunar meteorites (data from Cahill et al., 2004; Roberts et al., 2019; Russell et al., 2014; and Dhofar 280 in this study). For simulations based on reported mineral modes (D)-(F), the models assume the pyroxenes crystallized from trapped magma ocean liquid within the anorthositic flotation crust. Measured compositions of pyroxenes and plagioclase are used to calculate partition coefficients (Table A2). For all simulations, the crystallization sequence is from Charlier et al. (2018), assuming an LMO with a LPUM bulk major element composition, a slightly depleted trace element bulk composition, and using modeled plagioclase crystallized from 82 to 98 percent solidification of the LMO. The threshold to filter successful simulations for each plagioclase is calculated considering the propagation of errors (Table A3). Most successful simulations assume Ts of 1050-1250 °C, fO_2 ~IW-2, and less than 1% KREEPy component addition.

recent studies on the fO_2s of specific lunar interior reservoirs suggest the possibility of more oxidized conditions. Guenther et al. (2022) argue the Apollo 17 orange glass source may experience melting at relatively higher fO_2 (~IW+1.5) based on results of multisaturation experiments. Tartèse et al. (2021) suggested that moderately volatile element depletion of returned lunar samples is consistent with degassing of their source materials in a magma ocean with an fO_2 close to FMQ+2.3.

In our Monte Carlo simulations, we apply the average mineral modes of lunar FANs according to our compilation (95.2% plagioclase + 3.6% low-Ca pyroxene + 1.2% high-Ca pyroxene, Table A1) as well as the average major element concentrations of plagioclase and pyroxenes for both Apollo FANs and lunar anorthositic meteorites (Table A3) to calculate representative partition coefficients. We consider simulations that recover a natural sample within the errors of its Eu/Eu* and $(Ce/Sm)_{CI}$ successful (Table A3). We compare the successful results for plagioclase from Apollo FANs and lunar anorthositic meteorites and find that the slightly depleted initial bulk LMO composition produces the most successful simulations (Figures 1.6A to 1.6C; 3,431 and 7,753 successful simulations out of 100,000 attempts for FANs and meteorites respectively; for comparison, the number of successful simulations for the moderately depleted bulk composition are 2,722 and 5,656, for the chondritic are 3,136 and 7,404; Figure A8). Most successful reequilibration temperatures range from 1050 to 1250 ℃, fO_2 is ~IW-2, and the added KREEPy component percentage is less than one. Such high temperature implies the nonnegligible contribution of thermal metamorphism to lunar anorthositic crust (e.g., Pernet-Fisher and Joy, 2022), and conforms to the petrographic description of some FANs (e.g., granulitic texture; McGee, 1993).

The temperature range is consistent with the equilibrium temperatures of lunar granulitic noritic anorthosites suggested by McLeod et al. (2016), 1050 to 1100℃, which also support lunar crustal reworking subsequent to LMO crystallization. We note that the temperatures of successful simulations are ~100°C higher for anorthositic meteorites, otherwise, parameter combinations in successful models are similar for FANs and anorthositic meteorites. After considering the propagation of errors, we observe that a bulk Moon with an enriched REE initial trace element bulk LMO composition cannot reproduce natural samples with low $(Ce/Sm)_{CI}$ and high Eu anomalies (Figure A8D), while other initial bulk trace element compositions successfully reproduce almost all plagioclase, except one from clast H4 in lunar meteorite NWA 10986, which shows the lowest $(Ce/Sm)_{CI}$ of all plagioclase (Roberts et al., 2019; Figure A8).

We investigated alternatives to the addition of KREEP basalt 15386 prior to subsolidus reequilibration, such as Mg-suite liquid (represented by Apollo samples 15455, 77215). Owing to the relatively lower REE concentrations and small Eu anomaly compared to KREEP basalt, it is necessary to add 8 % or even more into anorthosites to achieve the effect similar to that of adding 1% KREEP basalt, which is impossible in practice as introducing so much Mg-suite liquid will produce excessive mafic mineral modes inconsistent with the ferroan anorthosites (Figure A2). We additionally tested addition of other KREEPy components (e.g., high-K KREEP; Warren, 1989), which did not significantly change the Monte-Carlo simulation results.

Subsolidus reequilibration can reproduce the REE patterns of almost all plagioclase in different subgroups of FANs as subdivided by McGee (1994), assuming Ts between 1050 and 1250℃ and fO_2 between IW-1 to IW-2 by adding <1 % KREEPy component, with a slightly depleted initial trace element bulk composition (Figures 1.7A to 1.7D). For sample 67215 which has been classified as a mafic ferroan anorthosite (Floss et al., 1998), we need to add more KREEPy component (but still less than 2%) to reproduce the REE pattern (Figure 1.7B).

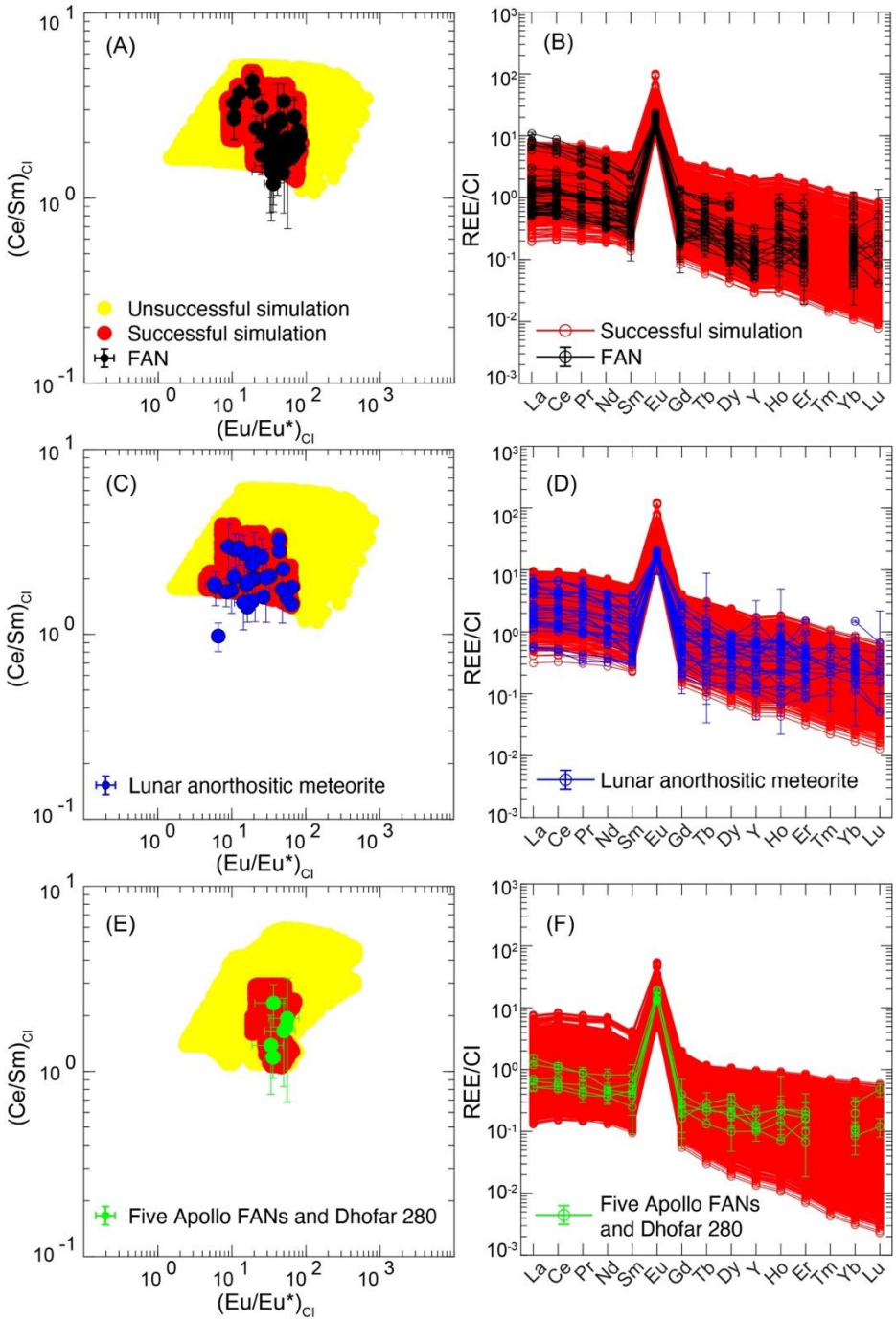


Figure 1.7. Successful Monte-Carlo simulation results assuming Ts between 1050 and 1250°C, fO_2 between IW-1 to IW-2, and addition of <2% KREEPy component. (A)-(D): Simulations assuming fixed mineral modes; (E)-(F): Simulations assuming reported mineral modes. All simulations assume a slightly depleted initial trace element bulk composition during subsolidus reequilibration. We find that within this combination of parameters almost all the plagioclase can be reproduced, by the standard of Eu/Eu* and $(Ce/Sm)_{CI}$ or the entire REE pattern.

We note the higher K content in plagioclase in 67215 also implies the addition of more KREEPy component (K varies from 148 to 262 ppm, Floss et al., 1998).

1.5.2 Simulations with reported mineral modes

In the above simulations, the pyroxene modes and compositions assumed (initially in equilibrium with LMO liquids from which they crystallized) impose model dependence. In real lunar samples, both low-Ca pyroxenes and high-Ca pyroxenes exist, but some LMO crystallization models only have one or no crystallization sequence including plagioclase, high-Ca pyroxene and low-Ca pyroxene, limiting the crystallization sequences that we can model. Considering the nonlinear relationship between An in plagioclase and Mg# in coexisting pyroxenes in lunar anorthosites, part or all of pyroxenes could crystallize from trapped liquid (e.g., Jolliff and Haskin, 1995), if we assume they are not magma ocean cumulates (e.g., Dygert et al., 2017; Raedeke and McCallum, 1980; Piskorz and Stevenson, 2014). To reduce model dependence, here we model a smaller number of samples with measured mineral modes. During the subsolidus reequilibration calculations, we use the site parameters for ions in pyroxenes and plagioclase based on measured major element compositions (Table A2) to calculate the partition coefficients and assume all pyroxenes crystallized from trapped magma ocean liquid between plagioclase grains. We ran 100,000 simulations per sample. Despite the small number of samples available owing to data limitations (Apollo FAN 15415, 60025, 60135, 60015, 65325; and lunar meteorite Dhofar 280 in this study; Table A2), the results are similar to those presented assuming fixed mineral modes. Again, parameter combinations in successful models for Apollo FANs are similar to those for lunar anorthositic meteorites. The assumption of a slightly depleted (Figures 1.6D and 1.6F) initial bulk LMO produces the most successful simulations (1,417 out of 600,000 simulations) among different initial compositions and can reproduce every plagioclase, with subsolidus reequilibration Ts around 1100 °C, fO_2 around IW-2, and the percentage of KREEPy component less than 1% (Figures 1.7E and 1.7F). A number of the successful simulations utilized plagioclase that crystallized at a relatively late stage of LMO solidification (Figures A9 and A10), which may be consistent with the asymmetric crustal growth model (Arai et al., 2008; Ohtake et al., 2012).

Simulation results for other bulk trace element LMO compositions and experimentally determined crystallization sequences are shown in Figures A9 and A10. Different models showed highly similar results in T, fO_2 and the percentage of KREEPy component added. Simulations testing enriched and chondritic bulk LMO produce fewer successful simulations (64 and 1,302 out of 600,000 simulations, respectively).

1.5.3 Reconciling a LREE depleted bulk Moon with isotopic characteristics of lunar samples

The number of successful simulations and successful simulation conditions are similar for models assuming a slightly depleted and moderately depleted initial lunar trace element bulk composition (Figure A9). However, the moderately depleted model has superchondritic Sm/Nd while slightly depleted model has near-chondritic Sm/Nd (Figure 1.2A). Isotopic study of urKREEP rich samples (KREEPy Mg-suite rocks and KREEP basalt) has revealed isotopically negative initial $\varepsilon^{143}Nd$ (e.g., 15386, 76535, 78238 and NWA 773; Borg et al., 2017; Borg et al., 2009; Edmunson et al., 2009; Gaffney and Borg, 2014), suggesting their KREEPy component originated from an LMO residual liquid with subchondritic Sm/Nd. If the LREE of the initial LMO is too depleted, the late residual liquid produced by LMO crystallization would be LREE depleted and have a superchondritic Sm/Nd (Figure 1.2B). Because a slightly

depleted pattern has a near chondritic Sm/Nd ratio, the residual liquid in simulations assuming slightly depleted REE abundances is consistent with isotopic variations in natural samples (Figure 1.2B). Remelting of cumulates of this residual liquid produces melt with KREEPy REE patterns with KREEPy negative Eu anomalies (Figure 1.2C).

Isotopic studies that applied the long and short lived Sm-Nd systems to lunar samples suggest the anorthosites formed from a LREE-depleted source or the initial bulk Moon is LREE-depleted (e.g., Borg et al., 1999; Boyet and Carlson, 2007). Alternatively, measured ^{142}Nd anomalies in meteorites may suggest the Moon accreted from material with a chondritic REE pattern but an enstatite chondrite-like initial ^{142}Nd composition (Boyet et al., 2015), i.e., their apparently depleted ^{142}Nd source reflects nucleosynthetic anomalies. Subsolidus reequilibration of lunar anorthosites following LMO solidification would produce apparently depleted initial sources, but addition of a KREEPy component would make the initial sources apparently more enriched. Thus, depending on the geologic history of each sample, either proposed explanation for apparently depleted initial ^{142}Nd may be consistent with our model.

1.6. Magmatic evolution after a cumulate mantle overturn event and its significance for geochronology

In the process of LMO crystallization, the olivine and pyroxenes that crystallized in the early LMO are magnesium rich. As LMO solidification progresses, iron and heavy incompatible element abundances (e.g., Ca, Ti) in the magma increase continuously, forming a gravitationally unstable cumulate pile with density increasing upward (Hess and Parmentier, 1995). This unstable density structure may produce gravitationally driven overturn, causing the denser shallower material, especially ilmenite-rich cumulates, to sink into the lunar interior as viscous solids, displacing deep mantle cumulates that rose to the crust-mantle boundary and melted to form the intrusive Mg-suite (Prissel and Gross, 2020). New constraints on the petrogenesis of lunar anorthosites provide an opportunity to reevaluate lunar magmatic evolution in the context of mantle overturn. After demonstrating the important role of a KREEPy component and subsolidus reequilibration for the formation of the FANs, we propose a post-LMO model for petrogenesis and secondary magmatic processing of the lunar anorthosites (Figure 1.8).

We start with a simplistic physical model that can help us understand the petrogenesis of lunar anorthosites as well as the evolution of the Moon (Figure 1.8A). As the deep cumulates migrated upward during cumulate mantle overturn, they experienced decompression melting and brought heat to the crust-mantle boundary, promoting subsolidus reequilibration (Longhi, 2003). At this time, a small amount of KREEPy melt penetrated into the anorthositic crust, promoting and participating in the subsolidus reequilibration. This model restricts most reequilibrated anorthosites to the deeper crust (i.e., at or near the crust-mantle boundary), since only in the relatively lower crust, anorthosites contact upwelling, hot mantle materials and mantle melts which would facilitate reequilibration (e.g., Pernet-Fisher and Joy, 2022; Figure 1.8A). Without a mechanism for emplacing the deep cumulates in shallower crust, reequilibrated anorthosites would not be sampled unless they were excavated by deep impacts. In addition, elemental redistribution between plagioclase and pyroxene in lunar anorthosites could require hundreds of millions of years for some anorthosites with large grain size as we suggested above. Radiogenic heat production in KREEPy melt beneath the crust would provide a longer-lived heat source, with the magnitude of heat production controlled by heat-producing element (HPE) abundances and the volume of the HPE-rich reservoir. Without a global mechanism to carry enough KREEPy materials into the crust, heat provided by injected magma may not be sufficiently prolonged to produce reequilibration.

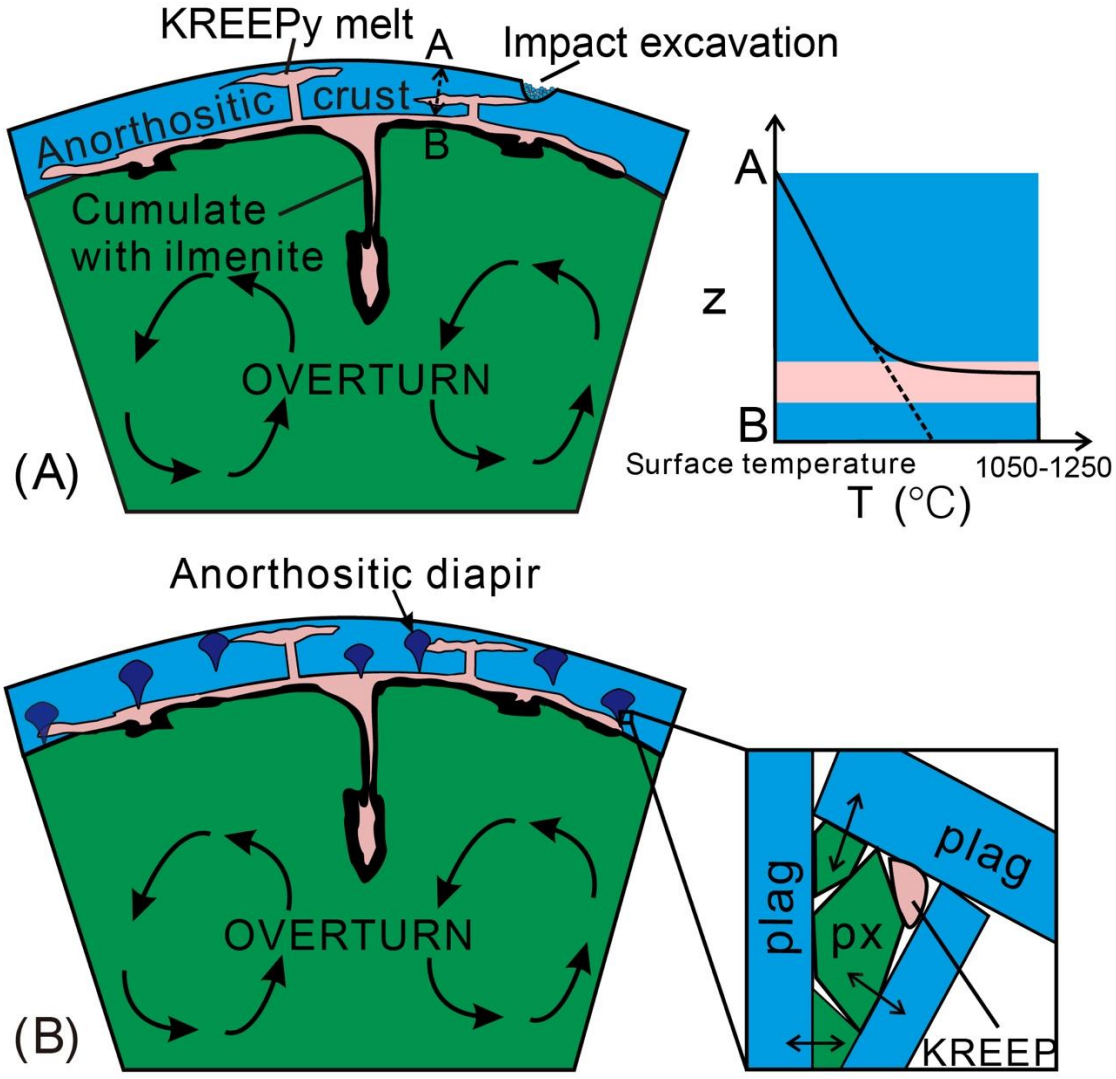


Figure 1.8. Schematic illustrations showing two scenarios for the magmatic evolution of the lunar crust after magma ocean solidification and a cumulate mantle overturn event. (A) A simple scenario that accounts for the input of a KREEPy component and heat source in the crust. After gravitational overturn, KREEPy components beneath the anorthositic crust intrude into the anorthositic crust. These intruding melts may be the parental magmas of KREEP basalts, Mg-suite and alkali-suite. The KREEPy melts interact with the surrounding anorthosites and provide a heat source to promote subsolidus reequilibration. (B) A more complex model invoking upwelling of anorthositic diapirs. In this scenario, the overturn event brings hot material from the lunar interior to the base of the crust, heating anorthosites hybridized by KREEPy melt. Extensive diapirism transports the anorthosites toward the crustal surface while and/or after they reequilibrate. These models reconcile an LMO scenario with the contemporaneous ages of the anorthosites and Mg-suite rocks (see Section 1.6). The source of the KREEPy melt in these illustrations is schematic, it may originate from heterogeneities in a previously hybridized mantle.

In order to address aforementioned weaknesses of the more simplistic model, a second model is proposed (Figure 1.8B). In this second scenario, the hot materials originating from the interior of the Moon heat the lower crust, forming a multitude of low-density anorthositic subsolidus diapirs which buoyantly migrate into the upper crust. They are contaminated by KREEPy melt before and/or during upwelling, resulting in extensive high-temperature subsolidus reequilibration. A large number of diapirs are emplaced on or near the lunar surface, burying older crust (Dygert et al., 2017), explaining the universality of moderate Eu anomalies in both Apollo sampled anorthosites and lunar anorthositic meteorites (e.g., Figure 1.1B). This model agrees with our Monte-Carlo simulation results that suggest the resurfaced anorthosites were located in the deeper crust before they upwelled, as they precipitated in the last LMO solidification stages (Figures A8 - A10). Moreover, the time required for subsolidus reequilibration can be satisfied by the radiogenic heat from the KREEP-rich material residing beneath the crust, which is widely injected into the crust through diapirism.

The model we propose here is also supported by geochronological research. Age overlap between ferroan anorthosites (e.g., 4290 ± 85 to 4573 ± 160 Ma; Borg et al., 2015) and the Mg-suite, which intrudes the anorthosites, (e.g., 4283 ± 23 to 4450 ± 270 Ma; Carlson et al., 2014) is perplexing and often considered to be related to post-crystallization metamorphic histories. A traditional LMO crystallization model cannot explain this age overlap because anorthosite is a product of LMO crystallization, while the parental magma of Mg-suite is formed by melting of early LMO cumulates that were hybridized by late LMO crystallization products (e.g., urKREEP and plagioclase; Prissel and Gross, 2020). A similar discordance appears for the lunar KREEPy component, which is the product of very late stage LMO crystallization (solidification equal or higher than 99 percent; Jing et al., 2022) but the model ages for ur-KREEP are 4350 ± 34 Ma (Borg et al., 2015), overlapping with ages of FAN (which crystallizes when the LMO PCS is ~80). The geochronological evidence strongly suggests a globally perturbing thermal event (presumably during a cumulate mantle overturn event) that disrupted the chronometers of anorthosites (Shearer and Papike, 2005). Subsolidus reequilibration and deformation-induced grain size reduction (e.g., Mehl and Hirth, 2008) associated with upwelling of anorthositic diapirs would raise the temperature above the closure temperature of radiogenic isotope chronometers and thus reset the ages, making them consistent with ages of Mg-suite rocks produced in the aftermath of cumulate mantle overturn.

According to remote sensing data, the distribution of a KREEPy signature on the lunar surface presents clear dichotomy with the nearside being highly enriched compared to the farside (e.g., Lawrence et al., 2000). Plagioclase in lunar anorthositic meteorites (many presumably from the farside highlands; e.g., Korotev et al., 2003) generally have less pronounced Eu anomalies than those in Apollo FANs (e.g., Figure 1.3A). To reproduce the compositions of the meteorites, our Monte Carlo simulations require a higher temperature and similar KREEPy component during subsolidus reequilibration compared with the nearside Apollo anorthosites (Figure 1.6). This implies that a KREEP signature was globally distributed in the lunar subsurface at the time the crust reequilibrated. The apparent present day hemispheric dichotomy in KREEP reflects bias related to the surface expression of KREEP (perhaps owing to a thicker farside crust, Wieczorek et al., 2013), or suggests hemispheric redistribution of KREEP in the Moon during or subsequent to crustal reequilibration (e.g., Ghods and Arkani-Hamed, 2007; Li et al., 2019), which would have also postdated formation of the South Pole Aitken basin (Lawrence et al., 2000; Moriarty et al., 2021).

1.7. A depleted bulk Moon

Although the Monte-Carlo simulations cannot exclude the possibility of a chondritic Moon as the initial lunar trace element bulk composition, assuming a LREE depleted initial bulk composition produces more successful simulations and reconciles the trace element and isotopic constraints recorded by other lunar samples as mentioned above. We therefore infer the initial bulk Moon is LREE depleted (e.g., Borg et al., 1999; Boyet and Carlson, 2007). According to traditional models, the origin of the Moon is by accretion of material ejected from the impact between a Mars-sized planetary body (Theia) and proto-Earth, implying that most of Moon's initial composition was inherited from Theia (e.g., Canup, 2004). A multitude of isotopic studies have demonstrated isotopic similarity between the Moon and Earth (e.g., the O, K, Si, W, Ti and ^{53}Mn-^{53}Cr isotopic systems; see Melosh, 2014 and references therein), motivating impact simulations that produce a Moon that accretes from mostly terrestrial material (e.g., Ćuk and Stewart, 2012), or that reequilibrates with Earth in the aftermath of the giant impact (e.g., Lock et al., 2018; Pahlevan and Stevenson, 2007). According to the difference in ^{142}Nd/^{144}Nd ratio between the terrestrial samples and chondrites, it is possible that the proto-Earth is LREE depleted or an initial differentiation on Earth finished before 4.53 Ga (Boyet and Carlson, 2005). A complementary LREE enriched reservoir could be lost during accretion (e.g., Allibert et al., 2021; Bourdon et al., 2008), or hidden in Earth's deep interior (e.g., Boyet and Carlson, 2005). If the bulk Earth is chondritic, the new constraints from LREE signatures in the anorthosites imply that the part of the proto-Earth and/or Theia sampled by the Moon-forming giant impact that produced the lunar magma ocean is LREE depleted, consistent with a pre-giant impact differentiation event.

1.8. Summary and Conclusions

Using a new model for Eu partitioning between plagioclase and melt (Dygert et al., 2020), we calculated the REE concentrations of plagioclase in lunar anorthosite assuming they formed from solidification of a lunar magma ocean (LMO). Comparison to natural samples revealed that under Moon-relevant fO_2s, lunar anorthosites cannot be reproduced by LMO solidification alone. An investigation of processes that could subsequently modify the plagioclase compositions showed that subsolidus reequilibration after the addition of a minor KREEPy component can be successfully invoked to fit the variations in REEs in the natural samples.

We used Monte-Carlo simulations to constrain the lunar trace element bulk composition and the conditions under which lunar anorthosites experienced secondary processing after their initial formation. Our results suggest the lunar ferroan anorthosites evolved in an environment with an fO_2 of ~IW-2 at Ts of 1050 - 1250°C after addition of a <1% KREEPy component. Simulations that best fit the lunar anorthosites assume a lunar magma ocean with a LREE depleted bulk composition, represented in our simulations by a slightly depleted trace element bulk composition, which is also consistent with isotopic evidence from lunar samples.

We propose a post-LMO model to explain the petrogenesis of lunar anorthosites. In our model, plagioclase formed from LMO crystallization and coexisting mafic minerals in anorthosites crystallized from the interstitial tapped liquid and/or from the LMO. Because of the gravitational instability of late LMO cumulates, deep magma ocean cumulates upwelled as a complement to the denser sinking ilmenite-bearing cumulates, introducing heat to the lower crust and promoting the formation of anorthositic diapirs. Some KREEPy melts below the anorthosites ascended into the crust under this Moon-wide agitation, producing subsolidus reequilibration which reconciles the Eu anomalies and REE patterns of the anorthosites, as well as the overlap in ages of Mg-suite, KREEP basalt and ferroan anorthosites.

1.9. Acknowledgments

We thank Yan Liang for helpful discussions, Allan Patchen for his help with electron microprobe analysis, and Soumen Mallick and Brendan Anzures for their assistance with LA-ICP-MS analysis at Brown University. We thank Katherine Joy and Wim van Westrenen for their constructive reviews, Frederic Moynier for efficient editorial handling, and two anonymous reviewers for comments on an earlier version of this manuscript. This work was supported by NASA Solar System Workings award 80NSSC20K0467 to N.D.

REFERENCES

Allibert, L., Charnoz, S., Siebert, J., Jacobson, S.A., Raymond, S.N., 2021. Quantitative estimates of impact induced crustal erosion during accretion and its influence on the Sm/Nd ratio of the Earth. Icarus 363, 114412.

Arai, T., Takeda, H., Yamaguchi, A., Ohtake, M., 2008. A new model of lunar crust: asymmetry in crustal composition and evolution. Earth Planets Space 60, 433-444.

Arevalo, R., McDonough, W.F., 2010. Chemical variations and regional diversity observed in MORB. Chem. Geol. 271, 70-85.

Barford, N.C., 1985. Experimental measurements: precision, error and truth. Chichester: Wiley.

Binder, A.B., 1974. On the origin of the moon by rotational fission. The moon 11, 53-76.

Borg, L., Norman, M., Nyquist, L., Bogard, D., Snyder, G., Taylor, L., Lindstrom, M., 1999. Isotopic studies of ferroan anorthosite 62236: A young lunar crustal rock from a light rare-earth-element-depleted source. Geochim. Cosmochim. Acta 63, 2679-2691.

Borg, L.E., Connelly, J.N., Cassata, W.S., Gaffney, A.M., Bizzarro, M., 2017. Chronologic implications for slow cooling of troctolite 76535 and temporal relationships between the Mg-suite and the ferroan anorthosite suite. Geochim. Cosmochim. Acta 201, 377-391.

Borg, L.E., Gaffney, A.M., Shearer, C.K., 2015. A review of lunar chronology revealing a preponderance of 4.34–4.37 Ga ages. Meteorit. Planet. Sci. 50, 715-732.

Borg, L.E., Gaffney, A.M., Shearer, C.K., DePaolo, D.J., Hutcheon, I.D., Owens, T.L., Ramon, E., Brennecka, G., 2009. Mechanisms for incompatible-element enrichment on the Moon deduced from the lunar basaltic meteorite Northwest Africa 032. Geochim. Cosmochim. Acta 73, 3963-3980.

Bourdon, B., Touboul, M., Caro, G., Kleine, T., 2008. Early differentiation of the Earth and the Moon. Philos. Trans. Royal Soc. A 366, 4105-4128.

Boyet, M., Carlson, R.W., 2005. 142Nd evidence for early (> 4.53 Ga) global differentiation of the silicate Earth. Science 309, 576-581.

Boyet, M., Carlson, R.W., 2007. A highly depleted moon or a non-magma ocean origin for the lunar crust? Earth Planet. Sci. Lett. 262, 505-516.

Boyet, M., Carlson, R.W., Borg, L.E., Horan, M., 2015. Sm–Nd systematics of lunar ferroan anorthositic suite rocks: constraints on lunar crust formation. Geochim. Cosmochim. Acta 148, 203-218.

Cahill, J.T., Floss, C., Anand, M., Taylor, L.A., Nazarov, M.A., Cohen, B.A., 2004. Petrogenesis of lunar highlands meteorites: Dhofar 025, Dhofar 081, Dar al Gani 262, and Dar al Gani 400. Meteorit. Planet. Sci. 39, 503-529.

Canup, R.M., 2004. Origin of Terrestrial Planets and the Earth--Moon System. Phys. Today 57, 56-62.

Carlson, R.W., Borg, L.E., Gaffney, A.M., Boyet, M., 2014. Rb-Sr, Sm-Nd and Lu-Hf isotope systematics of the lunar Mg-suite: the age of the lunar crust and its relation to the time of Moon formation. Philos. Trans. Royal Soc. A 372, 20130246.

Charlier, B., Grove, T.L., Namur, O., Holtz, F., 2018. Crystallization of the lunar magma ocean and the primordial mantle-crust differentiation of the Moon. Geochim. Cosmochim. Acta 234, 50-69.

Cherniak, D., 2003. REE diffusion in feldspar. Chem. Geol. 193, 25-41.

Cherniak, D.J., Liang, Y., 2007. Rare earth element diffusion in natural enstatite. Geochim. Cosmochim. Acta 71, 1324-1340.

Ćuk, M., Stewart, S.T., 2012. Making the Moon from a Fast-Spinning Earth: A Giant Impact Followed by Resonant Despinning. Science 338, 1047-1052.

Dixon, J.R., Papike, J.J., 1975. Petrology of anorthosites from the Descartes region of the moon-Apollo 16, Lunar and Planetary Science Conference Proceedings, pp. 263-291.
Dowty, E., Keil, K., Prinz, M., 1972. Anorthosite in the Apollo 15 rake sample from Spur Crater. The Apollo 15 Lunar Samples, 62-66.
Dygert, N., Draper, D.S., Rapp, J.F., Lapen, T.J., Fagan, A.L., Neal, C.R., 2020. Experimental determinations of trace element partitioning between plagioclase, pigeonite, olivine, and lunar basaltic melts and an *f*O2 dependent model for plagioclase-melt Eu partitioning. Geochim. Cosmochim. Acta 279, 258-280.
Dygert, N., Liang, Y., Hess, P., 2013. The importance of melt TiO2 in affecting major and trace element partitioning between Fe-Ti oxides and lunar picritic glass melts. Geochim. Cosmochim. Acta 106, 134-151.
Dygert, N., Liang, Y., Sun, C., Hess, P., 2014. An experimental study of trace element partitioning between augite and Fe-rich basalts. Geochim. Cosmochim. Acta 132, 170-186.
Dygert, N., Lin, J.-F., Marshall, E.W., Kono, Y., Gardner, J.E., 2017. A Low Viscosity Lunar Magma Ocean Forms a Stratified Anorthitic Flotation Crust With Mafic Poor and Rich Units. Geophys. Res. Lett. 44.
Dymek, R., Albee, A., Chodos, A., 1975. Comparative petrology of lunar cumulate rocks of possible primary origin-Dunite 72415, troctolite 76535, norite 78235, and anorthosite 62237, Lunar and Planetary Science Conference Proceedings, pp. 301-341.
Elardo, S.M., Draper, D.S., Shearer Jr, C.K., 2011. Lunar Magma Ocean crystallization revisited: Bulk composition, early cumulate mineralogy, and the source regions of the highlands Mg-suite. Geochim. Cosmochim. Acta 75, 3024-3045.
Edmunson, J., Borg, L., Nyquist, L., Asmerom, Y., 2009. A combined Sm–Nd, Rb–Sr, and U–Pb isotopic study of Mg-suite norite 78238: further evidence for early differentiation of the Moon. Geochim. Cosmochim. Acta 73, 514-527.
Fabbrizio, A., Schmidt, M.W., Petrelli, M., 2021. Effect of fO2 on Eu partitioning between clinopyroxene, orthopyroxene and basaltic melt: Development of a Eu3+/Eu2+ oxybarometer. Chem. Geol. 559, 119967.
Floss, C., James, O.B., McGee, J.J., Crozaz, G., 1998. Lunar ferroan anorthosite petrogenesis: Clues from trace element distributions in FAN subgroups. Geochim. Cosmochim. Acta 62, 1255-1283.
Gaffney, A.M., Borg, L.E., 2014. A young solidification age for the lunar magma ocean. Geochim. Cosmochim. Acta 140, 227-240.
Ghods, A., Arkani-Hamed, J., 2007. Impact-induced convection as the main mechanism for formation of lunar mare basalts. Journal of Geophysical Research: Planets 112.
Gromet, L.P., Silver, L.T., 1983. Rare earth element distributions among minerals in a granodiorite and their petrogenetic implications. Geochimica et Cosmochimica Acta 47, 925-939.
Gross, J., Joy, K.H., 2016. Evolution, lunar: from magma ocean to crust formation. Encyclopedia of lunar science, 1-20.
Gross, J., Treiman, A.H., Mercer, C.N., 2014. Lunar feldspathic meteorites: Constraints on the geology of the lunar highlands, and the origin of the lunar crust. Earth Planet. Sci. Lett. 388, 318-328.
Guenther, M.E., Krein, S.M.B., Grove, T.L., 2022. The influence of variable oxygen fugacity on the source depths of lunar high-titanium ultramafic glasses. Geochim. Cosmochim. Acta 334, 217-230.

Hahn Jr, T.M., Lunning, N.G., McSween Jr, H.Y., Bodnar, R.J., Taylor, L.A., 2017. Dacite formation on Vesta: Partial melting of the eucritic crust. Meteorit. Planet. Sci. 52, 1173-1196.

Haskin, L., Lindstrom, M., Salpas, P., 1981. Some observations on compositional characteristics of lunar anorthosites, Lunar and Planetary Science Conference, pp. 406-408.

Hess, P.C., Parmentier, E.M., 1995. A model for the thermal and chemical evolution of the Moon's interior: implications for the onset of mare volcanism. Earth Planet. Sci. Lett. 134.

Jing, J.-J., Lin, Y., Knibbe, J.S., van Westrenen, W., 2022. Garnet stability in the deep lunar mantle: Constraints on the physics and chemistry of the interior of the Moon. Earth Planet. Sci. Lett. 584, 117491.

Jochum, K.P., Weis, U., Stoll, B., Kuzmin, D., Yang, Q., Raczek, I., Jacob, D.E., Stracke, A., Birbaum, K. and Frick, D.A. (2011) Determination of reference val-ues for NIST SRM 610–617 glasses following ISO guidelines. Geostandards and Geoanalytical Research 35, 397-429.

Jochum, K.P., Willbold, M., Raczek, I., Stoll, B. and Herwig, K. (2005) Chemical Characterisation of the USGS Reference Glasses GSA‐1G, GSC‐1G, GSD‐1G, GSE‐1G, BCR‐2G, BHVO‐2G and BIR‐1G Using EPMA, ID‐TIMS, ID‐ICP‐MS and LA‐ICP‐MS. Geostandards and Geoanalytical Research 29, 285-302.

Jolliff, B., Haskin, L., 1995. Cogenetic rock fragments from a lunar soil: Evidence of a ferroan noritic-anorthosite pluton on the Moon. Geochim. Cosmochim. Acta 59, 2345-2374.

Krättli, G., Schmidt, M.W., 2021. Experimental settling, floatation and compaction of plagioclase in basaltic melt and a revision of melt density. Contrib. to Mineral. Petrol. 176, 1-27.

Korotev, R.L., Jolliff, B.L., Zeigler, R.A., Gillis, J.J., Haskin, L.A., 2003. Feldspathic lunar meteorites and their implications for compositional remote sensing of the lunar surface and the composition of the lunar crust. Geochim. Cosmochim. Acta 67, 4895-4923.

Lawrence, D., Feldman, W., Barraclough, B., Binder, A., Elphic, R., Maurice, S., Miller, M., Prettyman, T., 2000. Thorium abundances on the lunar surface. Journal of Geophysical Research: Planets 105, 20307-20331.

Li, H., Zhang, N., Liang, Y., Wu, B., Dygert, N.J., Huang, J., Parmentier, E., 2019. Lunar cumulate mantle overturn: A model constrained by ilmenite rheology. Journal of Geophysical Research: Planets 124, 1357-1378.

Lin, Y., Tronche, E.J., Steenstra, E.S., Van Westrenen, W., 2017. Experimental constraints on the solidification of a nominally dry lunar magma ocean. Earth Planet. Sci. Lett. 471, 104-116.

Liu, T., Michael, G., Zhu, M.H., Wünnemann, K., 2021. Predicted sources of samples returned from Chang'e− 5 landing region. Geophys. Res. Lett. 48, e2021GL092434.

Lock, S.J., Stewart, S.T., Petaev, M.I., Leinhardt, Z., Mace, M.T., Jacobsen, S.B., Cuk, M., 2018. The Origin of the Moon Within a Terrestrial Synestia. J. Geophys. Res. Planets 123, 910-951.

Lodders, K., 2021. Relative atomic solar system abundances, mass fractions, and atomic masses of the elements and their isotopes, composition of the solar photosphere, and compositions of the major chondritic meteorite groups. Space Science Reviews 217, 1-33.

Longhi, J., 1978. Pyroxene stability and the composition of the lunar magma ocean, Lunar and Planetary Science Conference Proceedings, pp. 285-306.

Longhi, J., 2003. A new view of lunar ferroan anorthosites: Postmagma ocean petrogenesis. J. Geophys. Res. Planets 108.

Longhi, J., 2006. Petrogenesis of picritic mare magmas: Constraints on the extent of early lunar differentiation. Geochim. Cosmochim. Acta 70, 5919-5934.
Maurice, M., Tosi, N., Schwinger, S., Breuer, D., Kleine, T., 2020. A long-lived magma ocean on a young Moon. Sci. Adv. 6.
McCubbin, F.M., Jones, R.H., 2015. Extraterrestrial apatite: Planetary geochemistry to astrobiology. Elements 11, 183-188.
McDonough, W.F., Sun, S.-S., 1995. The composition of the Earth. Chem. Geol. 120, 223-253.
McGee, J., 1994. Lunar ferroan anorthosite subgroups, Lunar and Planetary Science Conference, p. 875.
McGee, J.J., 1993. Lunar Ferroan Anorthosites - Mineralogy, Compositional Variations, and Petrogenesis. J. Geophys. Res. Planets 98, 9089-9105.
McLeod, C.L., Brandon, A.D., Fernandes, V.A., Peslier, A.H., Fritz, J., Lapen, T., Shafer, J.T., Butcher, A.R., Irving, A.J., 2016. Constraints on formation and evolution of the lunar crust from feldspathic granulitic breccias NWA 3163 and 4881. Geochim. Cosmochim. Acta 187, 350-374.
Mehl, L., Hirth, G., 2008. Plagioclase preferred orientation in layered mylonites: Evaluation of flow laws for the lower crust. J. Geophys. Res. Solid Earth 113.
Melosh, H., 2014. New approaches to the Moon's isotopic crisis. Philos. Trans. Royal Soc. A 372, 20130168.
Moriarty III, D., Watkins, R., Valencia, S., Kendall, J., Evans, A., Dygert, N., Petro, N., 2021. Evidence for a Stratified Upper Mantle Preserved Within the South Pole-Aitken Basin. Journal of Geophysical Research: Planets 126, e2020JE006589.
Namur, O., Charlier, B., Pirard, C., Hermann, J., Liégeois, J.-P., Vander Auwera, J., 2011. Anorthosite formation by plagioclase flotation in ferrobasalt and implications for the lunar crust. Geochim. Cosmochim. Acta 75, 4998-5018.
Neal, C., Kramer, G., 2003. The composition of KREEP: A detailed study of KREEP basalt 15386, Lunar and Planetary Science conference, p. 2023.
Norman, M.D., Borg, L.E., Nyquist, L.E., Bogard, D.D., 2003. Chronology, geochemistry, and petrology of a ferroan noritic anorthosite clast from Descartes breccia 67215: Clues to the age, origin, structure, and impact history of the lunar crust. Meteorit. Planet. Sci. 38, 645-661.
Nord Jr, G.L., Wandless, M.V., 1983. Petrology and comparative thermal and mechanical histories of clasts in breccia 62236. J. Geophys. Res. Solid Earth 88, A645-A657.
Nyquist, L., Wiesmann, H., Shih, C., Bansal, B., 1976. 15405 Quartz monzodiorite: Super KREEP, Interdisciplinary Studies by Imbrium Consortium. Center for Astrophysics Publ Cambridge, MA, pp. 30-41.
O'Neill, H.S.C., 1991. The origin of the Moon and the early history of the Earth—A chemical model. Part 1: The Moon. Geochim. Cosmochim. Acta 55, 1135-1157.
Ohtake, M., Takeda, H., Matsunaga, T., Yokota, Y., Haruyama, J., Morota, T., Yamamoto, S., Ogawa, Y., Hiroi, T., Karouji, Y., 2012. Asymmetric crustal growth on the Moon indicated by primitive farside highland materials. Nat. Geosci. 5, 384-388.
Pahlevan, K., Stevenson, D.J., 2007. Equilibration in the aftermath of the lunar-forming giant impact. Earth Planet. Sci. Lett. 262, 438-449.
Papike, J.J., Fowler, G.W., Shearer, C.K., 1997. Evolution of the lunar crust: SIMS study of plagioclase from ferroan anorthosites. Geochim. Cosmochim. Acta 61, 2343-2350.
Pernet-Fisher, J., Joy, K., Martin, D., Donaldson Hanna, K., 2017. Assessing the shock state of the lunar highlands: implications for the petrogenesis and chronology of crustal anorthosites. Sci Rep-Uk 7, 1-12.

Pernet-Fisher, J.F., Deloule, E., Joy, K.H., 2019. Evidence of chemical heterogeneity within lunar anorthosite parental magmas. Geochim. Cosmochim. Acta 266, 109-130.
Pernet-Fisher, J.F., Joy, K.H., 2022. Thermal metamorphism on the Moon as recorded by the granulite suite. Journal of the Geological Society 179, jgs2021-2044.
Phinney, W., 1992. Partition coefficients for iron between plagioclase and basalt as a function of oxygen fugacity: Implications for Archean and lunar anorthosites. Geochim. Cosmochim. Acta 56, 1885-1895.
Piskorz, D., Stevenson, D.J., 2014. The formation of pure anorthosite on the Moon. Icarus 239, 238-243.
Potts, N.J., Barnes, J.J., Tartèse, R., Franchi, I.A., Anand, M., 2018. Chlorine isotopic compositions of apatite in Apollo 14 rocks: Evidence for widespread vapor-phase metasomatism on the lunar nearside∼ 4 billion years ago. Geochimica et Cosmochimica Acta 230, 46-59.
Prinz, M., Dowty, E., Keil, K., Bunch, T.E., 1973. Spinel Troctolite and Anorthosite in Apollo-16 Samples. Science 179, 74-76.
Prissel, T.C., Gross, J., 2020. On the petrogenesis of lunar troctolites: New insights into cumulate mantle overturn & mantle exposures in impact basins. Earth Planet. Sci. Lett. 551, 116531.
Prowatke, S., Klemme, S., 2006. Trace element partitioning between apatite and silicate melts. Geochim. Cosmochim. Acta 70, 4513-4527.
Qian, Y., Xiao, L., Head, J.W., van der Bogert, C.H., Hiesinger, H., Wilson, L., 2021. Young lunar mare basalts in the Chang'e-5 sample return region, northern Oceanus Procellarum. Earth Planet. Sci. Lett. 555, 116702.
Raedeke, L.D., McCallum, I., 1980. A comparison of fractionation trends in the lunar crust and the Stillwater Complex, *Proceedings of the Conference on the Lunar Highlands Crust*. Pergamon Press, pp. 133-153.
Rapp, J.F., Draper, D.S., 2018. Fractional crystallization of the lunar magma ocean: Updating the dominant paradigm. Meteorit. Planet. Sci. 53, 1452-1455.
Roberts, S.E., McCanta, M.C., Jean, M.M., Taylor, L.A., 2019. New lunar meteorite NWA 10986: A mingled impact melt breccia from the highlands-A complete cross section of the lunar crust. Meteorit. Planet. Sci. 54, 3018-3035.
Rudnick, R., Gao, S., 2014. Composition of the Continental Crust, *The Crust*, p. 47.
Russell, S.S., Joy, K.H., Jeffries, T.E., Consolmagno, G.J., Kearsley, A., 2014. Heterogeneity in lunar anorthosite meteorites: implications for the lunar magma ocean model. Philos. Trans. Royal Soc. A 372.
Rutherford, M.J., Head, J.W., Saal, A.E., Hauri, E., Wilson, L., 2017. Model for the origin, ascent, and eruption of lunar picritic magmas. American Mineralogist: Journal of Earth and Planetary Materials 102, 2045-2053.
Schmidt, M.W., Kraettli, G., 2022. Experimental crystallization of the lunar magma ocean, initial selenotherm and density stratification, and implications for crust formation, overturn and the bulk silicate Moon composition. Journal of Geophysical Research: Planets, e2022JE007187.
Shearer, C.K., Papike, J., 2005. Early crustal building processes on the moon: Models for the petrogenesis of the magnesian suite. Geochim. Cosmochim. Acta 69, 3445-3461.
Shervais, J.W., Taylor, L.A., Laul, J., Smith, M., 1984. Pristine highland clasts in consortium breccia 14305: Petrology and geochemistry. Journal of Geophysical Research: Solid Earth 89, C25-C40.

Snyder, G.A., Taylor, L.A., Neal, C.R., 1992a. A chemical model for generating the sources of mare basalts: Combined equilibrium and fractional crystallization of the lunar magmasphere. Geochim. Cosmochim. Acta 56, 3809-3823.

Snyder, G., Taylor, L., Crozaz, G., 1992b. Zircon/melt partition coefficients for the rare-earth elements in evolved rocks: the usefulness of accessory minerals in petrogenetic studies on the Earth and Moon, Lunar and Planetary Science Conference.

Steele, I.M., Smith, J., 1971. Mineralogy of Apollo 15415 "genesis rock": Source of anorthosite on Moon. Nature 234, 138-140.

Sun, C.G., Liang, Y., 2013a. The importance of crystal chemistry on REE partitioning between mantle minerals (garnet, clinopyroxene, orthopyroxene, and olivine) and basaltic melts. Chem. Geol. 358, 23-36.

Sun, C.G., Graff, M., Liang, Y., 2017. Trace element partitioning between plagioclase and silicate melt: The importance of temperature and plagioclase composition, with implications for terrestrial and lunar magmatism. Geochim. Cosmochim. Acta 206, 273-295.

Sun, C.G., Liang, Y., 2013b. Distribution of REE and HFSE between low-Ca pyroxene and lunar picritic melts around multiple saturation points. Geochim. Cosmochim. Acta 119, 340-358.

Sun, C.G., Liang, Y., 2014. An assessment of subsolidus re-equilibration on REE distribution among mantle minerals olivine, orthopyroxene, clinopyroxene, and garnet in peridotites. Chem. Geol. 372, 80-91.

Tang, M., Chen, K., Rudnick, R.L., 2016. Archean upper crust transition from mafic to felsic marks the onset of plate tectonics. Science 351, 372-375.

Tartèse, R., Sossi, P.A., Moynier, F., 2021. Conditions and extent of volatile loss from the Moon during formation of the Procellarum basin. Proceedings of the National Academy of Sciences 118, e2023023118.

Taylor, G.J., Wieczorek, M.A., 2014. Lunar bulk chemical composition: a post-Gravity Recovery and Interior Laboratory reassessment. Philos. Trans. Royal Soc. A 372, 20130242.

Taylor, S.R., 1982. *Planetary science: A lunar perspective*. Lunar and Planetary Institute, Houston, p. 502.

Treiman, A.H., Maloy, A.K., Shearer, C.K., Gross, J., 2010. Magnesian anorthositic granulites in lunar meteorites Allan Hills A81005 and Dhofar 309: Geochemistry and global significance. Meteorit. Planet. Sci. 45, 163-180.

Tian, H.-C., Wang, H., Chen, Y., Yang, W., Zhou, Q., Zhang, C., Lin, H.-L., Huang, C., Wu, S.-T., Jia, L.-H., 2021. Non-KREEP origin for Chang'E-5 basalts in the Procellarum KREEP Terrane. Nature 600, 59-63.

Van Orman, J.A., Grove, T.L., Shimizu, N., 2001. Rare earth element diffusion in diopside: influence of temperature, pressure, and ionic radius, and an elastic model for diffusion in silicates. Contrib. to Mineral. Petrol. 141, 687-703.

Warren, P.H., 1989. KREEP: major-element diversity, trace-element uniformity (almost), Workshop on Moon in Transition: Apollo 14, KREEP, and Evolved Lunar Rocks, pp. 149-153.

Warren, P.H., 1990. Lunar Anorthosites and the Magma-Ocean Plagioclase-Flotation Hypotheses: Importance of FeO Enrichment in the Parent Magma. Am. Mineral. 75, 46-58.

Warren, P., 2012. Let's get real: not every lunar rock sample is big enough to be repre-sentative for every purpose, Second Conference on the Lunar Highlands Crust, pp. 59-60.

Warren, P.H., Taylor, G.J., Keil, K., Kallemeyn, G.W., Shirley, D.N., Wasson, J.T., 1983. Seventh Foray: Whitlockite‐rich lithologies, a diopside‐bearing troctolitic anorthosite, Ferroan anorthosites, and KREEP. J. Geophys. Res. Solid Earth 88, B151-B164.

Warren, P.H., Wasson, J.T., 1978. Compositional-petrographic investigation of pristine nonmare rocks, Lunar and Planetary Science Conference Proceedings, pp. 185-217.

Warren, P.H., Jerde, E.A., Kallemeyn, G.W., 1987. Pristine Moon rocks: A "large" felsite and a metal‐rich ferroan anorthosite. J. Geophys. Res. Solid Earth 92, E303-E313.

Wieczorek, M.A., Neumann, G.A., Nimmo, F., Kiefer, W.S., Taylor, G.J., Melosh, H.J., Phillips, R.J., Solomon, S.C., Andrews-Hanna, J.C., Asmar, S.W., 2013. The crust of the Moon as seen by GRAIL. Science 339, 671-675.

Workman, R.K., Hart, S.R., 2005. Major and trace element composition of the depleted MORB mantle (DMM). Earth Planet. Sci. Lett. 231, 53-72.

APPENDIX A

Methods for collection of mineral modes of Dhofar 280

Mineral modes and major and trace element concentration data for each mineral in lunar anorthositic samples are required for the most accurate subsolidus reequilibration modeling, and comprehensive datasets with all necessary sample properties reported are scarce. To augment existing data in the literature, here we measured the petrological and geochemical characteristics of lunar anorthositic meteorite Dhofar 280, an anorthositic fragmental breccia mainly consisting of abundant mineral fragments and lithic clasts in a glassy matrix.

One thin section of Dhofar 280 was investigated using an Olympus BX53M microscope in transmitted and reflected light at the University of Tennessee. Warren, (2012) warned that taking small clasts from lunar samples as the pristine rock composition is risky. Although we indeed observed some small clasts and glassy matrix in our Dhofar 280 material, the grain sizes of plagioclase we examined are larger than 200 μm (e.g., the ~900 μm plagioclase grain in the lower right corner of Figure A12). No metal particles suspected to be from the impactor are observed.

Mineral modes were obtained by point counting. For minerals that could not be confidently identified optically, we used a Phenom benchtop Scanning Electron Microscope (SEM) equipped with an Energy-Dispersive Spectrometer to obtain qualitative geochemical data to aid in identification. Mineral modes are reported in Figure A2 and Table A2.

Methods for characterization of major and trace element geochemistry of Dhofar 280

We measured the major element compositions using a Cameca SX-100 electron microprobe (EMP) at the University of Tennessee using a 1 μm spot size and beam current of 30 nA for mafic minerals and a 5 μm spot size and 10 nA current to analyze plagioclase at an accelerating voltage of 15 keV for all minerals. Trace element concentrations in minerals were determined by laser ablation inductively coupled plasma mass spectrometry (LA-ICP-MS) using a 193 nm wavelength excimer Analyte G2 laser coupled to a Thermo Scientific X-Series II at Brown University. Samples were ablated with 40–50 μm diameter beams with a laser fluence of 3.78 J/cm^2 at 50% energy level and a frequency of 10 Hz. For pyroxenes and plagioclase, analyses were calibrated using CaO as a reference analyte from EMP analyses. Primary trace element standard materials are BCR-2G and BHVO-2G, secondary standard materials are BIR-1G and NIST glass SRM 612. Secondary standard analytical recoveries are 0.69% to 23.96% of reference values, with an average recovery of 8.99% (Jochum et al., 2011; Jochum et al., 2005; Table A6). Analytical precision for elements with concentrations greater than 10 ppm ranges from 10 to 15% (RSD) on average; for elements with concentrations less than 1 ppm precision was typically 20–35% (RSD). The results are shown in Figure 1.1, Figure A3 and Table A2.

Geochemical characteristics of plagioclase in Apollo FANs and lunar anorthositic meteorites

Characteristics of major and REEs in Apollo samples

Lunar anorthositic plagioclase from Apollo returned samples are highly calcic, displaying limited compositional variation (data come from McGee, 1993; Papike et al., 1997; Pernet-Fisher et al., 2019), with An#s of 95.8 to 97.7 (where the An# = 100 × molar Ca/[Ca + Na + K] or An# = 100 × molar Ca/[Ca + Na] where K is not reported), while coexisting pyroxenes are ferroan to magnesian (Mg# = 43 - 67 for low-Ca pyroxenes and Mg# = 59 - 77 for high-Ca pyroxenes, where Mg# = 100 × molar Mg/[Mg + Fe]). As has long been recognized, comparison of An# in plagioclase with Mg# in coexisting pyroxenes show neither positive nor negative correlations (Figure 1.1A), as would be expected in an LMO-type fractional

crystallization scenario. Instead, the samples show a vertical trend which is thought to be the result of trapped intercumulus liquid crystallization (e.g., Raedeke and McCallum, 1980). Apollo FAN plagioclase have low total FeO (0.05 - 0.23 wt%) and MgO (0.02 - 0.13 wt%), and exhibit a horizontal trend when compared to An in plagioclase (Figures A3A and A3B), which has previously been attributed to subsolidus reequilibration during metamorphism (McGee, 1993; Phinney, 1992). The plagioclase show variable enrichment in light REEs (LREEs) compared with heavy REEs (HREEs) with $(La/Yb)_{CI}$ of 2 - 32, as well as a positive Eu anomalies (Eu/Eu*) which range from 10 to 81 (Figure 1.1B).

Characteristics of major and REEs in lunar anorthositic Meteorites

Plagioclase in lunar anorthositic meteorites also show a high An number range from 94.8 to 98.0 (Cahill et al., 2004; Gross et al., 2014; Roberts et al., 2019; Russell et al., 2014; Treiman et al., 2010, and this study). On average, the coexisting pyroxenes are more magnesian than in FANs (Mg# = 48 - 87 for low-Ca pyroxenes and 70 - 87 for high-Ca pyroxenes; Figure 1.1A). The difference in Mg# range may be attributed to the random sampling of the lunar surface provided by meteorites, some of which bridge the compositional "gap" between Mg-suite and FAN, and have been inferred to sample the lunar farside (e.g., Gross et al., 2014; Ohtake et al., 2012; Roberts et al., 2019). In contrast, mafic minerals in Dhofar 280 show a much lower Mg# (62 - 70, Figure 1.1A), consistent with Apollo anorthosites from the lunar nearside. Plagioclase FeO (0.12 - 0.53 wt%) and MgO (0.08 - 0.81 wt%) contents are more variable, but they still have no linear relationship with An# (Figures A3A and A3B). These plagioclase also have obvious Eu anomalies (Eu/Eu* = 6 - 65) but less fractionated REE patterns [$(La/Yb)_{CI}$ = 4 - 18] compared with plagioclase from Apollo FANs (Figure 1.1B). The REE concentrations of Dhofar 280 plagioclase are similar to reported plagioclase in Dhofar 081 (Table A3; Cahill et al., 2004), a meteorite paired with Dhofar 280.

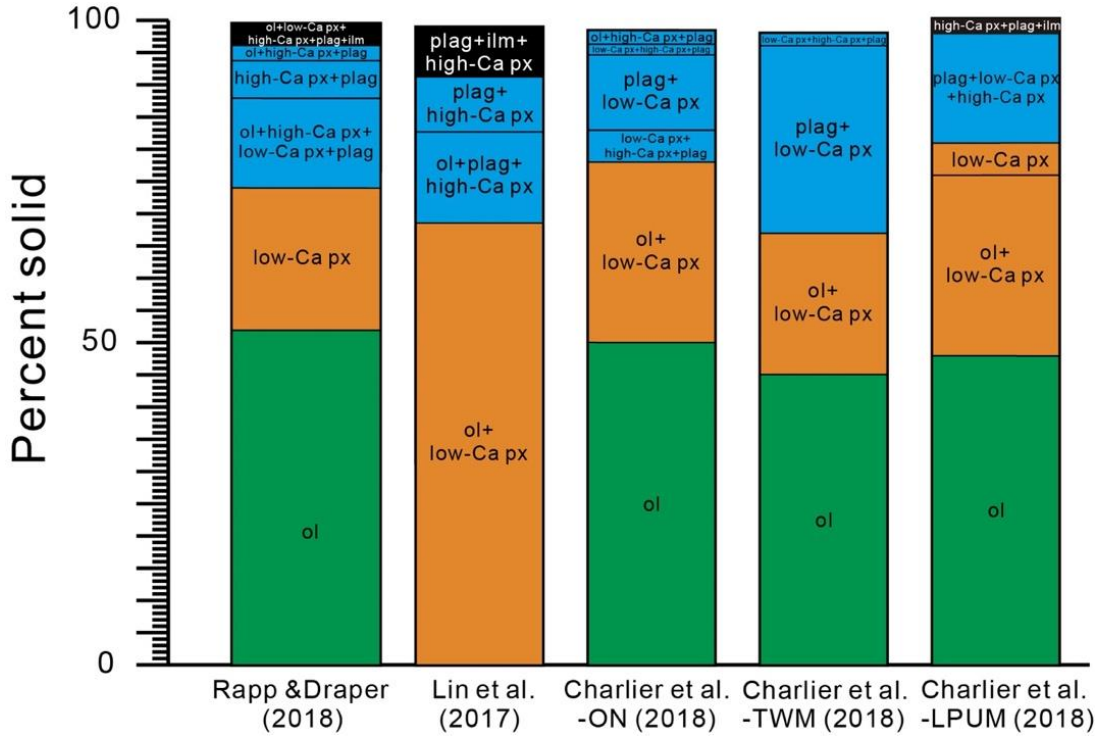


Figure A1. Comparison of experimentally determined LMO crystallization sequences (Charlier et al., 2018; Lin et al., 2017; Rapp and Draper, 2018) for different bulk Moon compositions. An O'Neill bulk Moon (O'Neill, 1991) is indicated by ON, TWM indicates the Taylor Whole Moon (Taylor, 1982) and the LPUM represents Lunar Primitive Upper Mantle (Longhi, 2006). Here we report pigeonite and orthopyroxene as low-Ca pyroxene, and augite and clinopyroxene as high-Ca pyroxene.

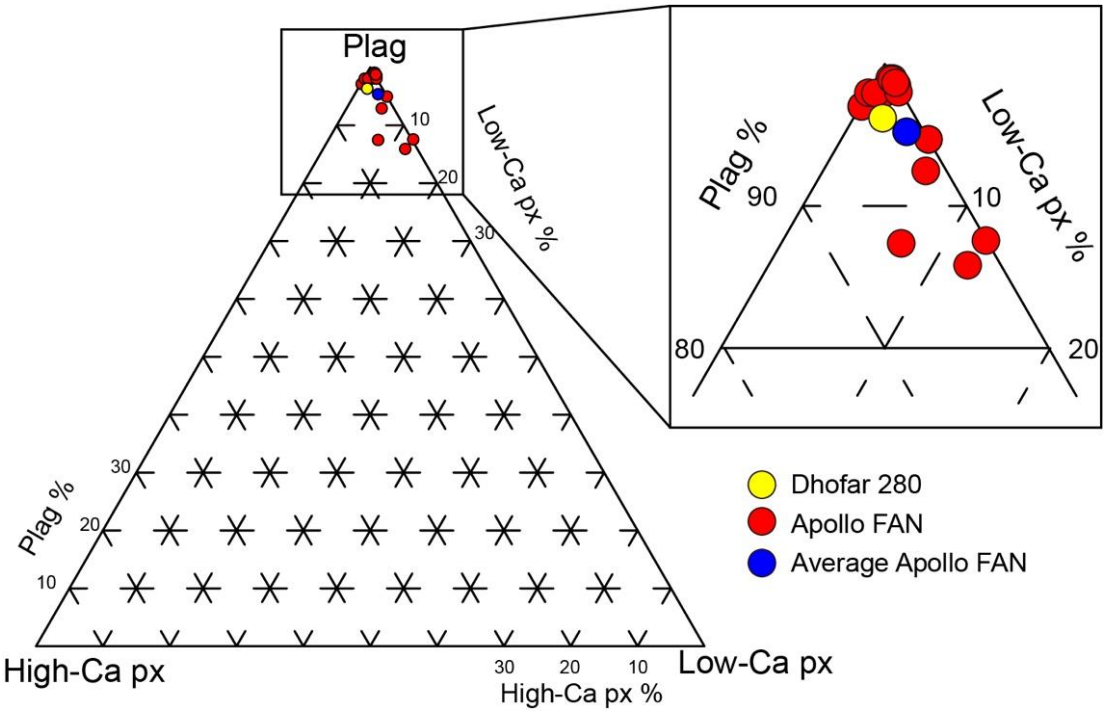


Figure A2. Mineral modes for Apollo ferroan anorthosites and Dhofar 280. We use a three-phase basis to plot the modes of Apollo ferroan anorthosites (red circles, the data sources are listed in Table A1), the average mineral mode of Apollo anorthosites (95.2% plag + 3.6% low-Ca px + 1.2% high-Ca px, blue circle) and lunar anorthositic meteorite Dhofar 280 (yellow circle, this study). We only consider plagioclase and pyroxenes because of their dominant control on subsolidus reequilibration of REEs in lunar anorthosites. Note that the Dhofar 280 is an anorthositic fragmental breccia, therefore, its modal mineralogy (determined by characterization of an entire thin section) may not be equivalent to that of the original crust.

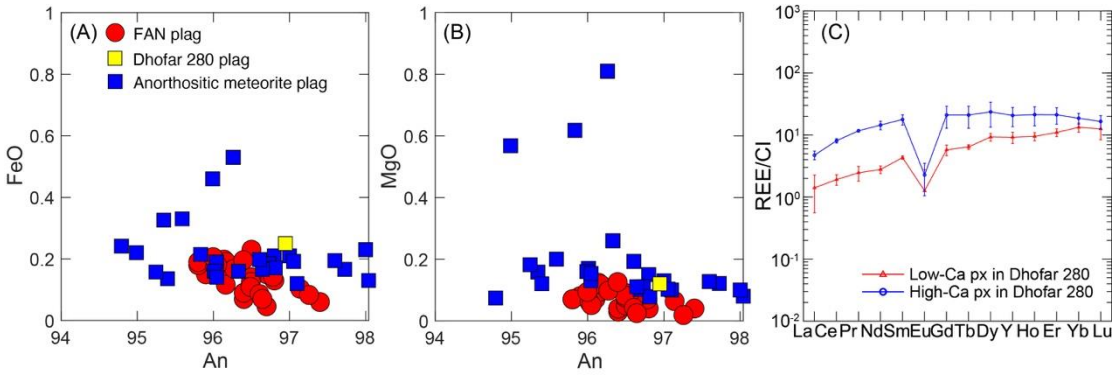


Figure A3. Major and trace element characteristics of minerals in Apollo ferroan anorthosites and lunar anorthositic meteorites. (A) FeO contents (wt %) versus anorthite content (An) in plagioclase (100 × Ca/(Ca+Na+K), in moles), (B) MgO contents (wt %) versus An in plagioclase from ferroan anorthosites, Dhofar 280 and other lunar meteorites, and (C) chondrite-normalized REE patterns for pyroxenes in Dhofar 280. The major element data come from Cahill et al. (2004), Gross et al. (2014), McGee (1993), Papike et al. (1997), Pernet-Fisher et al. (2019), Roberts et al. (2019), Russell et al. (2014), Treiman et al. (2010) and this study (Table A2). Chondrite normalization is from Lodders (2021).

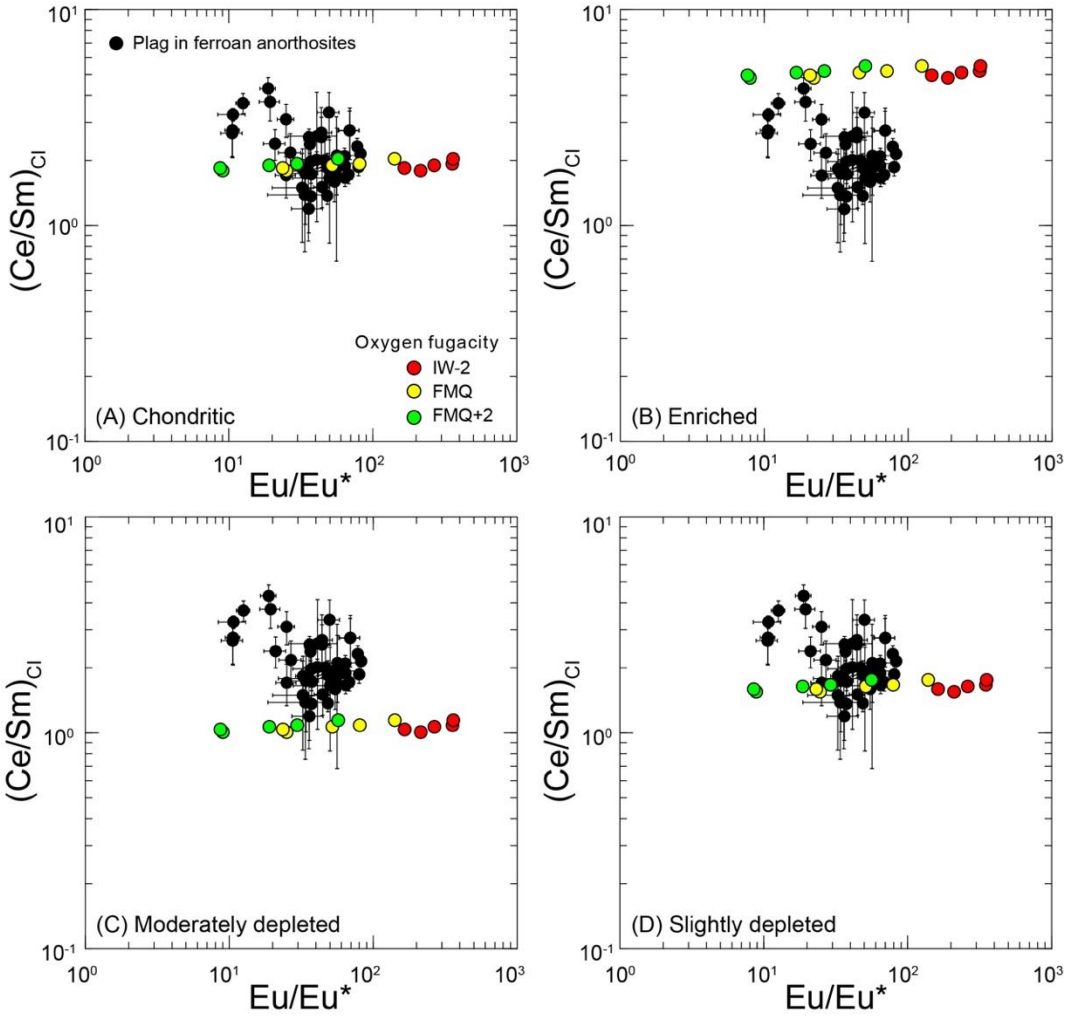


Figure A4. Comparison between modeled lunar magma ocean crystallized plagioclase and plagioclase in Apollo ferroan anorthosites assuming different bulk lunar magma ocean trace element compositions. The bulk trace element abundances assumed are (A) chondritic, (B) LREE enriched, (C) moderately depleted and (D) slightly depleted. The crystallization sequence used for all these simulations assumes a Lunar Primitive Upper Mantle major element bulk composition (Charlier et al., 2018). The calculated lunar magma ocean crystallized plagioclase under three fO_2 conditions are shown by colored circles, while plagioclase in Apollo ferroan anorthosites are shown by black circles (Floss et al., 1998; Papike et al., 1997; Pernet-Fisher et al., 2019). The chondrite-normalized Ce/Sm ratio is shown on the y-axis and Eu anomalies (Eu/Eu*, where Eu is the chondrite normalized abundance and Eu* is the interpolated value from neighboring elements on a REE diagram) is shown on the x-axis. Collectively, the models show that regardless of the fO_2 and bulk trace element abundance assumed, the Apollo anorthosites cannot be modeled as direct solidification products of a lunar magma ocean, particularly for low lunar-relevant fO_2s. The bulk trace element data are from Anders and Grevesse (1989), Rudnick and Gao (2014), Workman and Hart (2005) and Arevalo and McDonough (2010), respectively. The error bars are calculated based on error propagation (Table A3).

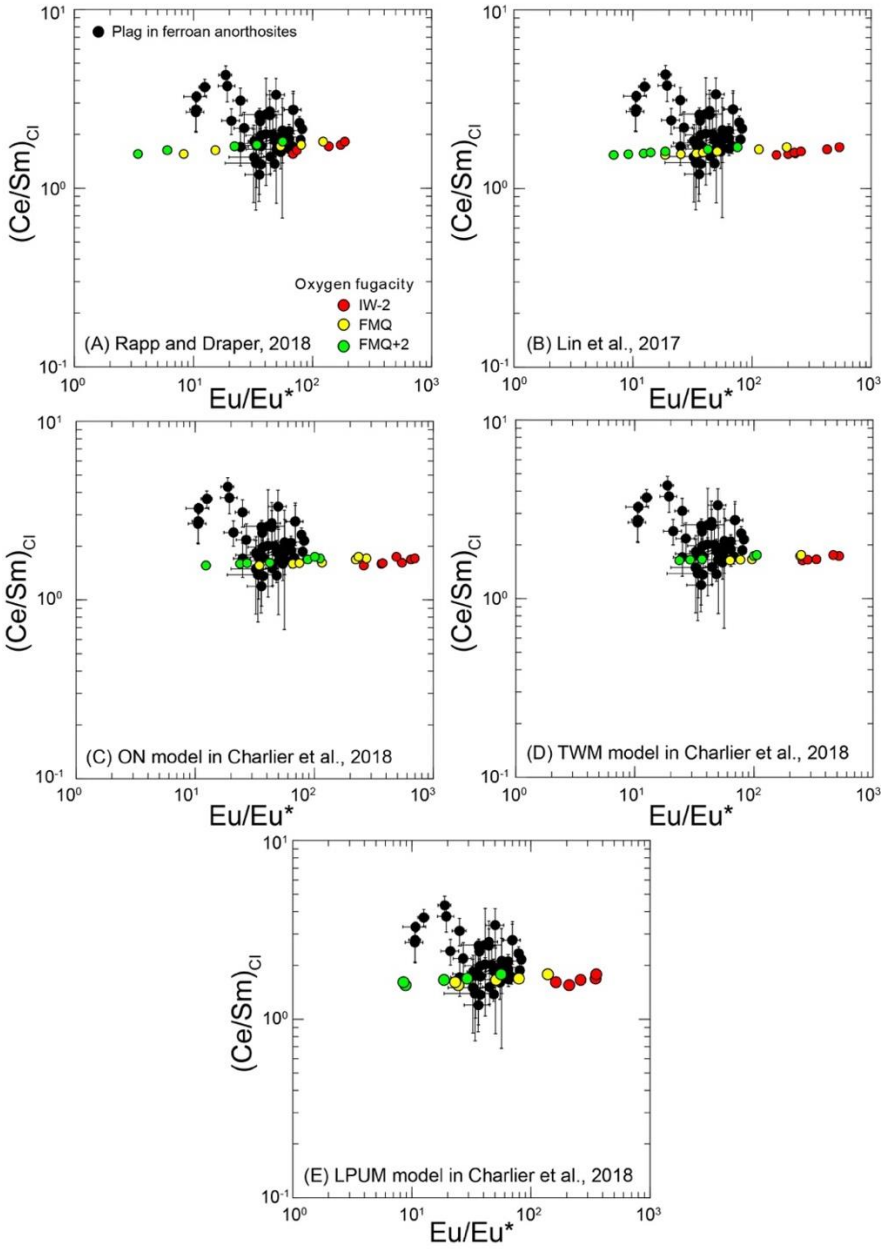


Figure A5. Comparison between modeled lunar magma ocean crystallized plagioclase and plagioclase in Apollo ferroan anorthosites assuming different crystallization sequences. Crystallization sequences are from (**A**) Rapp and Draper (2018), (**B**) Lin et al. (2017), (**C**) the ON model (O'Neill, 1991) in Charlier et al. (2018), (**D**) the TWM model (Taylor, 1982) in Charlier et al. (2018), and (**E**) the LPUM model (Longhi, 2006) in Charlier et al. (2018). All simulations assume a bulk LMO with slightly depleted trace element abundances (Arevalo and McDonough, 2010). Modeling conditions are the same as those described in Figure A4. Collectively, the models show that regardless of the fO_2 and solidification sequence assumed, many of the Apollo anorthosites cannot be modeled as direct solidification products of a lunar magma ocean, particularly for low lunar-relevant fO_2s. Due to the general similarity of REE concentrations between plagioclase from Apollo FANs and lunar anorthositic meteorites (e.g., Figure 1.3A), plagioclase in lunar anorthositic meteorites cannot be explained here either. The error bars are calculated based on error propagation (Table A3).

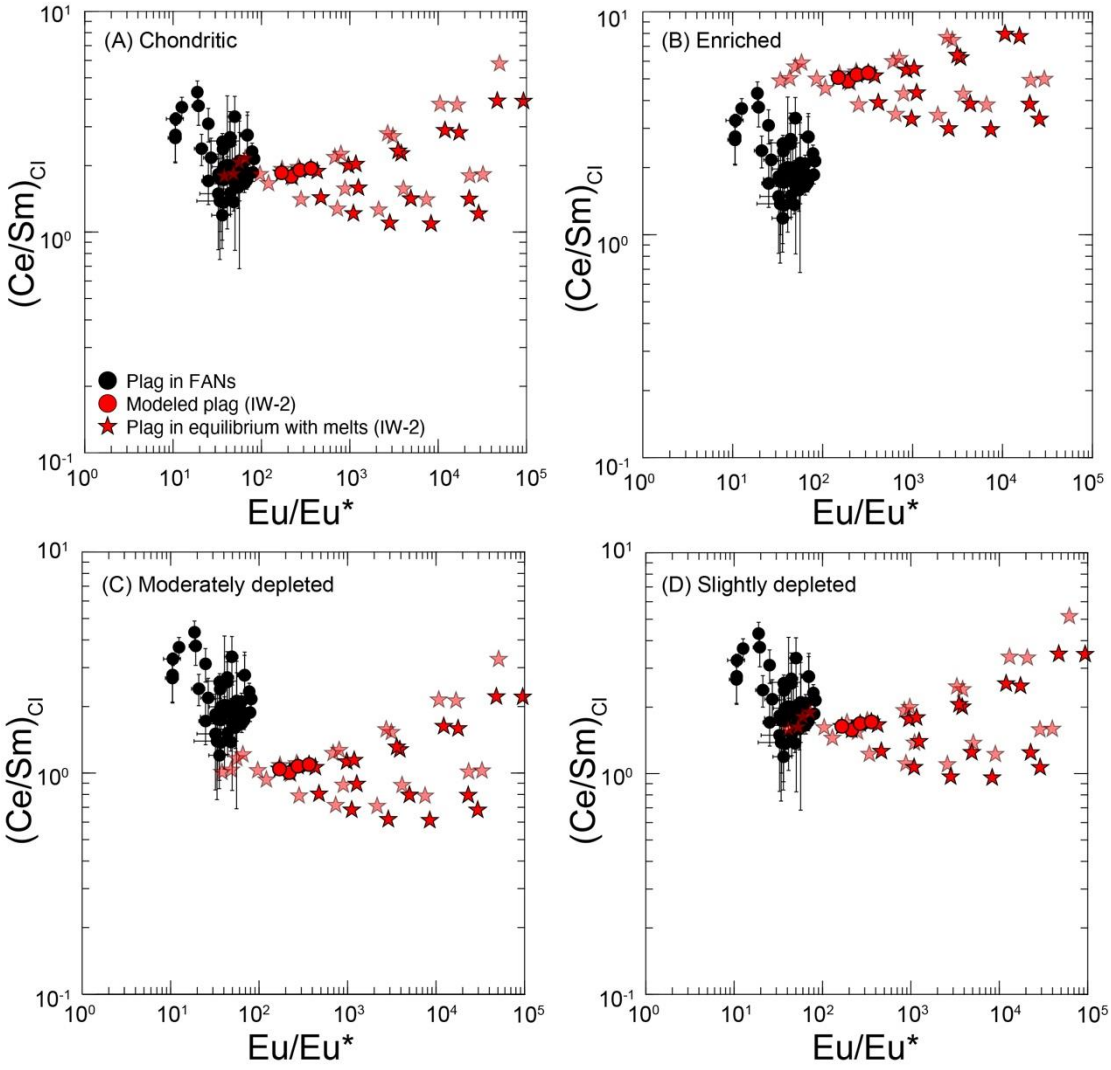


Figure A6. Comparison between modeled plagioclase in equilibrium with partial melts of the lunar crust and in Apollo ferroan anorthosites assuming different bulk lunar magma ocean trace element compositions. Bulk trace element abundances are (A) chondritic, (B) LREE enriched, (C) moderately depleted and (D) slightly depleted. In all simulations, the LMO crystallization sequence is from Charlier et al. (2018), assuming a Lunar Primitive Upper Mantle bulk major element composition. The compositions of plagioclase in equilibrium with partial melts of the anorthositic lunar crust are shown by red stars (fO_2 = IW-2). Simulations assuming addition of 4% trapped LMO liquid are shown by the partially transparent stars. The chondrite-normalized Ce/Sm ratio is shown on the y-axis and Eu/Eu* is shown on the x-axis. The mineral mode assumed for anorthosite is 95.1 % plagioclase and 4.9 % low-Ca pyroxene. Collectively, the models show that regardless of the bulk trace element abundance assumed, partial melting of the anorthosites cannot reproduce the observed REE patterns in Apollo FAN samples. The error bars are calculated based on errors propagation (Table A3).

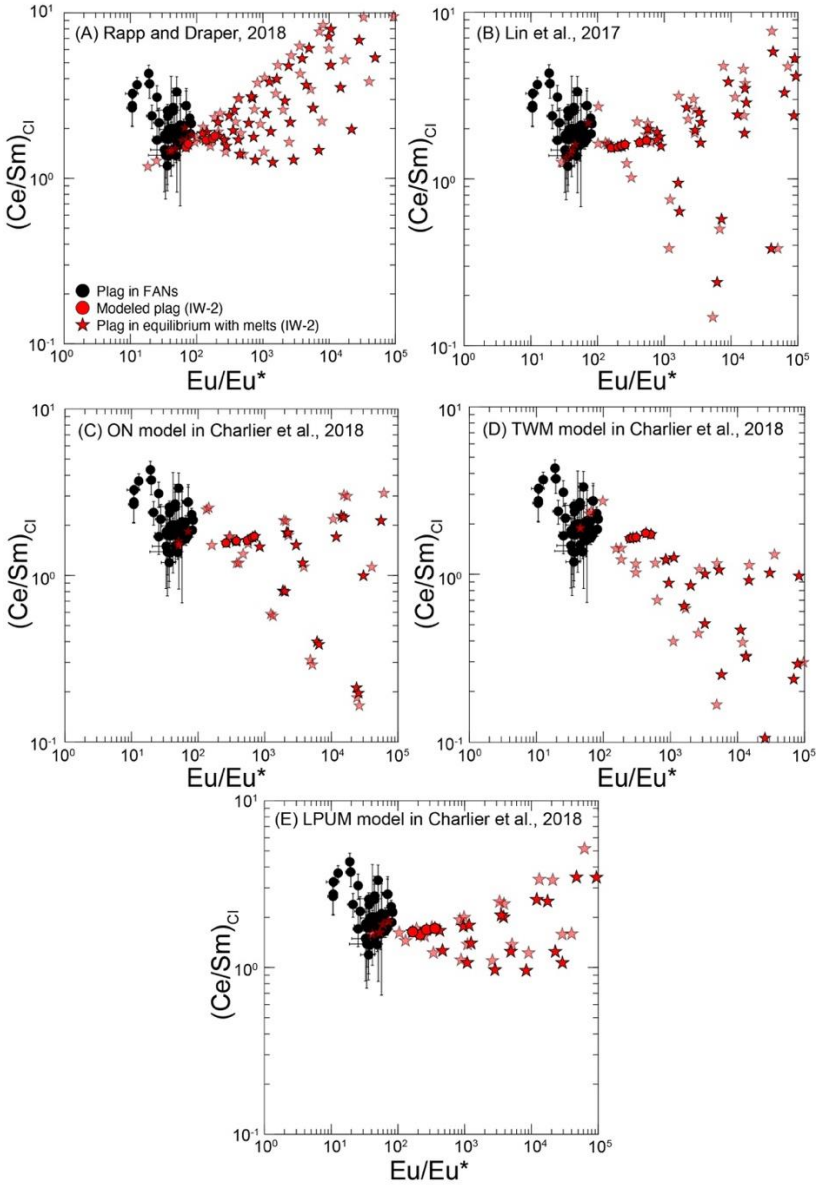


Figure A7. Comparison between plagioclase in equilibrium with partial melts of the lunar crust and in Apollo ferroan anorthosites assuming different crystallization sequences. The LMO crystallization sequences are from (A) Rapp and Draper (2018), (B) Lin et al. (2017), (C) the ON (O'Neill, 1991) model in Charlier et al. (2018), (D) the TWM model (Taylor, 1982) in Charlier et al. (2018), and (E) the LPUM model (Longhi, 2006) in Charlier et al. (2018). All models assume a bulk LMO with slightly depleted trace element abundances (Arevalo and McDonough, 2010). The mineral mode assumed for anorthosite is 95.1 % plagioclase plus 4.9 % high-Ca pyroxenes for (A) and (B) and 95.1 % plagioclase plus 4.9 % low-Ca pyroxenes for (C) to (E). Modeling conditions and symbols are the same as those in Figure A6. Collectively, the models show that regardless of the solidification sequence assumed, partial melting of the anorthosites cannot reproduce the observed REE patterns in Apollo FAN samples. Due to the general similarity of REE concentrations between plagioclase from Apollo FANs and lunar anorthositic meteorites (e.g., Figure 1.3A), plagioclase in lunar anorthositic meteorites cannot be explained here either. The diverse trend of $(Ce/Sm)_{CI}$ after partial melting among models is because of mineralogical and compositional differences among the crystallization sequences.

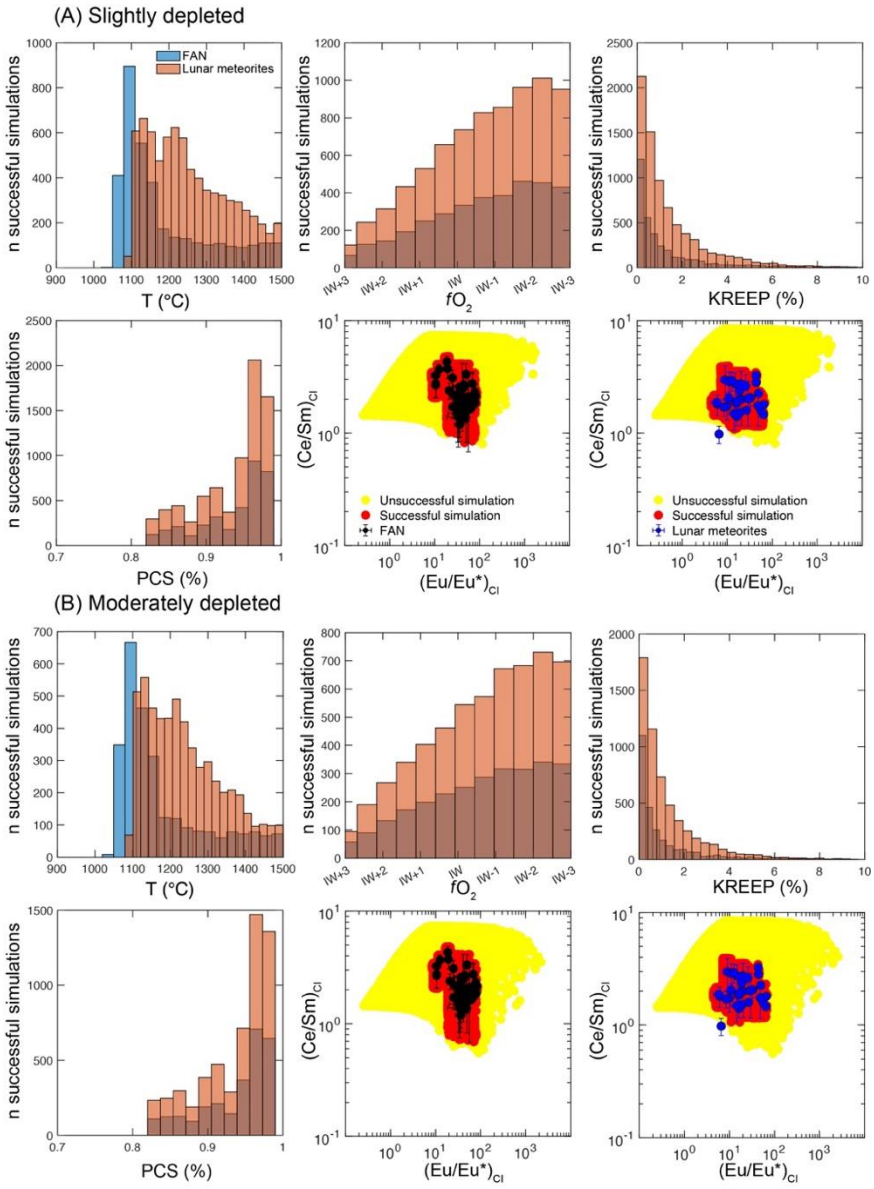


Figure A8. Monte-Carlo simulations assuming different conditions during subsolidus reequilibration to fit plagioclase compositions from Apollo ferroan anorthosites and lunar anorthositic meteorites assuming constant mineral modes. Different temperatures, fO_2, the percentage of KREEPy component added to the lithology, the percentage of LMO solidification (PCS) were tested during subsolidus reequilibration with different bulk LMO trace element abundances: (A) slightly depleted (3,431 and 7,753 successful simulations out of 100,000 attempts for FANs and meteorites respectively), (B) moderately depleted (2,722 and 5,656 successful simulations out of 100,000 attempts), (C) chondritic (3,136 and 7,404 successful simulations out of 100,000 attempts) and (D) enriched (2,777 and 6,758 successful simulations out of 100,000 attempts). All the crystallization sequences are based on Lunar Primitive Upper Mantle magma ocean solidification sequence in Charlier et al. (2018). The mineral mode of anorthosite is the average mineral modes calculated from lunar ferroan anorthosites (95.2% plag + 3.6% low-Ca px + 1.2% high-Ca px, table A1). The success threshold for each plagioclase is based on error propagation calculation (Table A3). Among all the assumed initial bulk trace element abundances, slightly depleted case has most successful simulations while enriched fails to fit many of the ferroan anorthosites.

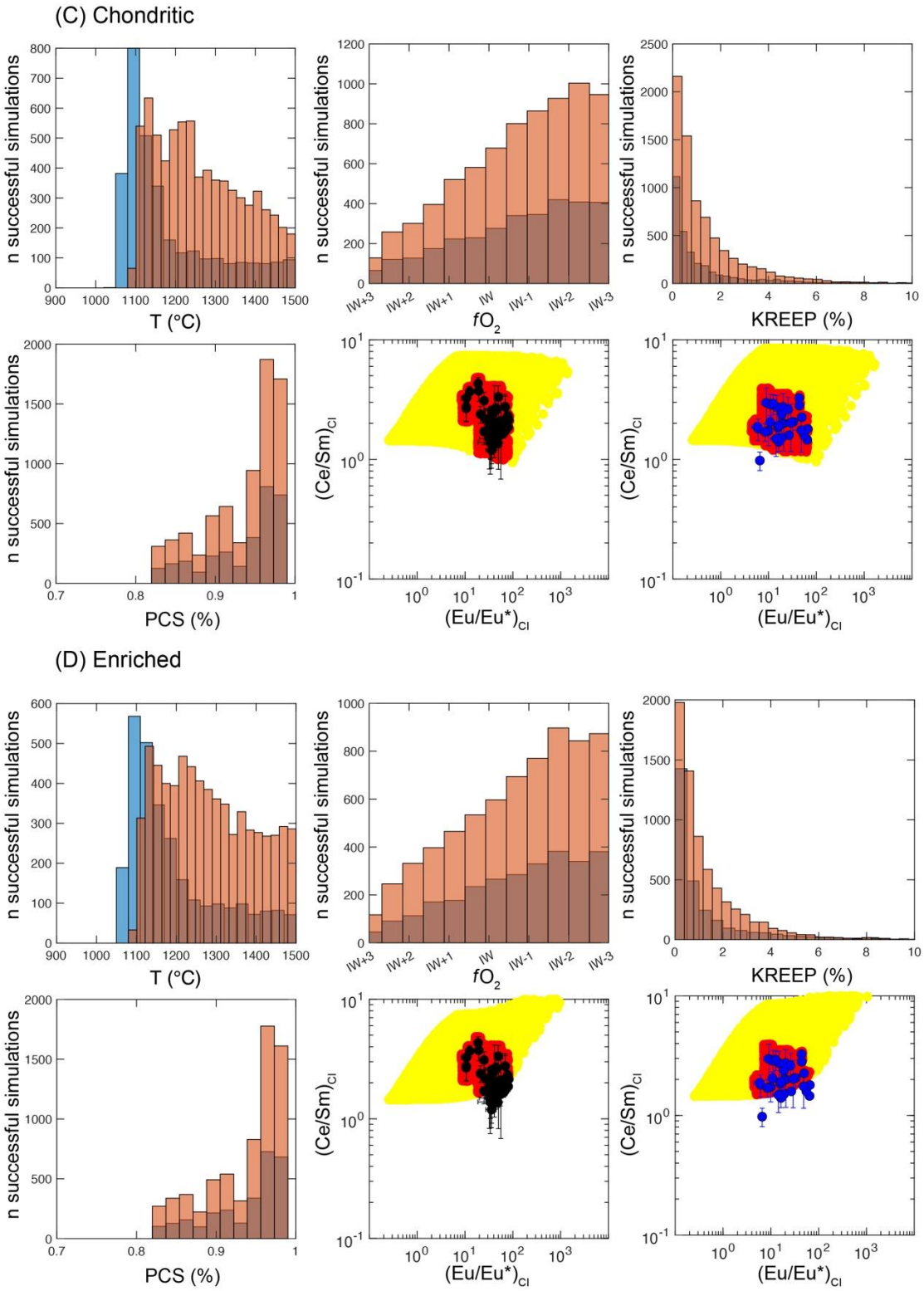


Figure A8. *Continued*

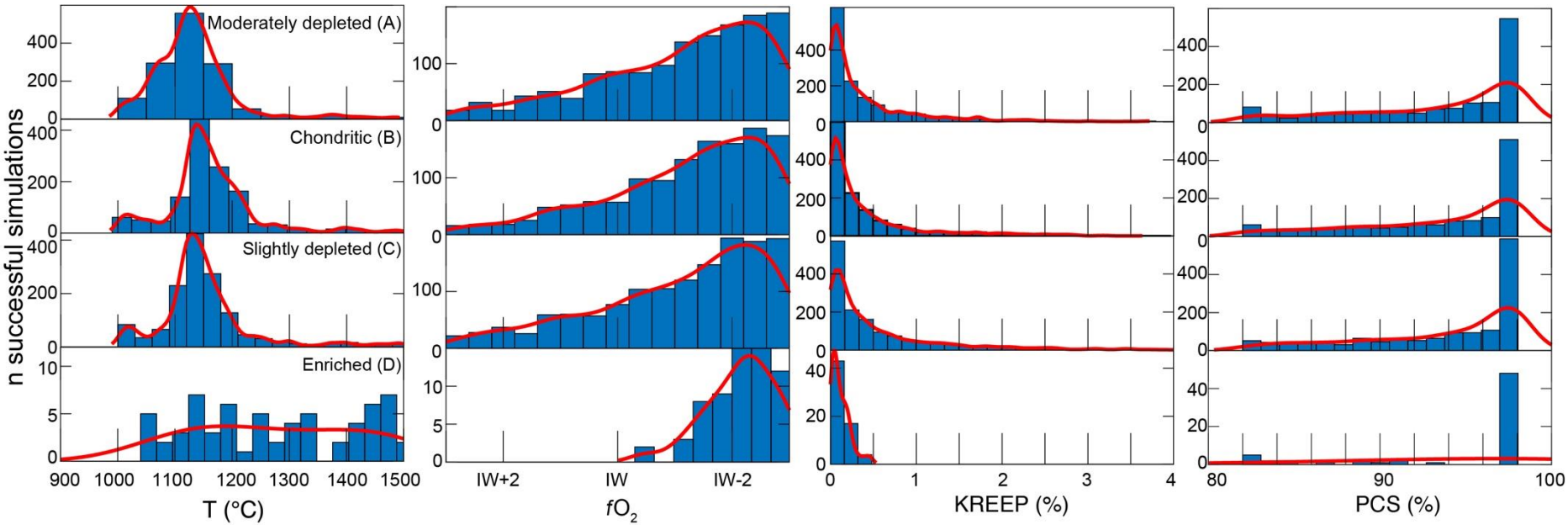


Figure A9. Monte-Carlo simulations testing different initial bulk LMO compositions using mineral modes from reported samples. Variations in temperature, fO_2, the percentage of KREEPy component added to the lithology and the percentage of LMO solidification (PCS) were tested during subsolidus reequilibration with the initial bulk LMO trace element abundances are (A) moderately depleted (1,379 successful simulations out of 600,000 attempts), (B) chondritic (1,302 successful simulations out of 600,000 attempts), (C) slightly depleted (1,417 successful simulations out of 600,000 attempts) and (D) enriched (64 successful simulations out of 600,000 attempts) using mineral modes from five reported Apollo lunar ferroan anorthosites samples (Apollo FAN 15415, 60025, 60135, 60015, 65325) and lunar meteorite Dhofar 280. Simulations assume the lunar magma ocean solidification sequence for a magma ocean with an LPUM bulk major element composition in Charlier et al. (2018). In the simulations presented here, pyroxenes are assumed to have crystallized from trapped liquid in ferroan anorthosites. The threshold to filter successful simulations for each plagioclase is calculated considering the propagation of errors (Table A3). Using enriched bulk LMO produces the fewest successful simulations, while using slightly depleted composition produces most successful simulations. Combined with the simulation results assuming constant mineral modes, the results suggest the initial bulk LMO trace element abundance pattern is closer to slightly LREE depleted. The red line in each figure is the nonparametric kernel smoothing distribution.

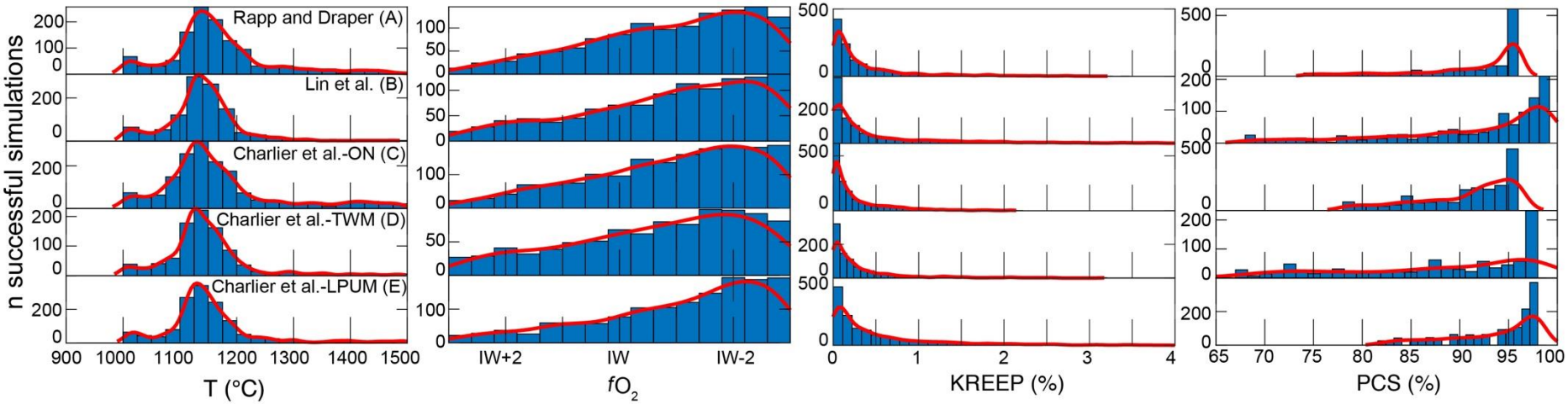


Figure A10. Monte-Carlo simulations testing different solidification sequences with a slightly depleted bulk trace element composition using mineral modes from reported samples. The simulations assume lunar magma ocean solidification sequences from (A) Rapp and Draper (2018), (B) Lin et al. (2017), (C) ON model (O'Neill, 1991) in Charlier et al. (2018), (D) TWM model (Taylor, 1982) in Charlier et al. (2018) and (E) LPUM model (Longhi, 2006) in Charlier et al. (2018). Modeling conditions are otherwise as in Figure A9.

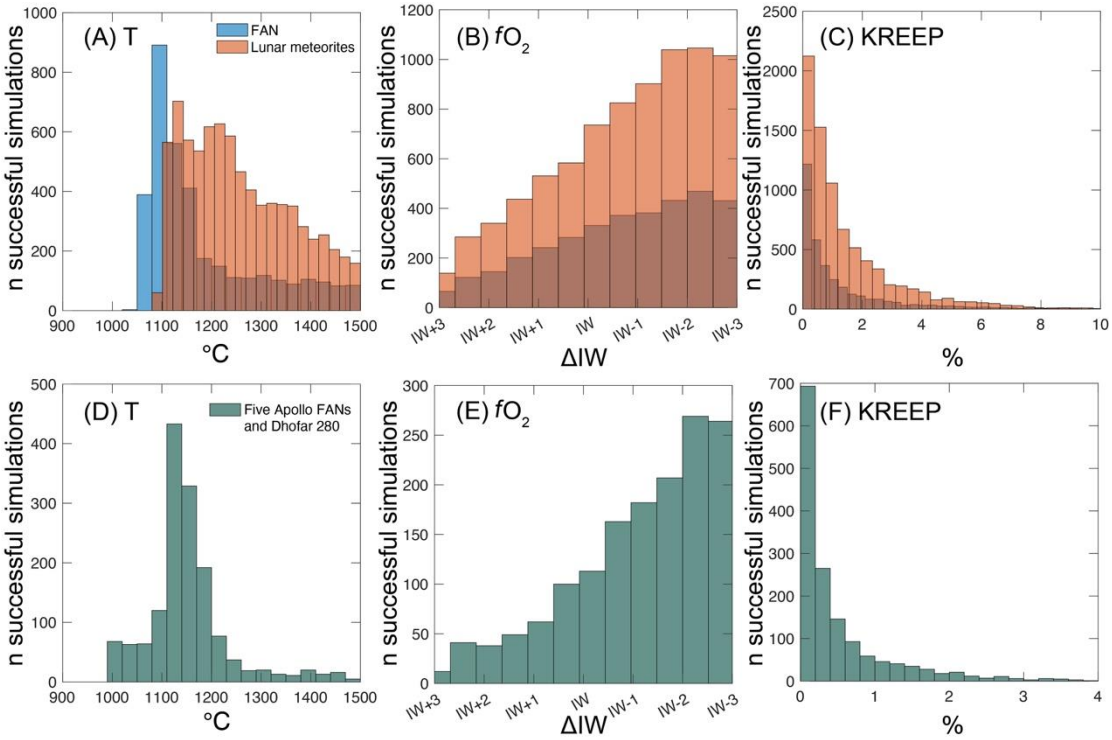


Figure A11. Monte-Carlo simulations incorporating fO_2-dependent partitioning models with fixed and reported mineral modes of Apollo FANs and lunar anorthositic meteorites. Different temperatures, fO_2, the percentage of KREEPy component added (15386; Table A4) to the lithology were tested during subsolidus reequilibration using fixed (A-C) and reported (D-F) mineral modes of anorthosites. Except for the partitioning model of Eu in pyroxene from (Fabbrizio et al., 2021), the other simulation parameters are the same as those in Figure 1.6. The simulation results are highly consistent with the trivalent Eu partitioning model used in the Section 1.5.1 and 1.5.2 of main text, demonstrating the dominance of plagioclase for determining the distribution of Eu in lunar anorthosites. The introduction of this preliminary, multivalent pyroxene partitioning model does not change the results, justifying the simplifying assumption of trivalent Eu partitioning in pyroxene employed in the main text.

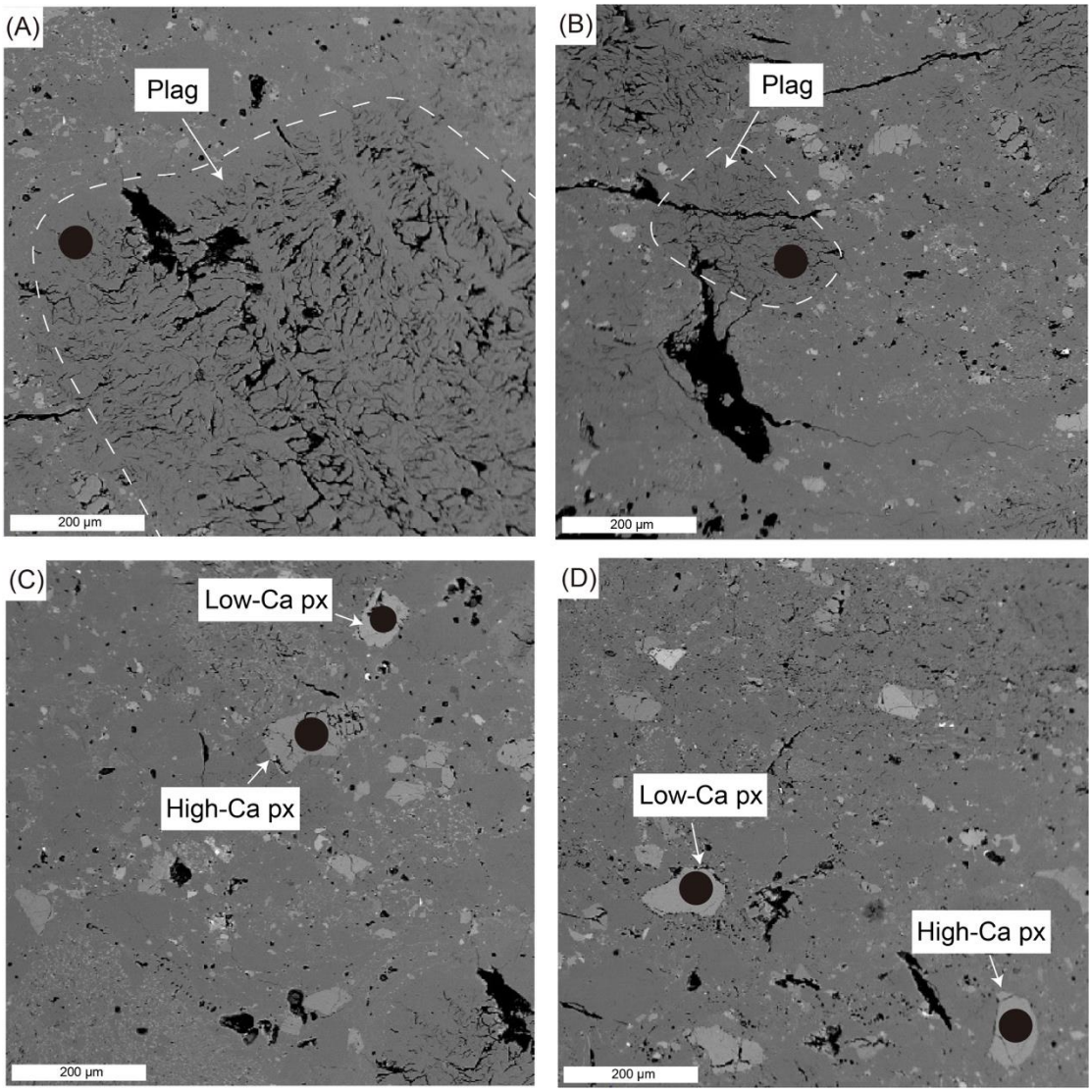


Figure A12. Backscatter photomicrographs of Dhofar 280 plagioclase and pyroxene. All the clasts we examined are relatively coarse. The minerals we point out are clasts that were analyzed to obtain trace element data reported in Table A2. (A) ~900 µm plagioclase clast, (B) ~200 µm plagioclase clast, (C) ~85 µm low-Ca pyroxene and ~150 µm high-Ca pyroxene, and (D) ~120 µm low-Ca pyroxene and ~110 µm high-Ca pyroxene. The black circles represent the locations of laser spots.

Table A1. Reported mineral modes of Apollo ferroan anorthosites and measured modes in lunar anorthositic meteorite Dhofar 280. Because plagioclase and pyroxene control subsolidus reequilibration of REEs in lunar anorthosites, mineral modes are reported on a three phase basis. Note that the Dhofar 280 is an anorthositic fragmental breccia, therefore, its modal mineralogy (determined by characterization of an entire thin section) may not be equivalent to that of the original crust.

Samples	Plagioclase (%)	Low-Ca pyroxene (%)	High-Ca pyroxene (%)	Ref.
62236	87.4	7.3	5.3	Warren and Wasson, 1978
60025	87.5	12.5	0	Warren and Wasson, 1978
60055	98	0	2	Floss et al., 1998
62275	98.9	1.1	0	Prinz et al., 1973
60135	95	5	0	Warren et al., 1983
64435	98	1	1	Floss et al., 1998
60015	98.5	1.5	0	Dixon and Papike, 1975
15415	97	0	3	Steele and Smith, 1971
62236	92.9	5.1	2	Nord Jr and Wandless, 1983
65325	98.1	1.9	0	Warren, 1990
65315	98.6	1.2	0.2	Dixon and Papike, 1975
15362	98	0.5	1.5	Dowty et al., 1972
15363	85.9	12.1	2	Warren et al., 1987
62237	98.9	1	0.1	Dymek et al., 1975
Average for Apollo samples	95.2	3.6	1.2	
Dhofar 280	96.7	1.5	1.8	This study

Table A2. Mineral modes of plagioclase and coexisting pyroxenes (on a three-phase basis) and their major and rare earth element compositions in five reported Apollo FANs and lunar anorthositic meteorite Dhofar 280. Concentrations for Dhofar 280 are reported as averages of replicate analyses: plagioclase, n=2, low-Ca pyroxene, n=2; high-Ca pyroxene, n=2; the same grains were analyzed by electron microprobe and LA-ICP-MS.

Sample	60025	60135	65325	15415	60015	Dhofar 280
Plagioclase (%)	87.5	95	98.1	97	98.5	96.7
Low-Ca pyroxene (%)	12.5	5	1.9	0	1.5	1.5
High-Ca pyroxene (%)	0	0	0	3	0	1.8
Ref.	Warren and Wasson, 1978	Warren et al., 1983	Warren, 1990	Steele and Smith, 1971	Dixon and Papike, 1975	This study
(wt.%)			Plagioclase			
SiO_2	44.18	43.58	44.05	43.4	43.8	43.85
TiO_2	-	-	-	-	-	0.02
Al_2O_3	34.82	34.89	34.71	35.27	36.50	35.57
FeO	0.18	0.15	0.14	0.07	0.20	0.25
MnO	-	-	-	-	-	-
MgO	0.07	0.09	0.08	0.03	0.124	0.12
CaO	19.47	19.72	19.81	19.54	19.4	19.48
Na_2O	0.46	0.36	0.39	0.39	0.42	0.33
K_2O	0.01	0.01	0.01	0.02	0.01	0.01
P_2O_5	-	-	-	-	-	-
Cr_2O_3	-	-	-	-	-	-
Total	99.2	98.8	99.2	98.7	100.5	99.6
(ppm)						
La	0.373	0.159	0.126	0.125	0.171	0.293
Ce	0.720	0.373	0.301	0.347	0.461	0.653
Pr	0.083	0.054	0.037	0.042	-	0.085

Table A2. *Continued*

Sample	60025	60135	65325	15415	60015	Dhofar 280
Nd	0.383	0.201	0.172	0.173	0.219	0.235
Sm	0.127	0.055	0.038	0.071	0.064	0.091
Eu	1.120	0.788	0.767	0.754	1.070	0.871
Gd	0.083	0.043	0.047	0.059	0.057	0.034
Tb	0.009	0.009	0.005	0.008	-	0.011
Dy	0.067	0.045	0.025	0.052	0.047	0.086
Y	0.290	0.290	0.150	0.164	0.190	0.185
Ho	0.013	0.013	0.008	0.004	-	0.011
Er	0.031	0.035	0.011	0.026	0.016	0.027
Yb	0.033	0.048	0.014	0.018	0.017	0.020
Lu	-	0.012	0.003	0.005	-	0.005
Error (σ)						
La	0.048	0.017	0.017	0.015	0.009	0.014
Ce	0.082	0.030	0.028	0.016	0.023	0.093
Pr	0.020	0.011	0.009	0.007	-	0.011
Nd	0.096	0.045	0.042	0.035	0.011	0.008
Sm	0.056	0.027	0.024	0.016	0.003	0.028
Eu	0.087	0.049	0.045	0.065	0.054	0.106
Gd	0.064	0.031	0.027	0.023	0.003	0.018
Tb	-	-	-	-	-	0.005
Dy	0.036	0.016	0.013	0.006	0.009	0.012
Y	0.095	0.058	0.045	0.012	-	0.012
Ho	0.008	0.005	0.004	0.040	0.010	0.005
Er	0.018	0.012	0.008	0.008	0.003	0.039
Yb	0.019	0.011	0.004	0.011	0.003	0.004
Lu	-	0.003	0.001	0.028[b]	-	0.008[b]
Ref.	Pernet-Fisher et al., 2019	Pernet-Fisher et al., 2019	Pernet-Fisher et al., 2019	Pernet-Fisher et al., 2019	Papike et al., 1997[a]	This study

Table A2. *Continued*

Sample	60025	60135	65325	15415	60015	Dhofar 280
(wt.%)			Low-Ca pyroxene			
SiO_2	51.14	53.33	52.83	-	52.73	50.67
TiO_2	0.19	0.24	0.34	-	0.23	0.47
Al_2O_3	0.31	0.64	0.53	-	0.53	0.70
FeO	27.59	19.51	22.73	-	22.63	21.45
MnO	0.59	0.37	0.56	-	0.56	0.40
MgO	17.61	22.69	21.93	-	21.90	19.09
CaO	1.80	2.69	0.92	-	0.96	6.04
Na_2O	0.01	0.01	0.02	-	-	0.00
K_2O	0.01	-	0.01	-	-	0.01
P_2O_5	-	-	-	-	-	-
Cr_2O_3	-	-	-	-	0.07	0.30
Total	99.20	99.50	99.90	-	99.61	99.13
Mg#	53.20	67.40	63.20	-	62.94	61.30
(ppm)						
La	0.027	0.125	0.040	-	-	0.337
Ce	0.046	0.266	0.153	-	-	1.179
Pr	0.083	0.049	0.028	-	-	0.224
Nd	0.053	0.052	0.024	-	-	1.288
Sm	0.015	0.004	0.001	-	-	0.652
Eu	0.116	0.080	0.059	-	-	0.072
Gd	0.312	0.222	0.230	-	-	1.166
Tb	0.309	0.192	0.223	-	-	0.240
Dy	0.567	0.236	0.566	-	-	2.327

Table A2. *Continued*

Sample	60025	60135	65325	15415	60015	Dhofar 280
Y	-	-	-	-	-	-
Ho	0.068	0.033	0.069	-	-	0.545
Er	-	-	-	-	-	1.799
Yb	-	-	-	-	-	2.232
Lu	-	-	-	-	-	0.314
Error (σ)[c]						
La	-	-	-	-	-	0.204
Ce	-	-	-	-	-	0.226
Pr	-	-	-	-	-	0.060
Nd	-	-	-	-	-	0.185
Sm	-	-	-	-	-	0.041
Eu	-	-	-	-	-	0.086
Gd	-	-	-	-	-	0.227
Tb	-	-	-	-	-	0.020
Dy	-	-	-	-	-	0.325
Y	-	-	-	-	-	-
Ho	-	-	-	-	-	0.083
Er	-	-	-	-	-	0.261
Yb	-	-	-	-	-	0.372
Lu	-	-	-	-	-	0.105
(wt.%)			High-Ca pyroxene			
SiO_2	-	-	-	52.47	-	50.99
TiO_2	-	-	-	0.52	-	1.18
Al_2O_3	-	-	-	0.79	-	1.76
FeO	-	-	-	13.15	-	11.19

Table A2. *Continued*

Sample	60025	60135	65325	15415	60015	Dhofar 280
MnO	-	-	-	0.29	-	0.23
MgO	-	-	-	15.52	-	14.75
CaO	-	-	-	17.19	-	19.43
Na_2O	-	-	-	0.02	-	0.02
K_2O	-	-	-	0.01	-	0.00
P_2O_5	-	-	-	-	-	-
Cr_2O_3	-	-	-	-	-	0.67
Total	-	-	-	99.96	-	99.55
Mg#	-	-	-	68.30	-	70.10
(ppm)						
La	-	-	-	0.298	-	1.138
Ce	-	-	-	1.905	-	5.022
Pr	-	-	-	0.413	-	1.075
Nd	-	-	-	2.850	-	6.747
Sm	-	-	-	1.680	-	2.710
Eu	-	-	-	0.084	-	0.130
Gd	-	-	-	2.880	-	4.269
Tb	-	-	-	0.599	-	0.788
Dy	-	-	-	4.780	-	5.934
Y	-	-	-	-	-	-
Ho	-	-	-	1.032	-	1.225
Er	-	-	-	3.060	-	3.482
Yb	-	-	-	2.790	-	3.126
Lu	-	-	-	0.349	-	0.415
Error (σ)[c]						

Table A2. *Continued*

Sample	60025	60135	65325	15415	60015	Dhofar 280
La	-	-	-	0.513	-	0.181
Ce	-	-	-	0.017	-	0.417
Pr	-	-	-	0.095	-	0.048
Nd	-	-	-	0.021	-	1.087
Sm	-	-	-	0.113	-	0.512
Eu	-	-	-	0.100	-	0.070
Gd	-	-	-	0.012	-	1.668
Tb	-	-	-	0.100	-	0.307
Dy	-	-	-	0.021	-	2.593
Y	-	-	-	-	-	-
Ho	-	-	-	0.145	-	0.420
Er	-	-	-	0.034	-	1.038
Yb	-	-	-	0.098	-	0.623
Lu	-	-	-	0.110	-	0.101
Ref.	Pernet-Fisher et al., 2019	Pernet-Fisher et al., 2019	Pernet-Fisher et al., 2019	Pernet-Fisher et al., 2019	Dixon and Papike, 1975	This study

[a.] We calculate the analytical errors of Apollo 60015 plagioclase based on description (5% for LREE+Y and 20% for HREE) in (Papike et al., 1997).

[b.] For some Lu concentrations of plagioclase, the errors are so large that we ignore these data in figures.

[c.] We note that the errors of REEs for most pyroxenes are missing. However, we only use major element concentrations of pyroxene in order to calculate site parameters for ions in the modeling, so the lack of REE errors of pyroxenes will not affect the error propagation in this study.

Table A3. Rare earth element concentrations and their uncertainties for plagioclase in Apollo FANs and lunar anorthositic meteorites. The uncertainties of $(Ce/Sm)_{CI}$ and Eu* are calculated by propagation of errors considering analytical errors associated with CI chondrite (Lodders, 2021) and plagioclase trace element abundances (See Section 1.4 of the main text for equations).

Ref.	Pernet-Fisher et al., 2019											Papike et al., 1997 [a]					
Sample (ppm)	15415,18	62236,40	62275,31	65325,31	69955,28	60515,11	60135,17	60025,125	67215,5	67635,11	67636,7	68515,15	64435,304	65315.87	65035.179	60055.5	64425.4
La	0.125	0.206	0.201	0.126	0.250	0.225	0.159	0.373	1.376	0.352	0.329	0.131	0.116	0.123	0.162	0.143	0.148
Ce	0.347	0.446	0.477	0.301	0.671	0.562	0.373	0.720	3.029	0.845	0.772	0.345	0.359	0.342	0.405	0.402	0.449
Pr	0.042	0.050	0.043	0.037	0.091	0.076	0.054	0.083	0.318	0.099	0.085	-	-	-	-	-	-
Nd	0.173	0.266	0.221	0.172	0.407	0.343	0.201	0.383	1.249	0.380	0.395	0.142	0.157	0.160	0.203	0.205	0.214
Sm	0.071	0.061	0.078	0.038	0.096	0.053	0.055	0.127	0.198	0.098	0.094	0.049	0.047	0.036	0.053	0.059	0.058
Eu	0.754	0.717	0.699	0.767	0.802	0.910	0.788	1.120	1.032	1.212	1.239	1.000	0.795	0.935	1.190	1.010	1.010
Gd	0.059	0.063	0.057	0.047	0.102	0.089	0.043	0.083	0.137	0.045	0.072	0.042	0.039	0.038	0.040	0.040	0.041
Tb	0.008	0.007	0.007	0.005	0.012	0.013	0.009	0.009	0.018	0.009	0.010	-	-	-	-	-	-
Dy	0.052	0.035	0.040	0.025	0.056	0.053	0.045	0.067	0.101	0.044	0.036	0.033	0.031	0.036	0.028	0.025	0.027
Y	0.160	0.120	0.170	0.150	0.330	0.180	0.290	0.290	0.500	0.200	0.210	0.085	0.124	0.088	0.095	0.085	0.143
Ho	0.004	0.006	0.005	0.008	0.009	0.010	0.013	0.013	0.017	0.007	0.009	-	-	-	-	-	-
Er	0.026	0.026	0.019	0.011	0.021	0.025	0.035	0.031	0.044	0.024	0.017	0.018	0.013	0.007	0.010	0.015	0.017
Tm	-	-	-	-	-	-	-	-	-	-	-	-	-	-	-	-	-
Yb	0.018	0.024	0.024	0.014	0.034	0.022	0.048	0.033	0.046	0.020	0.016	0.011	0.012	0.008	0.007	0.009	0.014
Lu	0.005	0.002	0.004	0.003	0.002	0.006	0.012	-	0.003	-	0.001	-	-	-	-	-	-
Error (σ)																	
La	0.015	0.022	0.025	0.017	0.015	0.022	0.017	0.048	0.038	0.024	0.018	0.007	0.006	0.006	0.008	0.007	0.007
Ce	0.016	0.033	0.032	0.027	0.028	0.032	0.030	0.082	0.060	0.032	0.028	0.017	0.018	0.017	0.020	0.020	0.022

Table A3. *Continued*

Ref.	Pernet-Fisher et al., 2019											Papike et al., 1997 [a]					
Pr	0.007	0.011	0.011	0.009	0.009	0.013	0.011	0.020	0.018	0.012	0.009	-	-	-	-	-	-
Nd	0.035	0.054	0.047	0.042	0.037	0.058	0.044	0.096	0.078	0.056	0.041	0.007	0.008	0.008	0.010	0.010	0.011
Sm	0.016	0.032	0.034	0.024	0.020	0.032	0.027	0.056	0.034	0.033	0.024	0.002	0.002	0.002	0.003	0.003	0.003
Eu	0.065	0.042	0.049	0.045	0.031	0.056	0.049	0.087	0.041	0.046	0.042	0.050	0.040	0.047	0.060	0.051	0.051
Gd	0.023	0.035	0.035	0.027	0.022	0.037	0.031	0.063	0.033	0.027	0.021	0.002	0.002	0.002	0.002	0.002	0.002
Tb	-	-	-	-	-	-	-	-	-	-	-	-	-	-	-	-	-
Dy	0.006	0.005	0.015	0.013	0.012	0.017	0.016	0.036	0.016	0.015	0.010	0.007	0.006	0.007	0.006	0.005	0.005
Y	0.012	0.048	0.050	0.045	0.028	0.046	0.058	0.095	0.040	0.041	0.026	-	-	-	-	-	-
Ho	0.040	0.014	0.003	0.004	0.002	0.005	0.005	0.008	0.004	0.004	0.003	0.004	0.006	0.004	0.005	0.004	0.007
Er	0.008	0.005	0.012	0.008	0.005	0.011	0.012	0.018	0.010	0.009	0.006	0.004	0.003	0.001	0.002	0.003	0.003
Tm	-	-	-	-	-	-	-	-	-	-	-	-	-	-	-	-	-
Yb	0.011	0.012	0.012	0.004	0.008	0.010	0.011	0.019	0.010	0.008	0.006	0.002	0.002	0.002	0.001	0.002	0.003
Lu	0.028	0.005	0.002	0.001	0.001	0.002	0.003	-	0.001	-	0.001	-	-	-	-	-	-
Error of $(Ce/Sm)_{CI}$	0.274	0.942	0.661	1.250	0.373	1.554	0.828	0.632	0.686	0.720	0.522	0.156	0.169	0.211	0.169	0.151	0.172
Ce/Sm	1.193	1.784	1.492	1.933	1.706	2.588	1.655	1.383	3.733	2.104	2.004	1.718	1.864	2.318	1.865	1.663	1.889
Success threshold [b] (%)	23.02	52.80	44.26	64.67	21.89	60.07	50.04	45.70	18.38	34.20	26.02	9.09	9.09	9.09	9.09	9.09	9.09
Error of Eu*	8.727	13.835	12.372	24.427	3.998	15.142	22.267	15.151	3.088	19.676	9.341	5.218	4.418	5.993	6.099	4.921	4.902
Eu*	36.018	35.759	32.411	56.112	25.058	40.965	50.097	33.727	19.373	56.427	46.563	68.152	57.410	78.157	79.906	64.279	64.035
Success threshold [b] (%)	24.23	38.69	38.17	43.53	15.95	36.96	44.45	44.92	15.94	34.87	20.06	7.66	7.70	7.67	7.63	7.66	7.66

Table A3. *Continued*

Ref.	Papike et al., 1997 [a]										Floss et al., 1998						
Sample (ppm)	60015.122	69955,30	6106,222	60215,33	15415,19	67535,2	60025,132	62255,143	67525,3	67536,2	60055,5	62255,42	62255,42	65315,82	64435,268	64435,268	64435,268
La	0.171	0.171	0.163	0.189	0.161	0.188	0.290	0.309	0.335	0.451	0.150	0.300	0.340	0.130	0.140	0.140	0.130
Ce	0.461	0.431	0.454	0.483	0.498	0.508	0.833	0.827	0.998	1.130	0.370	0.760	0.890	0.310	0.320	0.350	0.360
Pr	-	-	-	-	-	-	-	-	-	-	0.047	0.089	0.094	0.034	0.039	0.042	0.042
Nd	0.219	0.219	0.226	0.260	0.265	0.285	0.408	0.424	0.502	0.597	0.200	0.330	0.410	0.160	0.160	0.150	0.180
Sm	0.064	0.049	0.053	0.086	0.065	0.091	0.101	0.117	0.095	0.116	0.060	0.069	0.100	0.041	0.049	0.031	0.032
Eu	1.070	1.120	1.010	1.180	1.020	0.988	1.210	1.220	1.000	1.120	0.850	0.990	0.910	0.660	0.760	0.800	0.780
Gd	0.057	0.036	0.045	0.066	0.057	0.074	0.083	0.087	0.077	0.077	0.058	0.070	0.110	0.043	0.038	0.041	0.038
Tb	-	-	-	-	-	-	-	-	-	-	0.009	0.011	0.014	0.008	0.013	0.006	0.008
Dy	0.047	0.024	0.036	0.047	0.046	0.056	0.061	0.061	0.067	0.049	0.035	0.053	0.065	0.029	0.030	0.023	0.028
Y	0.190	0.076	0.130	0.127	0.114	0.264	0.220	0.242	0.360	0.217	-	-	-	-	-	-	-
Ho	-	-	-	-	-	-	-	-	-	-	0.008	0.013	0.012	0.007	0.004	0.005	0.009
Er	0.016	0.007	0.017	0.018	0.016	0.032	0.026	0.025	0.026	0.020	0.022	0.019	0.032	0.011	0.008	0.013	0.014
Tm	-	-	-	-	-	-	-	-	-	-	-	-	-	-	-	-	-
Yb	0.017	0.008	0.015	0.016	0.009	0.027	0.018	0.023	0.026	0.031	0.026	0.021	0.032	0.019	0.013	0.015	0.010
Lu	-	-	-	-	-	-	-	-	-	-	-	-	-	-	-	-	-
Error (σ)																	
La	0.009	0.009	0.008	0.009	0.008	0.009	0.015	0.015	0.017	0.023	0.020	0.060	0.030	0.020	0.010	0.020	0.010
Ce	0.023	0.022	0.023	0.024	0.025	0.025	0.042	0.041	0.050	0.057	0.020	0.160	0.080	0.020	0.030	0.020	0.020
Pr	-	-	-	-	-	-	-	-	-	-	0.007	0.017	0.004	0.004	0.005	0.004	0.004
Nd	0.011	0.011	0.011	0.013	0.013	0.014	0.020	0.021	0.025	0.030	0.020	0.050	0.040	0.010	0.010	0.010	0.010

Table A3. *Continued*

Ref.	Papike et al., 1997 [a]										Floss et al., 1998						
Sm	0.003	0.002	0.003	0.004	0.003	0.005	0.005	0.006	0.005	0.006	0.011	0.015	0.020	0.006	0.008	0.008	0.007
Eu	0.054	0.056	0.051	0.059	0.051	0.049	0.061	0.061	0.050	0.056	0.060	0.100	0.010	0.030	0.040	0.050	0.040
Gd	0.003	0.002	0.002	0.003	0.003	0.004	0.004	0.004	0.004	0.004	0.001	0.013	0.030	0.009	0.007	0.004	0.008
Tb	-	-	-	-	-	-	-	-	-	-	0.004	0.005	0.001	0.002	0.002	0.002	0.002
Dy	0.009	0.005	0.007	0.009	0.009	0.011	0.012	0.012	0.013	0.010	0.008	0.020	0.004	0.003	0.004	0.007	0.004
Y	-	-	-	-	-	-	-	-	-	-	-	-	-	-	-	-	-
Ho	0.010	0.004	0.007	0.006	0.006	0.013	0.011	0.012	0.018	0.011	0.001	0.006	0.005	0.001	0.001	0.002	0.002
Er	0.003	0.001	0.003	0.004	0.003	0.006	0.005	0.005	0.005	0.004	0.002	0.006	0.012	0.005	0.003	0.002	0.003
Tm	-	-	-	-	-	-	-	-	-	-	-	-	-	-	-	-	-
Yb	0.003	0.002	0.003	0.003	0.002	0.005	0.004	0.005	0.005	0.006	0.009	0.014	0.007	0.009	0.004	0.007	0.003
Lu	-	-	-	-	-	-	-	-	-	-	-	-	-	-	-	-	-
Error of $(Ce/Sm)_{CI}$	0.160	0.195	0.190	0.125	0.170	0.124	0.183	0.157	0.233	0.216	0.300	0.828	0.492	0.313	0.314	0.745	0.639
Ce/Sm	1.758	2.146	2.090	1.370	1.870	1.362	2.013	1.725	2.563	2.377	1.505	2.688	2.172	1.845	1.594	2.755	2.745
Success threshold [b] (%)	9.09	9.09	9.09	9.09	9.09	9.09	9.09	9.09	9.09	9.09	19.95	30.80	22.66	16.98	19.67	27.04	23.28
Error of Eu*	4.188	6.299	4.895	3.696	3.965	2.851	3.118	2.852	2.768	2.799	5.567	7.971	4.712	6.976	7.721	10.993	11.541
Eu*	54.772	82.446	63.941	48.424	51.809	37.224	40.859	37.386	36.149	36.639	44.548	44.042	26.825	48.598	54.453	69.378	69.156
Success threshold [b] (%)	7.65	7.64	7.66	7.63	7.65	7.66	7.63	7.63	7.66	7.64	12.50	18.10	17.56	14.35	14.18	15.85	16.69

Table A3. *Continued*

Ref.	Floss et al., 1998											
Sample	60025, 702	60025, 702	60025,699	60025,699	64435,270	64435,270	67635,8	67215,6	67215,6	67215,6	67215,6	67215,6
(ppm)												
La	0.240	0.260	0.330	0.280	0.510	0.710	0.450	1.670	1.980	2.540	1.910	1.710
Ce	0.670	0.750	0.820	0.770	1.370	1.650	1.050	3.530	3.830	5.280	4.140	3.840
Pr	0.089	0.085	0.087	0.094	0.200	0.210	0.130	0.330	0.410	0.550	0.530	0.430
Nd	0.390	0.390	0.430	0.430	0.720	0.730	0.510	1.290	1.600	1.990	1.630	1.580
Sm	0.094	0.100	0.060	0.095	0.140	0.130	0.100	0.200	0.350	0.350	0.310	0.340
Eu	1.030	0.970	1.050	1.060	0.950	1.010	1.330	1.120	1.010	1.200	1.000	1.000
Gd	0.093	0.085	0.071	0.081	0.140	0.120	0.087	0.170	0.250	0.250	0.270	0.250
Tb	0.016	0.015	0.008	0.012	0.022	0.024	0.014	0.017	0.028	0.037	0.031	0.033
Dy	0.055	0.061	0.039	0.031	0.097	0.061	0.075	0.083	0.220	0.190	0.170	0.180
Y	-	-	-	-	-	-	-	-	-	-	-	-
Ho	0.013	0.012	0.012	0.009	0.020	0.019	0.017	0.026	0.046	0.038	0.048	0.041
Er	0.025	0.029	0.018	0.015	0.045	0.025	0.034	0.059	0.130	0.086	0.081	0.082
Tm	-	-	-	-	-	-	-	-	-	-	-	-
Yb	0.031	0.028	0.022	0.006	0.038	0.041	0.042	0.079	0.130	0.082	0.110	0.120
Lu	-	-	-	-	-	-	-	-	-	-	-	-
Error (σ)												
La	0.060	0.020	0.020	0.040	0.020	0.040	0.070	0.080	0.430	0.110	0.170	0.330
Ce	0.070	0.080	0.060	0.120	0.070	0.090	0.110	0.160	0.690	0.180	0.040	0.760
Pr	0.017	0.013	0.010	0.005	0.020	0.020	0.020	0.030	0.070	0.030	0.020	0.090
Nd	0.030	0.040	0.020	0.050	0.050	0.030	0.060	0.060	0.400	0.060	0.080	0.090

Table A3. *Continued*

Ref.	Floss et al., 1998											
Sm	0.038	0.020	0.013	0.028	0.020	0.020	0.020	0.020	0.040	0.030	0.010	0.050
Eu	0.040	0.010	0.060	0.090	0.040	0.050	0.070	0.060	0.130	0.040	0.210	0.060
Gd	0.012	0.002	0.016	0.031	0.040	0.020	0.007	0.030	0.040	0.040	0.010	0.020
Tb	0.001	0.001	0.003	0.004	0.001	0.004	0.003	0.005	0.008	0.006	0.007	0.004
Dy	0.013	0.004	0.007	0.017	0.006	0.007	0.028	0.001	0.070	0.010	0.010	0.010
Y	-	-	-	-	-	-	-	-	-	-	-	-
Ho	0.005	0.001	0.003	0.003	0.006	0.003	0.003	0.004	0.018	0.004	0.015	0.001
Er	0.007	0.009	0.006	0.008	0.005	0.005	0.015	0.009	0.050	0.001	0.023	0.004
Tm	-	-	-	-	-	-	-	-	-	-	-	-
Yb	0.002	0.005	0.007	0.003	0.004	0.006	0.042	0.010	0.070	0.008	0.050	0.050
Lu	-	-	-	-	-	-	-	-	-	-	-	-
Error of $(Ce/Sm)_{CI}$	0.733	0.428	0.786	0.669	0.387	0.536	0.597	0.533	0.590	0.399	0.216	0.698
Ce/Sm	1.739	1.830	3.335	1.978	2.388	3.097	2.562	4.307	2.670	3.681	3.259	2.756
Success threshold [b] (%)	42.14	23.37	23.57	33.83	16.21	17.29	23.29	12.37	22.09	10.85	6.63	25.31
Error of Eu*	7.511	3.617	8.586	9.717	3.598	3.300	5.653	2.319	1.777	1.340	2.312	1.196
Eu*	34.059	32.528	49.738	37.360	20.980	25.001	44.085	18.779	10.556	12.542	10.687	10.605
Success threshold [b] (%)	22.05	11.12	17.26	26.01	17.15	13.20	12.82	12.35	16.84	10.69	21.64	11.28

Table A3. *Continued*

Ref.	Roberts et al., 2019					Russell et al. 2014											
Sample	NWA 10986 -H4	NWA 10986- H4	NWA 10986 -H5	NWA 10986 -H5	NWA 10986 -H5	Dhofa r 908	Dhofa r 908	Dhofa r 908	Dhofa r 908	Dhofa r 908	Dhofa r 908	Dhofa r 908	Dhofa r 908	Dhofa r 908	Dhofa r 908	Dhofa r 081	Dhofa r 081
(ppm)																	
La	1.183	1.039	1.210	1.250	1.190	0.251	0.258	0.283	0.442	0.105	0.108	0.110	0.251	0.198	0.268	0.349	0.421
Ce	1.820	2.120	3.320	3.220	3.240	0.543	0.591	0.607	1.200	0.233	0.254	0.258	0.543	0.499	0.641	0.927	1.120
Pr	0.316	0.313	0.397	0.370	0.388	0.073	0.068	0.070	0.134	0.024	0.031	0.031	0.073	0.064	0.074	0.136	0.152
Nd	1.390	1.040	1.540	1.520	1.540	0.325	0.317	0.289	0.547	0.118	0.141	0.141	0.325	0.226	0.348	0.551	0.607
Sm	0.454	0.299	0.449	0.264	0.423	0.047	0.070	0.093	0.123	0.039	0.039	0.035	0.047	0.054	0.048	0.150	0.148
Eu	0.884	0.926	0.900	0.849	0.804	0.750	0.795	0.634	0.635	0.713	0.766	0.751	0.750	0.833	0.897	0.871	0.859
Gd	0.380	0.277	0.470	0.320	0.430	0.059	0.079	0.058	0.087	0.030	0.047	0.036	0.059	0.050	0.084	0.137	0.192
Tb	0.039	0.044	0.049	0.027	0.032	0.009	0.009	0.009	0.017	0.004	0.005	0.004	0.009	0.006	0.007	0.015	0.026
Dy	0.170	0.082	0.186	0.176	0.116	0.047	0.059	0.052	0.105	0.031	0.025	0.024	0.047	0.040	0.054	0.077	0.158
Y	1.790	0.863	0.748	1.090	0.769	0.250	0.290	0.290	0.450	0.150	0.150	0.130	0.250	0.180	0.320	0.420	0.830
Ho	0.025	0.031	0.022	0.029	0.023	0.011	0.010	0.011	0.015	0.004	0.006	0.003	0.011	0.005	0.009	0.015	0.034
Er	0.126	0.065	0.195	-	0.075	0.027	0.021	0.029	0.035	0.018	0.015	0.011	0.027	0.022	0.033	0.049	0.068
Tm	-	-	-	-	-	-	0.004	0.004	0.008	-	-	0.002	-	-	0.005	0.005	0.011
Yb	0.076	-	-	0.195	-	0.025	0.034	0.020	0.045	0.015	-	-	0.025	0.030	0.028	0.065	0.068
Lu	-	-	-	0.013	-	-	0.004	0.003	0.007	0.001	-	-	-	-	0.004	0.004	0.009
Error (σ)																	
La	0.160	0.180	0.350	0.340	0.110	0.001	0.001	0.002	0.003	0.001	0.001	0.001	0.001	0.001	0.002	0.002	0.002
Ce	0.030	0.026	0.037	0.035	0.019	0.004	0.004	0.004	0.009	0.002	0.002	0.002	0.002	0.004	0.005	0.007	0.008
Pr	0.140	0.110	0.160	0.160	0.110	0.000	0.000	0.001	0.001	0.001	0.001	0.001	0.001	0.001	0.001	0.001	0.001

Table A3. *Continued*

Ref.	Roberts et al., 2019					Russell et al. 2014											
Nd	0.085	0.063	0.082	0.061	0.080	0.005	0.005	0.004	0.008	0.002	0.002	0.002	0.002	0.003	0.005	0.008	0.009
Sm	0.075	0.072	0.089	0.084	0.029	0.000	0.001	0.001	0.001	0.001	0.001	0.001	0.001	0.001	0.001	0.001	0.001
Eu	0.100	0.073	0.130	0.110	0.190	0.006	0.006	0.005	0.005	0.006	0.006	0.006	0.005	0.007	0.007	0.007	0.007
Gd	0.011	0.009	0.010	0.010	0.030	0.001	0.001	0.001	0.001	0.001	0.001	0.001	0.001	0.001	0.001	0.002	0.003
Tb	0.040	0.032	0.042	0.040	0.230	0.001	0.001	0.001	0.001	0.001	0.001	0.001	0.001	0.001	0.001	0.001	0.001
Dy	0.010	0.008	0.009	0.008	0.064	0.001	0.001	0.001	0.001	0.001	0.001	0.001	0.001	0.001	0.001	0.001	0.001
Y	0.600	0.510	0.700	0.670	3.300	0.003	0.003	0.003	0.005	0.002	0.002	0.002	0.001	0.002	0.004	0.005	0.009
Ho	0.031	0.023	0.040	0.025	0.200	0.001	0.001	0.001	0.001	0.001	0.001	0.001	0.001	0.001	0.001	0.001	0.001
Er	0.007	0.006	0.007	0.008	0.056	0.001	0.001	0.001	0.001	0.001	0.001	0.001	0.001	0.001	0.001	0.001	0.001
Tm	0.032	0.029	0.032	0.040	0.280	-	0.001	0.001	0.001	-	-	0.001	-	-	0.001	0.001	0.001
Yb	0.007	0.006	0.007	0.007	0.083	0.001	0.001	0.001	0.001	0.001	-	-	-	0.001	0.001	0.001	0.001
Lu	0.029	0.027	0.028	0.030	0.120	-	0.001	0.001	0.001	0.001	-	-	-	-	0.001	0.001	0.001
Error of $(Ce/Sm)_{CI}$	0.172	0.429	0.373	0.963	0.167	0.162	0.122	0.093	0.138	0.092	0.100	0.116	0.172	0.137	0.200	0.087	0.107
Ce/Sm	0.978	1.730	1.804	2.976	1.869	2.819	2.060	1.593	2.381	1.458	1.589	1.799	2.819	2.255	3.259	1.508	1.847
Success threshold [b] (%)	17.56	24.78	20.66	32.34	8.94	5.75	5.92	5.85	5.81	6.32	6.31	6.43	6.10	6.05	6.13	5.80	5.79
Error of Eu*	0.975	1.512	1.099	1.904	1.433	2.124	1.592	1.311	0.922	3.361	2.779	3.368	2.166	2.436	2.115	0.896	0.754
Eu*	6.580	9.948	6.057	9.031	5.828	44.034	33.053	26.689	18.979	64.446	55.316	65.412	44.034	49.564	43.675	18.785	15.755
Success threshold [b] (%)	14.82	15.20	18.15	21.09	24.58	4.82	4.82	4.91	4.86	5.22	5.02	5.15	4.92	4.92	4.84	4.77	4.79

Table A3. *Continued*

Ref.	Cahill et al., 2004													This study
Sample (ppm)	Dho 025-AA	Dho 025-AI	Dho 025-108b	Dho 025-BA	Dho 025-BB	Dho 081-AE	Dho 081-C	DAG 262-1	DAG 262-2	DAG 262-3	DAG 400-1	DAG 400-2	DAG 400-3	Dhofar 280/2
La	0.680	0.490	1.060	0.820	0.310	0.230	0.320	0.760	0.380	0.290	0.800	0.510	0.950	0.293
Ce	1.690	1.150	2.350	1.910	0.820	0.630	0.810	2.040	1.040	0.670	1.880	1.330	2.260	0.653
Pr	0.210	0.160	0.290	0.310	0.100	0.100	0.130	0.250	0.120	0.100	0.260	0.170	0.300	0.085
Nd	0.850	0.620	1.110	1.000	0.420	0.410	0.380	0.930	0.390	0.390	1.020	0.660	1.070	0.235
Sm	0.150	0.200	0.200	0.170	0.100	0.076	0.100	0.170	0.097	0.110	0.270	0.170	0.270	0.091
Eu	0.840	0.850	0.720	0.740	0.700	0.710	0.720	0.670	0.810	0.440	0.680	0.880	0.750	0.871
Gd	0.110	0.130	0.200	0.140	0.110	0.074	0.140	0.160	0.098	0.081	0.230	0.160	0.170	0.034
Tb	0.021	0.015	0.017	0.024	0.029	0.007	0.016	0.013	0.006	0.012	0.025	0.025	0.026	0.011
Dy	0.092	0.130	0.087	0.095	0.130	0.034	0.120	0.110	0.093	0.077	0.140	0.130	0.130	0.086
Y	0.500	0.700	0.600	0.800	0.700	0.400	0.700	0.600	0.500	0.500	0.900	0.800	0.700	0.185
Ho	0.019	0.023	0.028	0.018	0.013	0.006	0.027	0.017	0.051	0.036	0.033	0.035	0.033	0.011
Er	0.052	0.035	0.051	0.081	0.056	0.012	0.037	0.050	0.068	0.049	0.055	0.043	0.051	0.027
Tm	0.006	-	-	-	0.006	-	-	-	-	-	0.011	-	0.005	-
Yb	0.031	0.046	0.040	0.092	-	-	0.021	0.056	0.035	0.038	0.036	0.055	0.043	0.020
Lu	-	-	-	-	-	-	0.001	-	-	-	-	0.005	-	0.005
Error (σ)														
La	0.080	0.040	0.080	0.080	0.040	0.030	0.030	0.040	0.030	0.030	0.050	0.040	0.050	0.014
Ce	0.180	0.070	0.180	0.110	0.080	0.070	0.060	0.090	0.070	0.050	0.110	0.070	0.110	0.093
Pr	0.030	0.020	0.030	0.030	0.020	0.010	0.010	0.020	0.010	0.010	0.020	0.010	0.020	0.011
Nd	0.070	0.040	0.070	0.060	0.040	0.040	0.030	0.050	0.030	0.030	0.050	0.030	0.040	0.008

Table A3. *Continued*

Ref.	Cahill et al., 2004													This study
Sm	0.040	0.030	0.040	0.040	0.040	0.031	0.030	0.030	0.024	0.030	0.040	0.020	0.030	0.028
Eu	0.050	0.040	0.050	0.050	0.040	0.050	0.030	0.030	0.080	0.060	0.040	0.040	0.030	0.106
Gd	0.050	0.030	0.050	0.050	0.040	0.027	0.030	0.030	0.023	0.023	0.040	0.030	0.030	0.018
Tb	0.009	0.006	0.009	0.001	0.010	0.006	0.007	0.006	0.004	0.005	0.008	0.006	0.006	0.005
Dy	0.020	0.020	0.020	0.021	0.030	0.014	0.020	0.020	0.015	0.013	0.020	0.010	0.010	0.012
Y	-	-	-	-	-	-	-	-	-	-	-	-	-	0.012
Ho	0.009	0.006	0.009	0.007	0.007	0.005	0.008	0.005	0.008	0.007	0.007	0.006	0.005	0.005
Er	0.018	0.013	0.018	0.020	0.020	0.013	0.014	0.012	0.014	0.012	0.015	0.010	0.011	0.039
Tm	0.006	-	-	-	-	-	-	-	-	-	0.008	-	0.006	-
Yb	0.024	0.019	0.024	0.030	-	-	0.017	0.019	0.021	0.019	0.019	0.019	0.015	0.004
Lu	-	-	-	-	0.008	-	0.006	-	-	-	-	0.004	-	0.008
Error of $(Ce/Sm)_{CI}$	0.805	0.241	0.635	0.682	0.832	0.863	0.621	0.558	0.687	0.429	0.287	0.269	0.274	0.602
Ce/Sm	2.749	1.403	2.867	2.742	2.001	2.023	1.977	2.928	2.616	1.486	1.699	1.909	2.043	1.751
Success threshold [b] (%)	29.28	17.16	22.16	24.89	41.57	42.66	31.42	19.06	26.27	28.85	16.92	14.10	13.41	34.38
Error of Eu*	5.542	2.488	2.011	3.398	5.783	8.384	3.664	1.812	5.201	3.523	1.155	2.116	1.311	16.107
Eu*	20.218	16.298	11.130	14.830	20.635	29.271	18.814	12.560	25.685	14.412	8.437	16.497	10.823	48.413
Success threshold [b] (%)	27.410	15.267	18.070	22.911	28.024	28.643	19.473	14.425	20.248	24.446	13.686	12.830	12.109	33.271

We do not consider samples with plagioclase that display high shock states (e.g., 60015,125 in Pernet-Fisher et al., 2019) or those missing REE data required for modeling (e.g., some Dhofar 081 data in Russell et al., 2014).

[a.] We calculate the errors of REEs in Papike et al. (1997) based on the description in the data source (5% for LREE+Y and 20% for HREE).

[b.] These success thresholds are used to screen successful simulations of the Monte-Carlo method presented in Section 1.5 of the main text, and are calculated according to the analytical errors of plagioclase and CI chondrite.

Table A4. Rare earth element compositions of different assumed initial bulk LMO trace element compositions and KREEPy component that we applied in the model. Note that all initial bulk LMO trace element compositions except chondritic bulk LMO are diluted by different factors such that their average REE concentrations are close to that of CI chondrite. See Section 1.3 in the main text for details.

	Moderately deplete bulk LMO	Slightly depleted bulk LMO	Chondritic bulk LMO	Enriched bulk LMO	KREEP basalt 15386 [a]
(ppm)					
La	0.096	0.189	0.244	1.000	84.1
Ce	0.275	0.575	0.627	2.150	213.1
Pr	0.054	0.087	0.095	0.245	30.0
Nd	0.291	0.490	0.472	1.000	125.6
Sm	0.120	0.163	0.153	0.195	36.5
Eu	0.048	0.061	0.058	0.055	2.78
Gd	0.179	0.220	0.208	0.185	43.9
Tb	0.035	0.037	0.038	0.030	7.51
Dy	0.253	0.256	0.252	0.180	45.7
Y	1.664	1.500	1.500	0.950	241.0
Ho	0.058	0.053	0.057	0.039	10.3
Er	0.174	0.158	0.163	0.105	28.3
Yb	0.183	0.150	0.167	0.095	26.2
Lu	0.029	0.023	0.025	0.015	3.59
Ref.	Workman and Hart, 2005	Arevalo and McDonough, 2010	Lodders, 2021	Rudnick and Gao, 2014	Neal and Kramer, 2003

Table A5. Summary of Arrhenius parameters and relevant fO_2, P and T conditions assumed in our kinetic model (Figure 1.5). We use Nd in anorthite, Dy in diopside and Eu in enstatite to estimate diffusion rates of REEs in constituent phases of lunar anorthosites.

Composition	Cation	Orientation	fO_2	P	T (°C)	D_0 (m^2 sec^{-1})	E (kJ mol^{-1})	Ref.
Anorthite	Nd	[010]	air	0.1MPa	1000-1348	5.9×10^{-6}	398	Cherniak, 2003
Diopside	Dy	[001]	QFM	0.1MPa	1100-1300	4.9×10^{-4}	461	Van Orman et al., 2001
Enstatite	Eu	[210],[001]	air	0.1MPa	1000-1200	1.7×10^{-8}	350	Cherniak and Liang, 2007

Table A6. Rare earth element concentrations in secondary standard materials analyzed as unknowns compared to preferred concentrations (data from Jochum et al., 2011; Jochum et al., 2005).

	Secondary Standard Concentration (ppm)	Reference Concentration (ppm)	Deviation (%)
	BIR-1G		
La	0.603	0.609	1.03
Ce	1.903	1.890	0.69
Pr	0.355	0.370	3.96
Nd	2.467	2.370	4.09
Sm	1.063	1.090	2.43
Eu	0.538	0.517	4.02
Gd	2.111	1.850	14.11
Tb	0.392	0.350	11.88
Dy	2.875	2.550	12.73
Y	16.346	14.300	14.31
Ho	0.604	0.560	7.77
Er	1.850	1.700	8.85
Tm	0.243	0.240	1.41
Yb	1.770	1.640	7.92
Lu	0.292	0.248	17.82
	NIST612		
La	36.860	36.000	2.39
Ce	41.328	38.400	7.62
Pr	41.411	37.900	9.26
Nd	38.058	35.500	7.21
Sm	38.981	37.700	3.40
Eu	38.103	35.600	7.03
Gd	44.327	37.300	18.84
Tb	43.455	37.600	15.57
Dy	39.285	35.500	10.66
Y	43.029	38.300	12.35
Ho	43.161	38.300	12.69
Er	41.395	38.000	8.93
Tm	38.786	36.800	5.40
Yb	43.662	39.200	11.38
Lu	45.866	37.000	23.96

CHAPTER 2
TRACE ELEMENT PARTITIONING BETWEEN APATITE AND SILICATE MELTS

Abstract

Apatite, as a common phase in igneous and metamorphic rocks, has important petrological significance due to its capacity to accommodate trace elements in its mineral structure. To better constrain trace element partitioning between apatite and silicate melts, we conducted 12 experiments that produced apatites approaching fluorapatite (FlAp), hydroxylapatite (OHAp) and chlorapatite (ClAp) endmembers separately under three different fO_2 and two T conditions at 1 GPa pressure. We demonstrate the ClAp exhibits lower trace element partition coefficients compared with FlAp and OHAp, especially for the Rare Earth Elements (REEs) under all run conditions explored, suggesting trace element partitioning is sensitive to anion site occupancy. Larger divalent cations (e.g., Sr) are less sensitive to anion occupancy. Positive Eu partitioning anomalies (DEu/DEu*, where Eu is the chondrite normalized abundance and Eu* is the interpolated value from neighboring elements on a REE diagram) are observed in ClAp experiments under the relatively low fO_2, whereas negative Eu anomalies are exhibited by FlAp and OHAp under the same fO_2 conditions. We infer that anionic occupancies have a direct impact on the substitution mechanisms of trace elements in apatite, thereby influencing their partition coefficients. Beyond the anions, correlations of apatite compositional components (X_{Ca}, X_{Na}, X_P and X_{Si}) with partition coefficients suggest they exert crystal chemical controls on trace element partitioning. Based on these observations, we developed parameterized lattice strain models to predict the partitioning of divalent and trivalent elements as a function of temperature and apatite composition. We further developed a Eu in apatite-plagioclase oxybarometer that enables us to calculate the fO_2 of magmatic systems, and evaluated the influence of the subsolidus reequilibration on the new oxybarometer. Applied to one of our experiments, winonaite HaH193, and samples from Sept-Iles layered intrusion, the oxybarometer recovers their anticipated fO_2s, ranging from about two long unit below iron-wüstite buffer to the fayalite-magnetite-quartz buffer. Using the new REE and fO_2-dependent Eu partitioning models, we constrained the petrogenesis of lunar KREEP basalt and estimated the relative volatile content in the late lunar magma ocean (LMO) cumulates. The model suggests a relative depletion of Cl in the LMO cumulates, which is consistent with previous Cl isotope studies, suggesting that differential loss of volatiles occurred before or during the late-stage evolution of the LMO.

2.1. Introduction

Apatite [$Ca_5(PO_4)_3(OH, F, Cl)$] is an omnipresent accessory mineral in different kinds of rocks on Earth as well as other bodies in the Solar System (e.g., McCubbin and Jones 2015). Although representing a small proportion of the rock and acting as a late-crystallizing mineral, apatite can harbor essential amounts of Rare Earth Elements (REEs) and other trace elements in magmatic systems because of the high partition coefficients (Ds) of these elements, which are often compatible or near compatible (Gromet and Silver, 1983).

Some apatites, as well as whitlockites [$Ca_3(PO_4)_2$], have also been discovered in returned Apollo samples (e.g., Shervais et al. 1984; Tartèse et al. 2014; Potts et al. 2018). Accordingly, apatite also occurs in the late stages of lunar magma ocean (LMO) crystallization experiments (e.g., Rapp and Draper 2018, Schmidt and Kraettli 2022). Since it has much higher partition coefficients for REEs than major minerals, apatite has enormous potential to control bulk elemental partitioning and affect elemental concentrations in major minerals during LMO crystallization as well as subsequent geological events (e.g., partial melting, subsolidus

reequilibration). Therefore, developing a predictive elemental partitioning model for trace elements between apatite and silicate melts is of importance to help us evaluate related fractionation processes.

Elemental partitioning between apatite and melt is complicated because of the uncertainty of the REE occupancy in the apatite. Because of the similarity of ion radius and valence state, divalent and trivalent cations often substitute for Ca^{2+} ions in mineral structures. In apatite, forty percent of the Ca atoms occupy the larger lattice site (nine-fold coordination, Ca1 site), while the rest enter the seven-fold coordinated site (Ca2 site), surrounding the anion-hosting X-site, which is usually occupied by F, OH, or Cl in naturally occurring apatites (Figure B1). There is controversy in the literature over whether REEs tend to occupy the Ca1 sites (Urusov and Khudolozhkin, 1974), Ca2 sites (Borisov and Klevtsova, 1963), or have no occupancy preference (Cockbain and Smith, 1967). More recent studies suggest that for three endmembers of apatite, i.e., fluorapatite, hydroxylapatite, and chlorapatite (FlAp, OHAp, and ClAp), REE substitution mechanisms are related to the occupancy of X-site anions (e.g., Fleet and Pan 1997; Fleet et al. 2000a; Fleet et al. 2000b). The problem also exists in the substitution of divalent cations, and it seems that the site preference for each cation is different (e.g., Pan and Fleet 2002 and references therein). Previous studies reveal that temperature (Li and Hermann, 2017), as well as the polymerization of the melt (Prowatke and Klemme, 2006; Watson and Green, 1981), have huge impacts on REE partition coefficients. However, because of a lack of data, relationships between the X-site occupancy (F, OH, Cl) and the REE partitioning behavior could not previously be quantified. In addition, a negative Eu anomaly (Eu/Eu*, where Eu is the chondrite normalized abundance and Eu* is the interpolated value from neighboring elements on a REE diagram) is generally reported in natural apatites (e.g., Chen et al. 2016), but with limited exceptions (Tailby et al., 2023), the dependence of Eu partitioning on fO_2 was unknown, meriting further exploration.

In this study, we experimentally determine trace element partition coefficients between apatite and silicate melt. We develop temperature and composition-dependent predictive partitioning models for divalent and trivalent elements, and quantify the effects of variations in composition and oxygen fugacity on Eu anomalies in apatite. We present a new Eu in apatite-plagioclase oxybarometer, explore the kinetic fractionation of trivalent and divalent Eu during subsolidus reequilibration, and evaluate its effect on the oxybarometer. Finally, we apply our predictive partitioning models to the LMO solidification and estimate the relative volatile abundance in the late-stage LMO cumulates.

2.2. Methods

2.2.1. Starting materials

Three different starting materials were used in our experiments with the same bulk composition with the exception of the anionic component (Table 2.1). The bulk composition of major element cations is from the liquid in a LMO solidification experiment by Rapp and Draper (2018), where the melt composition is in equilibrium with apatite after the solidification percentage reaches 97% (their L-GM25 experiment). Starting materials were prepared by grinding reagent-grade oxide and carbonate powders into three separate homogeneous mixtures. A mixture of REEs,

Table 2.1. Major element compositions of the three starting materials utilized in this study.

	OHAp-M[a]		FlAp-M		ClAp-M	
n.o.a.[b]	(20)	σ	(29)	σ	(20)	σ
SiO_2	37.62	0.35	37.29	0.30	37.69	0.36
TiO_2	3.40	0.05	3.54	0.05	3.54	0.05
Al_2O_3	5.78	0.47	5.63	0.10	5.76	0.08
FeO	30.82	0.27	31.86	0.32	31.03	0.33
MnO	0.81	0.02	0.79	0.02	0.71	0.02
MgO	0.96	0.02	0.99	0.02	0.96	0.02
CaO	11.10	0.10	10.93	0.11	10.90	0.12
Na_2O	0.83	0.04	0.82	0.03	0.64	0.08
K_2O	0.19	0.01	0.25	0.01	0.20	0.01
P_2O_5	4.22	0.07	4.25	0.05	4.34	0.07
F	0.00	-	0.20	0.01	0.00	-
Cl	0.03	0.01	0.03	0.01	0.78	0.02
Spec[c]	1.50	-	1.50	-	1.50	-
Tot.	97.26		98.08		98.05	

[a.] We can't analyze the OH concentration in the glass by EMP, the OH we doped is about 0.28 weight percent.

[b.] Numbers of EMP analyses.

[c.] The sum of REEs, HFSEs, and actinides that we doped intentionally.

HFSEs, and actinides, prepared from natural mineral sources was then added into the starting compositions as a dopant at a mass ratio of ~1.5:100. After decarbonating the mixtures in an 850 ℃ furnace overnight, we pre-conditioned each mixture in a 900 ℃ H_2-CO_2 gas mixing furnace for 4 hours according to the target fO_2s of three assembly types that utilize different metals to control fO_2 (Re-ReO_2, Mo, and Cr). Synthetic $Ca_5(PO_4)_3OH$, CaF_2 and NaCl were then added into the mixtures and mechanically dry mixed to keep the same molar percentage of F, Cl, OH, as well as other cations in each starting material as much as possible. The compositions were then stored in a vacuum furnace at 200 ℃ prior to running.

In order to get the accurate major element concentrations of starting materials, three quenching experiments were conducted in which each of the starting components was placed in a separate graphite-lined Mo capsule and heated to 1250 °C at a ramp rate of 70 ℃ per minute under 1 GPa in the piston-cylinder apparatus, and the target temperature was maintained for one hour prior to quenching. Because of the high concentrations of FeO in our initial compositions, the three powders we utilized are those designed and preconditioned for experiments with relatively high fO2 in order to avoid the formation of immiscible Fe metals during the heating (more details about experimental procedures are reported in Sections 2.2.2 and 2.2.3). The experimental product contains only quenched glass, and the results of EMP analysis are listed in Table 2.1.

2.2.2 Capsules and preconditioning procedure

Piston cylinder experiments utilized graphite-lined molybdenum or platinum capsules, depending on the target fO_2. Experiments with Pt capsules targeted high fO_2 conditions. To mitigate reaction of the Pt capsules with the starting material during experiments, we preconditioned platinum capsules by crimping and welding one end shut, then placing the capsule, in a platinum crucible in a bath of our starting materials (same as the composition in Table 2.1 but without phosphorous and volatile elements F, Cl, and OH), so that both the inner and outer wall of the capsule were surrounded. Preconditioning runs were conducted in a Deltech gas mixing furnace at 1200 ℃ for 24 hours, in an H_2-CO_2 mixture approximating the intended fO_2 of the subsequent piston cylinder run. After removal from the Deltech furnace, the basalt glass within and around the capsules was dissolved in a mixture of nitric and hydrofluoric acid.

The series of experiments that utilized Mo capsules with graphite liners targeted fO_2 values near the iron-wüstite buffer (e.g., Dygert et al. 2014; Fabbrizio et al. 2021). To target even more reducing conditions, a similar assembly design was used, but containing a layer of Cr metal powder isolated from the experimental powders and outer capsule by layers of graphite. To monitor fO_2 in a subset of the graphite-lined Mo and graphite-lined Mo with Cr experiments, we placed preconditioned platinum wire in the experimental powders, prepared using the same method as employed for conditioning the platinum capsules, but at a higher H_2-CO_2 conditioning ratio.

2.2.3 Run procedure and conditions

Twelve high-temperature and pressure experiments were conducted at the University of Tennessee using a 19.1mm end-loaded piston-cylinder apparatus. The assemblies utilized concentric shells of NaCl (as the pressure medium), an inner Pyrex® sleeve, and crushable MgO parts within a graphite furnace. In the oxidized experiments utilizing Pt capsules, a layer of Re and

Table 2.2. Experimental run conditions.

Experiment	Run pressure (GPa)	Run temperature (°C)	Ramp (°C/min)	Duration at target condition (h)	Starting material	Capsule type
FlAp-9[a]	1	1050	0.1	71	FlAp-M	C-lined Mo
OHAp-1	1	1050	0.1	64	OHAp-M	C-lined Mo
ClAp-1	1	1050	0.1	64	ClAp-M	C-lined Mo
FlAp-1	1	1100	0.1	48	FlAp-M	C-lined Mo
OHAp-6	1	1100	0.1	73	OHAp-M	C-lined Mo
ClAp-2	1	1100	0.1	72	ClAp-M	C-lined Mo
FlAp-8[a]	1	1100	0.1	76	FlAp-M	C-lined Cr & Mo
OHAp-5	1	1100	0.1	76	OHAp-M	C-lined Cr & Mo
ClAp-3	1	1100	0.1	73	ClAp-M	C-lined Cr & Mo
FlAp-7[a]	1	1100	0.1	54	FlAp-M	Pt-Re-ReO_2
OHAp-7[a b]	1	1100	0.1	72	OHAp-M	Pt-Re-ReO_2
ClAp-5[a]	1	1100	0.1	75	ClAp-M	Pt-Re-ReO_2

[a.] Experiment with a Pt fO_2 sensor (pre-conditioned platinum wire or platinum capsule). Details are provided in Section 2.3.4.

[b.] In this experiment we utilized synthetic $Ca_5(PO_4)_3OH$ in the starting material, however, because we used HF to dissolve the basaltic glass left in the platinum capsule after pre-conditioning, residue enriched in F^- contaminated the experiment, producing apatite close to the FlAp endmember.

ReO_2 was placed at the beneath the starting materials inside the preconditioned Pt capsules, with the ReO_2 in direct contact with the experimental powders. After loading experimental powders, the open capsule ends were crimped and welded shut. Experimental fO_2 values were monitored by measuring the composition of the platinum-iron alloy after the experiments. The method for calculating fO_2 from the composition of the alloy are reported in Section 2.3.4. All experiments were heated to 1200 °C at a ramp rate of 70 °C per minute, fused for one hour, and then cooled to the run temperature at a rate of 0.1 °C per minute, with pressure maintained at 1 GPa using a computerized pressure holding system. Temperatures were monitored using calibrated $W_{95}Re_5$ – $W_{75}Re_{25}$ thermocouples and run durations were 48 to 76 hours after reaching the target conditions (Table 2.2).

2.2.4. Analytical techniques

We analyzed the major and trace element concentrations of plagioclase in OHAP-1, as well as apatite and quenched glass in all experiments. Major element compositions were characterized using a Cameca SX-100 electron microprobe (EMP) at the University of Tennessee. We utilized a 5 μm spot size and 10 nA current to analyze apatite and quenched glass at an accelerating voltage of 15 keV. The standards used are fluorapatite and HgCl for apatite phosphorus and X-site occupancy, with mass deficit used to characterize the OHAp component. Other standards applied are diopside (Si and Ca), TiO_2 (Ti), hematite (Fe), spessartine garnet (Mn), olivine (Mg), spinel (Al), albite (Na), orthoclase (K), as well as Pt, Cr, and Re metal. Background and peak counting times for the major elements were typically 20–30 s, and ZAF corrections were applied using the Cameca PAP procedure.

Trace element concentrations in minerals were determined by a New Wave UP193FX laser unit with a dual-volume sample chamber coupled to an Agilent 7500ce Quadrupole Inductively Coupled Plasma Mass Spectrometer (ICP-MS) at the University of Texas, Austin. Most apatites were ablated with a 20 μm spot and a few small apatites were analyzed using a 15 μm spot. For glass and plagioclase, we chose 30, 40 and 60 μm diameter spots according to the size of the phase; care was taken to avoid phase mixing. Analyses were conducted with a laser fluence of 2.5 J/cm^2 at a frequency of 20 Hz. Data were calibrated using CaO for apatite and SiO_2 for glass and plagioclase as a reference analyte from EMP analyses. The primary trace element standard material of apatite is Apatite-NP-B01 (myStandards GmbH), secondary standard materials for the apatite analyses are BCR-2G, NIST glass SRM 610 and 612. The primary reference analyte for glass and plagioclase is NIST glass SRM 610; and secondary standard materials are BCR-2G and NIST glass SRM 612. Secondary standard analytical recoveries are 0.07 % to 51.58 % of reference values for apatite analysis, and are 0.001 % to 16.22 % of reference values for glass and plagioclase analysis, with an average recovery of 11.15 % and 4.91 %, respectively (Jochum et al., 2011; Jochum et al., 2005; Tables B1 and B2). Analytical results are reported in Tables B3 and B4.

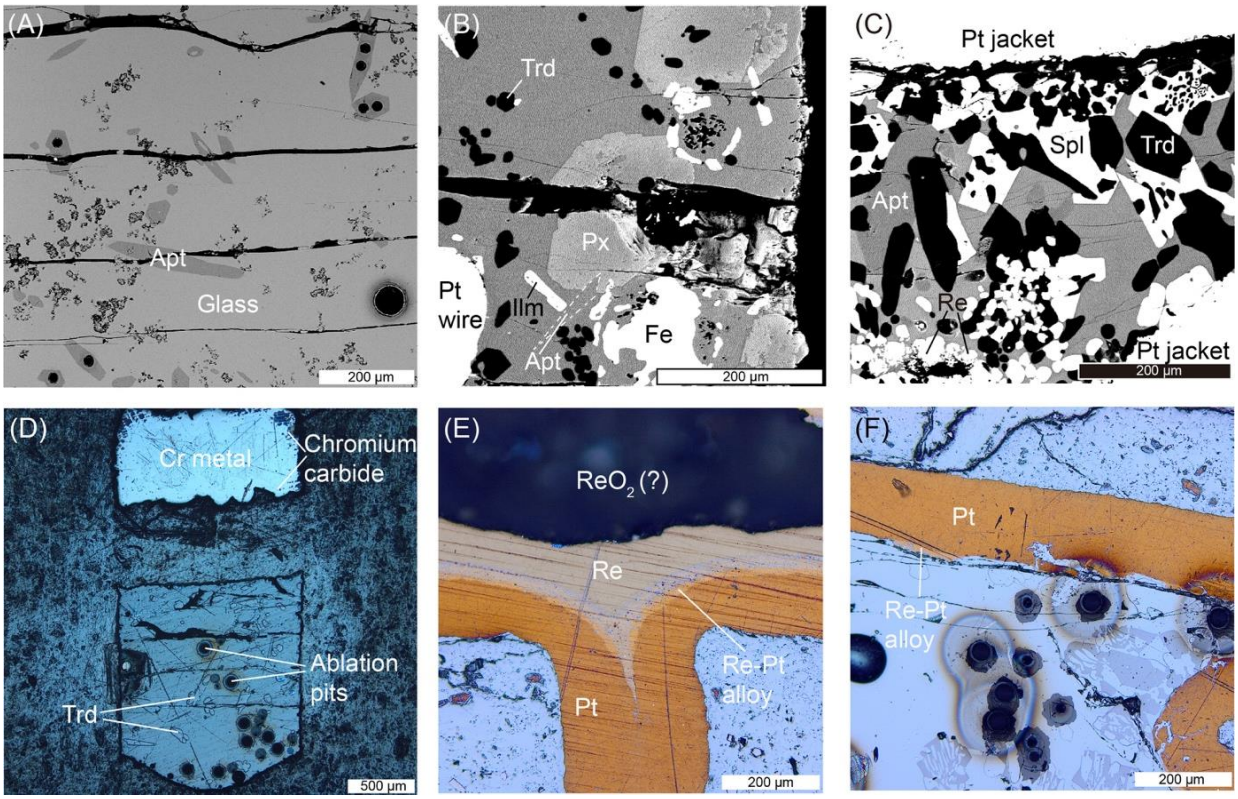


Figure 2.1. Representative backscatter electron (A-C) and reflected light (D-F) images of experimental run products. (A) OHAp-6, (B) FlAp-9, (C) OHAp-7, (D) OHAp-5, (E) the bottom and (F) the top of experiment ClAp-5. There are some Re stains on the surface of the experiment (C), which may have been smeared during polishing. At the bottom of the experiment (E), there is still some metal Re left, while some Re alloyed with Pt capsule. The location where ReO_2 was originally placed is now a void; the ReO_2 powder could be lost during polishing or consumed (reduced completely) during the experiment. At the top of the experiment shown in (F), Re-Pt alloy can still be seen in a few locations; we intentionally avoided these areas when measuring Fe alloyed concentrations.

2.3. Experimental results

2.3.1. Experimental run products

The mineral products of experiments conducted at 1100 ℃ with C-lined Cr and Mo metal and C-lined Mo capsules included apatite, tridymite, Fe metal, titanite, and quenched glass, while in the experiment ClAp-3 Ca-rich plagioclase was also observed. For the C-lined Mo experiments conducted at lower run temperatures (1050 ℃), there was no longer titanite, while ilmenite, pigeonite and clinopyroxene were present, consistent with the mineral assemblage described in Rapp and Draper (2018). For experiments utilizing Pt capsules with Re + ReO_2 layer at 1100 ℃, the experimental products included apatite, ulvöspinel, tridymite, and quenched glass. No Fe metal was present in those experiments. Among all experiments, no phosphate other than apatite was observed (Figure 2.1).

Major and trace element concentrations of apatites and melts in each experiment were homogenous or near homogeneous, as evidenced by low standard deviations of averaged core-rim analyses (Tables B3 and B4), and a lack of zoning visible in the backscatter electron images (Figure 2.1). No trace element zonation in apatite was observed (see the Yttrium map in Figure B2). We infer that the relatively long experimental durations and fast diffusion kinetics in apatite and silicate melt (Cherniak, 2000; Cherniak and Ryerson, 1993) produced apatites closely approaching equilibrium with the silicate melt.

2.3.2. Apatite major element composition

Only one anion component was added to each initial material (Table 2.1). The apatite crystallized in each experiment is generally close to each targeted endmember composition (FlAp, OHAp, and ClAp), with the exception of OHAp-7 (see below). In our mineral characterizations, the concentration of hydroxyl (OH^-) was calculated by assuming that the vacancy at X-site is filled by OH^- after considering the amount of Cl^- and F^-. We used the method described by Ketcham (2015) to calculate the apatite mineral formula, which calibrates the influence of OH^- that can't be directly analyzed by EMP. Different degrees of Cl^- and OH^- contamination were found in our experiments, but the target anion occupancies are always higher than 80%, except ClAp-1 and ClAp-5 where the Cl^- occupancy are 69% and 60% respectively (Table 2.3). The ClAp experiments are apparently more susceptible to OH^- contamination compared with FlAp experiments, indicating that F generally has a higher apatite-silicate melt partition coefficient compared with Cl, consistent with the suggestion of McCubbin et al. (2015a). The OHAp-7 experiment produced apatites containing more than 80% F^- in X-site because of contamination caused by residue remaining after the HF dissolution following preconditioning of the platinum capsule.

Among all the analyzed apatites, those in ClAp experiments are unique, as they always have higher Na_2O (0.04 – 0.15 wt. %), and lower CaO (50.23 – 52.09 wt. %) compared with other experiments (where Na_2O varies from 0.01 to 0.08 wt. % and CaO from 52.05 to 54.43 wt. %). In addition, higher MnO concentration was observed in ClAp (0.31 – 0.41 wt. %), consistent with the suggestion of Klement and Haselbeck (1965) that there is a higher solubility of Mn in ClAp. No significant relationship was found between the concentrations of other major elements and the species of anions. Major element concentrations in quenched glass vary because of different mineral assemblages and temperatures, but the quenched melts in assemblies with C-lined Mo and Cr capsules have lower FeO concentrations (17.22 – 22.18 wt. %) than melts with C-lined Mo

Table 2.3. Unit formulas (cpfu) of apatite and the apatite-silicate melt trace element partition coefficients with 1 sigma uncertainties reported for each experiment.

Sample	FlAp-9	OHAp-1	ClAp-1	FlAp-1	OHAp-6	ClAp-2	FlAp-8	OHAp-5	ClAp-3	FlAp-7	OHAp-7	ClAp-5
cpfu												
Si	0.11	0.13	0.16	0.14	0.11	0.32	0.09	0.32	0.24	0.07	0.09	0.10
Ti	0.01	0.01	0.00	0.01	0.01	0.01	0.01	0.02	0.01	0.00	0.00	0.00
Al	0.00	0.01	0.01	0.00	0.01	0.01	0.01	0.01	0.01	0.01	0.02	0.01
Fe	0.22	0.29	0.36	0.25	0.29	0.30	0.15	0.22	0.25	0.23	0.22	0.20
Mn	0.04	0.04	0.06	0.03	0.03	0.05	0.04	0.04	0.06	0.05	0.05	0.06
Mg	0.03	0.01	0.01	0.04	0.03	0.03	0.03	0.03	0.03	0.06	0.07	0.05
Ca	9.77	9.77	9.55	9.87	9.80	9.45	9.78	9.72	9.68	9.64	9.67	9.73
Na	0.01	0.02	0.05	0.01	0.01	0.04	0.00	0.03	0.04	0.01	0.01	0.01
K	0.00	0.00	0.00	0.00	0.00	0.00	0.00	0.00	0.00	0.00	0.00	0.00
P	5.88	5.83	5.86	5.80	5.84	5.80	5.91	5.72	5.79	5.94	5.91	5.89
F	1.45	0.00	0.00	2.12	0.00	0.00	1.82	0.00	0.00	1.62	1.63	0.00
Cl	0.01	0.01	1.38	0.00	0.07	1.76	0.01	0.08	1.75	0.01	0.01	1.20
OH	0.54	1.99	0.62	0.00	1.93	0.24	0.18	1.92	0.25	0.38	0.36	0.80
D												
Zn	0.11	0.28	0.05	0.25	0.10	0.10	0.24	0.11	0.14	0.27	0.06	0.11
Sr	2.59	1.83	3.01	1.88	1.32	2.00	1.63	1.13	2.08	1.84	1.55	1.50
La	2.44	1.99	0.89	2.22	1.83	0.62	2.06	1.31	0.68	1.35	1.11	0.89
Ce	2.99	2.80	1.13	3.05	2.56	0.88	2.85	1.87	0.98	1.88	1.60	1.20
Pr	3.32	3.36	1.30	3.63	3.11	0.95	3.44	2.25	1.07	2.33	2.02	1.45
Nd	3.38	3.45	1.30	3.46	3.51	0.96	3.86	2.31	1.14	2.59	2.03	1.38
Sm	3.59	3.78	1.36	3.96	3.56	1.12	4.09	2.68	1.19	2.90	2.60	1.51
Eu	2.34	2.29	1.93	2.24	2.08	1.41	2.06	1.42	1.73	2.56	2.28	1.50
Gd	3.78	3.80	1.42	4.06	3.77	1.07	4.93	2.45	1.29	3.23	2.65	1.41
Tb	3.53	3.68	1.21	3.29	3.47	0.83	4.10	2.00	0.92	2.66	2.28	1.14
Dy	3.25	3.09	1.15	3.53	2.90	0.81	3.54	1.88	0.94	2.51	2.15	1.04
Y	3.61	2.81	1.09	3.43	3.02	0.70	3.59	1.89	0.85	2.69	2.38	1.02
Ho	3.46	2.93	1.08	2.89	2.84	0.67	3.47	1.77	0.80	2.49	2.10	1.02
Er	3.14	3.08	1.01	3.20	2.87	0.67	2.80	1.83	0.79	2.50	2.11	0.95
Tm	3.04	2.36	0.95	2.52	2.07	0.57	2.97	1.46	0.62	2.07	1.69	0.80
Yb	2.58	2.15	0.82	2.19	1.89	0.45	2.16	1.31	0.48	1.78	1.49	0.60
Lu	2.77	1.89	0.67	2.45	1.63	0.41	2.09	1.15	0.59	1.72	1.35	0.59
Th	2.50	2.68	0.50	0.91	1.00	0.26	0.85	1.82	0.32	0.65	0.49	0.30
U	2.60	5.85	0.79	0.99	2.35	0.50	1.33	4.23	0.36	0.64	0.53	0.30

Table 2.3. *Continued*

Sample	FlAp-9	OHAp-1	ClAp-1	FlAp-1	OHAp-6	ClAp-2	FlAp-8	OHAp-5	ClAp-3	FlAp-7	OHAp-7	ClAp-5
σ												
Zn	0.01	-	0.02	0.19	0.02	0.06	0.02	0.01	0.04	0.01	-	0.08
Sr	0.69	-	0.48	0.49	0.07	0.11	0.29	0.20	0.17	0.33	-	0.05
La	0.85	-	0.09	0.10	0.23	0.06	0.22	0.12	0.02	0.28	-	0.03
Ce	1.10	-	0.06	0.15	0.31	0.03	0.38	0.24	0.15	0.43	-	0.05
Pr	0.70	-	0.12	0.17	0.43	0.08	0.19	0.15	0.05	0.54	-	0.14
Nd	1.22	-	0.13	0.26	0.54	0.12	0.22	0.30	0.07	0.55	-	0.10
Sm	0.51	-	0.20	0.52	0.31	0.05	0.66	0.32	0.22	0.65	-	0.10
Eu	0.72	-	0.35	0.42	0.22	0.22	0.45	0.19	0.14	0.74	-	0.15
Gd	1.73	-	0.20	0.49	0.29	0.19	0.56	0.12	0.12	0.71	-	0.07
Tb	1.52	-	0.21	0.38	0.49	0.09	0.33	0.33	0.03	0.63	-	0.10
Dy	1.07	-	0.25	0.29	0.34	0.04	0.23	0.13	0.03	0.55	-	0.03
Y	0.97	-	0.29	0.22	0.34	0.03	0.16	0.15	0.08	0.50	-	0.04
Ho	1.43	-	0.24	0.23	0.34	0.04	0.21	0.21	0.16	0.53	-	0.07
Er	1.11	-	0.26	0.34	0.41	0.08	0.25	0.11	0.02	0.51	-	0.04
Tm	1.08	-	0.44	0.24	0.19	0.08	1.07	0.26	0.03	0.34	-	0.06
Yb	1.07	-	0.36	0.15	0.29	0.04	0.28	0.20	0.18	0.28	-	0.02
Lu	0.68	-	0.39	0.30	0.20	0.09	0.21	0.31	0.10	0.43	-	0.06
Th	1.25	-	0.17	0.52	0.15	0.01	0.35	0.16	0.15	0.22	-	0.02
U	1.35	-	0.07	0.79	0.52	0.15	0.58	0.75	0.09	0.30	-	0.02

capsules (25.98 – 31.22 wt. %) conducted at the same temperature. This reflects precipitation of more Fe metal in the lower fO_2 C-lined Mo and Cr experiments. We measured ~2 wt % Re in the quenched glass of three experiments conducted in the Re-ReO_2-bearing Pt capsules. Considering the low solubility of Re in silicate melts (Ertel et al., 2001), we believe the origin of the relatively high Re concentration may include: (1) Re micro-nuggets in the quenched glass (Ertel et al., 2001); (2) accidental mixing of Re and/or ReO_2 powders into the experimental powders, as they may adhere to the wall of the capsule during the loading procedure (suggested by the presence of some Pt-Fe-Re alloy on the capsule wall; Figure 2.1F); and (3) Re-ReO_2 loss during ultrasonic cleaning and polishing, followed by smearing on the surface of samples, as our experimental dwell temperature is lower than the melting point of the mixture of Re and ReO_2 (Figure 2.1C).

2.3.3. Apatite trace element composition

Apatites in ClAp experiments have lower REE concentrations than apatites in FlAp and OHAp experiments (Figure B4; Table B3), consistent with the experimental observation described in Fleet et al. (2000a), which found that compared with FlAp and OHAp, ClAp shows about two orders of magnitude lower REE uptake. Different degrees of negative Eu anomalies are observed, and the Eu anomalies are higher among apatites in ClAp experiments (0.38 – 0.58) than those in FlAp and OHAp experiments (0.22 – 0.32). Energy dispersive spectrometric elemental mapping was conducted for one Mo capsule experiment and one Pt-Re-ReO_2 capsule experiment, using Y as the proxy for REEs. We find no apatite exhibiting obvious elemental zonation (Figure B2).

2.3.4. Oxygen fugacity of experiments

In our experimental design, we attempted to control fO_2 using three different metal buffers, as accurate knowledge of experimental fO_2s is essential to determine the relationship between fO_2 and Eu anomalies in apatites. Previous work suggests experiments with graphite-lined Mo capsules control the oxygen fugacity close to IW-1 (e.g., Dygert et al. 2020), while experiments with a Re + ReO_2 layer may produce an fO_2 ~2 log units above quartz-fayalite-magnetite oxygen buffer (QFM + 2; Fabbrizio et al. 2021; Pownceby and O'Neill 1994). If effective, a Cr metal buffer should produce an fO_2 close to IW-5 (Holzheid and O'Neill, 1995). Rather than assuming our experimental fO_2s are consistent with the metal buffers, we took additional measures to characterize fO_2s for several reasons: (1) the temperature and pressure range recommended for empirical formulas in Pownceby and O'Neill (1994) and Holzheid and O'Neill (1995) differ from the experimental conditions in this study; (2) in Holzheid and O'Neill (1995) the buffer is Cr-Cr_2O_3, while in our experimental products, the Cr metal forms multiple chromium carbide layers, corresponding to different chromium carbide structures (Figure B3D to B3F). The chromium concentration gradually increases from the rim to the core, but no chromium oxide is observed; (3) in the Pt-capsule samples packed with a layer of Re-ReO_2, the presence of ReO_2 after the experiment was impossible to verify, as most of the Re and/or ReO_2 powder remaining in the experiment fell out of the charges during sectioning and polishing (Figure 2.1E).

To address these ambiguities, we used the EMP to analyze the Pt capsules and Pt wires in the experimental run products (Table 2.3). We calculated the fO_2 from the concentration of Fe in the Fe-Pt alloy according to Eq. (2.1), based on the method described in Médard et al. (2008):

Table 2.4. Calculated oxygen fugacities for experiments based on Pt-Fe alloy compositions.

Run	Conditions									fO_2		
	T (ºC)	Attempted buffer	n[a]	Fe (wt.%)	Pt (wt.%)	Total (wt.%)	X_{Fe}^{alloy}	X_{Pt}^{alloy}	X_{Fe}^{Melt}	logfO_2	ΔIW	ΔFMQ
FlAp-8	1100	Cr	6	69.15	26.9	96.05	0.90	0.10	0.15	-13.65	IW-0.73	FMQ-4.91
σ[b]				1.16	1.17		0.004	0.004	0.003	0.02	0.02	0.02
FlAp-9	1050	Mo	6	63.49	34.4	97.89	0.87	0.13	0.21	-13.88	IW-0.22	FMQ-4.48
σ				2.08	2.3		0.011	0.011	0.001	0.04	0.04	0.04
OHAp-7	1100	Re+ReO_2	6	4.13	93.05	97.18	0.13	0.87	0.22	-9.82	IW+3.10	FMQ-1.07
σ				0.62	1.77		0.011	0.011	0.003	0.13	0.13	0.13
FlAp-7	1100	Re+ReO_2	5	3.57	93.07	96.64	0.12	0.88	0.18	-9.95	IW+2.97	FMQ-1.21
σ				0.07	1.08		0.012	0.012	0.002	0.02	0.02	0.02
ClAp-5	1100	Re+ReO_2	6	4.07	91.38	95.45	0.13	0.87	0.17	-10.04	IW+2.88	FMQ-1.30
σ				0.53	1.57		0.008	0.008	0.001	0.10	0.10	0.10

[a.] Numbers of EMP analyses.

[b.] The σ takes into account analytical uncertainties and is calculated through the propagation of uncertainty formula.

$$log_{10} fO_2 = \frac{2}{ln\,(10)}\left[ln\left(\frac{X_{FeO}^{melt}}{X_{Fe}^{alloy}}\right) - ln\left(\gamma_{Fe}^{alloy}\right) + ln\left(\gamma_{FeO}^{melt}\right) - lnK\right] \quad (2.1),$$

where X_{FeO}^{melt} is the mole fraction of FeO in the melt, and X_{Fe}^{alloy} is the mole fraction of Fe in the alloy. Because Fe is zoned in both platinum wires and capsules (Figure B3C), we analyzed the compositions of the platinum rim that directedly contact the experiments. We set the FeO activity coefficient γ_{FeO}^{melt} to 1 as suggested by Médard et al. (2008), and we calculate the activity coefficient γ_{FeO}^{melt} and equilibrium constant K by the empirical formulas in Kessel et al. (2001) and Médard et al. (2008) respectively.

When we analyzed the capsule alloy by EMP, we observed a layer of Pt-Fe-Re alloy at the bottom of the capsule, which forms owing to direct contact of Re metal with the pre-conditioned Pt capsule. Because of the powder loading sequence of the experiments with a Re + ReO_2 layer, there are also small amounts of Re residue in certain areas on the capsule wall, which form an alloy during the experiment (Figure 2.1F). Therefore, the measured points selected for constraining the experimental fO_2 are located in the area directly in contact with the starting material without any intervening Re alloy (e.g., Figures 2.1C and 2.1F). The calculated fO_2 data are reported in Table 2.4. The fO_2 in the experiment with C-lined Mo capsule (FlAp-9) is IW-0.22, close to the fO_2 suggested by previous studies (e.g., Dygert et al. 2014). However, for Cr metal experiments, the fO_2 that we calculated (~IW-0.73) is much more oxidized than the Cr-CrO_2 buffer (Holzheid and O'Neill, 1995). Apparently, the Cr metal was ineffective for controlling the experimental fO_2 and the fO_2 in FlAP-8 is controlled by the pre-conditioning process. In Figure 2.1D, we found a layer of chromium carbide, instead of chromium oxide, formed at the rim of the Cr metal (Figures 2.1D and B3E), perhaps providing a barrier that prevented oxidation of the Cr metal and further reduction of the experiment.

For experiments in Pt capsules with a Re + ReO_2 layer, according to the composition of the Fe-Pt alloy, the experiments exhibit the fO_2s varying from FMQ-1.30 to FMQ-1.07, which are about 3 log units lower than assumed anticipated according to the Re-ReO_2 buffer (e.g., Ertel et al., 2001; Fabbrizio et al. 2021). We analyzed the Fe concentration in the ClAp-5 Pt capsule and found from the inner wall (in direct contact with the initial compositions) to the outer wall (in direct contact with graphite), the concentration of Fe first decreases and then increases, and the composition varies continuously (Figure B3C). The outer wall reflects the alloyed condition after the capsule pre-conditioning process, which is relatively Fe enriched as it occurred under more reduced conditions than the target fO_2, while the inner wall demonstrates the role of the Re-ReO_2 layer, which apparently helped decrease the Fe concentrations close to the inner side by oxidizing Fe initially alloyed in the capsule. After the experiments, we observed and analyzed Re metal within the capsule, but the location where ReO_2 powder had originally placed was vacant (Figure 2.1E). ReO_2 could have been completely consumed during the experiment by oxidation of Fe metal initially alloyed with the Pt capsule, or have been or be lost during ultrasonic cleaning and polishing. If the latter scenario is correct (where ReO_2 still remained in the capsule after the experiment) then the efficacy of the Re-ReO_2 buffer should be reconsidered. In summary, although our attempts to vary the experimental fO_2 using metal buffers were not as effective as we hoped, our efforts produced ~4 orders of magnitude variation in fO_2 among the experiments owing to the different assembly types and conditioning procedures (Table 2.4).

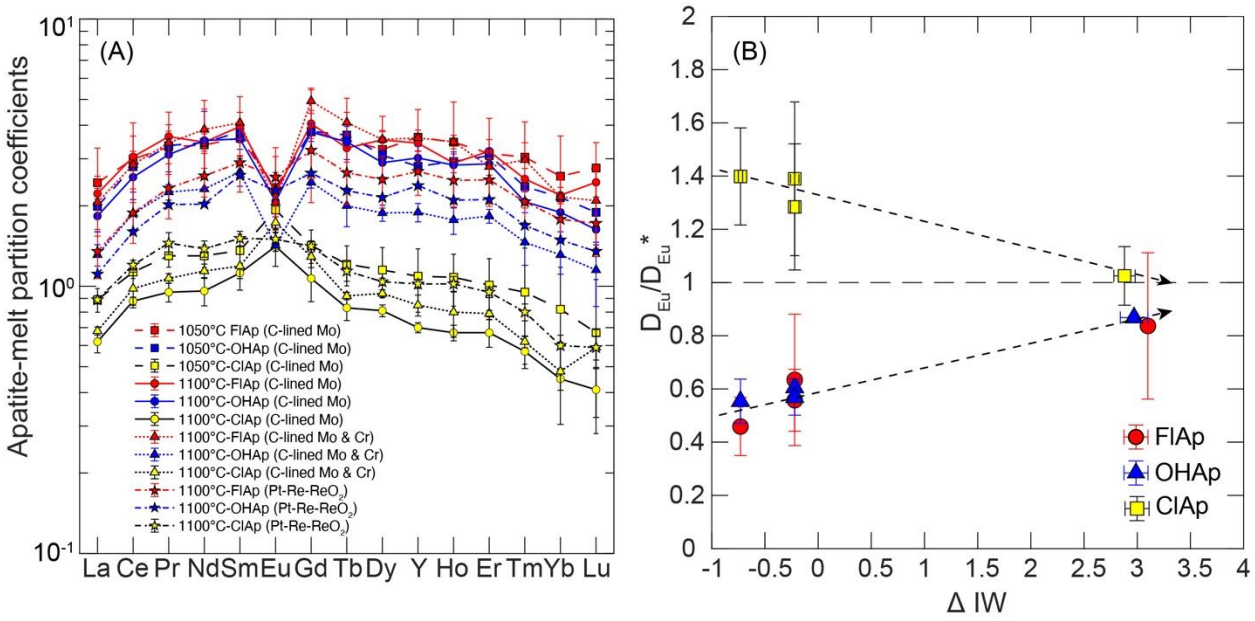


Figure 2.2. (A) apatite-silicate melt partition coefficients, and (B) anomalies of partition coefficient of Eu (D_{Eu}/D_{Eu}*) calculated based on LA-ICP-MS analysis. Red symbols are FlAp experiments, while blue and yellow symbols are OHAp and ClAp, respectively. In Figure 2.2A, solid lines show experiments conducted at higher T and C-lined Mo capsules, dotted lines represent the experiments under higher T and C-lined Mo and Cr capsules, and dash-dotted lines are experiments with Pt-Re-ReO_2 capsules. Lowest T experiments are plotted using dashed lines and low fO_2 experiments are plotted using dotted lines. In Figure 2.2B, the ClAp showed an opposite trend to OHAp and FlAp, as the partition coefficient of Eu^{2+}in ClAp is higher than that of Eu^{3+}, while in FlAp and OHAp the partition coefficient of Eu^{3+} is higher. All uncertainties are calculated by error propagation.

2.3.5. Apatite-silicate melt partition coefficients

Using the trace element concentrations acquired by LA-ICP-MS analysis, we calculate partition coefficients for REEs between apatite and silicate melts (Table 2.3; Figure 2.2). Consistent with the elemental concentrations, the REE partition coefficients of apatites in OHAp and FlAp experiments are similar at a given temperature, and those for ClAp are a factor of two to four lower depending on the experiment (yellow symbols in Figure 2.2A), in agreement with the trend reported in Fleet et al. (2000a). Apatites in ClAp experiments exhibit positive Eu partition coefficient anomalies (D_{Eu}/D_{Eu}^* = 1.03 – 1.40, where D_{Eu}/D_{Eu}^* is defined here as $D_{Eu}/\sqrt{D_{Sm} \times D_{Gd}}$), compared with apatites in FlAp and OHAp experiments (where D_{Eu}/D_{Eu}^* varies from 0.46 to 0.87; Figure 2.2B). It is also worth noting that the partition coefficient of Eu is much less affected by X-site occupancy than other REEs, indicating that the influence of X-site occupancy on trivalent elements is greater than that of divalent elements (Figure 2.2A).

Temperature also apparently affects the partition coefficients, as the experiments show that the lower the temperature, the higher the partition coefficient (Figure 2.2A), as suggested by Watson and Green (1981). In lower fO_2 experiments (C-lined Mo and Cr capsule), the D_{Eu}/D_{Eu}^* becomes more obvious (Figure 2.2B). No systematic effect of fO_2 on partition coefficients of other REEs, including Ce, was observed. The divalent elements show a regular pattern, as the element with the highest partition coefficient is always Ca, and the partition coefficients have no obvious relationship with the anion occupancy (Table 2.3). Discussion of trivalent and divalent substitution mechanisms can be found in Sections 2.4.3.1 and 2.4.3.2.

2.4. Discussion

2.4.1. Insights into cation site occupancies from application of the lattice strain model

Systematic variations of isovalent cation partition coefficients between minerals and melt have been observed in the Onuma diagram as a function of ionic radius (Onuma et al., 1968). This parabolic trend can be effectively described using the lattice strain model (e.g., Brice 1975; Blundy and Wood 1994):

$$D_i^{min-melt} = D_o exp\left[\frac{-4\pi E N_A}{\mathrm{RT}}\left(\frac{r_o}{2}(r_o - r_i)^2 - \frac{1}{3}(r_o - r_i)^3\right)\right] \quad (2.2),$$

where $D_i^{min-melt}$ is the mineral-melt partition coefficient of element *i*; D_o is the strain-free partition coefficient; *E* is the effective Young's modulus; r_o is the ideal ionic radius in Å; r_i is the ionic radius of substituting element, and for apatite predictive models here we choose radius in IX-fold coordination, consistent with the Ca1 site; R is the gas constant; N_A is Avogadro's number and T is the temperature in kelvin.

We use the nonlinear regression method to calculate the lattice strain parameters (D_o, *E*, and r_o) of divalent and trivalent elements of each experiment (Table 2.5). For each parabola, we use at least three partition coefficients of isovalent elements to define the parabola and ensure the partition coefficients do not vary monotonically with the ionic radius, in order to better constrain the ideal radius (r_o). All the divalent elements and trivalent elements, except Eu, display parabolic patterns in nine-fold coordination (e.g., Figure 2.3), supporting the quality of our data. In the apatite structure, there are two Ca sites where REEs can potentially reside, one is seven-fold coordination (Ca2), and the other is nine-fold (Ca1). REE site preference is controversial. The Ca2 preference has been proposed by Borisov and Klevtsova (1963), while Urusov and Khudolozhkin

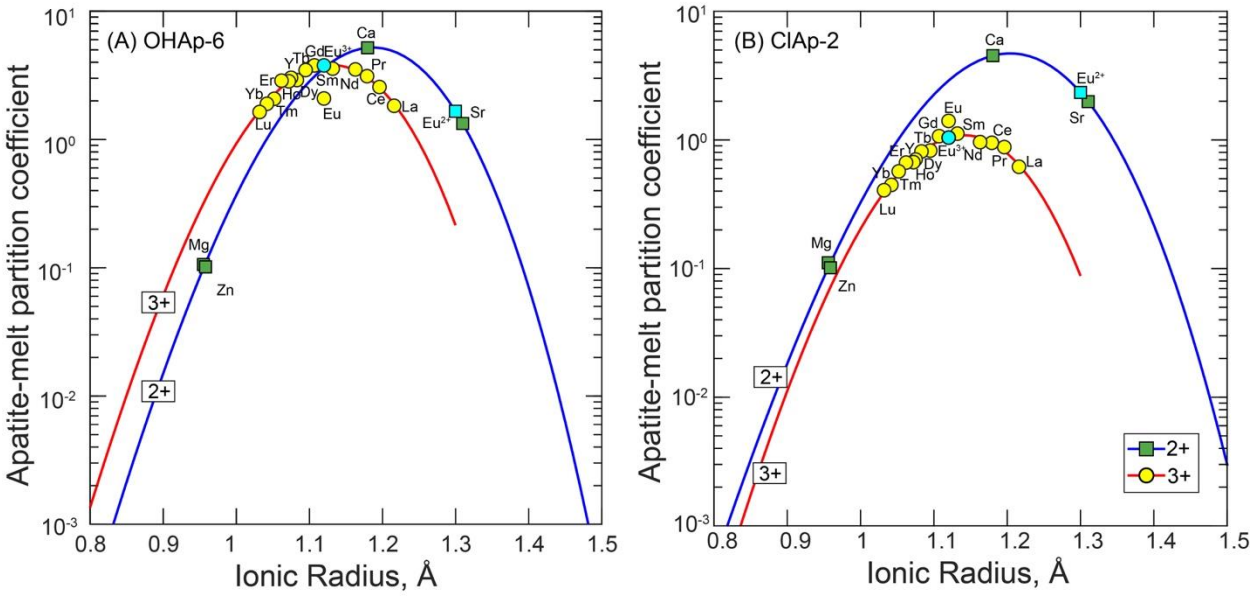


Figure 2.3. Onuma diagram showing measured apatite-silicate melt partition coefficients as a function of ionic radius for divalent and trivalent elements derived from experiments (A) OHAp-6 and (B) ClAp-2. The lattice strain parameters for all experiments in this study can be found in Table 2.5. The partition coefficients of Eu^{2+} and Eu^{3+} predicted by lattice strain model are also plotted, and the values of measured Eu partition coefficient are always between Eu^{2+} and Eu^{3+}.

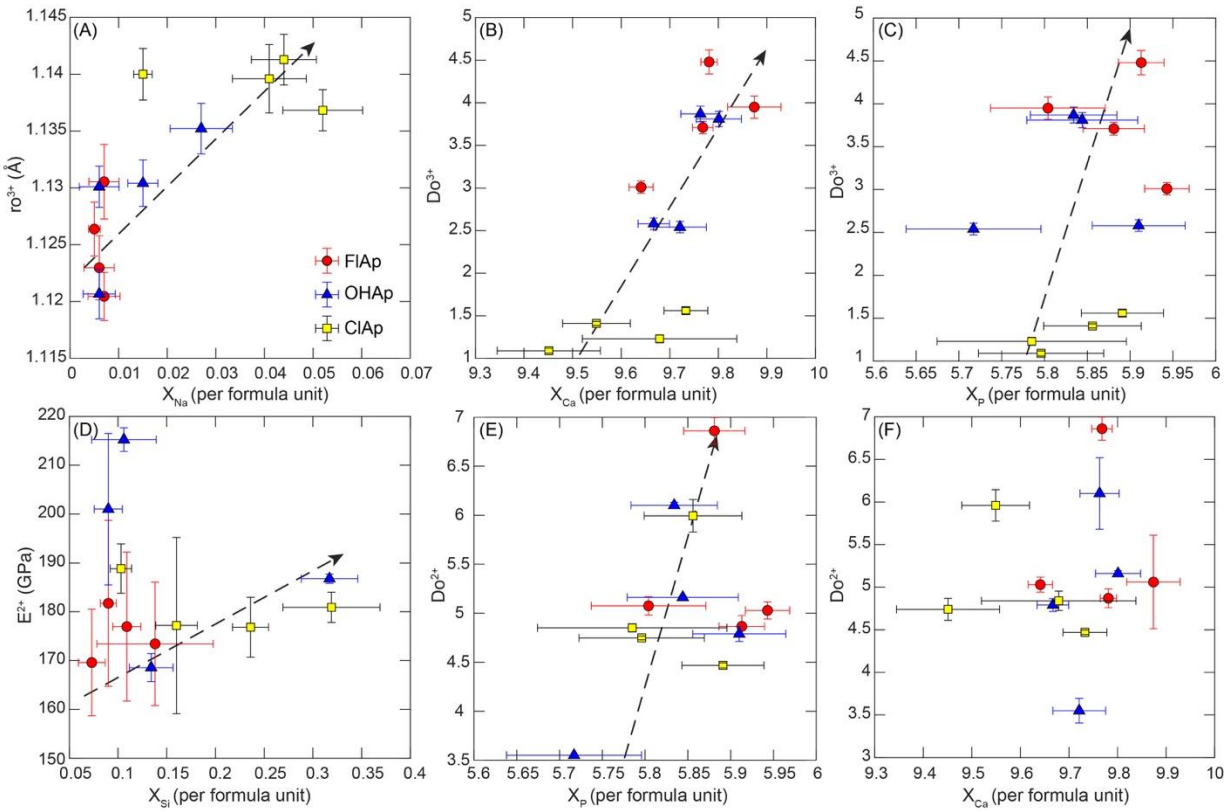


Figure 2.4. Lattice strain terms plotted against selected apatite cation site occupancies for trivalent elements (A) - (C) and divalent elements (D) - (F). All the data can be found in Table 2.5. The trends between lattice strain parameters of trivalent elements and apatite cations fit the substitution mechanisms (2.13) - (2.15), while in (F) the lattice strain parameters of divalent elements are insignificantly affected by $\boldsymbol{X_{Ca}}$, but are controlled by Si and P cations (D-E).

Table 2.5. Lattice strain parameters calculated from experiments in this study calculated using nine-fold ionic radii.

Run	E^{2+} (GPa)	ro^{2+} (Å)	Do^{2+}	E^{3+} (GPa)	ro^{3+} (Å)	Do^{3+}
FlAp-9	177	1.198	6.86	111	1.123	3.71
σ	15	0.004	0.14	13	0.003	0.07
OHAp-1	169	1.182	6.10	203	1.130	3.87
σ	3	0.001	0.03	17	0.002	0.09
ClAp-1	177	1.216	5.99	167	1.137	1.41
σ	18	0.003	0.17	12	0.002	0.02
FlAp-1	173	1.193	5.08	175	1.131	3.95
σ	13	0.004	0.09	24	0.003	0.13
OHAp-6	215	1.187	5.16	242	1.130	3.81
σ	2	0.001	0.01	18	0.002	0.09
ClAp-2	181	1.204	4.75	242	1.141	1.09
σ	3	0.001	0.02	21	0.002	0.03
FlAp-8	182	1.190	4.87	253	1.126	4.48
σ	17	0.006	0.11	25	0.002	0.14
OHAp-5	187	1.189	3.55	224	1.135	2.54
σ	1	0.000	0.00	20	0.002	0.07
ClAp-3	177	1.204	4.85	230	1.140	1.23
σ	6	0.002	0.04	27	0.003	0.04
FlAp-7	170	1.191	5.03	214	1.120	3.01
σ	11	0.004	0.09	19	0.002	0.07
OHAp-7	201	1.195	4.79	229	1.121	2.58
σ	16	0.004	0.08	21	0.002	0.07
ClAp-5	189	1.193	4.47	230	1.144	1.56
σ	5	0.001	0.03	19	0.002	0.04

(1974) argue for Ca1 occupancy. Cockbain and Smith (1967), however, advocate for no preference for REE occupancy in either Ca site in apatite. We developed our models based on nine-fold coordination, since Shannon (1976) did not report seven-fold ionic radii for some REEs, using nine-fold coordination can avoid the errors caused by extrapolating the seven-fold ionic radii and the propagation of related errors in the models. For divalent cations, because Shannon (1976) did not report the radii of IX-coordination Mg and Zn, we extrapolated their radii based on the correlation between eight-fold and nine-fold coordinated ionic radii for other divalent cations (Figure B5).

We find that the ideal ionic radii of trivalent elements (r_o^{3+}) are smaller than divalent elements (r_o^{2+}), which suggests the trivalent elements tend to enter small Ca2 site and divalent elements prefer to substitute into the larger Ca1 site (Figure 2.3; Table 2.5). We note that ClAp experiments exhibit larger ideal radii (1.137 to 1.144 Å; Figure 2.4A) for the trivalent elements (without Eu) compared to those in FlAp and OHAp (1.120 to 1.135 Å; Figure 2.4A; Table 2.5), perhaps suggesting that the REE in ClAp prefer larger Ca1 sites, while FlAp and OHAp enter the smaller Ca2 site. This observation is consistent with previous analysis of experiments conducted by Fleet et al. (2000a), Fleet et al. (2000b), and Fleet and Pan (1997), which used single crystal X-ray measurement to analyze high-temperature synthetic apatite. They calculated the atomic position and isotropic displacement parameters of apatite, which suggested the REEs prefer the Ca2 site in FlAp and OHAp, and the ratio of Ca2 occupancy will decrease with the decrease of ionic radius through the lanthanide series (Pan and Fleet, 2002). Because the radius of Cl^- is larger than that of F^- and OH^- (Shannon, 1976), in ClAp the REE prefer to occupy the Ca1 site (Fleet et al., 2000a), which accommodates proportionally more light-REEs than the Ca2 site, as suggested by higher D_{La} / D_{Yb} in ClAp experiments (1.09 to 1.48) than FlAp and OHAp (0.75 to 1.01).

Because the radii of F^- and OH^- are similar, the REE partitioning behavior of OHAp and FlAp are very similar. The much lower D_o^{3+} in ClAp experiments suggest distortion of the apatite structure (Figure 2.4C), influencing REE substitution owing to the larger anion in the X-site (Fleet et al., 2000a). A similar inference can be made from the lattice site parameters of divalent cations (Table 2.5), but it is not as obvious as in the trivalent parameters.

2.4.2. Calibrating dataset for predictive trace element partitioning models

In order to develop predictive trace element partitioning models for apatite and silicate melts, we compiled the data from previous published experimental studies (Prowatke and Klemme, 2006; Stepanov et al., 2023; Tailby et al., 2023; Watson and Green, 1981), and data from an apatite-melt inclusion partitioning study (Li et al., 2023), in addition to our new apatite-melt experiments. The experimental data we used to develop our predictive models include 29 experiments and 1 apatite-melt inclusion pair for a total of 292 trivalent and 92 divalent partition coefficients. Tailby et al. (2023) recently reported a series of apatite-melt partitioning data at 1 bar. They used five different capsule types in order to evaluate the effect of fO_2 on Eu partitioning from IW to HM buffer. However, they did not mention whether they pre-conditioned their starting materials, which may cause the reaction between the starting material and capsules and thus change the bulk compositions. For this reason we include two of their experiments applying graphite capsules in our compilation (ApREE-09 and ApREE-12; Tailby et al. 2023). The apatite-silicate melt partitioning experiments from Li and Hermann 2017 were not considered here for several reasons: (1) as Li and Hermann 2017 pointed out in the description of their method, the grain sizes of their

apatites are too small (1-5 μm) for single phase analyses by LA-ICP-MS such that the apatite measurements are actually the mixture of apatite and melt. Corrections were applied to remove the glass contribution from the apatite analyses, but the accuracy of the data cannot be guaranteed; (2) the running temperature of their experiments is very low (800 ℃), and their experimental durations were not reported. In this circumstance, it is impossible to evaluate whether apatite is in equilibrium with melt, as zonation may exist in their apatites which were analyzed in bulk; (3) in their experimental results, significant anomalies in the Onuma diagram exist (e.g., C3927, C4049, C4059), suggesting chemical disequilibrium and/or analytical issues.

The compiled data used to parameterize our partitioning models are summarized in the supplementary materials. We compiled as many trivalent (REE+Y) and divalent element (Mg, Zn, Ca, and Sr) partition coefficients as possible, however, we did not consider Ba, because of its low concentration in apatite and correspondingly large analytical uncertainties. All the data we compiled include at least three partition coefficients for elements in the same valence state (Figure 2.3), which is required to establish lattice strain parabolas for individual experiments given the three unknowns in the lattice strain model (Eq. 2.2; Wood and Blundy, 1997).

2.4.3. Predictive trace element partitioning models

2.4.3.1. Trivalent element model

In order to constrain the parameters that can strongly affect the D_o, *E*, and r_o, we considered temperature (Watson and Green, 1981), as well as compositional terms, as candidates. We tested the contribution of these candidate parameters to the overall fitness by simultaneous inversion until we obtained a parameter combination that returned the best overall fitness (e.g., Yao et al. 2012). We used the Pearson's Chi-square below to evaluate the fitting effect as described in Sun and Liang (2012):

$$\chi_p^2 = \sum_{i=1}^{N} \frac{\left(D_i^p - D_i^m\right)^2}{D_i^p} \quad (2.3),$$

where D_i^p and D_i^m are the modeled, and measured mineral-melt partition coefficients of element *i* respectively. The predictive model with the best fitness returns the smallest χ_p^2 value.

Applying the lattice strain model to 292 experimental trivalent element partitioning data (Prowatke and Klemme, 2006; Stepanov et al., 2023; Tailby et al., 2023; Watson and Green, 1981; this study), and 1 apatite-melt inclusion pair from Li et al. (2023), we obtain the following expressions that maximize the quality of the fit:

$$ln{D_o}^{3+} = -194.75(\pm 14.73) + \frac{6.66(\pm 1.46)}{RT} \times 10^4 + 8.10(\pm 0.77)X_{Ca} + 14.16(\pm 1.47)X_{Si} + 18.62(\pm 1.66)X_P \quad (2.4),$$

$$E^{3+}(\text{GPa}) = -2.17(\pm 1.00) \times 10^3 + 417(\pm 170)X_P \quad (2.5),$$

$${r_o}^{3+}(\text{Å}) = 1.134(\pm 0.002) + 0.137(\pm 0.030)X_{Na} \quad (2.6),$$

where X_{si}, X_{Ca}, X_{Na} and X_P are the Si, Ca and P contents in apatite per formula unit (Table 2.2). Values in parentheses are 1σ uncertainties in the model coefficients (see supplementary materials for details). No significant relationship between experimental pressure and lattice strain parameters was observed (Figure B6). Adding more fitting parameters may further improve the quality of the fit (e.g., melt composition terms), but the model we developed fits the measured partitioning data

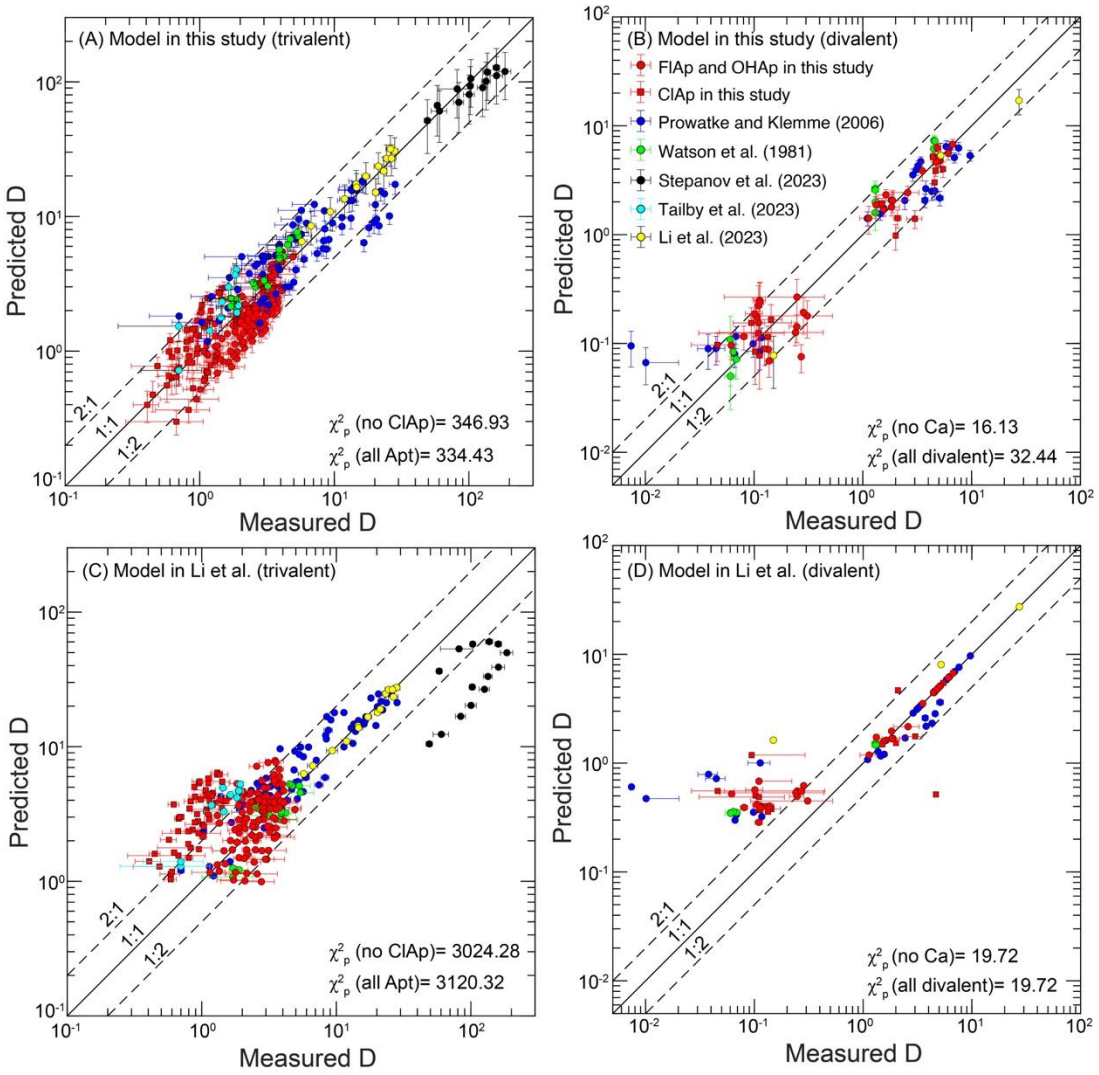


Figure 2.5. Comparison between measured partition coefficients and partition coefficients calculated by Eqs. (2.3), (2.4–2.6) and (2.10–2.12) for trivalent elements and divalent elements by (A-B) our predictive models and (C-D) predictive models in Li et al. (2023). The error bars represent one sigma error, and the calculation details can be found in supplementary materials. Considering the uncertainties, almost all trivalent and divalent elements have been plotted between 2:1 and 1:2 dashed lines by our new predictive models (A-B). The trivalent predictive model (C) cannot reproduce apatites in ClAp experiments (red squares) and apatite in equilibrium at low temperature (black circles) and returns $\boldsymbol{\chi_p^2}$ values about an order of magnitude higher than $\boldsymbol{\chi_p^2}$ values of predictive model in (A), with or without considering the ClAp data. The divalent predictive model (D) shows less bias associated with anionic occupancy, but fails to reproduce Zn and Mg partition coefficients. We note that in (D), the model of Li et al. (2023) returns an apparently lower $\boldsymbol{\chi_p^2}$ than our model, because the model requires inputting the partition coefficient of Ca (perfectly fit elements on the 1:1 line). If we compare the fitness for elements excluding Ca, our model in (B) will return a $\boldsymbol{\chi_p^2}$ value of 16.13, still smaller than 19.72 in (D).

well, and has the advantage of using major element composition of apatite only to reproduce almost all partition coefficients from this study and previous work within a factor of two (Figure 2.5A).

The compositional terms in our predictive model are consistent with the substitution mechanisms proposed in previous studies. The Si, Ca, and P contents in apatite play an important role in the partitioning behavior of REEs in FlAp and OHAp, which can be explained by following two substitution mechanisms (Watson and Green 1981; Chen et al. 2002):

$REE^{3+} + Si^{4+} = Ca^{2+} + P^{5+}$ (2.7),

$2REE^{3+} + [v] = 3Ca^{2+}$ (2.8),

where [v] represents a cation vacancy. The above mechanisms are suggested by correlations between lattice strain parameters in FlAp, OHAp and X_{Ca}, X_P in apatite (Figure 2.4B and 2.4C), that apatite with more Ca sites and higher P concentrations also have higher REE partition coefficients. However, according to the suggestion by Fleet et al. (2000a), a parallel substation mechanism that controls the REE partitioning in ClAp is:

$REE^{3+} + Na^{+} = 2Ca^{2+}$ (2.9),

which can explain the higher Na_2O concentration in ClAp as shown in Figure 2.4A. The relatively low X_{Ca} in ClAp (Figure 2.4B) can be also explained by the mechanism above, as the intake of one REE^{3+} corresponds to expulsion of two Ca cations, higher than the REE^{3+} : Ca^{2+} ratio in Eqs. (2.7) and (2.8).

2.4.3.2. Divalent element partitioning model

Applying the lattice strain model to 92 analyses from 26 experiments (Prowatke and Klemme, 2006; Watson and Green, 1981; this study), and one apatite-melt inclusion pair from Li et al. (2023), we obtain the following expressions that maximize the quality of the fit:

$$ln{D_o}^{2+} = -61.93(\pm16.96) + \frac{6.58(\pm1.52)}{RT} \times 10^4 + 2.54(\pm0.87)X_{Ca} + 3.22(\pm1.78)X_{Si} + 5.57(\pm1.75)X_P \quad (2.10),$$

$$E^{2+}(\text{GPa}) = -2.47(\pm1.23) \times 10^3 + 449(\pm204)X_P + 208(\pm177)X_{Si} \quad (2.11),$$

$${r_o}^{2+}(\text{Å}) = 0.818(\pm0.276) + 0.065(\pm0.047)X_P \quad (2.12),$$

numbers in parentheses are 1σ uncertainties. Consistent with discussion in Li et al. (2023), we found the influence of pressure on the trace element partitioning is relatively insignificant compared to temperature and composition, and therefore we did not add the pressure term in our models (Figure B6).

The substitution mechanism for divalent cations is more straightforward than for trivalent ions (e.g., Pan and Fleet, 2002). As the same valent state with Ca^{2+}, divalent cations will substitute the Ca site directly:

$M^{2+} = Ca^{2+}$ (2.13).

However, direct exchange between the divalent element and Ca cannot explain the partitioning behavior we observed in entirety, otherwise the content of all divalent elements in apatite with higher Ca content would be higher (Figure 2.4F). This complexity was pointed out in the elemental diffusion study of apatite by Cherniak and Ryerson (1993). Since the radii of Ca1 and Ca2 sites are distinct (1.18Å and 1.06Å, respectively; Shannon 1976), the preference for divalent cation substitution for the specific lattice site must be considered.

The divalent cations that we evaluated prefer to enter larger Ca1 sites according to our predictive model (Figure 2.3). In previous studies, strontium has been considered to primarily occupy the Ca2 site (e.g., Hughes et al. 1991), but Sudarsanan and Young (1980) suggested the

Ca2 preference will decrease as the concentrations of Sr in apatite increase. Experimental work indicates Mg prefers to enter Ca1 sites and can be exchanged with REE (Ito, 1968). Likewise, as the major substituting ion for REE, the predictive partitioning of Ca^{2+} needs to combine the trivalent mechanisms above, as more Ca in apatite can facilitate Eqs. (2.7)-(2.9). Anion site occupancy will also affect the divalent cation partitioning, as Cl^- is larger than F^- and OH^-, the Ca2 substitution of divalent cations will be restricted in ClAp, by distorting or shrinking the Ca2 site (Figure B1). It can be seen that the overall structure of apatite and the combined contribution of several mechanisms, rather than merely considering Ca cation in the structure, contribute to the substitution of divalent cations. In view of this, we added X_P and X_{Si} to improve the quality of the fit. Covariation of these terms with lattice strain parameters for divalent element (Figures 2.4D and 2.4E) suggests they may significantly contribute to divalent element partitioning, in addition to X_{Ca}, or perhaps these elements represent a proxy for structural changes that affect divalent element partitioning.

2.4.3.3. Comparison with another predictive model

A recent study developed an apatite trace element partitioning model and a Eu-in-apatite oxybarometer (Li et al., 2023). Their models are calibrated using partition coefficients between FlAp and alkaline melts in natural samples, with no ClAp data in their dataset. All of their models, including the divalent predictive model, trivalent predictive model and Eu-in-apatite oxybarometer, require knowledge of the melt composition in equilibrium with the apatite, limiting its application to magmatic (and excluding application to subsolidus) processes. We used their trace element predictive models to reproduce our experimental results (Figures 2.5C and 2.5D) and the results show a scattered distribution with a systematic overestimation of REE partition coefficient of all ClAp and underestimation of apatite equilibrium at low temperature (800 °C; Stepanov et al. 2023; Figure 2.5C). Their divalent model fails to reproduce almost all Mg and Zn data (Figure 2.5D). We calculated Pearson's Chi-square for models by Eq. (2.3). The χ_p^2 of each model is reported in Figures 2.5C and 2.5D. Our trivalent predictive model shows about an order of magnitude smaller χ_p^2 values with or without the ClAp data. We note that when we compare χ_p^2 values of divalent models, we must recalculate the χ_p^2 value of our model by removing the Ca in Figure 2.5B, because the predictive model in Li et al. (2023) requires the input of the Ca partition coefficient between apatite and silicate melt, such that the fit of Ca is always apparently perfect. After the re-calculation excluding Ca, the χ_p^2 of our divalent model is 16.13, in contrast to 19.72 using the model of Li et al. (2023).

We believe our model produces an improved fit to the data because: (1) in their predictive model, Li et al. assumed two lattice strain parameters ($r_o{}^{3+}$ and E^{3+}) are constants, which is acceptable for FlAp and OHAp because of their similar anion radii, but not for ClAp which has larger anion radius (Shannon, 1976). As discussed in Section 2.4.3.1, different apatite X-site occupancy and cation species can both affect the substitution mechanisms and the Ca site preference, thereby modifying $r_o{}^{3+}$ and E^{3+}; (2) the predictive model of Li et al. (2023) is based on temperature and the composition of the silicate melt, but the melt composition can't directly reflect the differences in apatite structure, or coupled substitution mechanisms that produce differences in partitioning in FlAp and ClAp-bearing systems.

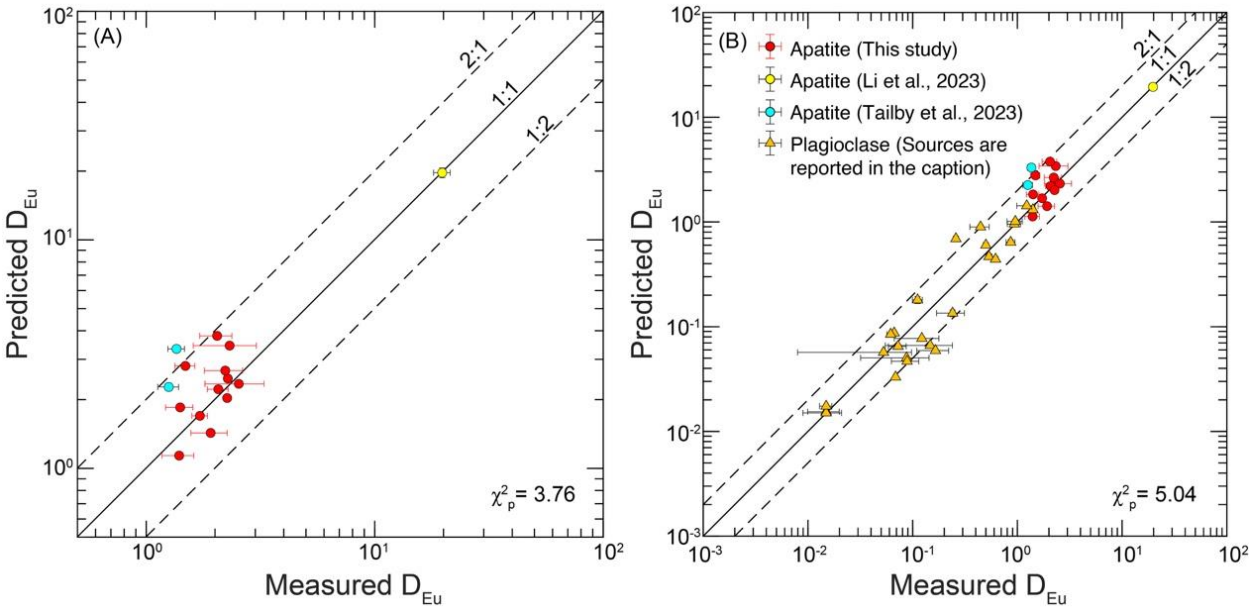


Figure 2.6. Comparison between measured and predicted partition coefficients of Eu. (A) D_{Eu} predictions calculated using a model calibrated only using the partition coefficient between apatite and silicate melt (Eqs. 2.15, 2.16); predictions shown in (B) are calculated using an equilibrium constant constrained using apatite-melt and plagioclase-melt partitioning data (Eqs. 2.18, 2.19). Plagioclase data are the calibrating dataset from Dygert et al. (2020), and include Sun et al. (2017), Aigner-Torres et al. (2007), Bindeman and Davis (2000), Tepley III et al. (2010), McKay et al. (1994) (Table B5).

2.4.3.4. Eu anomalies and Eu in apatite-plagioclase oxybarometer

Due to the strong dependence of the valence state of middle REE Eu on oxygen fugacity, Eu fractionation can provide a reliable method to probe fO_2 of a magmatic system (e.g., McCanta et al. 2009; Wadhwa 2001). This is supported by our experimental results which demonstrate the more oxidized the fO_2, the closer the partition coefficient of Eu is to the Eu^{3+} partition coefficient and the closer D_{Eu}/D_{Eu}^* is to 1 (Figure 2.2B). For FlAp and OHAp, however, the divalent Eu has lower partition coefficients than trivalent Eu, causing the overall trend opposite to ClAp experiments (Figure 2.2B). Regardless of the anion occupancy, the ratio of Eu^{2+} to Eu^{3+} in apatite is closely related to the fO_2, such that here, we develop an fO_2-dependent Eu partitioning model.

Eu partitioning between apatite and silicate melts involves both divalent and trivalent Eu. We express the Eu species in the melt by the following reaction (e.g., Drake 1975):

$$Eu^{3+}O_{1.5} = Eu^{2+}O + \frac{1}{4}O_2 \quad (2.14).$$

Here we define a constant K_{melt}^{apt} to represent the heterogeneous equilibrium for the silicate melt in equilibrium with apatite. The partition coefficient of Eu between apatite and silicate melt can be expressed as the function of K_{melt}^{apt}, fO_2, and the partition coefficient of Eu^{2+} and Eu^{3+} in apatite (e.g., Dygert et al. 2020; Mallmann et al. 2021):

$$D_{Eu}^{apt} = \frac{K_{melt}^{apt} \times D_{Eu^{2+}}^{apt} + D_{Eu^{3+}}^{apt} \times (fO_2)^{\frac{1}{4}}}{K_{melt}^{apt} + (fO_2)^{\frac{1}{4}}} \quad (2.15),$$

where $D_{Eu^{2+}}^{apt}$ and $D_{Eu^{3+}}^{apt}$ are partition coefficients of Eu^{2+} and Eu^{3+} between apatite and silicate melts that can be calculated by our predictive models in Sections 2.4.3.1 and 2.4.3.2. Through fitting compiled experimental and natural apatite-melt partitioning data (see Section 2.4.2), we determined the K_{melt}^{apt} by nonlinear least squares regression:

$$K_{melt}^{apt} = 6.22 \times 10^{-4} \pm 9.62 \times 10^{-5} \quad (2.16).$$

By applying the K_{melt}^{apt} value, we can calculate the D_{Eu} and compare the results with measured partition coefficients in this study, Li et al. (2023), and Tailby et al., (2023) (Figure 2.6A). Considering the analytical and model uncertainties, our calculations show a good agreement between the experimental and predicted D_{Eu} at the relevant fO_2.

Through rearranging the Eq. (2.15), we obtain a new equation that enables us to calculate fO_2 by K_{melt}^{apt}, predicted $D_{Eu^{2+}}^{apt}$ and $D_{Eu^{3+}}^{apt}$ (Eqs. 2.4-2.6 and 2.10-2.12), and D_{Eu}^{apt} acquired directly from analysis:

$$\log fO_2 = -4 \times log\left(\frac{D_{Eu^{3+}}^{apt} - D_{Eu}^{apt}}{K_{melt}^{apt} \times \left(D_{Eu}^{apt} - D_{Eu^{2+}}^{apt}\right)}\right) \quad (2.17).$$

We note application of Eq. (2.17) is meaningless if the predicted $D_{Eu^{2+}}^{apt}$ and $D_{Eu^{3+}}^{apt}$ are higher or lower than measured D_{Eu}^{apt} (e.g., Dygert et al. 2020). Because the difference between $D_{Eu^{2+}}^{apt}$ and $D_{Eu^{3+}}^{apt}$ is usually not significant (Figure 2.3), the impact of uncertainties in measurement of the Eu partition coefficient strongly affects the accuracy of the oxybarometer. This was also observed by Tailby et al. (2023), making the oxybarometer especially difficult to apply in oxidized systems (e.g., Figure 2.7).

Taking advantage of our experimental constraints on the partitioning behavior of Eu in apatite, and a published model for Eu partitioning in plagioclase (Dygert et al 2020), we developed a Eu

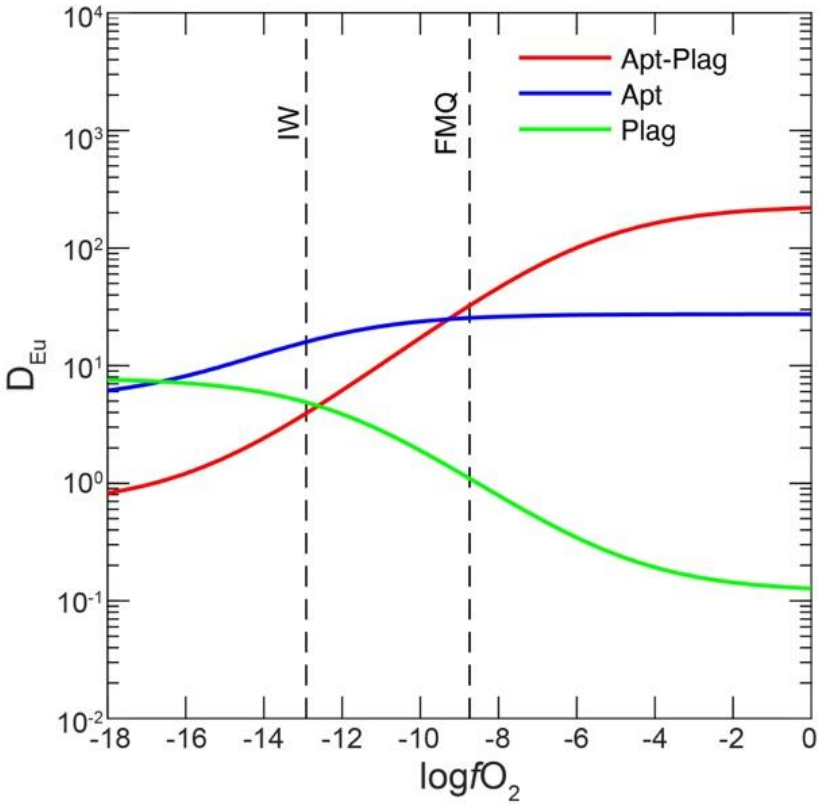


Figure 2.7. The partition coefficient of Eu as a function of predictive oxygen fugacity for Eu-in-apatite (Eq. 2.17), Eu-in-plagioclase and Eu in apatite-plagioclase (Eq. 2.18) based on coexisting apatite and plagioclase from winonaite HaH 193 (Table B6). The slope of the apatite-plagioclase partitioning behavior is much steeper than that of apatite, making Eu in apatite-plagioclase partitioning behavior sensitive to the fO_2 change and effective as a mineral-mineral oxybarometer.

in apatite-plagioclase oxybarometer (red line, Figure 2.7). Underlying assumptions are that both phases are saturated in the system and they are in equilibrium. Thus, the equilibrium constant of Eq. (2.16), which defines the Eu speciation in coexisting liquid in the system as a function of fO_2, should be the same for both apatite and plagioclase. Given the very limited amount of experimentally constrained coexisting apatite and plagioclase data, and observation that our calculated K_{melt}^{apt} (Eq. 2.16) is similar to value of K_{melt}^{plag} reported in Dygert et al. (2020), we utilized apatite-silicate melt and plagioclase-silicate melt partitioning data from different experiments and developed a model to fit them simultaneously. We compiled the Eu partitioning data from 15 experiments and an inclusion-host pair (Li et al., 2023, Tailby et al., 2023, and this study), and 25 plagioclase data (Aigner-Torres et al., 2007, Bindeman and Davis, 2000, Dygert et al., 2020, Tepley III et al., 2010, McKay et al., 1994, Sun et al., 2017, and this study; Table B5), to fit the K value for both minerals simultaneously. The relationship between fO_2 and $D_{Eu}^{apt-plag}$ can be expressed as:

$$D_{Eu}^{apt-plag} = \frac{\left(K \times D_{Eu^{2+}}^{apt} + D_{Eu^{3+}}^{apt} \times (fO_2)^{\frac{1}{4}}\right)}{\left(K \times D_{Eu^{2+}}^{plag} + D_{Eu^{3+}}^{plag} \times (fO_2)^{\frac{1}{4}}\right)} \quad (2.18),$$

where $D_{Eu^{2+}}^{plag}$ and $D_{Eu^{3+}}^{plag}$ are partition coefficients of Eu^{2+} and Eu^{3+} between plagioclase and silicate melt that can be calculated by predictive models in Sun et al. (2017). By nonlinear least squares regression, we determined the K as:

$$K = 6.17 \times 10^{-4} \pm 5.72 \times 10^{-5} \quad (2.19),$$

which is very close to the value obtained from apatite data (Eq. 2.16) or plagioclase-melt data (Dygert et al., 2020) alone. Applying this K value, we successfully reproduce almost all D_{Eu} of plagioclase and apatite (Figure 2.6B). After the rearrangement of Eq. (2.18), we can calculate the fO_2 of the mineral-mineral system by:

$$\log fO_2 = 4 \times log\left(\frac{K\left(D_{Eu}^{apt-plag} \times D_{Eu^{2+}}^{plag} - D_{Eu^{2+}}^{apt}\right)}{\left(D_{Eu^{3+}}^{apt} - D_{Eu}^{apt-plag} \times D_{Eu^{3+}}^{plag}\right)}\right) \quad (2.20),$$

where $D_{Eu}^{apt-plag}$ is the measured Eu distribution between the two phases. The new apatite-plagioclase oxybarometer reveals more variation between fO_2 and $D_{Eu}^{apt-plag}$ than the Eu-in-apatite oxybarometer, and is more sensitive than the Eu-in-plagioclase oxybarometer in the relatively reduced environment (Figure 2.7), making it applicable in a variety of natural systems.

Because predictive partitioning models for plagioclase and apatite are only sensitive to the composition of the crystalline phase, in order to apply this apatite-plagioclase oxybarometer, we only need to analyze the major and Eu concentrations in coexisting apatite and plagioclase that are in equilibrium. After measuring the apatite-plagioclase Eu partition coefficient, Eu^{2+} and Eu^{3+} partition coefficients calculated by models in this study and Sun et al. (2017), we then calculate the fO_2 of the magmatic system using Eq. (2.20). As an experimental test of our new oxybarometer, we calculated the apatite-plagioclase pair in our experimental product (OHAp-1). The calculated $\log(fO_2)$ is -13.9 at 1050 °C, which is consistent with the $\log(fO_2)$ value that we determined by the Fe-Pt alloy in a wire sensor in the experiment under the same experimental condition (-13.9; Table 2.4; Figure B7).

Although the model is parameterized using mineral-melt partitioning data, lacking any melt composition terms, it can be extrapolated to subsolidus systems. As a preliminary application, we calculated the fO_2 in a coexisting apatite-plagioclase pair from a winonaite Hammadah al Hamra

193 (HaH 193; data from Floss et al. 2007 and Floss et al. 2008). We assume the equilibrium temperature is ~1100 ℃ as suggested by two pyroxene thermometry to Winona (Benedix et al., 2005; Kretz, 1982), and a pressure of 100 bars. The log(fO_2) we calculate by Eq. (2.20) is -14.9 at 1100 ℃ (IW-1.6, close to the fO_2 range from IW-3.0 to IW-2.0 suggested by previous research (e.g., Wadhwa 2008). As an application to a more oxidized system, we investigated 5 pairs of coexisting apatite-plagioclase from Sept Iles Intrusive Suite (Kieffer et al., 2023). We assume the equilibrium temperature is 1050 ℃ based on the estimated temperature of megacyclic unit I (MCU I) residual liquid after the crystallization of apatite-rich layer (Namur et al., 2011). Assuming a pressure of 100 bars, the calculated log(fO_2) varies from -10.3 to -9.6 (FMQ-0.1 to FMQ+0.6), in agreement with suggestion of Namur et al. (2010) that most of the Sept Iles layered intrusion crystallized under the fO_2 close to the FMQ buffer. The major and trace element data we used in the calculation are compiled in Table B6.

2.5. Application and Implication

2.5.1. Kinetic fractionation of divalent and trivalent Eu during subsolidus reequilibration and its effect on Eu in apatite-plagioclase oxybarometer

The Eu in apatite-plagioclase oxybarometer that we developed in Section 2.4.3.4 takes advantage of differences in the partitioning behavior of Eu^{2+} and Eu^{3+} between minerals to quantify fO_2. An important aspect to consider is the response of the oxybarometer to cooling. Specifically, if a sample is in equilibrium and then quenched or cooling very fast, the fO_2 can be recorded accurately by oxybarometer. However, if the sample cools slowly, or experiences subsolidus reequilibration, then the Eu will be redistributed according to the partition coefficients and diffusion rates of Eu^{2+} and Eu^{3+} between apatite and plagioclase. If we do not correctly evaluate the temperature at which the new equilibrium is established, then applying oxybarometer may lead to misleading results. Previous studies suggest the diffusion rate of Eu^{2+} is several orders of magnitude faster than Eu^{3+} in FlAp and plagioclase (e.g., Cherniak and Watson 1992; Cherniak 2003; Cherniak 2010). This difference in diffusion rate has the potential to produce kinetic fractionation, as Eu^{2+} can approach the new equilibrium much faster than Eu^{3+}, and thus affect the prediction of our oxybarometer under unbuffered disequilibrium conditions. Due to the lack of data on the diffusion of trace elements in ClAp and the similarity in mineral structures between FlAp and OHAp, the following calculations are relevant to Eu fractionation between FlAp/OHAp and plagioclase.

We evaluate the effect of kinetic fractionation of Eu on oxybarometric determinations in a forward model. We made the following simplifying assumptions: (1) Eu^{3+} and Eu^{2+} diffuse through a one-dimensional apatite-plagioclase pair; (2) the system is closed and unbuffered. It is only composed of apatite and plagioclase, and the grain size ratio of minerals equals the mass proportions of minerals; (3) flux is conserved at the apatite-plagioclase interface, and the interface always maintains equilibrium partitioning; (4) there is no flux at far side boundary of the minerals; (5) because the Eu^{2+} diffusion in plagioclase is approximately higher by nine orders of magnitude higher than Eu^{3+} (at 900 ℃), we assume diffusion of Eu^{2+} in plagioclase is instantaneous; (6) although the new equilibrium is established at a lower temperature, we assume that one ignores the elemental redistribution caused by temperature reduction and still considers that apatite and plagioclase reach equilibrium at the initial temperature, and use this to calculate the partition

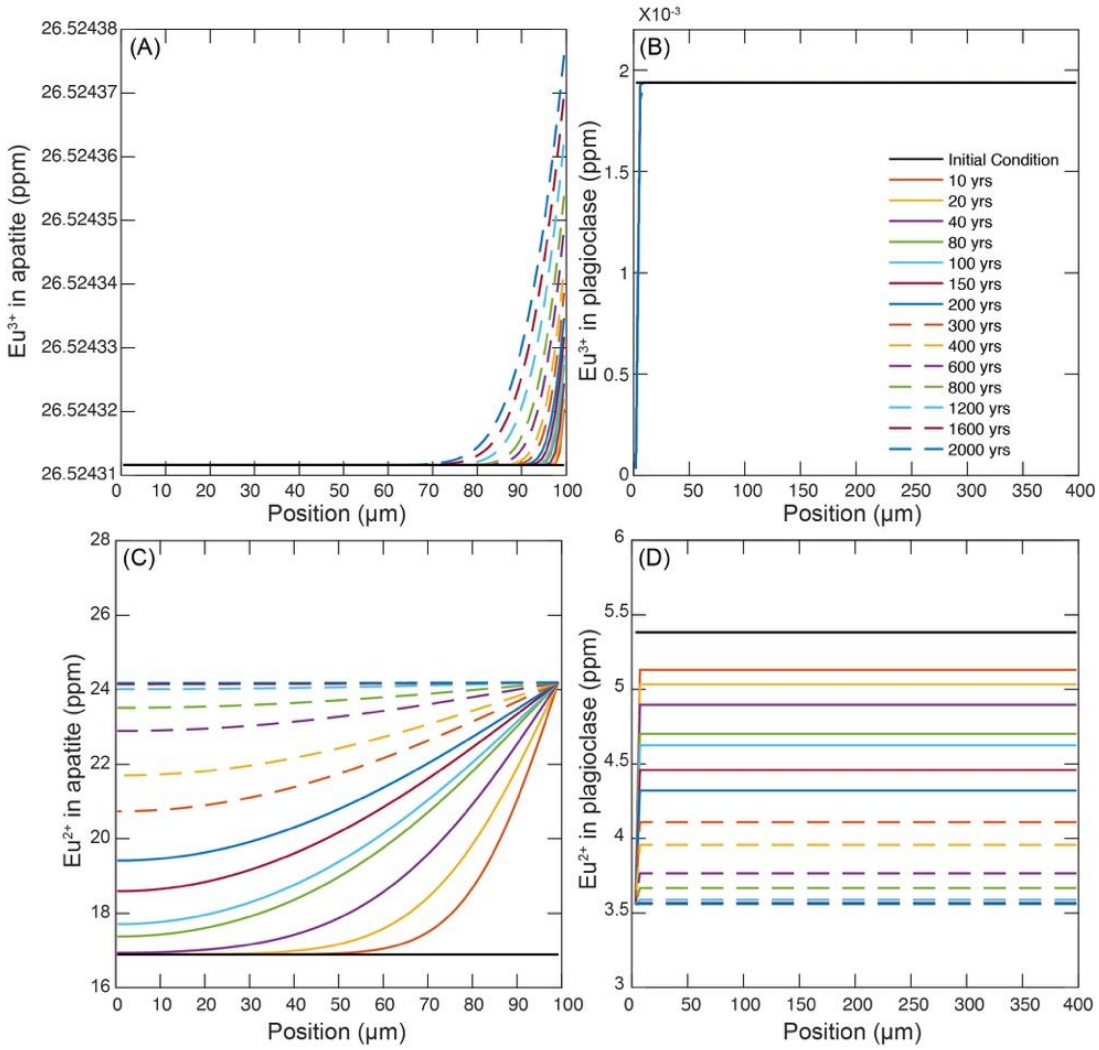


Figure 2.8. Calculated diffusion profiles for (A-B) Eu^{3+} and (C-D) Eu^{2+} between apatite and plagioclase at 14 selected times during subsolidus reequilibration simulations. The apatite ($\boldsymbol{L_{apt}}$=100 μm) and plagioclase ($\boldsymbol{L_{plag}}$=400 μm) initially are in equilibrium at 1100 ℃, and the system instantaneously cools to 900 ℃ (subsolidus temperature) which triggers the reequilibration.

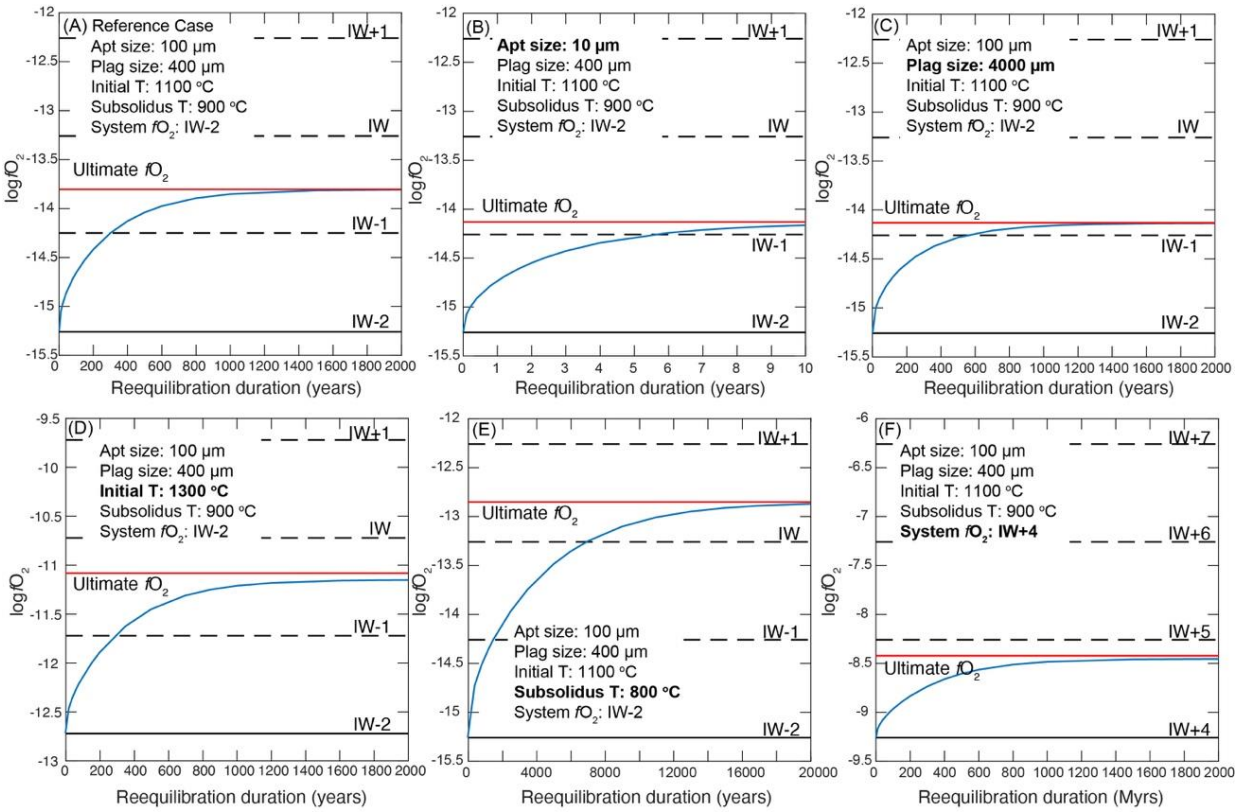


Figure 2.9. Figures illustrating the effect of grain size of plagioclase and apatite, initial temperature, subsolidus temperature and fO_2 of the system to our oxybarometer during subsolidus reequilibration. Here we assume (A) the apatite grain is 100 μm, the plagioclase grain is 400 μm, the initial temperature is 1100 °C, the subsolidus temperature is 900 °C, and the fO_2 of the system is IW-2. Then we varied one parameter each time relative to Figure 2.9A to test the effect: (B) the apatite grain is 10 μm; (C) the plagioclase grain is 4000 μm; (D) the initial temperature is 1300 °C; (E) the subsolidus temperature is 800 °C; and (E) the fO_2 of the system is IW+4.

coefficients for Eu^{2+} and Eu^{3+}, which leads to discrepancies between the calculation and the actual fO_2. The major and trace element concentrations of apatite used in the modeling are from lunar granulite 79215 (Treiman et al., 2014). We calculate the Eu^{2+} concentration in the plagioclase (except for the boundary) by mass balance:

$$C_{plag}^{Subsolidus} = \frac{C_{Bulk}^{Subsolidus}}{\phi_{apt} \times D_i^{apt-plag} + \phi_{plag}} \quad (2.21),$$

where $C_{Bulk}^{Subsolidus}$ is the bulk concentration, ϕ_{plag} and ϕ_{apt} are the mass proportions of the two minerals in the system, which we approximate here by mineral grain size proportions, $D_i^{apt-plag}$ is the partition coefficient of element *i* between apatite and plagioclase, $C_{plag}^{Subsolidus}$ is the elemental concentration of the element in plagioclase at subsolidus temperature.

In a reference model, we assume the apatite (L_{apt}=100 μm) and plagioclase (L_{plag}=400 μm) at first in equilibrium at 1100 ℃ and record the fO_2 of the system at an initial fO_2 of IW-2 (the same initial fO_2 is used in all simulations). Then the temperature of the system instantaneously decreases to 900 ℃. The diffusive concentration profiles are solved numerically using a finite difference method and are given in Figure 2.8. The modeling method and related equations are described in Yao and Liang (2015) and Zhang (2009). We take the average Eu concentration along the profile as the analyzed mineral Eu concentration and calculated the fO_2 of the system by our Eu in apatite-plagioclase oxybarometer to evaluate the effect produced by subsolidus reequilibration (Figure 2.9). We use the mass balance equation and the subsolidus temperature to calculate the Eu^{2+} and Eu^{3+} concentrations in apatite and plagioclase when reequilibration is completed, and we mark the calculated fO_2 at this time as the ultimate fO_2, which is the artifact of mistakenly assuming an elevated (magmatic) temperature rather than a subsolidus temperature (red lines in Figure 2.9).

As shown in Figure 2.8, the Eu^{2+} between apatite and plagioclase reaches a new equilibrium after ~1000 years of diffusion, while the Eu^{3+} takes much longer, especially in plagioclase. However, because the Eu^{3+} concentration in plagioclase is much lower than in apatite, Eu^{3+} variations in both apatite and plagioclase are limited, which makes the exchange of Eu^{3+} between apatite and plagioclase negligible. This can be further demonstrated by our calculation that after ~1000 years, the calculated fO_2 is close to the ultimate fO_2 which is about 1.45 log units more oxidized than the initial fO_2 of the system (Figure 2.9A). In other words, the diffusion of Eu^{2+}, instead of Eu^{3+}, controls the fO_2 variation after the reequilibration relative to a buffer (in addition to the temperature assumption).

We then varied the grain size of plagioclase and apatite respectively (Figures 2.9B and 2.9C). The results suggest that because the diffusion rate of Eu^{2+} in plagioclase is rapid, changing the plagioclase size will not cause any obvious effect on reequilibration timescale, and the larger plagioclase can reduce the fO_2 deviation after the subsolidus reequilibration by decreasing the significant Eu changes caused by apatite (Figure 2.9C). For apatite, however, the one order of magnitude smaller grain will bring two orders of magnitude shorter reequilibration time (Figure 2.9B). Smaller apatite grains will make the reequilibration effect less pronounced.

We then tested the effect of the cooling path by modifying the initial and subsolidus temperatures (Figures 2.9D and 2.9E). We found the initial temperatures have a very limited effect on the reequilibration timescale and attainment of ultimate fO_2 (compare Figures 2.9A and 2.9D), but subsolidus temperatures have an enormous impact as 100 ℃ lower subsolidus temperature will generate one order of magnitude longer equilibration timescale, and one log unit further overestimation of fO_2 (compare Figures 2.9A and 2.9E).

According to the calculation above, in an unbuffered system, subsolidus reequilibration during cooling will induce an overestimation of the fO_2 value, if the new equilibrium temperature is not considered. The larger the grain size and the higher proportion of apatite in the system, the more oxidized fO_2 will be provided by the samples that have undergone the subsolidus process, and the longer the time required to achieve reequilibration. The degree of overestimation of fO_2 is mainly controlled by the diffusion of Eu^{2+}, applying the new Eu in apatite-plagioclase oxybarometer in a relatively oxidized system with higher $Eu^{3+}/\Sigma Eu$ can return a more accurate fO_2 (Figure 2.9F). Estimating the accurate subsolidus reequilibration temperature is the key to avoiding the overestimation. Since the diffusivity of Eu^{2+} in apatite governs the reequilibration timescale, future research should focus on developing an apatite thermometer with closure temperature analogous to Eu^{2+} to help calibrate the divergence from the real fO_2.

2.5.2. The volatile budget of lunar magma ocean cumulates

Prior to this study, estimates of the volatile contents of the interior of the Moon were mainly achieved through two approaches: direct measurement of the compositions of lunar rocks and minerals (e.g., Hui et al. 2013; Treiman et al. 2014) and direct measurements of volcanic glass (e.g., Hauri et al. 2011; Hauri et al. 2015) in the returned samples. Nominally anhydrous minerals have very low partition coefficients of volatiles as the volatile can only enter the lattice defects (Bell and Rossman, 1992; Libowitzky and Beran, 2006), resulting in increased concentrations of volatiles in LMO residual liquid as well as late-formed minerals (i.e., apatite; McCubbin et al. 2015b). In apatite, because the X-site can accommodate volatile elements, volatile abundances can be directly measured to characterize a magmatic system. Nonetheless, special care must be taken, as the volatile partition coefficient between apatite and silicate melt varies ($D_F > D_{Cl} > D_{OH}$; McCubbin et al. 2015a); the volatile concentrations in the lunar apatite cannot be directly equated with the volatile concentration in the LMO. In addition, lunar apatites in returned samples may be highly misleading as some might be products of fractional crystallization after apatite saturation, especially for apatites relatively enriched in Cl and OH (Boyce et al., 2014). On the other hand, volatiles are difficult to estimate in volcanic glasses because of the difficulty of quantifying diffusive degassing after eruption (McCubbin et al., 2015b).

We can take advantage of our partition coefficient models to provide an indirect method to evaluate the relative volatile contents during the LMO crystallization, circumventing the complex secondary effects. The slope of the REE partition coefficients across the lanthanides is distinct for ClAp compared to OHAp and FlAp. To explore the consequences of potential apatite species on lunar trace element patterns, we use LMO crystallization sequence in Rapp and Draper (2018) to calculate trace element fractionation during LMO solidification, assuming that the apatite reaches saturation at 97% solidification. The apatite compositions we applied are from two experiments (FlAp-9 and ClAp-1) since our experimental initial composition and fO_2 are highly lunar relevant. We applied our new predictive models to calculate the concentrations of trivalent, divalent element and Eu of apatite during lunar magma ocean solidification. For other minerals, we use the major element concentrations reported in (Rapp and Draper, 2018) to calculate their trace element partition coefficients and the calculation details are the same as Ji and Dygert (2023).

First, we test the scenario that partial melting of late-stage LMO cumulates explains the petrogenesis of lunar KREEP basalt. We simplify the partial melting as the modal fractional

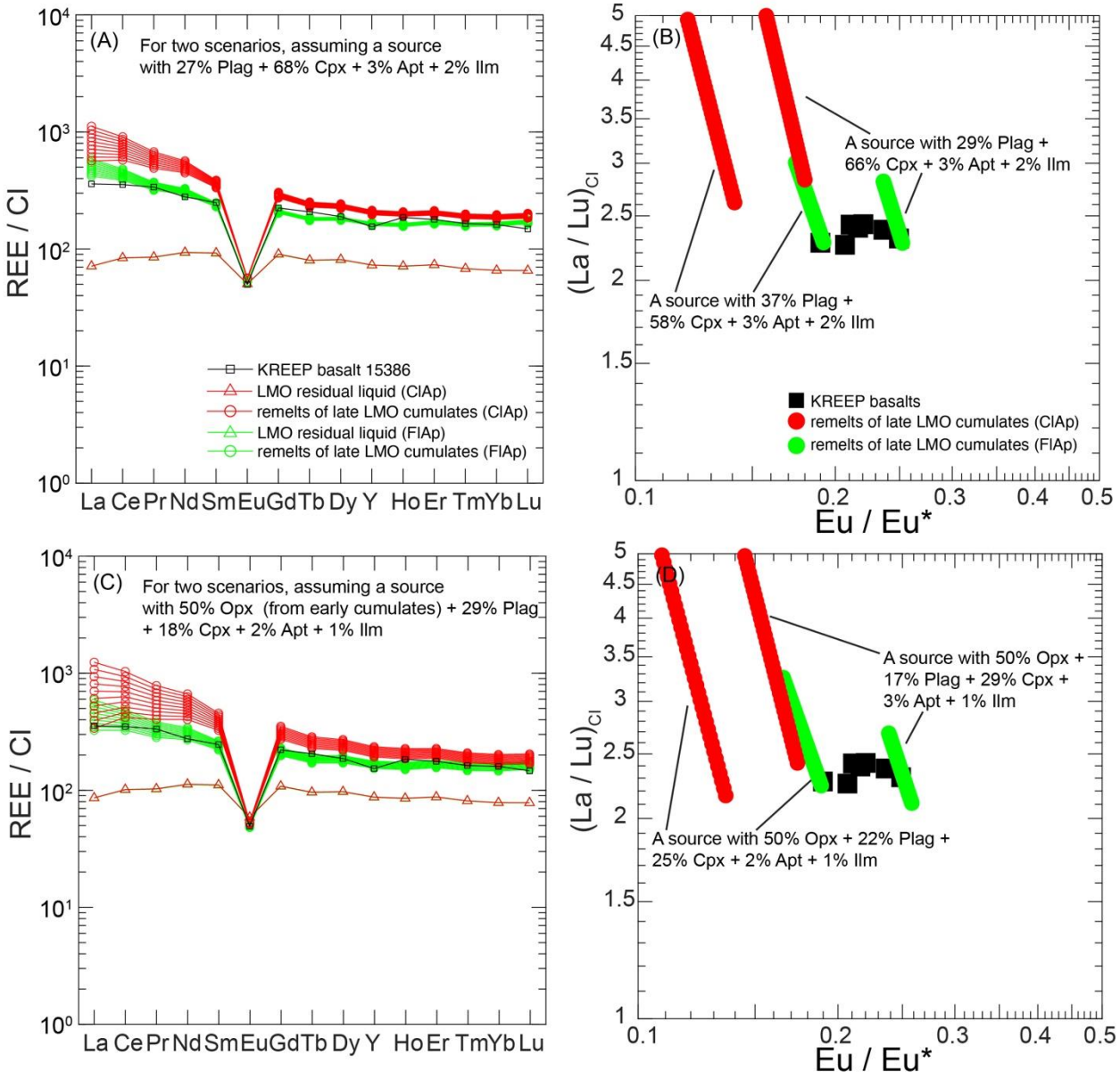


Figure 2.10. (A) Chondrite-normalized REE patterns of residual liquids after 98.9 percent solidification of the LMO, and remelts of late LMO cumulates compared to KREEP basalt 15386 (Neal and Kramer, 2003), and (B) $(La / Lu)_{CI}$ versus Eu / Eu* showing remelts of late LMO cumulates with different source mineral modes and apatite species compared to KREEP basalts (Helmke et al., 1973; Hubbard et al., 1973; McKay et al., 1979; Neal and Kramer, 2003); (C) Chondrite-normalized REE patterns of residual liquids after 90.1 percent solidification of the LMO, and remelts with a source of 50% late LMO cumulates and 50% of early LMO crystallized Opx (PCS=52%; Rapp and Draper 2018) compared to KREEP basalt 15386; (D) $(La / Lu)_{CI}$ versus Eu / Eu* showing remelts of late LMO cumulates with different source mineral modes and apatite species compared to KREEP basalts. Chondrite normalization is from Lodders (2021).

melting and apply the equation from Shaw (1970) to calculate the concentration of element *i* in the incremental liquid:

$$C_L^i = C_o^i \times (1 - F)^{\left(\frac{1}{D_{Bulk}^i - 1}\right)} \quad (2.22),$$

where C_L^i is the concentration of element i in the incremental liquid, C_o^i is the concentration of element i in the source of the KREEP basalt, F is the degree of melting, and D_{Bulk}^i is the bulk partition coefficient of the KREEP basalt source calculated by the weighted average of partition coefficients between mineral and liquid based on assumed mineral modes. The results show that the compositions of the LMO residual liquid are similar under the assumption that different species of apatite are crystallized, but the compositions of the remelts of late LMO cumulates are very different among the apatite species, especially for light REEs (Figure 2.10A). We compare our calculation with KREEP basalts, and observe that the first 5 % of remelting produced when apatites are assumed to be FlAp or OHAp, with a source of 27% plagioclase, 68% clinopyroxene, 3% apatite and 2% of ilmenite, fit the KREEP basalts very well, including their Eu anomalies. However, in ClAp scenario, because of its lower REE partition coefficients, all the REE, especially the light REE, have been overestimated with the same source component (Figures 2.10A and 2.10B). This suggests that the apatite in the late-stage LMO cumulates must be relatively enriched in F^- and OH^- and depleted in Cl^- before any post-cumulate interference.

Based on the higher Mg# of orthopyroxene (Opx) in the Apollo 15 KREEP basalt, previous studies suggested the source of the KREEP basalt should be dominated by early stage LMO crystallized Opx, with plagioclase and variable amount of phosphates and ilmenite (e.g., Taylor et al. 2012; Cronberger and Neal 2017). We tested this possibility and assumed that the source is composed of 50% early LMO crystallized Opx (PCS=52%; Rapp and Draper 2018) and 50% late LMO cumulates, and continued to compare the remelted compositions of the two endmembers scenarios. We found that again, the presence of ClAp in the KREEP basalt source would still cause the overestimation of light REE, which could not explain the petrogenesis of KREEP basalt (Figures 2.10C and 2.10D).

We chose the content of major elements of apatite in the ClAP-1 experiment (69 mol % Cl + 31 mol % OH). Because of the similarity of the partition coefficients of FlAp and OHAp, and the fact that almost all lunar apatites in meteorites and returned samples are closer to the F endmember than the OH endmember (e.g., Potts et al. 2018), we assume that the anionic occupancy of ClAp-1 apatite is 69 mol % Cl + 31 mol % F in our simulation. In order to correlate the volatile content in apatite with that in LMO, we use the volatile partition coefficient reported by McCubbin et al. (2015a); i.e., that $D_{Cl\text{-}F} = 0.21$. Under these assumptions, Cl : F in late-stage LMO is ~ 1 : 2, but the light REE concentrations of remelted materials are still overestimated compared with KREEP basalt, which implies that apatite that precipitated from the lunar magma ocean should have less Cl than 69 mol %, that is, the actual Cl : F in late LMO should be even smaller than 1 : 2. Accordingly, we infer a high (F+OH)/Cl late stage LMO cumulates, i.e., relatively depleted in Cl compared with the sum of F and OH in mole percent, distinct from Cl-rich chondritic precursor materials (Jones et al., 2014). Using analyses of natural materials and assumed partition coefficients, McCubbin et al. (2015b) evaluated of the volatile abundance in urKREEP and determined it has 660 ppm F, 1100-1350 ppm Cl and 300-1250 ppm H_2O. If we convert the abundances from weight percent to mol percent, the Cl / (F + OH) = 0.29 - 0.73, consistent with our prediction.

A caveat in our modeling is the absence of merrillite (or whitlockite) in the late-stage LMO cumulates here. Merrillite has been discovered in lunar samples (e.g., Jolliff et al. 2006). As

merrillite is anhydrous and should not be treated as the indicator of the water concentrations in the magma (McCubbin et al., 2014), the appearance of merrillite can indicate either phosphorus enrichment or halogen depletion (Douce and Roden, 2006). Therefore, the mineral mode of merrillite should be very limited compared with apatite during LMO stage with enough halogen (e.g., McCubbin et al. 2015b; Hauri et al. 2015), as well as moderate phosphorus content (e.g., Charlier et al., 2018; Lin et al., 2017; Rapp and Draper, 2018; Schmidt and Kraettli, 2022). Although there is currently no predictive model for merrillite REE partition coefficients, Jolliff et al. (1993) reported that the REE concentrations of coexisting merrillite and apatite in lunar samples, merrillites have nearly parallel patterns, but much higher REE concentrations compared with apatites. We tested the scenario that there is a small amount of whitlockite (0.2 to 0.5 weight percent) coexisting with apatite (1.0 to 3.0 weight percent) during LMO crystallization and results show that the existence of whitlockite will not change the overall REE slope of late-stage LMO remelts and the overestimation of light REE in ClAp scenario (Figure B8).

The depletion of volatile elements in the Moon relative to the Earth has long been noted (e.g., Taylor et al. 2006), but the scale and duration of the associated degassing process is a controversial topic. Some previous studies argue the LMO degassing mainly happened during the giant impact (e.g., Barnes et al. 2016; Gargano et al. 2020). Although researchers proposed that the degassing during the LMO solidification is very limited due to the existence of an atmosphere in contact with LMO (e.g., Barnes et al. 2016), recent studies also emphasize the degassing process during the LMO evolution (e.g., Boyce et al. 2015; Ji et al. 2022). Under low oxygen fugacity, due to differences in diffusion rates, the lunar magma ocean residual liquid will preferentially lose H (Sharp et al., 2013), resulting in a relatively dry Moon. Subsequently, Cl will combine with metal cations in the magma, such that light ^{35}Cl prefers to evaporate (Sharp et al., 2010), leaving widespread positive δ^{37}Cl values in lunar samples (e.g., Treiman et al. 2014; Wang et al. 2019). Fluorine is the least susceptible to volatilization (Ustunisik et al., 2011; Ustunisik et al., 2015), resulting in a relatively less of loss by degassing. Although difficult to quantify, the differential degassing process and the relative loss of Cl and OH are expected to exist pre- and syn- LMO evolution, which may help to explain the relative Cl depletion in the late-stage LMO cumulates. Impact-related vapor metasomatism and condensation have been proposed to explain the high δ^{37}Cl values of old mare basalt (Barnes et al., 2019), highland breccia (Treiman et al., 2014), and ferroan anorthosites (Gargano et al., 2020). Considering a modest water content in young Chang'e 5 mare basalt (Hu et al., 2021), it is possible that the distribution of lunar volatile is heterogeneous during the LMO evolution, such that multiple reservoirs with distinct volatile concentrations and isotopic compositions developed (e.g., Wang et al. 2019), or a partly un-degassed reservoir exists despite the giant impact (Boyce et al. 2018 and references therein).

All the above hypotheses imply that the overall volatile abundance of the Moon has been constantly changing since accretion, accompanied by differentiation and degassing processes, indicating that extreme caution should be exercised when we trying to evaluate the volatile budget of the Moon from the returned samples. Our predictive model provides a method to bypass the interference of volatile loss and intrasample volatile heterogeneity on the returned samples, independently constraining the initial volatile inventory of the lunar magma ocean.

2.6. Conclusions

The high trace element partition coefficients of apatite are essential for successfully modeling the early-stage evolution of Earth and other bodies, and to track the geochemical evolution of evolved magmas. In this study, we measured trace elements partition coefficients between three endmember apatites (FlAp, OHAp, and ClAp) and silicate melt at 1050-1100 ℃ at 1 GPa. With the help of these new data, as well as previous experimental work, we developed temperature and composition-dependent predictive partitioning models based on the lattice strain model which enable us to calculate the apatite-melt partition coefficients. We observed that the X-site occupancy plays an important role in controlling the substitution mechanisms in the apatite structure and we use the compositional terms of apatite (X_{Ca}, X_{Na}, X_P and X_{Si}) to quantify the influence of the structure and substitutions controlled by anions. We also evaluated the impact of fO_2 on Eu anomalies of apatites and conducted three groups of parallel experiments with different capsules, to constrain the fO_2 dependence of Eu partition coefficients between apatite and silicate melt . We developed Eu in apatite-melt and Eu in apatite-plagioclase oxybarometers, and applied the latter model to calculate the fO_2 of our experiments, the winonaite HaH 193, and Sept Iles layered intrusion. The predictions reproduce their anticipated fO_2s, ranging from about two log units below IW buffer to the FMQ buffer, consistent with previous studies that applied alternative methods. We evaluated the impact of fractionation between trivalent and divalent Eu on our oxybarometer in post-crystallization geological processes (e.g., subsolidus reequilibration), and found the incorrect evaluation of equilibrium temperature will overestimate the system fO_2, as the larger the grain size of apatite and the lower the new equilibrium temperature, the larger the calculated fO_2 deviation. Finally, we modeled the petrogenesis of lunar KREEP basalt using our predictive partition coefficient models and found that in the late-stage LMO cumulate, Cl is relatively depleted in mole percent compared with the sum of F and OH. Because chondritic precursor materials have subequal F and Cl abundances, a Cl depleted lunar interior suggests that differential degassing occurred before or during the late stages of LMO crystallization.

2.7. Acknowledgments

We thank Allan Patchen for his help with electron microprobe analysis, Nathan Miller for his assistance with LA-ICP-MS analysis at the University of Texas, Austin, and Shichun Huang for his help with the dissolution experiments. This work was supported by an MSA Student Research Grant to D.J. and the NASA Solar System Workings award 80NSSC20K0467 to N.D.

REFERENCES

Aigner-Torres, M., Blundy, J., Ulmer, P. and Pettke, T. (2007) Laser ablation ICPMS study of trace element partitioning between plagioclase and basaltic melts: an experimental approach. *Contributions to Mineralogy and Petrology* 153, 647-667.

Barford, N.C., 1985. Experimental measurements: precision, error and truth. Chichester: Wiley.

Barnes, J.J., Franchi, I.A., McCubbin, F.M. and Anand, M. (2019) Multiple reservoirs of volatiles in the Moon revealed by the isotopic composition of chlorine in lunar basalts. *Geochimica et Cosmochimica Acta* 266, 144-162.

Barnes, J.J., Tartese, R., Anand, M., McCubbin, F.M., Neal, C.R. and Franchi, I.A. (2016) Early degassing of lunar urKREEP by crust-breaching impact (s). *Earth and Planetary Science Letters* 447, 84-94.

Bell, D.R. and Rossman, G.R. (1992) Water in Earth's mantle: the role of nominally anhydrous minerals. *Science* 255, 1391-1397.

Benedix, G.K., Lauretta, D.S. and McCoy, T.J. (2005) Thermodynamic constraints on the formation conditions of winonaites and silicate-bearing IAB irons. Geochimica et Cosmochimica Acta 69, 5123-5131.

Bindeman, I.N. and Davis, A.M. (2000) Trace element partitioning between plagioclase and melt: investigation of dopant influence on partition behavior. Geochimica et cosmochimica acta 64, 2863-2878.

Blundy, J. and Wood, B. (1994) Prediction of crystal–melt partition coefficients from elastic moduli. *Nature* 372, 452-454.

Borisov, S. and Klevtsova, R. (1963) The crystal structure of REE-Sr apatite. *Zhurnal Strukturnoi Khimii* 4, 629-631.

Boyce, J., Tomlinson, S., McCubbin, F., Greenwood, J. and Treiman, A. (2014) The lunar apatite paradox. *Science* 344, 400-402.

Boyce, J.W., Kanee, S.A., McCubbin, F.M., Barnes, J.J., Bricker, H. and Treiman, A.H. (2018) Early loss, fractionation, and redistribution of chlorine in the Moon as revealed by the low-Ti lunar mare basalt suite. *Earth and Planetary Science Letters* 500, 205-214.

Boyce, J.W., Treiman, A.H., Guan, Y., Ma, C., Eiler, J.M., Gross, J., Greenwood, J.P. and Stolper, E.M. (2015) The chlorine isotope fingerprint of the lunar magma ocean. *Science Advances* 1, e1500380.

Brice, J. (1975) Some thermodynamic aspects of the growth of strained crystals. *Journal of crystal growth* 28, 249-253.

Charlier, B., Grove, T.L., Namur, O. and Holtz, F. (2018) Crystallization of the lunar magma ocean and the primordial mantle-crust differentiation of the Moon. *Geochimica et Cosmochimica Acta* 234, 50-69.

Chen, N., Pan, Y., Weil, J.A. and Nilges, M.J. (2002) Electron paramagnetic resonance spectroscopic study of synthetic fluorapatite: Part II. Gd3+ at the Ca1 site, with a neighboring Ca2 vacancy. *American Mineralogist* 87, 47-55.

Chen, Y., Li, H., Sun, W., Ireland, T., Tian, X., Hu, Y., Yang, W., Chen, C. and Xu, D. (2016) Generation of Late Mesozoic Qianlishan A2-type granite in Nanling Range, South China: implications for Shizhuyuan W–Sn mineralization and tectonic evolution. *Lithos* 266, 435-452.

Cherniak, D. (2000) Rare earth element diffusion in apatite. *Geochimica et Cosmochimica Acta* 64, 3871-3885.
Cherniak, D. (2003) REE diffusion in feldspar. *Chemical Geology* 193, 25-41.
Cherniak, D. (2010) Diffusion in accessory minerals: zircon, titanite, apatite, monazite and xenotime. *Reviews in mineralogy and geochemistry* 72, 827-869.
Cherniak, D. and Ryerson, F. (1993) A study of strontium diffusion in apatite using Rutherford backscattering spectroscopy and ion implantation. *Geochimica et Cosmochimica Acta* 57, 4653-4662.
Cherniak, D. and Watson, E. (1992) A study of strontium diffusion in K-feldspar, Na-K feldspar and anorthite using Rutherford Backscattering Spectroscopy. *Earth and Planetary Science Letters* 113, 411-425.
Cockbain, A. and Smith, G. (1967) Alkaline-earth-rare-earth silicate and germanate apatites. *Mineralogical magazine and journal of the Mineralogical Society* 36, 411-421.
Cronberger, K. and Neal, C.R. (2017) KREEP basalt petrogenesis: Insights from 15434, 181. *Meteoritics & Planetary Science* 52, 827-841.
Douce, A.E.P. and Roden, M. (2006) Apatite as a probe of halogen and water fugacities in the terrestrial planets. *Geochimica et Cosmochimica Acta* 70, 3173-3196.
Drake, M.J. (1975) The oxidation state of europium as an indicator of oxygen fugacity. *Geochimica et Cosmochimica Acta* 39, 55-64.
Dygert, N., Draper, D.S., Rapp, J.F., Lapen, T.J., Fagan, A.L. and Neal, C.R. (2020) Experimental determinations of trace element partitioning between plagioclase, pigeonite, olivine, and lunar basaltic melts and an *f*O2 dependent model for plagioclase-melt Eu partitioning. *Geochimica et Cosmochimica Acta* 279, 258-280.
Dygert, N., Liang, Y., Sun, C. and Hess, P. (2014) An experimental study of trace element partitioning between augite and Fe-rich basalts. *Geochimica et Cosmochimica Acta* 132, 170-186.
Ertel, W., O'Neill, H.S.C., Sylvester, P.J., Dingwell, D. and Spettel, B. (2001) The solubility of rhenium in silicate melts: Implications for the geochemical properties of rhenium at high temperatures. *Geochimica et Cosmochimica Acta* 65, 2161-2170.
Fabbrizio, A., Schmidt, M.W. and Petrelli, M. (2021) Effect of fO2 on Eu partitioning between clinopyroxene, orthopyroxene and basaltic melt: Development of a Eu3+/Eu2+ oxybarometer. *Chemical Geology* 559, 119967.
Fleet, M.E., Liu, X. and Pan, Y. (2000a) Rare-earth elements in chlorapatite [Ca10 (PO4) 6Cl2]: Uptake, site preference, and degradation of monoclinic structure. *American Mineralogist* 85, 1437-1446.
Fleet, M.E., Liu, X. and Pan, Y. (2000b) Site preference of rare earth elements in hydroxyapatite [Ca10 (PO4) 6 (OH) 2]. *Journal of Solid State Chemistry* 149, 391-398.
Fleet, M.E. and Pan, Y. (1997) Site preference of rare earth elements in fluorapatite: Binary (LREE+ HREE)-substituted crystals. *American Mineralogist* 82, 870-877.
Floss, C., Crozaz, G., Jolliff, B., Benedix, G. and Colton, S. (2008) Evolution of the winonaite parent body: Clues from silicate mineral trace element distributions. *Meteoritics & Planetary Science* 43, 657-674.
Floss, C., Jolliff, B.L., Benedix, G.K., Stadermann, F.J. and Reid, J. (2007) Hammadah al Hamra 193: The first amphibole-bearing winonaite. *American Mineralogist* 92, 460-467.

Gargano, A., Sharp, Z., Shearer, C., Simon, J.I., Halliday, A. and Buckley, W. (2020) The Cl isotope composition and halogen contents of Apollo-return samples. *Proceedings of the National Academy of Sciences* 117, 23418-23425.

Gromet, L.P. and Silver, L.T. (1983) Rare earth element distributions among minerals in a granodiorite and their petrogenetic implications. *Geochimica et Cosmochimica Acta* 47, 925-939.

Hauri, E.H., Saal, A.E., Rutherford, M.J. and Van Orman, J.A. (2015) Water in the Moon's interior: Truth and consequences. *Earth and Planetary Science Letters* 409, 252-264.

Hauri, E.H., Weinreich, T., Saal, A.E., Rutherford, M.C. and Van Orman, J.A. (2011) High pre-eruptive water contents preserved in lunar melt inclusions. *Science* 333, 213-215.

Helmke, P.A., Blanchard, D.P., Haskin, L.A., Telander, K., Weiss, C. and Jacobs, J.W. (1973) Major and trace elements in igneous rocks from Apollo 15. *The moon* 8, 129-148.

Holzheid, A. and O'Neill, H.S.C. (1995) The Cr-Cr2O3 oxygen buffer and the free energy of formation of Cr2O3 from high-temperature electrochemical measurements. *Geochimica et cosmochimica acta* 59, 475-479.

Hu, S., He, H., Ji, J., Lin, Y., Hui, H., Anand, M., Tartèse, R., Yan, Y., Hao, J. and Li, R. (2021) A dry lunar mantle reservoir for young mare basalts of Chang'e-5. *Nature* 600, 49-53.

Hubbard, N.J., Rhodes, J.M., Gast, P.W., Bansal, B., Shih, C.-Y., Wiesmann, H. and Nyquist, L.E. (1973) Lunar rock types: The role of plagioclase in non-mare and highland rock types, Lunar and Planetary Science Conference Proceedings, p. 1297.

Hughes, J.M., Cameron, M. and Crowley, K.D. (1991) Ordering of divalent cations in the apatite structure: Crystal structure refinements of natural Mn-and Sr-bearing apatite. *American Mineralogist* 76, 1857-1862.

Hui, H., Peslier, A.H., Zhang, Y. and Neal, C.R. (2013) Water in lunar anorthosites and evidence for a wet early Moon. *Nature Geoscience* 6, 177-180.

Ito, J. (1968) Silicate apatites and oxyapatites. *American Mineralogist: Journal of Earth and Planetary Materials* 53, 890-907.

Ji, D. and Dygert, N. (2023) Trace element evidence for serial processing of the lunar flotation crust and a depleted bulk Moon. *Earth and Planetary Science Letters* 602, 117958.

Ji, J., He, H., Hu, S., Lin, Y., Hui, H., Hao, J., Li, R., Yang, W., Yan, Y. and Tian, H. (2022) Magmatic chlorine isotope fractionation recorded in apatite from Chang'e-5 basalts. *Earth and Planetary Science Letters* 591, 117636.

Jolliff, B.L., Haskin, L.A., Colson, R.O. and Wadhwa, M. (1993) Partitioning in REE-saturating minerals: Theory, experiment, and modelling of whitlockite, apatite, and evolution of lunar residual magmas. *Geochimica et Cosmochimica Acta* 57, 4069-4094.

Jolliff, B.L., Hughes, J.M., Freeman, J.J. and Zeigler, R.A. (2006) Crystal chemistry of lunar merrillite and comparison to other meteoritic and planetary suites of whitlockite and merrillite. *American Mineralogist* 91, 1583-1595.

Jones, R.H., McCubbin, F.M., Dreeland, L., Guan, Y., Burger, P.V. and Shearer, C.K. (2014) Phosphate minerals in LL chondrites: A record of the action of fluids during metamorphism on ordinary chondrite parent bodies. *Geochimica et Cosmochimica Acta* 132, 120-140.

Kessel, R., Beckett, J.R. and Stolper, E.M. (2001) Thermodynamic properties of the Pt-Fe system. *American Mineralogist* 86, 1003-1014.

Ketcham, R.A. (2015) Calculation of stoichiometry from EMP data for apatite and other phases with mixing on monovalent anion sites. *American Mineralogist* 100, 1620-1623.

Kieffer, M.A., Dare, S.A. and Namur, O. (2023) The use of trace elements in apatite to trace differentiation of a ferrobasaltic melt in the Sept-Iles Intrusive Suite, Quebec, Canada: Implications for provenance discrimination. *Geochimica et Cosmochimica Acta* 342, 169-197.

Klement, R. and Haselbeck, H. (1965) Apatite und Wagnerite zweiwertiger Metalle. *Zeitschrift für anorganische und allgemeine Chemie* 336, 113-128.

Kretz, R. (1982) Transfer and exchange equilibria in a portion of the pyroxene quadrilateral as deduced from natural and experimental data. *Geochimica et Cosmochimica Acta* 46, 411-421.

Li, H. and Hermann, J. (2017) The effect of fluorine and chlorine on trace element partitioning between apatite and sediment melt at subduction zone conditions. *Chemical geology* 473, 55-73.

Li, W., Costa, F., Oppenheimer, C. and Nagashima, K. (2023) Volatile and trace element partitioning between apatite and alkaline melts. *Contributions to Mineralogy and Petrology* 178, 9.

Libowitzky, E. and Beran, A. (2006) The structure of hydrous species in nominally anhydrous minerals: Information from polarized IR spectroscopy. *Reviews in Mineralogy and Geochemistry* 62, 29-52.

Lin, Y., Tronche, E.J., Steenstra, E.S. and Van Westrenen, W. (2017) Experimental constraints on the solidification of a nominally dry lunar magma ocean. *Earth and Planetary Science Letters* 471, 104-116.

Lodders, K. (2021) Relative atomic solar system abundances, mass fractions, and atomic masses of the elements and their isotopes, composition of the solar photosphere, and compositions of the major chondritic meteorite groups. *Space Science Reviews* 217, 1-33.

Mallmann, G., Burnham, A.D. and Fonseca, R.O. (2021) Mineral-Melt Partitioning of Redox-Sensitive Elements. *Magma Redox Geochemistry*, 345-367.

McCanta, M.C., Elkins-Tanton, L. and Rutherford, M.J. (2009) Expanding the application of the Eu-oxybarometer to the lherzolitic shergottites and nakhlites: Implications for the oxidation state heterogeneity of the Martian interior. *Meteoritics & Planetary Science* 44, 725-745.

McCubbin, F.M. and Jones, R.H. (2015) Extraterrestrial apatite: Planetary geochemistry to astrobiology. *Elements* 11, 183-188.

McCubbin, F.M., Shearer, C.K., Burger, P.V., Hauri, E.H., Wang, J., Elardo, S.M. and Papike, J.J. (2014) Volatile abundances of coexisting merrillite and apatite in the martian meteorite Shergotty: Implications for merrillite in hydrous magmas. *American Mineralogist* 99, 1347-1354.

McCubbin, F.M., Vander Kaaden, K.E., Tartèse, R., Boyce, J.W., Mikhail, S., Whitson, E.S., Bell, A.S., Anand, M., Franchi, I.A. and Wang, J. (2015a) Experimental investigation of F, Cl, and OH partitioning between apatite and Fe-rich basaltic melt at 1.0–1.2 GPa and 950–1000 C. *American Mineralogist* 100, 1790-1802.

McCubbin, F.M., Vander Kaaden, K.E., Tartèse, R., Klima, R.L., Liu, Y., Mortimer, J., Barnes, J.J., Shearer, C.K., Treiman, A.H. and Lawrence, D.J. (2015b) Magmatic volatiles (H, C, N, F, S, Cl) in the lunar mantle, crust, and regolith: Abundances, distributions, processes, and reservoirs. *American Mineralogist* 100, 1668-1707.

McKay, G., Le, L., Wagstaff, J. and Crozaz, G. (1994) Experimental partitioning of rare earth elements and strontium: Constraints on petrogenesis and redox conditions during crystallization of Antarctic angrite Lewis Cliff 86010. *Geochimica et Cosmochimica Acta* 58, 2911-2919.

McKay, G., Wiesmann, H., Bansal, B. and Shih, C.-Y. (1979) Petrology, chemistry, and chronology of Apollo 14 KREEP basalts, Lunar and Planetary Science Conference Proceedings, pp. 181-205.

Médard, E., McCammon, C.A., Barr, J.A. and Grove, T.L. (2008) Oxygen fugacity, temperature reproducibility, and H2O contents of nominally anhydrous piston-cylinder experiments using graphite capsules. *American Mineralogist* 93, 1838-1844.

Namur, O., Charlier, B., Toplis, M.J., Higgins, M.D., Hounsell, V., Liégeois, J.-P. and Vander Auwera, J. (2011) Differentiation of tholeiitic basalt to A-type granite in the Sept Iles layered intrusion, Canada. *Journal of Petrology* 52, 487-539.

Namur, O., Charlier, B., Toplis, M.J., Higgins, M.D., Liégeois, J.-P. and Vander Auwera, J. (2010) Crystallization sequence and magma chamber processes in the ferrobasaltic Sept Iles layered intrusion, Canada. *Journal of Petrology* 51, 1203-1236.

Neal, C. and Kramer, G. (2003) The composition of KREEP: A detailed study of KREEP basalt 15386, Lunar and Planetary Science conference, p. 2023.

Onuma, N., Higuchi, H., Wakita, H. and Nagasawa, H. (1968) Trace element partition between two pyroxenes and the host lava. *Earth and Planetary Science Letters* 5, 47-51.

Pan, Y. and Fleet, M.E. (2002) Compositions of the apatite-group minerals: substitution mechanisms and controlling factors. *Reviews in mineralogy and geochemistry* 48, 13-49.

Potts, N.J., Barnes, J.J., Tartèse, R., Franchi, I.A. and Anand, M. (2018) Chlorine isotopic compositions of apatite in Apollo 14 rocks: Evidence for widespread vapor-phase metasomatism on the lunar nearside~ 4 billion years ago. *Geochimica et Cosmochimica Acta* 230, 46-59.

Pownceby, M.I. and O'Neill, H.S.C. (1994) Thermodynamic data from redox reactions at high temperatures. IV. Calibration of the Re-ReO2 oxygen buffer from EMF and NiO+ Ni-Pd redox sensor measurements. *Contributions to Mineralogy and Petrology* 118, 130-137.

Prowatke, S. and Klemme, S. (2006) Trace element partitioning between apatite and silicate melts. *Geochim. Cosmochim. Acta* 70, 4513-4527.

Rapp, J.F. and Draper, D.S. (2018) Fractional crystallization of the lunar magma ocean: Updating the dominant paradigm. *Meteoritics & Planetary Science* 53, 1452-1455.

Schmidt, M.W. and Kraettli, G. (2022) Experimental crystallization of the lunar magma ocean, initial selenotherm and density stratification, and implications for crust formation, overturn and the bulk silicate Moon composition. *Journal of Geophysical Research: Planets*, e2022JE007187.

Shannon, R.D. (1976) Revised effective ionic radii and systematic studies of interatomic distances in halides and chalcogenides. *Acta crystallographica section A: crystal physics, diffraction, theoretical and general crystallography* 32, 751-767.

Sharp, Z., Shearer, C., McKeegan, K., Barnes, J. and Wang, Y. (2010) The chlorine isotope composition of the Moon and implications for an anhydrous mantle. *Science* 329, 1050-1053.

Sharp, Z.D., McCubbin, F.M. and Shearer, C.K. (2013) A hydrogen-based oxidation mechanism relevant to planetary formation. *Earth and Planetary Science Letters* 380, 88-97.

Shaw, D.M. (1970) Trace element fractionation during anatexis. *Geochim. Cosmochim. Acta* 34, 237-243.

Shervais, J.W., Taylor, L.A., Laul, J. and Smith, M. (1984) Pristine highland clasts in consortium breccia 14305: Petrology and geochemistry. *Journal of Geophysical Research: Solid Earth* 89, C25-C40.

Stepanov, A.S., Zhukova, I.A. and Jiang, S.-Y. (2023) Experimental constraints on miscibility gap between apatite and britholite and REE partitioning in an alkaline melt. *American Mineralogist* 108, 1043-1052.

Sudarsanan, K. and Young, R. (1980) Structure of partially substituted chlorapatite (Ca2Sr) 5 (PO4) 3Cl. *Acta Crystallographica Section B: Structural Crystallography and Crystal Chemistry* 36, 1525-1530.

Sun, C. and Liang, Y. (2012) Distribution of REE between clinopyroxene and basaltic melt along a mantle adiabat: effects of major element composition, water, and temperature. *Contributions to Mineralogy and Petrology* 163, 807-823.

Sun, C.G., Graff, M. and Liang, Y. (2017) Trace element partitioning between plagioclase and silicate melt: The importance of temperature and plagioclase composition, with implications for terrestrial and lunar magmatism. *Geochimica et Cosmochimica Acta* 206, 273-295.

Tailby, N.D., Trail, D., Watson, B., Lanzirotti, A., Newville, M. and Wang, Y. (2023) Eu speciation in apatite at 1 bar: An experimental study of valence-state partitioning by XANES, lattice strain, and Eu/Eu* in basaltic systems. *American Mineralogist* 108, 789-813.

Tartèse, R., Anand, M., McCubbin, F.M., Elardo, S.M., Shearer, C.K. and Franchi, I.A. (2014) Apatites in lunar KREEP basalts: The missing link to understanding the H isotope systematics of the Moon. *Geology* 42, 363-366.

Taylor, G.J., MARTEL, L.M. and Spudis, P.D. (2012) The Hadley-Apennine KREEP basalt igneous province. *Meteoritics & Planetary Science* 47, 861-879.

Taylor, S.R., Pieters, C.M. and MacPherson, G.J. (2006) Earth-Moon system, planetary science, and lessons learned. *Reviews in Mineralogy and Geochemistry* 60, 657-704.

Tepley III, F.J., Lundstrom, C.C., McDonough, W.F. and Thompson, A. (2010) Trace element partitioning between high-An plagioclase and basaltic to basaltic andesite melt at 1 atmosphere pressure. *Lithos* 118, 82-94.

Treiman, A.H., Boyce, J.W., Gross, J., Guan, Y., Eiler, J.M. and Stolper, E.M. (2014) Phosphate-halogen metasomatism of lunar granulite 79215: Impact-induced fractionation of volatiles and incompatible elements. *American Mineralogist* 99, 1860-1870.

Urusov, V.S. and Khudolozhkin, V.O. (1974) An energy analysis of cation ordering in apatite. *Geochem. Int.* 11, 1048-1053.

Ustunisik, G., Nekvasil, H. and Lindsley, D. (2011) Differential degassing of H2O, Cl, F, and S: Potential effects on lunar apatite. *American Mineralogist* 96, 1650-1653.

Ustunisik, G., Nekvasil, H., Lindsley, D.H. and McCubbin, F.M. (2015) Degassing pathways of Cl-, F-, H-, and S-bearing magmas near the lunar surface: Implications for the composition and Cl isotopic values of lunar apatite. *American Mineralogist* 100, 1717-1727.

Wadhwa, M. (2001) Redox state of Mars' upper mantle and crust from Eu anomalies in shergottite pyroxenes. *Science* 291, 1527-1530.

Wadhwa, M. (2008) Redox conditions on small bodies, the Moon and Mars. *Reviews in Mineralogy and Geochemistry* 68, 493-510.

Wang, Y., Hsu, W. and Guan, Y. (2019) An extremely heavy chlorine reservoir in the Moon: Insights from the apatite in lunar meteorites. *Scientific Reports* 9, 1-8.

Watson, E.B. and Green, T.H. (1981) Apatite/liquid partition coefficients for the rare earth elements and strontium. *Earth and Planetary Science Letters* 56, 405-421.

Wood, B.J. and Blundy, J.D. (1997) A predictive model for rare earth element partitioning between clinopyroxene and anhydrous silicate melt. *Contributions to Mineralogy and Petrology* 129, 166-181.

Yao, L. and Liang, Y. (2015) Closure temperature in cooling bi-mineralic systems: I. Definition and with application to REE-in-two-pyroxene thermometer. *Geochimica et Cosmochimica Acta* 162, 137-150.

Yao, L.J., Sun, C.G. and Liang, Y. (2012) A parameterized model for REE distribution between low-Ca pyroxene and basaltic melts with applications to REE partitioning in low-Ca pyroxene along a mantle adiabat and during pyroxenite-derived melt and peridotite interaction. *Contributions to Mineralogy and Petrology* 164, 261-280.

Zhang, Y. (2009) Geochemical kinetics. Princeton University Press.

APPENDIX B

Calculation of uncertainties of predicted partition coefficients

The partition coefficient between apatite and silicate melt can be calculated by our trace element predictive models (Eqs. 2.4-2.6 and 2.10-2.12 in the main text). The predictive model is built based on the lattice strain model:

$$D_i^{min-melt} = D_o exp\left[\frac{-4\pi EN_A}{\mathrm{RT}}\left(\frac{r_o}{2}(r_o - r_i)^2 - \frac{1}{3}(r_o - r_i)^3\right)\right] \quad \text{(B.1)}$$

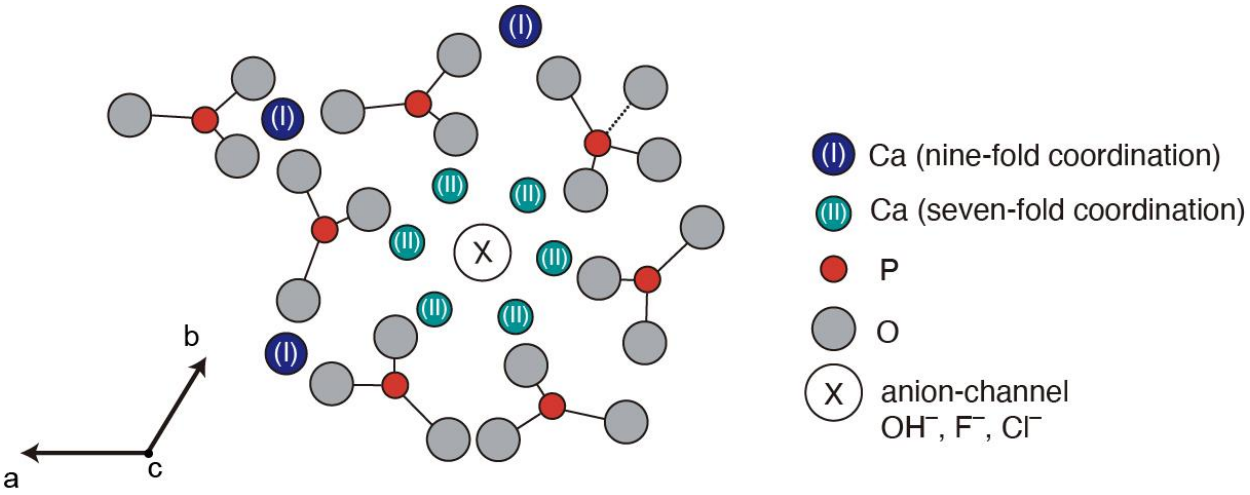
We use MATLAB® functions "nlinfit" and "nlpredci" to predict three lattice strain parameters, $\ln(D_0)$, E, and r_o, for each experiment separately, and recover their uncertainties at the same time. Uncertainties in the lattice strain parameters are calculated from fit residuals assuming normal distribution about the optimal fit (Table 2.5). Then we estimated the uncertainty of the predicted partition coefficients by propagating the lattice strain model parameter uncertainties by a Taylor series expansion using Eqs. B.2 and B.3 (e.g., Barford, 1985):

$$s_{D_o} = \sqrt{\exp\left(\ln(D_0)\right) s_{lnD_o}^2} \quad \text{(B.2)}$$

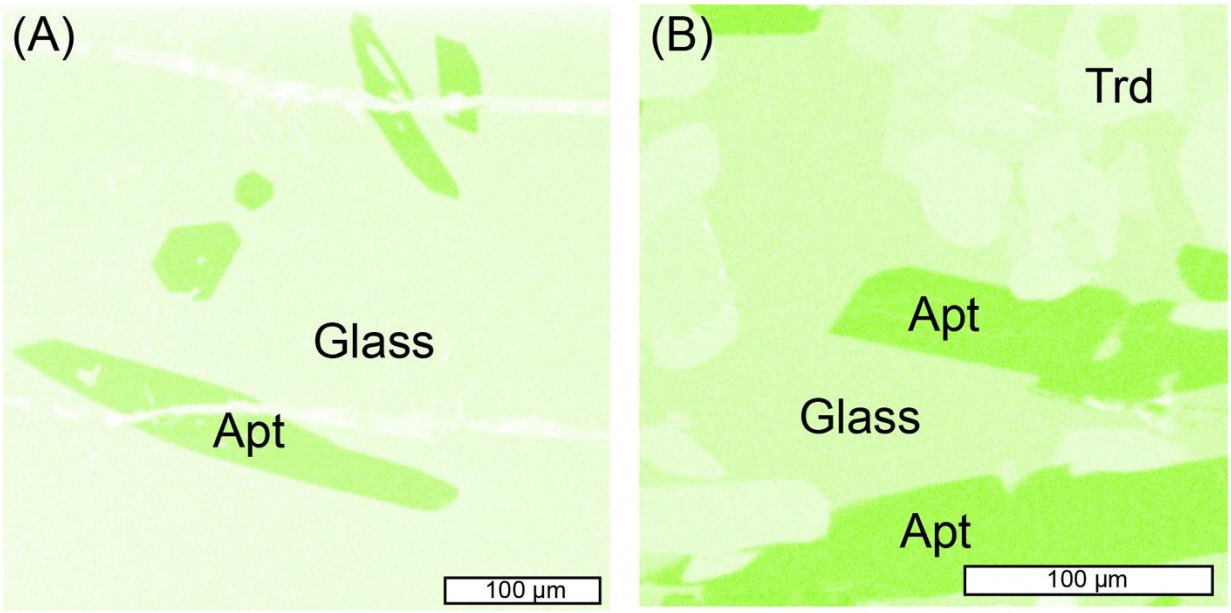
$$s_{D_i^{min-melt}} = \sqrt{\left(\frac{\partial D_i^{min-melt}}{\partial D_o}\right)^2 s_{D_o}^2 + \left(\frac{\partial D_i^{min-melt}}{\partial E}\right) s_E^2 + \left(\frac{\partial D_i^{min-melt}}{\partial r_o}\right)^2 s_{r_o}^2}$$

$$= \sqrt{\begin{array}{c} exp\left[\frac{-4\pi EN_A}{\mathrm{RT}}\left(\frac{r_o}{2}(r_o - r_i)^2 - \frac{1}{3}(r_o - r_i)^3\right)\right]^2 s_{D_o}^2 \\ + \left\{\left[\frac{-4D_o\pi N_A}{\mathrm{RT}}\left(\frac{r_o}{2}(r_o - r_i)^2 - \frac{1}{3}(r_o - r_i)^3\right)\right] exp\left[\frac{-4\pi EN_A}{\mathrm{RT}}\left(\frac{r_o}{2}(r_o - r_i)^2 - \frac{1}{3}(r_o - r_i)^3\right)\right]\right\}^2 s_E^2 \\ + \left\{\left[\frac{-4D_oE\pi N_A}{\mathrm{RT}}\left(r_o(r_o - r_i) - \frac{1}{2}(r_o - r_i)^2\right)\right] exp\left[\frac{-4\pi EN_A}{\mathrm{RT}}\left(\frac{r_o}{2}(r_o - r_i)^2 - \frac{1}{3}(r_o - r_i)^3\right)\right]\right\}^2 s_{r_o}^2 \end{array}} \quad \text{(B.3)}$$

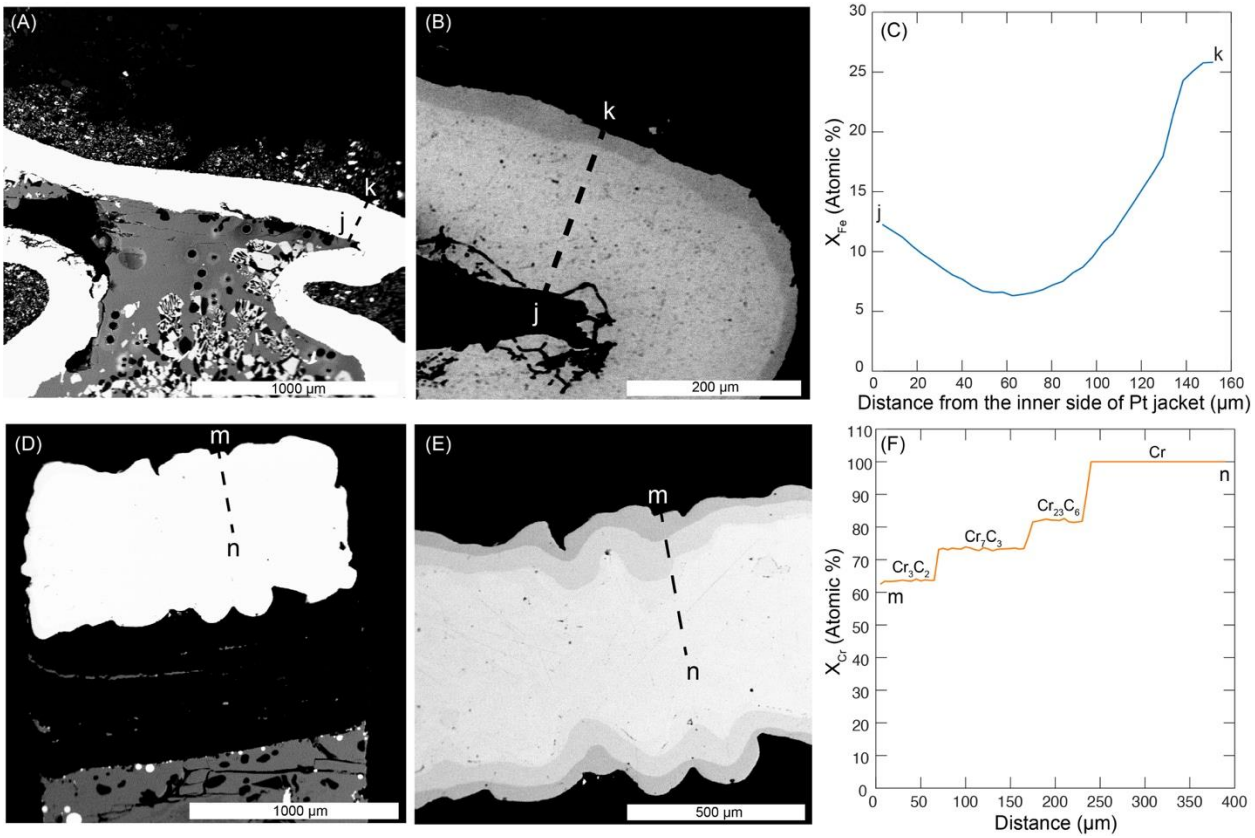
where $s_{\ln(D_0)}$ and s_{D_o} represent the errors (1σ) of $\ln(D_0)$ and D_o, $s_{D_i^{min-melt}}$ represents the error of predicted partition coefficients (Figure 4), S_E and s_{r_o} represents the error of E and r_o, $\frac{\partial D_i^{min-melt}}{\partial D_o}$ denotes the partial derivative of $D_i^{min-melt}$ with respect to D_o, and so forth. All lattice strain parameters are defined in the main text and their values are reported in Table 2.5. For trivalent elements, the uncertainties vary from 9.86% to 42.93% with an average of 17.64%, while for the uncertainties of divalent elements range from 8.08% to 34.09% with an average of 16.93%.



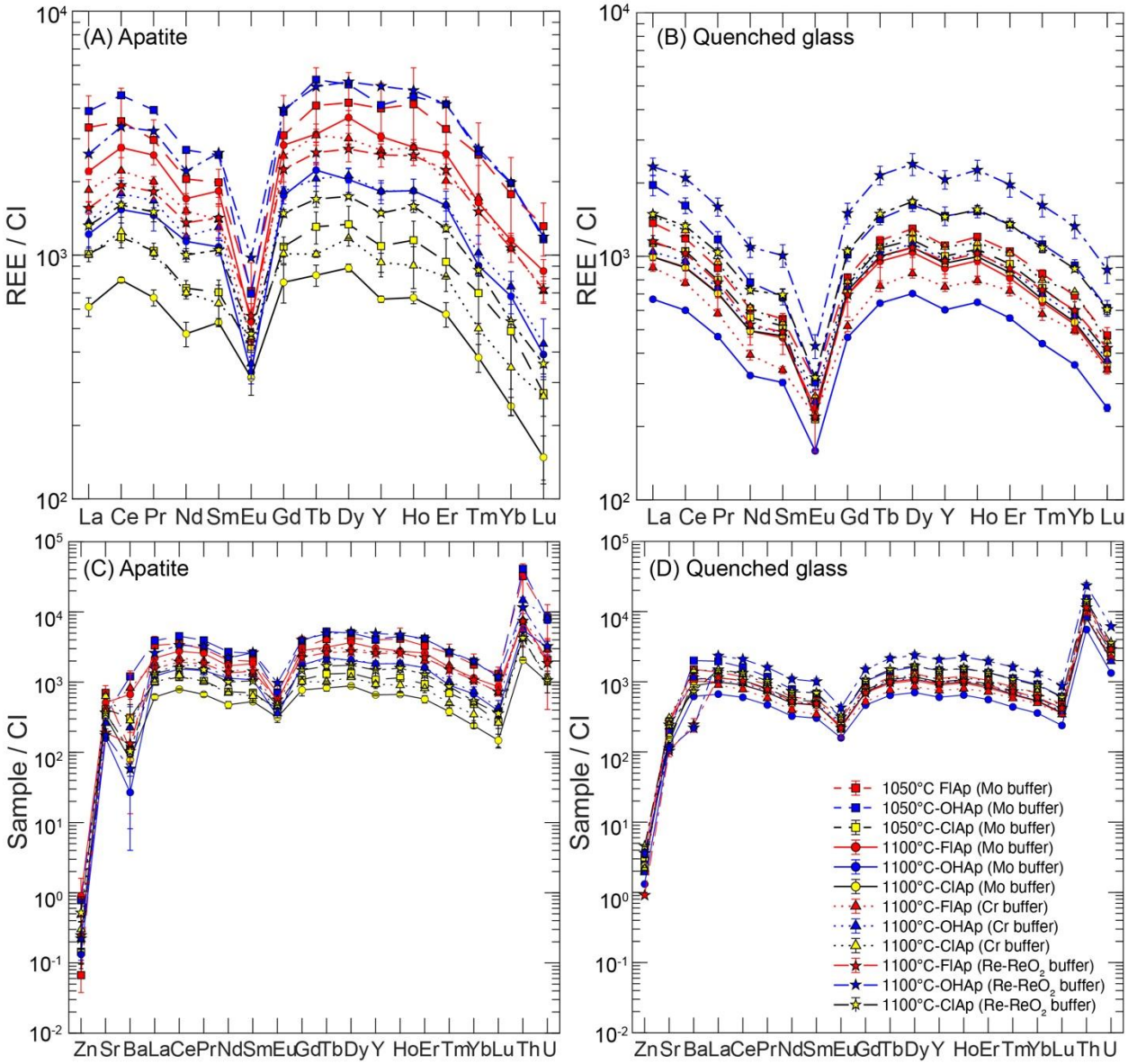
Figures B1. The crystal structure of apatite. Note the positioning of the Ca1 and Ca2 polyhedra relative to the PO_4 tetrahedron and X site. The X-site can be occupied by OH, Cl or F, or other monovalent anions (e.g., iodine).



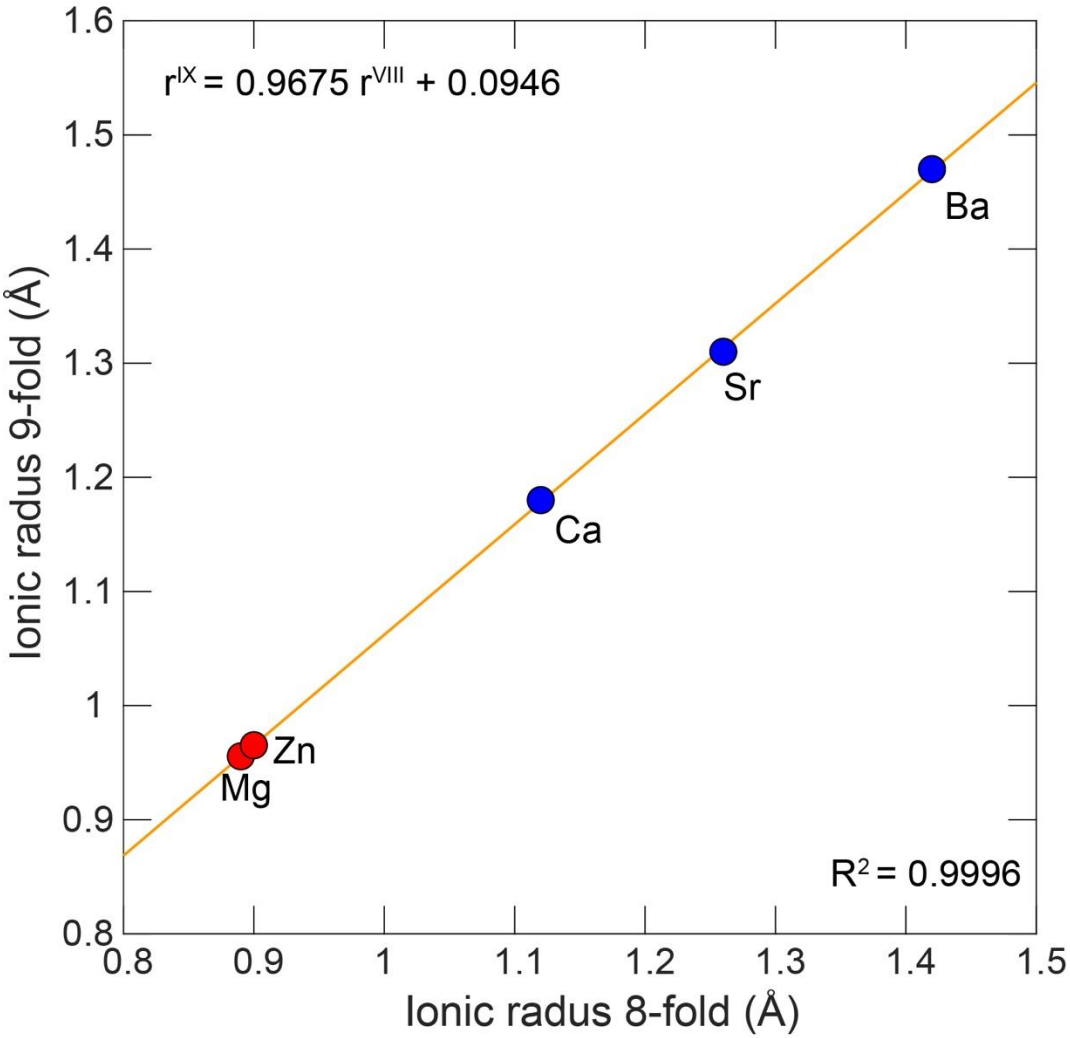
Figures B2. Energy dispersive spectrometry (EDS) mapping of Yttrium for experiment (A) OHAp-6 and (B) OHAp-7. The area showing deeper green is apatite; no obvious Y zoning is observed.



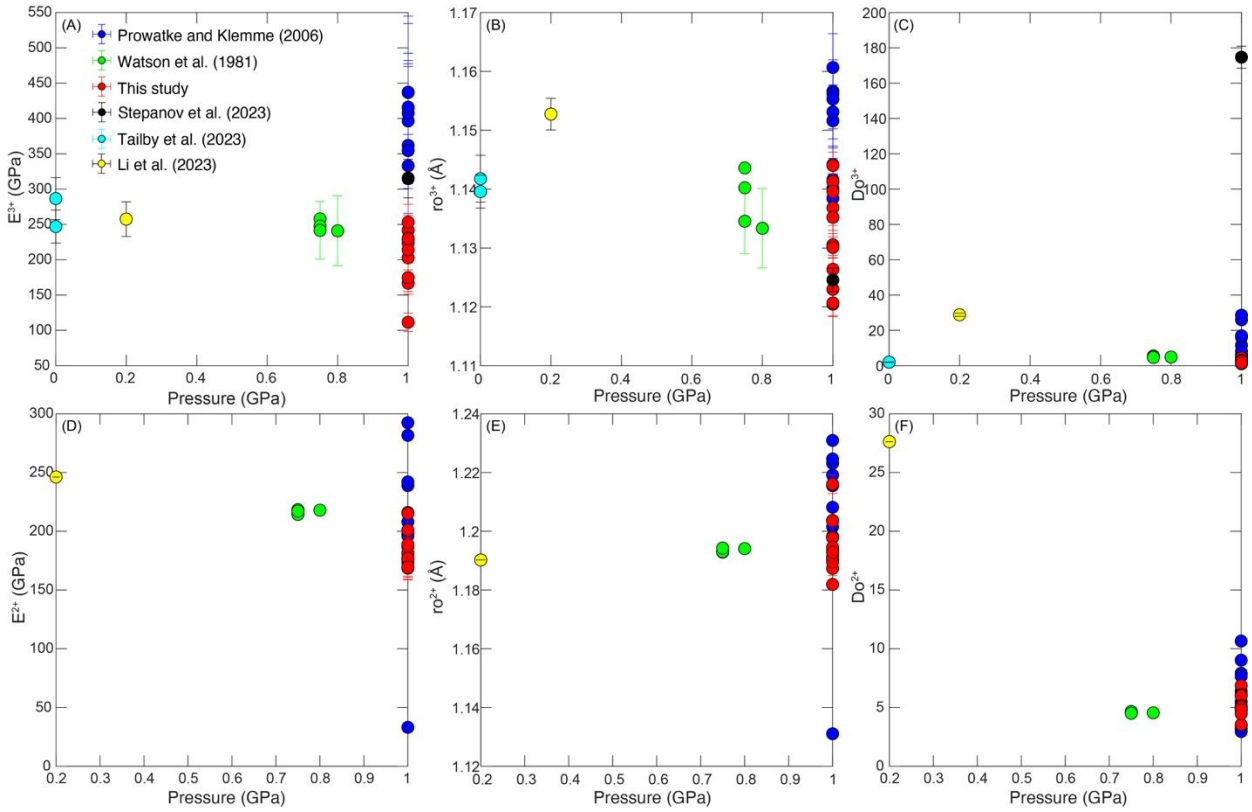
Figures B3. Images of the platinum jacket and Cr metal in the experimental assemblies, and variations in Fe and Cr concentrations with distance. (A-C). The Fe concentrations in the Pt jacket as a function of distance from the inner to the outer wall (j to k) of experiment ClAp-5 are shown in (C). The outer wall reflects the alloyed condition after the pre-condition process, which was more reduced than the target fO_2, while the inner wall demonstrates the role of ReO_2 as its reduction by the preconditioned starting material increased the fO_2; (D-F) the Cr concentrations in the Cr metal as a function of distance from the rim to the center (m to n) of metal in experiment OHAp-5. There are three different chromium carbide layers from the rim to the core, and they correspond to three different structures of chromium carbide, with the Cr content gradually increasing toward the interior. No oxidized Cr is observed, suggesting the Cr was ineffective as a metal buffer.



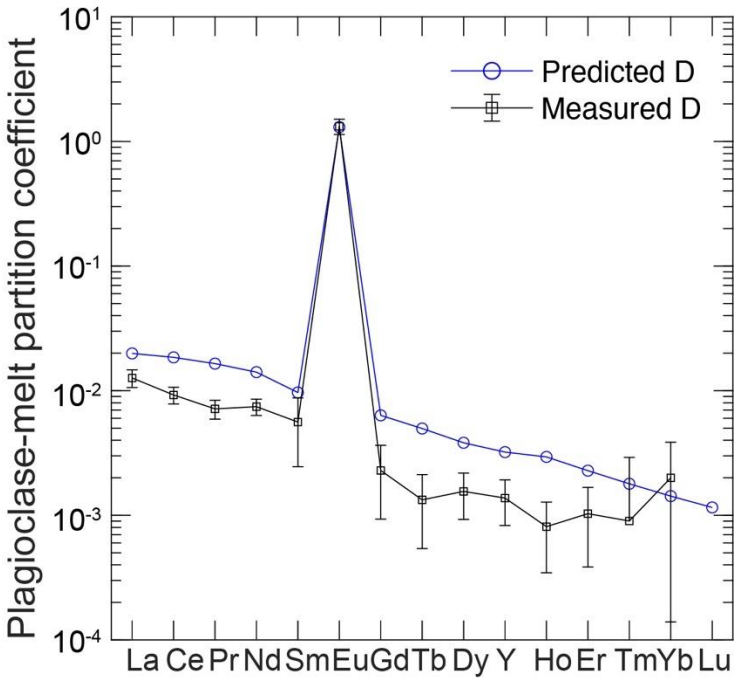
Figures B4. (A-B) Chondrite normalized REE patterns, and (C-D) trace element patterns of apatite and quenched glass from experiments in this study. All the major and trace element concentrations and uncertainties are reported in Table B3 and Table B4. Chondritic normalization is from Lodders (2021).



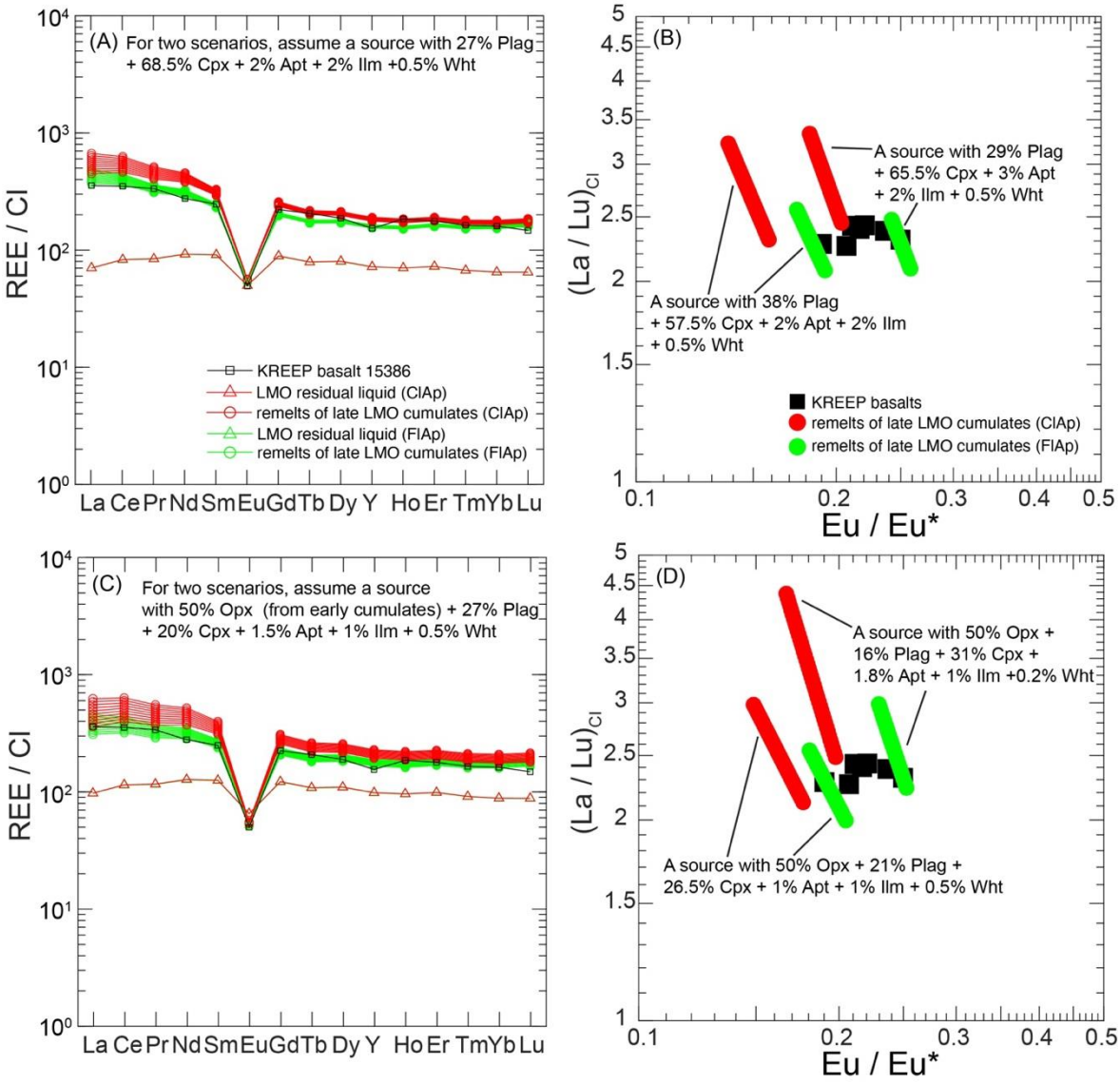
Figures B5. Correlation between 8-fold and 9-fold radii for divalent cations. The blue circles represent three divalent cations with the 9-fold radii reported in Shannon (1976); as they were not reported by Shannon, the 9-fold radii for Mg (0.956 Å) and Zn (0.958 Å) are extrapolated based on linear regression.



Figures B6. The lattice strain parameters of (A) - (C) trivalent element and (D) - (F) divalent element as a function of equilibrium pressure between apatite and silicate melt. No obvious correlation between lattice strain parameters and pressures was observed.



Figures B7. Measured REE partition coefficients of plagioclase in OHAP-1 experiments in this study and the predicted REE partition coefficients of plagioclase calculated by major element concentrations reported in Table B6 using predictive models in Sun et al. (2017) and Dygert et al. (2020). The measured data fit the overall trend of plagioclase REE partition coefficients and the Eu partitioning data that we used to calculate the fO_2 is consistent with the prediction.



Figures B8. (A) Chondrite-normalized REE patterns of residual liquids after 98.9 percent solidification of the LMO, and remelts of late LMO cumulates compared to KREEP basalt 15386 (Neal and Kramer, 2003), and (B) $(La / Lu)_{CI}$ versus Eu / Eu* showing remelts of late LMO cumulates with different source mineral modes and apatite species compared to KREEP basalts. (C) Chondrite-normalized REE patterns of residual liquids after 90.1 percent solidification of the LMO, and remelts of a source with 50% late LMO cumulates and 50% early LMO crystallized Opx (PCS=52%; Rapp and Draper, 2018) compared to KREEP basalt 15386; (D) $(La / Lu)_{CI}$ versus Eu / Eu* showing remelts of late LMO cumulates with different source mineral modes and apatite species compared to KREEP basalts. Here we assume there is 0.2% to 0.5% whitlockite (Wht) that crystallized during LMO solidification. Consistent with Figure 2.10 in the main text, in the ClAp scenario remelts can't reproduce the KREEP basalts because of their higher LREE concentrations. The partition coefficients of whitlockite are from Jolliff et al. (1993). Chondrite normalization is from Lodders (2021).

Table B1. Rare earth and other trace element concentrations in secondary standard materials analyzed as unknowns compared to preferred concentrations. Primary standard is Apatite-NP-B01 (data from Jochum et al., 2011; Jochum et al., 2005).

	Secondary Standard Concentration (ppm)	Reference Concentration (ppm)	Deviation (%)
		NIST612	
Zn	53.82	39.10	37.64
Sr	82.68	78.40	5.45
Y	37.46	38.30	2.20
Ba	47.93	39.30	21.95
La	35.43	36.00	1.58
Ce	46.70	38.40	21.62
Pr	47.90	37.90	26.38
Nd	38.62	35.50	8.79
Sm	43.09	37.70	14.29
Eu	37.51	35.60	5.38
Gd	31.75	37.30	14.89
Tb	35.35	37.60	5.99
Dy	34.00	35.50	4.21
Ho	34.66	38.30	9.51
Er	35.46	38.00	6.69
Tm	33.43	36.80	9.15
Yb	36.08	39.20	7.96
Lu	33.17	37.00	10.34
Th	39.11	37.79	3.50
U	47.95	37.38	28.28
		NIST610	
Zn	456.30	460.00	0.80
Sr	529.85	515.50	2.78
Y	428.09	462.00	7.34
Ba	476.47	452.00	5.41
La	441.92	440.00	0.44
Ce	526.55	453.00	16.24
Pr	530.81	448.00	18.48
Nd	478.10	430.00	11.19
Sm	508.74	453.00	12.31
Eu	456.38	447.00	2.10
Gd	421.48	449.00	6.13
Tb	414.30	437.00	5.20

Table B1. *Continued*

	Secondary Standard Concentration (ppm)	Reference Concentration (ppm)	Deviation (%)
Dy	394.19	437.00	9.80
Ho	399.22	449.00	11.09
Er	410.14	455.00	9.86
Tm	386.12	435.00	11.24
Yb	401.59	450.00	10.76
Lu	392.67	439.00	10.55
Th	470.99	457.20	3.02
U	581.85	461.50	26.08
		BCR-2G	
Zn	187.52	125.00	50.02
Sr	347.99	342.00	1.75
Y	36.01	35.00	2.89
Ba	683.72	683.00	0.11
La	24.68	24.70	0.07
Ce	58.34	53.30	9.46
Pr	7.64	6.70	13.99
Nd	30.27	28.90	4.73
Sm	7.63	6.59	15.72
Eu	1.93	1.97	2.14
Gd	6.56	6.71	2.24
Tb	1.19	1.02	16.79
Dy	6.41	6.44	0.45
Ho	1.33	1.27	4.98
Er	4.24	3.70	14.58
Tm	0.53	0.51	4.26
Yb	3.84	3.39	13.26
Lu	0.60	0.50	18.52
Th	6.78	5.90	14.84
U	2.56	1.69	51.59

Table B2. Rare earth and other trace element concentrations in secondary standard materials analyzed as unknowns compared to preferred concentrations in glass. Primary standard is NIST glass SRM 610 (data from Jochum et al., 2011; Jochum et al., 2005).

	Secondary Standard Concentration (ppm)	Reference Concentration (ppm)	Deviation (%)
		NIST612	
Zn	37.39	39.10	4.38
Sr	75.52	78.40	3.67
Y	37.21	38.30	2.85
Ba	36.75	39.30	6.49
La	37.77	36.00	4.91
Ce	38.15	38.40	0.64
Pr	36.49	37.90	3.72
Nd	35.72	35.50	0.61
Sm	38.14	37.70	1.16
Eu	36.69	35.60	3.05
Gd	36.04	37.30	3.39
Tb	37.60	37.60	0.00
Dy	34.84	35.50	1.85
Ho	37.74	38.30	1.45
Er	35.39	38.00	6.86
Tm	35.49	36.80	3.55
Yb	38.83	39.20	0.95
Lu	35.87	37.00	3.06
Th	37.77	37.79	0.06
U	37.63	37.38	0.67
		BCR-2G	
Zn	145.27	125.00	16.22
Sr	304.43	342.00	10.99
Y	30.94	35.00	11.59
Ba	595.70	683.00	12.78
La	24.51	24.70	0.78
Ce	48.31	53.30	9.37
Pr	5.91	6.70	11.72
Nd	26.81	28.90	7.24
Sm	6.21	6.59	5.74
Eu	1.83	1.97	7.01
Gd	6.06	6.71	9.72
Tb	0.98	1.02	3.64

Table B2. *Continued*

	Secondary Standard Concentration (ppm)	Reference Concentration (ppm)	Deviation (%)
Dy	6.12	6.44	4.90
Ho	1.26	1.27	0.67
Er	3.32	3.70	10.39
Tm	0.46	0.51	10.50
Yb	3.43	3.39	1.05
Lu	0.48	0.50	4.06
Th	5.64	5.90	4.46
U	1.69	1.69	0.24

Table B3. Major and trace element concentrations and their uncertainties for apatites in experiments. Reported uncertainties (σ) represent 1 sigma error based on replicate analyses.

Sample	FlAp-9		OHAp-1		ClAp-1		FlAp-1		OHAp-6		ClAp-2	
n.o.a.	(7)	σ	(9)	σ	(7)	σ	(8)	σ	(8)	σ	(7)	σ
SiO_2	0.65	0.12	0.79	0.17	0.93	0.17	0.81	0.52	0.64	0.26	1.84	0.42
TiO_2	0.04	0.01	0.07	0.02	0.04	0.02	0.07	0.06	0.04	0.02	0.05	0.01
Al_2O_3	0.02	0.01	0.04	0.02	0.07	0.06	0.02	0.09	0.07	0.08	0.04	0.02
FeO	1.53	0.06	1.99	0.26	2.47	0.24	1.70	0.22	2.03	0.16	2.02	0.07
MnO	0.25	0.02	0.30	0.04	0.39	0.03	0.23	0.02	0.21	0.01	0.31	0.01
MgO	0.14	0.02	0.06	0.04	0.05	0.01	0.14	0.02	0.10	0.01	0.11	0.01
CaO	53.64	0.26	53.21	0.61	50.96	0.39	53.41	0.63	54.31	0.91	50.23	0.35
Na_2O	0.02	0.01	0.05	0.01	0.15	0.03	0.02	0.01	0.02	0.02	0.13	0.03
K_2O	0.01	0.01	n.d.	-	n.d.	-	n.d.	-	0.00	0.01	0.01	0.01
P_2O_5	40.87	0.40	40.24	0.30	39.55	0.41	39.73	0.69	40.98	0.30	38.98	0.37
F	2.70	0.16	0.00	0.00	0.00	0.00	3.88	0.52	0.00	0.00	0.00	0.00
Cl	0.04	0.01	0.04	0.04	4.65	0.24	0.01	0.01	0.25	0.02	5.93	0.40
Total	99.92		96.78		99.26		100.00		98.66		99.68	
n.o.a.	(2)	σ	(1)	σ	(2)	σ	(2)	σ	(4)	σ	(2)	σ
Zn	20.9	9.1	244.0	-	45.0	19.2	282.3	218.3	41.3	7.3	75.9	45.8
Sr	5473.3	1463.1	2634.8	-	3210.5	513.6	3979.9	1034.6	1240.5	62.9	2532.6	115.1
Y	6230.5	1671.6	6427.5	-	1697.8	429.1	4770.7	179.2	2842.1	312.2	1028.4	30.4
Ba	258.4	227.2	2818.8	-	729.0	607.2	1564.4	1825.7	62.9	43.8	183.1	22.4
La	783.2	271.3	914.3	-	237.1	16.7	517.6	15.6	285.9	35.7	144.1	12.7
Ce	2132.9	784.5	2726.0	-	713.0	33.9	1664.0	50.1	926.7	110.6	476.6	11.5
Pr	264.2	55.6	350.7	-	92.7	7.0	228.8	1.6	129.7	17.8	59.6	4.5
Nd	927.9	335.1	1220.3	-	330.7	25.1	770.7	38.0	514.7	79.3	215.1	24.8

Table B3. *Continued*

Sample	FlAp-9		OHAp-1		ClAp-1		FlAp-1		OHAp-6		ClAp-2	
Sm	292.1	38.5	378.8	-	103.5	12.7	269.4	30.5	158.9	12.9	77.8	3.0
Eu	39.9	12.2	38.9	-	23.1	4.1	29.8	5.6	18.5	1.9	17.6	2.7
Gd	608.9	277.5	760.8	-	212.8	20.2	554.9	55.3	344.7	26.3	152.0	27.0
Tb	148.9	64.0	190.2	-	47.4	7.1	113.7	11.4	80.9	11.3	30.0	3.0
Dy	1022.9	337.3	1215.8	-	324.6	60.4	888.9	61.2	494.9	56.7	214.8	7.9
Ho	230.8	95.3	248.6	-	64.0	12.5	154.1	11.2	102.0	12.0	37.2	2.1
Er	522.7	183.4	660.4	-	149.0	36.4	413.4	38.5	254.2	36.0	90.9	10.5
Tm	62.4	21.9	64.0	-	16.9	7.6	39.7	3.4	21.9	1.9	9.2	1.2
Yb	288.9	119.7	320.5	-	79.2	33.4	186.8	12.7	110.1	16.8	39.0	3.4
Lu	31.9	7.8	28.2	-	6.6	3.7	20.9	2.4	9.5	1.1	3.6	0.8
Th	951.0	475.0	1207.5	-	142.5	45.8	217.1	124.8	162.7	24.0	60.5	0.2
U	67.7	35.1	63.6	-	16.9	1.4	17.0	13.7	25.4	5.6	8.2	2.5

Table B3. *Continued*

Sample	FlAp-8		OHAp-5		ClAp-3		FlAp-7		OHAp-7		ClAp-5	
n.o.a.	(7)	σ	(7)	σ	(7)	σ	(6)	σ	(10)	σ	(6)	σ
SiO_2	0.53	0.07	1.87	0.22	1.36	0.15	0.43	0.11	0.54	0.12	0.60	0.09
TiO_2	0.06	0.01	0.14	0.03	0.07	0.02	0.02	0.02	0.03	0.02	0.03	0.01
Al_2O_3	0.06	0.11	0.05	0.01	0.04	0.01	0.04	0.05	0.09	0.13	0.03	0.04
FeO	1.04	0.14	1.51	0.14	1.68	0.12	1.58	0.23	1.53	0.15	1.37	0.18
MnO	0.25	0.02	0.27	0.01	0.41	0.02	0.32	0.01	0.38	0.03	0.38	0.03
MgO	0.14	0.01	0.13	0.01	0.10	0.01	0.23	0.02	0.28	0.02	0.20	0.00
CaO	52.86	0.13	52.98	0.94	51.49	0.83	52.05	0.35	53.27	0.47	52.10	0.26
Na_2O	0.01	0.01	0.08	0.02	0.12	0.03	0.02	0.01	0.02	0.01	0.04	0.01
K_2O	0.01	0.01	0.01	0.01	0.01	0.00	0.00	0.00	0.01	0.01	0.01	0.01
P_2O_5	40.44	0.30	39.43	0.56	38.95	0.55	40.60	0.17	41.21	0.59	39.91	0.45
F	3.32	0.28	0.00	0.00	0.00	0.00	2.95	0.07	3.05	0.33		
Cl	0.02	0.01	0.29	0.07	5.89	0.61	0.03	0.01	0.03	0.01	4.05	0.14
Total	98.73		96.76		100.15		98.27		100.41		98.73	
n.o.a.	(3)	σ	(4)	σ	(2)	σ	(3)	σ	(1)	σ	(2)	σ
Zn	151.2	10.3	67.6	5.0	94.2	25.0	77.0	2.5	69.5	-	161.7	112.4
Sr	3250.9	581.7	2036.3	354.9	4925.8	397.4	1482.1	69.5	1359.6	-	2849.9	73.4
Y	4198.7	57.3	2853.9	226.6	1456.2	130.6	4017.7	436.3	7683.3	-	2319.2	56.9
Ba	1932.0	1142.0	529.0	519.6	663.6	457.3	311.0	138.9	136.1	-	242.9	44.6
La	433.8	44.8	319.6	29.8	235.1	0.1	365.7	20.6	610.2	-	310.1	8.0
Ce	1337.7	175.7	1078.9	139.2	754.1	108.4	1166.2	83.2	2025.8	-	967.8	29.1
Pr	178.4	8.6	148.8	9.7	90.8	2.7	162.2	11.2	287.6	-	133.9	12.0
Nd	686.2	23.0	538.7	69.5	316.6	17.5	614.2	71.1	999.9	-	452.8	28.2
Sm	205.4	32.3	191.3	22.3	93.3	17.4	208.8	24.2	385.9	-	154.2	3.7

Table B3. *Continued*

Sample	FlAp-8		OHAp-5		ClAp-3		FlAp-7		OHAp-7		ClAp-5	
Eu	25.2	5.4	20.1	2.7	25.9	2.0	31.5	1.9	54.6	-	26.6	0.5
Gd	500.9	50.9	359.3	16.6	199.0	17.7	441.2	49.4	782.3	-	291.4	10.5
Tb	112.3	6.8	74.6	12.4	36.6	1.1	95.5	9.5	178.0	-	61.6	4.6
Dy	729.6	35.9	514.1	35.0	284.5	2.1	660.9	75.5	1246.9	-	422.3	8.4
Ho	153.3	7.2	102.0	11.8	50.3	9.8	142.1	12.7	263.4	-	88.1	5.0
Er	320.2	24.2	255.8	14.9	129.7	0.6	354.6	42.0	659.5	-	204.5	7.2
Tm	41.6	14.8	24.7	4.4	12.1	0.6	36.5	4.3	66.2	-	21.0	1.2
Yb	173.7	21.8	120.6	18.5	56.2	20.4	173.6	6.0	322.2	-	86.8	0.2
Lu	17.3	1.7	10.5	2.8	6.4	1.1	17.6	2.2	28.9	-	8.7	0.8
Th	223.6	90.9	433.7	37.3	122.7	56.3	218.5	59.5	341.3	-	125.2	8.3
U	23.7	10.2	67.1	11.7	9.5	2.1	15.1	6.1	26.2	-	8.6	0.3

Table B4. Major and trace element concentrations and their uncertainties for quenched glass and plagioclase in experiments. Reported uncertainties (σ) represent 1 sigma error based on replicate analyses.

Sample	FlAp-9	glass	OHAp-1	glass	ClAp-1	glass	FlAp-1	glass	OHAp-6	glass	ClAp-2	glass
n.o.a.	(7)	σ	(5)	σ	(4)	σ	(10)	σ	(7)	σ	(9)	σ
SiO_2	47.69	0.14	40.29	0.34	40.23	0.27	41.89	0.28	40.41	0.24	40.32	0.29
TiO_2	2.85	0.07	3.13	0.08	3.97	0.05	5.15	0.04	3.52	0.04	5.09	0.04
Al_2O_3	10.80	0.09	8.17	0.18	8.41	0.15	7.96	0.08	5.71	0.12	8.00	0.05
FeO	22.43	0.16	29.29	0.44	29.51	0.22	26.48	0.07	31.22	0.12	25.98	0.15
MnO	0.97	0.03	1.05	0.02	1.18	0.01	1.03	0.01	0.78	0.02	1.09	0.02
MgO	0.55	0.03	0.18	0.02	0.40	0.02	1.26	0.02	0.98	0.01	0.98	0.02
CaO	8.00	0.10	8.72	0.13	9.34	0.11	10.65	0.10	10.57	0.09	11.01	0.17
Na_2O	1.48	0.04	0.71	0.02	0.61	0.02	0.89	0.02	0.81	0.03	0.66	0.03
K_2O	0.62	0.04	n.d.	-	n.d.	-	n.d.	-	0.26	0.01	0.26	0.02
P_2O_5	1.33	0.05	3.89	0.07	3.08	0.07	1.55	0.06	3.91	0.07	3.32	0.06
F	0.05	0.01	0.00	0.00	0.00	0.00	0.84	0.01	0.00	0.00	0.00	0.00
Cl	0.02	0.01	0.01	0.01	0.44	0.03	0.02	0.01	0.02	0.01	0.36	0.03
ReO_2	0.00	0.00	0.00	0.00	0.00	0.00	0.00	0.00	0.00	0.00	0.00	0.00
Total	96.81		95.44		97.17		97.77		98.19		97.08	
n.o.a.	(3)	σ	(2)	σ	(2)	σ	(3)	σ	(7)	σ	(7)	σ
Zn	712.9	17.0	859.5	14.1	979.3	14.3	1121.0	35.6	409.1	11.4	742.1	14.4
Sr	2117.1	28.7	1443.2	170.4	1066.2	7.6	2117.9	35.3	939.1	22.7	1265.7	36.4
Y	1727.9	56.4	2284.9	202.5	1561.1	136.2	1392.0	72.2	940.1	18.0	1460.3	46.1
Ba	3514.8	139.0	4678.8	524.2	2541.0	17.2	2382.3	35.8	1449.0	28.8	2048.0	64.0
La	321.2	5.0	460.2	44.4	266.1	19.5	233.4	8.3	156.4	2.0	232.9	6.5
Ce	714.1	11.4	975.1	71.9	633.5	17.2	545.2	20.4	361.9	5.5	541.8	14.0
Pr	79.7	1.7	104.5	8.0	71.2	4.0	63.1	3.0	41.7	0.6	62.7	1.9

Table B4. *Continued*

Sample	FlAp-9	glass	OHAp-1	glass	ClAp-1	glass	FlAp-1	glass	OHAp-6	glass	ClAp-2	glass
Nd	274.6	7.4	353.7	30.3	253.7	15.2	222.9	12.5	146.6	2.0	223.5	7.5
Sm	81.3	4.1	100.2	7.4	76.2	6.6	68.1	4.4	44.6	1.3	69.4	1.8
Eu	17.1	0.3	17.0	1.1	12.0	0.2	13.3	0.3	8.9	0.2	12.5	0.4
Gd	161.2	5.1	200.1	12.7	149.9	16.0	136.6	9.2	91.4	1.0	142.1	5.6
Tb	42.1	1.5	51.6	2.7	39.2	3.2	34.6	1.9	23.3	0.3	36.3	1.3
Dy	315.1	8.3	393.5	22.9	283.3	30.2	251.9	11.8	170.6	3.5	264.0	9.2
Ho	66.8	1.8	85.0	5.0	59.4	6.1	53.3	1.9	36.0	0.7	55.4	1.9
Er	166.5	5.2	214.4	12.8	147.7	11.5	129.2	6.4	88.6	2.4	136.2	3.7
Tm	20.5	0.8	27.1	2.1	17.9	2.0	15.7	0.6	10.6	0.2	16.1	0.6
Yb	112.1	2.4	149.1	8.2	96.1	9.6	85.3	1.4	58.2	1.5	87.2	2.9
Lu	11.5	0.3	14.9	1.1	9.8	1.3	8.5	0.3	5.8	0.2	8.8	0.3
Th	379.8	8.2	450.6	38.0	284.5	31.3	239.7	1.3	163.0	2.0	237.3	8.6
U	26.1	0.4	20.7	0.2	21.3	0.4	17.3	0.3	10.8	0.2	16.6	0.6

Table B4. *Continued*

Sample	FlAp-8	glass	OHAp-5	glass	ClAp-3	glass	FlAp-7	glass	OHAp-7	glass	ClAp-5	glass	OHAp-1	plag
n.o.a.	(11)	σ	(9)	σ	(10)	σ	(6)	σ	(8)	σ	(12)	σ	(4)	σ
SiO_2	48.07	0.38	43.65	0.34	42.87	0.38	45.14	0.20	41.65	0.59	45.26	0.22	56.52	0.48
TiO_2	4.94	0.12	4.55	0.06	5.77	0.06	2.21	0.04	2.32	0.14	2.72	0.06	n.d.	-
Al_2O_3	9.49	0.12	7.35	0.08	8.69	0.09	11.24	0.15	10.35	0.37	10.43	0.14	27.19	0.18
FeO	17.22	0.32	18.03	0.14	22.18	0.06	18.47	0.22	22.84	0.40	17.25	0.12	0.59	0.02
MnO	1.31	0.02	1.05	0.01	1.52	0.02	1.06	0.01	1.27	0.02	1.04	0.03	n.d.	-
MgO	1.69	0.03	1.20	0.02	1.06	0.02	1.66	0.03	2.06	0.05	1.53	0.02	n.d.	-
CaO	10.95	0.13	15.02	0.23	11.03	0.15	10.44	0.18	11.31	0.09	11.81	0.09	9.88	0.30
Na_2O	1.31	0.04	0.97	0.08	0.74	0.05	0.49	0.07	0.35	0.01	0.45	0.02	4.87	0.22
K_2O	0.44	0.02	0.25	0.02	0.50	0.02	0.08	0.01	0.03	0.01	0.16	0.02	1.25	-
P_2O_5	1.30	0.03	4.35	0.06	2.37	0.06	2.00	0.05	3.37	0.14	1.85	0.09	n.d.	-
F	0.28	0.01	0.00	0.00	0.00	0.00	0.19	0.01	0.08	0.02	0.00	0.00	0.00	0.00
Cl	0.02	0.01	0.03	0.01	0.36	0.03	0.02	0.01	0.01	0.01	0.46	0.02	0.00	0.00
ReO_2	0.00	0.00	0.00	0.00	0.00	0.00	2.21	0.16	2.24	0.10	2.26	0.16	0.00	0.00
Total	97.03		96.44		97.10		95.21		97.88		95.23		98.30	
n.o.a.	(2)	σ	(4)	σ	(2)	σ	(2)	σ	(4)	σ	(6)	σ	(4)	σ
Zn	633.0	28.0	598.7	22.4	676.3	28.7	284.1	11.9	1125.7	94.5	1423.4	33.0	38.8	3.6
Sr	1998.8	42.7	1797.0	24.7	2366.7	34.3	806.6	139.4	878.2	83.8	1900.3	35.4	4001.1	275.3
Y	1168.0	50.1	1513.6	20.8	1704.0	8.6	1492.5	228.2	3224.1	280.7	2265.3	65.1	3.1	1.2
Ba	3031.7	6.0	2674.0	83.3	3346.9	168.7	573.9	126.1	516.1	51.9	1704.6	72.7	2401.3	360.6
La	210.9	7.5	244.8	1.8	344.6	12.0	270.1	54.1	548.1	45.6	349.2	8.6	5.8	0.8
Ce	468.9	12.8	576.8	11.6	769.5	40.8	620.2	135.7	1265.6	91.8	803.5	23.4	9.0	1.2
Pr	51.9	1.4	66.0	1.2	84.5	2.5	69.5	15.4	142.4	12.2	92.4	2.8	0.7	0.1
Nd	178.0	8.3	232.9	2.1	278.5	7.7	237.4	42.0	493.4	46.4	328.6	10.4	2.6	0.3

Table B4. *Continued*

Sample	FlAp-8	glass	OHAp-5	glass	ClAp-3	glass	FlAp-7	glass	OHAp-7	glass	ClAp-5	glass	OHAp-1	plag
Sm	50.2	1.7	71.3	0.9	78.2	1.1	71.9	13.8	148.3	15.8	102.1	6.0	0.6	0.3
Eu	12.3	0.4	14.2	0.4	14.9	0.2	12.3	3.5	24.0	2.7	17.8	0.4	22.5	2.7
Gd	101.6	5.2	146.6	1.7	154.7	2.5	136.8	26.0	295.5	28.8	206.3	6.6	0.5	0.3
Tb	27.4	1.4	37.3	0.4	39.7	0.4	36.0	7.8	78.1	6.9	54.2	2.2	0.1	0.0
Dy	206.3	8.7	273.1	2.3	303.4	9.3	263.4	49.2	580.4	60.1	406.8	9.7	0.6	0.2
Ho	44.2	1.7	57.8	1.1	63.1	1.4	57.1	11.0	125.7	12.1	86.4	3.0	0.1	0.0
Er	114.4	5.1	139.7	1.7	163.5	4.5	141.6	23.5	313.0	35.3	214.9	6.4	0.2	0.1
Tm	14.0	0.8	16.9	0.2	19.3	0.0	17.6	2.1	39.2	4.1	26.2	1.1	0.0	0.1
Yb	80.5	2.8	92.4	1.3	116.0	0.2	97.5	15.2	215.9	23.7	144.4	4.3	0.3	0.3
Lu	8.3	0.3	9.1	0.3	10.9	0.2	10.2	2.2	21.4	2.6	14.7	0.7	b.d.	-
Th	263.6	6.4	238.8	1.8	384.2	29.8	334.2	66.0	690.9	73.0	421.0	15.2	0.1	0.1
U	17.9	1.0	15.8	0.4	26.3	2.8	23.6	5.5	49.7	3.6	29.1	1.2	0.1	0.1

Table B5. Major and trace element data of plagioclase used to develop Eu-in-plagioclase-apatite oxybarometer.

Sample	EU14-13	An-Red-2	An-MORB-2	16	28	17	34	99-1	100-1	101-1	99-7	99-2
T (°C)	1100	1400	1350	1220	1220	1200	1180	1187	1257	1297	1187	1187
P (GPa)	0	0.6	0.6	0	0	0	0	0	0	0	0	0
$\log_{10}(fO_2)$	-13.25	-11.72	-11.22	-11.70	-8.18	-11.90	-8.65	-0.70	-0.70	-0.70	-0.70	-0.70
wt %												
SiO_2	47.14	43.29	46.84	49.98	48.09	50.06	49.3	50.5	47.7	46.2	51.4	52.1
TiO_2	0.09	0.13	0.03	0.05	0.05	0.05	0.04					
Al_2O_3	32.84	35.91	34.77	31.62	31.34	31.35	30.1	29.7	32.3	33.2	29.3	29.1
Cr_2O_3												
FeO	0.88	0.18	0.14	0.3	1.07	0.32	0.86	1.43	1.29	1.09	1.25	1.18
MgO	0.37	0.15	0.22	0.28	0.23	0.31	0.38					
MnO	0.01			0.03	0.02	0.01	0.01					
CaO	17.55	18.78	17.25	15.26	15.92	15.16	14.8	12.3	14.8	16.2	11.8	11.4
Na_2O	1.13	0.18	1.58	2.61	2.31	2.67	2.93	5.5	3.37	2.9	5.51	5.38
K_2O		0.02	0.01	0.02	0.01	0.03	0.02					
NiO												
P_2O_5	0.02			0.04		0.09						
Total	100.03	98.64	100.84	100.19	99.04	100.05	98.44	99.43	99.46	99.59	99.26	99.16
Predicted D_{Eu2+}	1.60	1.30	1.45	1.80	1.75	1.83	1.92	3.07	2.00	1.85	3.07	2.97
Predicted D_{Eu3+}	0.003	0.028	0.044	0.036	0.024	0.029	0.024	0.063	0.057	0.049	0.075	0.084
Measured DEu	0.447	0.538	0.622	0.869	0.242	0.260	0.112	0.148	0.166	0.088	0.123	0.067
Measured sigma DEu	0.093	0.036	0.025	0.084	0.072	0.01	0.012	0.093	0.056	0.056	0.056	-

Table B5. *Continued*

Sample	EU14-13	An-Red-2	An-MORB-2	16	28	17	34	99-1	100-1	101-1	99-7	99-2
Reference	Dygert et al., 2020	Sun et al., 2016	Sun et al., 2016	Aigner-Torres et al., 2007	Aigner-Torres et al., 2007	Aigner-Torres et al., 2007	Aigner-Torres et al., 2007	Bindeman and Davis, 2000	Bindeman and Davis, 2000	Bindeman and Davis, 2000	Bindeman and Davis, 2000	Bindeman and Davis, 2000

Table B5. *Continued*

Sample	99-5	100-4	100-6	101-4	101-3	NP5	SDP	DAD1	DAD2	SDD	AR 992	377
T (°C)	1187	1257	1257	1299	1299	1176	1142	1264	1263	1265	1127	1177
P (GPa)	0	0	0	0	0	0	0	0	0	0	0	0
$\log_{10}(fO_2)$	-0.70	-0.70	-0.70	-0.70	-0.70	-12.94	-12.94	-0.68	-0.68	-0.68	-13.91	-12.23
wt %												
SiO_2	50.1	46.7	47.80	48.20	44.80	49.77	51.99	46.25	46.14	46.45	53.24	43.2
TiO_2												0.02
Al_2O_3	29.1	31.9	32.10	32.30	33.20	31.77	29.97	33.62	33.83	33.87	29.67	36.6
Cr_2O_3												
FeO	1.41	1.22	1.05	0.81	0.91	0.39	0.28	0.06	0.04	0.03	0.39	0.27
MgO												0.25
MnO												
CaO	12.3	15.3	14.90	15.00	17.1	15.36	14.69	18.38	18.43	18.15	13.3	20.4
Na_2O	6.13	3.97	3.50	3.00	3.13	2.64	3.01	1.47	1.43	1.45	3.17	
K_2O						0.07	0.05	0.21	0.13	0.05	0.23	
NiO												
P_2O_5												
Total	99.04	99.09	99.35	99.31	99.14	100	99.99	99.99	100	100	100	100.74
Predicted D_{Eu2+}	3.61	2.22	2.04	1.87	1.92	1.84	1.95	1.57	1.57	1.57	2.00	1.45
Predicted D_{Eu3+}	0.062	0.045	0.055	0.083	0.031	0.020	0.018	0.014	0.014	0.016	0.024	0.002
Measured D_{Eu}	0.073	0.089	0.053	0.062	0.069	0.942	0.961	0.015	0.015	0.015	1.416	0.503

Table B5. *Continued*

Sample	99-5	100-4	100-6	101-4	101-3	NP5	SDP	DAD1	DAD2	SDD	AR 992	377
Measured sigma D_{Eu}	0.014	0.026	0.045	0.005	-	0.135	0.160	0.005	0.006	0.002	0.035	-
Reference	Bindeman and Davis, 2000	Bindeman and Davis, 2000	Bindeman and Davis, 2000	Bindeman and Davis, 2000	Bindeman and Davis, 2000	Tepley et al., 2010	Tepley et al., 2010	Tepley et al., 2010	Tepley et al., 2010	Tepley et al., 2010	Tepley et al., 2010	McKay et al., 1994

Table B6. Major and trace element data of coexisting apatite and plagioclase used to calculate the fO_2s using the Eu-in-plagioclase-apatite oxybarometer.

	OHA p-1-plag	σ	OHA P-1-apt	σ	HaH 193-plag	σ	HaH 193-apt	σ	ON-07–120-plag	σ	ON-07–120-apt	σ	ON-07–125-plag	σ	ON-07–125-apt	σ
SiO_2	56.52	0.48	0.79	0.17	61.9	0.3	b.d.	-	0.37	-	59.90	-	0.21	-	57.79	-
TiO_2	n.d.	-	0.07	0.02	n.d.	-	n.d.	-	n.d.	-	n.d.	-	n.d.	-	n.d.	-
Al_2O_3	27.19	0.18	0.04	0.02	23.3	0.2	b.d.	-	n.d.	-	25.56	-	n.d.	-	26.63	-
FeO	0.59	0.02	1.99	0.26	0.19	0.14	0.4	0.07	n.d.	-	0.68	-	n.d.	-	1.01	-
MnO	n.d.	-	0.3	0.04	n.d.	-	n.d.	-	n.d.	-	n.d.	-	n.d.	-	n.d.	-
MgO	n.d.	-	0.06	0.04	n.d.	-	n.d.	-	n.d.	-	n.d.	-	n.d.	-	n.d.	-
CaO	9.88	0.3	53.21	0.61	4.44	0.08	54.4	0.8	54.57	-	6.86	-	54.57	-	7.93	-
Na_2O	4.87	0.22	0.05	0.01	8.92	0.03	b.d.	-	0.05	-	13.83	-	0.06	-	13.25	-
K_2O	1.25	-	n.d.	-	0.4	0.03	b.d.	-	0.00	-	0.91	-	0.00	-	0.57	-
P_2O_5	n.d.	-	40.24	0.3	b.d.	-	41.8	0.3	40.71	-	n.d.	-	40.77	-	n.d.	-
Cr_2O_3	n.d.	-	n.d.	-	n.d.	-	n.d.	-	n.d.	-	n.d.	-	n.d.	-	n.d.	-
F	0	0	0	0	b.d.	-	3.38	0.73	2.92	-	n.d.	-	3.22	-	n.d.	-
Cl	0	0	0.04	0.04	b.d.	-	0.71	0.08	0.12	-	n.d.	-	0.12	-	n.d.	-
(ppm)																
La	5.5	0.9	914.3	-	0.71	0.13	7.1	0.04	12.26	-	906.59	-	6.6	-	776.45	-
Ce	8.8	1.1	2726	-	1	0.3	20	1	18.28	-	2424.89	-	10.78	-	1997.41	-
Pr	0.7	0.1	350.7	-	0.072	0.017	2.9	0.2	1.72	-	375.76	-	1.06	-	287.09	-
Nd	2.7	0.3	1220.3	-	0.19	0.04	17	1	5.48	-	1808.46	-	3.59	-	1373.74	-
Sm	0.6	0.3	378.8	-	0.025	0.007	6.2	0.5	0.66	-	411.05	-	0.5	-	288.4	-
Eu	21	3.9	38.9	-	0.4	0.09	0.69	0.07	11.39	-	56.81	-	7.25	-	47.52	-
Gd	0.6	0.3	760.8	-	0.015	0.007	8	0.7	0.41	-	387.89	-	0.35	-	271.24	-
Tb	0.1	0.1	190.2	-	b.d.	-	1.7	0.1	0.05	-	48.55	-	0.04	-	32.5	-

Table B6. *Continued*

	OHAp-1-plag	σ	OHAP-1-apt	σ	HaH 193-plag	σ	HaH 193-apt	σ	ON-07–120-plag	σ	ON-07–120-apt	σ	ON-07–125-plag	σ	ON-07–125-apt	σ
Dy	0.7	0.3	1215.8	-	0.012	0.003	9.7	0.5	0.23	-	266.6	-	0.19	-	164.52	-
Y	3.9	1.9	6427.5	-	0.064	0.006	n.d.	-	1.01	-	1196.93	-	0.88	-	734.33	-
Ho	0.1	0.1	248.6	-	b.d.	-	2.4	0.2	0.04	-	48.07	-	0.03	-	28.07	-
Er	0.3	0.2	660.4	-	b.d.	-	5.5	0.3	0.1	-	120.44	-	0.08	-	64.57	-
Tm	0	0.1	64	-	b.d.	-	0.7	0.08	0.01	-	13.03	-	0.01	-	6.91	-
Yb	0.3	0.2	320.5	-	0.003	0.002	5.2	0.3	0.09	-	66.11	-	0.06	-	35.74	-
Lu	b.d.	-	28.2	-	b.d.	-	0.59	0.09	0	-	8.91	-	0	-	4.6	-
Ref.	This study		This study		Floss et al. (2007)		Floss et al. (2007)		Kieffer et al. (2023)[a]		Kieffer et al. (2023)[a]		Kieffer et al. (2023)[a]		Kieffer et al. (2023)[a]	

Table B6. *Continued*

	S9-148-plag	σ	S9-148-apt	σ	S9-208,8-plag	σ	S9-208,8-apt	σ	S9-214,8-plag	σ	S9-214,8-apt	σ
SiO_2	0.12	-	55.02	-	0.26	-	60.17	-	0.12	-	52.99	-
TiO_2	n.d.	-	n.d.	-	n.d.	-	n.d.	-	n.d.	-	n.d.	-
Al_2O_3	n.d.	-	27.65	-	n.d.	-	25.94	-	n.d.	-	30.00	-
FeO	n.d.	-	2.38	-	n.d.	-	0.39	-	n.d.	-	0.56	-
MnO	n.d.	-	n.d.	-	n.d.	-	n.d.	-	n.d.	-	n.d.	-
MgO	n.d.	-	n.d.	-	n.d.	-	n.d.	-	n.d.	-	n.d.	-
CaO	53.65	-	8.54	-	53.84	-	6.22	-	53.92	-	10.55	-
Na_2O	0.04	-	11.69	-	0.06	-	14.25	-	0.02	-	11.01	-
K_2O	0.00	-	0.23	-	0.01	-	1.68	-	0.00	-	0.10	-
P_2O_5	40.44	-	n.d.	-	40.90	-	n.d.	-	40.73	-	n.d.	-
Cr_2O_3	n.d.	-	n.d.	-	n.d.	-	n.d.	-	n.d.	-	n.d.	-
F	3.33	-	n.d.	-	3.69	-	n.d.	-	3.19	-	n.d.	-
Cl	0.09	-	n.d.	-	0.05	-	n.d.	-	0.08	-	n.d.	-
(ppm)												
La	6.71	-	492.33	-	16.38	-	1045.43	-	3.44	-	328.59	-
Ce	10.31	-	1307.82	-	21.89	-	2620.46	-	5.72	-	896.56	-
Pr	0.97	-	191.06	-	1.87	-	361.86	-	0.6	-	143.61	-
Nd	3.17	-	899.07	-	5.53	-	1661.21	-	2.24	-	734.69	-
Sm	0.33	-	197.23	-	0.57	-	341.3	-	0.29	-	175.5	-
Eu	2.99	-	45.65	-	6.69	-	37.56	-	2.63	-	57.38	-
Gd	0.22	-	188.49	-	0.62	-	306.83	-	0.17	-	176.29	-
Tb	0.02	-	22.78	-	0.03	-	38.07	-	0.02	-	21.22	-
Dy	0.08	-	121.33	-	0.21	-	201.04	-	0.15	-	108.21	-
Y	0.32	-	547.16	-	0.43	-	987.68	-	0.27	-	456.64	-

Table B6. *Continued*

	S9-148-plag	σ	S9-148-apt	σ	S9-208,8-plag	σ	S9-208,8-apt	σ	S9-214,8-plag	σ	S9-214,8-apt	σ
Ho	0.01	-	21.17	-	0.04	-	34.79	-	0.02	-	18.53	-
Er	0.03	-	49.44	-	0.08	-	84.42	-	0.05	-	42.76	-
Tm	0	-	5.39	-	0.06	-	8.96	-	0.01	-	4.4	-
Yb	0.02	-	27.94	-	0.02	-	45.8	-	0.1	-	22.3	-
Lu	0	-	3.73	-	0.06	-	6	-	0.12	-	2.94	-
Ref.	Kieffer et al. (2023)[a]		Kieffer et al. (2023)[a]		Kieffer et al. (2023)[a]		Kieffer et al. (2023)[a]		Kieffer et al. (2023)[a]		Kieffer et al. (2023)[a]	

[a]. The major element concentrations of plagioclase are calculated by La-ICM-MS results in Table S5B from Kieffer et al. (2023).

CONCLUSION

Geochemical modeling is a widely applied method that researchers use to constrain the elemental fractionation of the Earth and other celestial bodies, and is especially useful when physical samples are limited, as with astromaterials (e.g., Elardo et al., 2011; Tang et al., 2016; Hahn Jr et al., 2017). This thesis includes new modeling approaches and experimentally-determined model inputs that advance our knowledge of lunar evolution. In Chapter 1, we modeled the REE concentrations and Eu anomalies of plagioclase crystallized by LMO solidification using recent experimentally-determined fractional crystallization experiments and mineral-silicate melt partition coefficient models. We compared our calculation with plagioclase from Apollo ferroan anorthosites and lunar anorthositic meteorites. Plagioclase directly crystallized from the LMO exhibits larger Eu positive anomalies and relatively constant REE slopes under lunar related fO_2. We tested a series of possible secondary processes and found that subsolidus reequilibration after the addition of ~1% of the KREEPy component can help to reproduce the plagioclase trace element characteristics. Monte-Carlo simulations showed that the lunar anorthosites evolved in an environment with an fO_2 of ~IW-2 at Ts of 1050 - 1250℃ after addition of a <1% KREEPy component, and that the initial REE pattern of the LMO is slightly light REE depleted, which is consistent with the isotopic evidence from lunar samples. A model for the evolution of the crust after the LMO stage has been proposed. As the LMO solidified, the abundance of Fe and incompatible elements in the residual liquid continued to increase, forming a gravitationally unstable cumulate pile. The unstable density structure triggered lunar mantle cumulates overturn so that the hot materials from the interior of the Moon upwelled and heated the lunar crust, forming a large number of low-density subsolidus diapirs that floated and migrated to the lunar surface. Diapirs were contaminated by KREEPy melts before or during upwelling, leading to extensive subsolidus reequilibration.

Apatite, as an accessory mineral in igneous and metamorphic rocks, plays an important role in tracking element fractionation and redistribution due to its capacity to substitute trace elements into its mineral structure. However, during the LMO solidification modeling conducted in Chapter 1, we found that there was no partitioning model that could predict the trace element partition coefficients between apatite and silicate melts. In Chapter 2, we conducted high-temperature and high-pressure experiments in order to expand the apatite partitioning dataset, reporting data from 12 experiments, and used the new data to develop predictive partitioning models. The experiments explored the temperature range of 1050 to 1100 ℃, with approximately 4 log unit fO_2 variation, from IW-0.7 to IW+3.1, at 1GPa. In each experiment we doped only one species of anion to create apatite compositions close to three endmembers (i.e., fluorapatite (FlAp), hydroxylapatite (OHAp) and chlorapatite (ClAp)). The results show that apatites in ClAp experiments are unique as they exhibit a factor of two to three lower REE partition coefficients than those of FlAp and OHAp, and positive Eu anomalies, whereas apatites in the FlAp and OHAp experiments exhibit negative Eu anomalies. We developed temperature and composition-dependent predictive partitioning models for divalent and trivalent elements and the models successfully reproduce almost all the apatite REE partitioning data within a factor of two. Due to the dependence of Eu^{2+}/Eu^{3+} on fO_2, we developed an fO_2-dependent predictive partitioning model for Eu between apatite and silicate melt, and a new Eu in apatite-plagioclase oxybarometer. Utilizing this oxybarometer, we calculated the fO_2s of rocks from three different systems: a piston-cylinder experiment, the winonaite HaH 193, and several samples from Sept Iles layered intrusion; the results are consistent

with anticipated fO_2s determined using other methods. In addition, we evaluated the effect of time-dependent subsolidus reequilibration on our oxybarometer. We observed that the incorrect evaluation of equilibrium temperature will overestimate the fO_2 of the system, that during subsolidus cooling, the larger the grain size of apatite and the lower the new equilibrium temperature, the larger the calculated fO_2 deviation from the actual fO_2. Finally, we applied our predictive apatite-melt partitioning model to evaluate trace element fractionation during LMO solidification, and found that partial melting of apatite-bearing LMO cumulates can successfully model the petrogenesis of lunar KREEP basalt. We find the late-stage LMO cumulates are relatively Cl depleted in mole percent compared with the sum of F and OH, suggesting the differential degassing of Cl relative to F and/or OH occurred before or during the late-stage of LMO crystallization.

VITA

Dian Ji was born in Wuhan, Hubei Province, China. After graduating from NO.1 Middle School Affiliated to Central China Normal University, he enrolled in China University of Petroleum in Beijing to study Resource Exploration Engineering. Unlike the experience of many geologists, since growing up in the city Dian had little access to nature and knew almost nothing about geology before attending college. But when he actually had the opportunity to learn about geoscience, he was soon fascinated. Although his undergraduate major was more focused on petroleum geology and engineering, his interest led him to look for research opportunities in igneous petrology. In the summer of 2019, Dian was offered the opportunity to travel to the University of Texas at Dallas as a short-term scholar to work with Dr. Robert J. Stern. The two months in Texas allowed him to learn more cutting-edge igneous geochemistry theory and strengthened his resolve to become an igneous petrologist. In early 2020, Dian published his first first-author paper in *International Geology Review* under the supervision of Dr. Huichuan Liu, studying the petrogenesis of Early Cretaceous adakite in Northeast China. This work also helped him to be awarded the 2020 Li Siguang Outstanding Student Award, the highest undergraduate geoscience award in China. The same year Dian was admitted by the Department of Earth and Planetary Sciences at the University of Tennessee as a master's student. Unfortunately, the COVID-19 Pandemic stopped Dian from coming to Tennessee, but he continued his research on numerical simulations of lunar anorthositic crustal with the help of his advisor, Dr. Nicholas Dygert. This work was published in *Earth and Planetary Science Letters* in early 2023. He finally arrived at the University of Tennessee in May 2021, where he systematically studied mineralogy, igneous petrology, lunar geology, numerical modeling, and geochemical kinetics. His proposal for the apatite-silicate melt trace element partitioning experimental research was funded by the Mineralogical Society of America Grant for Student Research in Mineralogy and Petrology in the summer of 2023. Dian will move to Houston and join the Ph.D. program at Rice University after obtaining his M.S. degree.